Scalable Networks of Engineered Extracellular Matrix as Biomimetic Tissue Culture Models with Defined Heterogeneity

by

Dylan B. Neale

A dissertation submitted in partial fulfillment
of the requirements for the degree of
Doctor of Philosophy
(Chemical Engineering)
in the University of Michigan
2022

Doctoral Committee:

Professor Joerg Lahann, Chair
Assistant Professor Brendon Baker
Professor Gary Luker
Professor Sunitha Nagrath

Dylan B. Neale

dneale@umich.edu

ORCID iD: 0000-0002-0306-9498

Dedication

To my daughter, Blaire, and my mother, Nancy, I would be nothing without your love, support, and inspiration.

Acknowledgements

Graduate school was the most challenging, rewarding, and transformative experience of my life. From the time I was 11, my passion to pursue bioengineering was founded, but having attended a high school with more cows and chickens on campus than scientists in the community, this journey would not have been realized without the amazing individuals that have supported me along the way. I want to recognize my high school teachers Fran Copp, Edwin Fretz, and Judy Castillo who catalyzed my love for math, chemistry and literature that coalesced during my Ph.D. training. To my mother, Nancy, you have supported me with the deepest and most sincere love I have ever known. I would not have made it here were it not for you. Dedicated to self-betterment, you juggled so many things in order to improve our lives and provide your family. From this, I learned resilience and dedication that have seen me through numerous challenges in graduate school. I have learned to enjoy the process and the little successes along the way from you as well as my incredible Ph.D. advisor.

To my advisor, Joerg Lahann, from the first time I chased you down in the hallway to discuss a situation gone awry, to now, you have been an incredible support, and I'm deeply grateful that our paths aligned. Under your mentorship, I have grown tremendously as a scientist and engineer into a better human, and fortified my ability give back to society with an outstanding education. Your pragmatic judgement coupled with boundless academic curiosity was the balance I needed to flourish. Your multi-national lab is a transformative experience transcending beyond the typical academic experience. Not only do you attract scientists that are among the best in the world, but the unique cultural diversity of your lab opened my mind to

global struggles and perspectives that have transformed me for the better. Right out of the gate, the expectation to present updates every week to this large group was daunting, but now I appreciate the output driven mindset and toughness it fosters. I'll never forget one Thursday night that I thought I made it off the hook, just to see "...and Dylan" come in a few minutes later to the group listserv, which I fondly laugh about in reflection. The way you encourage your students and postdocs to explore their individual scientific curiosities is incredibly unique. With humility, you welcome new ideas and take an optimistic, success-driven mindset when their proof of concept is vetted. Despite your incredible successes, you are always willing to listen and adjust, even if it means changing up entire group-wide structures. You are truly committed to your students, and in these ways, organically cultivate scientific independence and train high-powered generations of scientists, engineers and leaders. You have empowered me, pushed me, or taken a step back from the professional relationship to support me as an individual when I needed it. I have all the respect, admiration and appreciation for you believing in me and supporting me over these years.

To my committee, Gary Luker, Sunitha Nagrath, and Brendon Baker – you all have been wonderful mentors, didacts, and scientific collaborators over the years. You all embody the beauty of Michigan's multi-disciplinary collaborative scientific community. You all were always willing to spare time to meet, discuss new ideas, commit resources, and follow through on the success of these endeavors. You all provided astute judgement that critically directed the successes of my projects while being approachable and incredibly pleasant to work with. I could not have asked for a more supportive and wonderful committee to see me through the challenges of graduate school. I would also like to extend a special thank you to Jeffery Raymond, who joined our group toward the end of my Ph.D., but in this short time has made a huge impact in

providing scientific mentorship while being an all-around amazing person. To all of my scientific mentors, through your commitment and support, we have co-authored multiple manuscripts, and I am incredibly thankful to you all for fostering my development and thereby my success in graduate school.

I'd like to acknowledge funding primarily from the National Science Foundation as well as the National Institute of Health that supported the work in my dissertation. Additionally, I want to thank the BioInterfaces Institute (University of Michigan), the NSF's Cell-Met consortium, the NIH's U01-Physical Sciences in Oncology (PS-ON), the Michigan/Israel Partnership for Research and Education, the Helmholtz Association for BioInterfaces in Technology and Medicine, as well as the NIH T32 Cellular Biotechnology Training Program (CBTP) which supported me personally as an NIH-trainee. A specific thanks to the U01 PS-ON network which over the years was comprised of wonderful researchers from Sunitha Nagrath's, Gary Luker's, Joerg Lahann's, and Max Wicha's lab who were instrumental in my dissertation work. I want to thank Jeffery Raymond, Johanna Buschhaus, Grace Bushnell and Ella Wawrysyzn for your commitment, especially in this last year. You all helped me to ensure success of this final work and provided various levels of support. I am excited to see this publication make its way to print in the near future to exemplify our progress on this challenging, multi-disciplinary topic that could not have been successful without the deep expertise that you all brought to the project in your respective fields.

I'd like to acknowledge all of the other people at UM ChE that helped me along the way. Lola Eniola-Adefeso, I will never forget the late-night call we had as I was floundering on my graduate school decision – thank you for giving me a chance and bringing me to this wonderful community. To the other amazing people in my cohort, especially, Abdulla Alqubati, Vyas

Ramasubramani, Alison Banka, and Sarah Owen – thank you so much for being amazing colleagues and delightful humans. To the staff that keep things running: Susan Hamlin, Mary Beth Westin, Lisa Moran, Karl Olsen, and especially Nadine Wong – thank you all. You all selflessly commit to keeping the wheels turning so graduate students can focus on our research, and you do so with a wonderful demeanor that makes the community an enriching place to work. Thanks to my work colleagues, and scientific collaborators turned friends that have contributed to the success of my work whilst making the experience more enjoyable along the way: Johanna Buschhaus, Michael Brooks, William Wang, and Brock Humphries.

To the members of the Lahann Lab early on that helped me get started: Stacy Jordahl, Jake Jordahl, Ramya Kumar, Kenneth Cheng, Luis Solorio – thank you all for your guidance, support and the foundation that I built upon. To those lab mates that became incredible friends: Nahal Habibi, Ayşe Muñiz, and Artak Shaknas, thank you for the plethora of memories, the enlightening discussions, the hilarity at the bench, the successful research, and even those 4 AM lab selfies Nahal and I shared in our final months in the lab. To my closest mentees: Grayson Rice, Robert Stinson, Diego Vargas and Malini Mukherji, your dedication is deeply valued, and I hope you found that commitment to your individual successes reciprocated. To all of the other members of the Lahann Lab (or honorary Lahannians), thank you for making the lab an amazing place and for the support that we all provided each other at the bench, at group meetings, in subgroup or outside the lab: Angela Sze, Daniel Quevedo, Yeongun Ko, John Kim, Fjorela Xhyliu, Albert Chang, Yao Yao, Xiaoyang Zhong, Anthony Berardi, Laura Saunders, Ava Mauser, Jason Gregory, Divya Varadharajan, Marvin Klaiber, and Judith Witte (and any others I forgot to list). To the next generation of the tissue engineering subgroup, Do Hoon Kim, I am excited to see your unique ideas and dedication push the platform forward. I know the legacy

laid out before me will be carried on by you, and I am confident success will be realized with you at the helm. Nevertheless, I stay committed to your success and the success of the projects.

Thank you to all of the other contributors and amazing people at Michigan and abroad who have shared in enlightening discussions or helped in other ways to enable the success of the works presented in this dissertation: Tae Hwa Chun, Adrian Shimpi, Claudia Fischbach, Soroush Moghadam, Zackary Dodson, Leonel Munoz-Sagredo, Yvonne Heneka, Véronique Orian-Rousseau, Michael Smith, Todd Heron, Andre Monteiro Da Rocha, Nicole Kotov, Robin Wilhelm, Ariel Szklanny, and Shulamit Levenberg.

To the closest friends I've developed along the way: Mario Guitierrez, Steven Chavez, and Bobby Graham – there is nothing I can put into text to capture the innumerable experiences we have shared over the last years. Your advice, your comradery, and the countless moments of hilarity were part of what made everything worthwhile. Steven, I know you had your doubts about me at first given our seemingly disparate backgrounds, but I cherish the depth of relationship we cultivated. You have been through it all – from our first-year apartment that was way too far from the NCRC through all the successes, failures, fatherhood, and now our thesis defenses within a month of each other. It has been incredible to see this journey come full circle.

To my other family members that provided unconditional love and support: Clay, Matthew, Robert, Stephanie, Ryan, Rachel – thank you all. Also, to Lindsay Anderson, you have been such an amazing support these last months, inspiring me to support your endeavors in what became an amazing reciprocity. To my father, Robert, thank you for the curious discussions as a child that sparked my interest in academics and my thirst for knowledge which became actionable after a direct leap to university despite financial struggles. I knew it was the right decision within the first week, as the passion burning in my soul resulted in a self-affirmation

that I would pursue my Ph.D. with virtually no conception of what that entailed. I am grateful to those mentors at the University of Florida: Bradley Willenberg, Christopher Batich, Scott Perry, Chelsea Magin, Alex Rudy, Dave Sullivan that recognized and supported my passion.

To Scott Johnson and Mario Guitierrez, I have to extend a special thank you to you both. When I hit my lowest and thought about quitting something for the first time in my life, the two of you gave me an important life lesson that I've carried with me for the last five years embodied by the following quote:

"The ultimate measure of a man is not where he stands in moments of comfort and convenience, but where he stands at times of challenge and controversy"

– Martin Luther King Jr.

Finally, to my daughter, Blaire Adelaide Neale, you have been my guiding light these last 4 years. I have fallen back on memories of your charm, your wittiness, your sweet demeanor and the other amazing qualities you exude in order to get through the most challenging moments. Even in the craziest times of putting you into bed, heading to the lab and starting experiments at 9 PM, I had your love and your future in mind to empower me. I see the spark of curiosity for science and knowledge glint in your eyes when I explain the beautiful chemistry, physics, and biology surrounding us at all times. I am excited for what your future holds and will continue to support your successes, as you have mine in ways you cannot yet comprehend. I love you more than anything in the world, my little Blaire Bear.

Table of Contents

Dedication ii

Acknowledgements iii

List of Tables xiv

List of Figures xv

Abstract xxii

Chapter 1 Introduction 1

1.1 Publication Information 1

1.2 The Problem at Hand 1

1.2.1 The Global Burden of Cancer and Impact of the Microenvironment 1

1.2.2 The Inefficiencies and Complexities of Preclinical Drug Screening 1

1.2.3 The Need for 3D In Vitro Models 3

1.2.4 Clinical Translation and Regulatory Considerations 5

1.3 The Moving Target: Tissue Complexity and Heterogeneity 6

1.3.1 The Foundation of Tissue: The Extracellular Matrix 6

1.3.2 Tissue Remodeling in Breast Cancer 7

1.4 Biomaterial Candidates for Engineered Tissue Systems 8

1.4.1 Synthetic Materials 9

1.4.2 Naturally Derived Materials 12

1.5 The State of the Art: Approaches and Limitations 13

1.5.1 Polymeric Scaffolds and Synthetic Hydrogels 13

1.5.2 High Resolution Manufacturing – Two Photon Polymerization 14
1.5.3 Bioprinting and Natural Hydrogels 15
1.5.4 Cell-assemblies: Spheroids and Organoids 17
1.5.5 Cell Secretions and Decellularized Tissues 18
1.6 Defining the target: Biomaterial Characterization, Benchmarking, and Validation 18
1.6.1 Biomaterials characterization and its challenges 18
1.6.2 Functional Benchmarking and Tissue Characterization 20
1.7 A hybrid approach to biomaterials for preclinical modeling 21
1.7.1 Tissue as Composite Materials 21
1.7.2 Leveraging Engineered Extracellular Matrices to Model Native-ECM 22
1.8 Scope of this Work 23
Chapter 2 Engineered Fibrillar Fibronectin and its Characterization 26
2.1 Publication Information 26
2.2 Abstract 26
2.3 Introduction 27
2.3.1 Fibronectin, a Foundational ECM Molecule 27
2.3.2 Protein Adsorption on Surfaces 28
2.3.3 Biomaterial Mechanical Characterization 28
2.3.4 Fn Biomaterials 29
2.4 Results and Discussion 30
2.4.1 Fn EECM Stability, Degradability and Bioactivity Compared to Cell Secretions 30
2.4.2 Fn-Collagen EECMs and Fn EECM Mechanical Properties 36
2.5 Conclusions and Implications 38
Chapter 3 Aligned Networks of Engineered Fibrillar Fibronectin Guide Cellular Orientation and Motility 40
3.1 Publication Information 40

3.2 Abstract 40

3.3 Introduction 41

3.4 Results and Discussion 43

3.4.1 Polymer Scaffold Geometry and Orientation Induces Fibril Alignment During Hydrodynamically-induced Fibrillogenesis 43

3.4.2 Precisely aligned 3D fibronectin networks across the tissue length scale 47

3.4.3 Aligned Fibronectin Networks Influence Fibroblast Orientation and Polarity 55

3.4.4 Aligned Fibronectin Guides Fibroblast Motility 59

3.4.5 Supplemental Discussion and Figures 62

3.5 Conclusions and Implications 67

Chapter 4 Hyaluronan Decorated Fibrillar Fibronectin Constructs Modulate Metastatic Potential in Breast Tumor Cells 69

4.1 Publication Information 69

4.2 Abstract 69

4.3 Introduction 70

4.4 Results and Discussion 73

4.4.1 Defined Derivatization of HA Enables Minimally Modified Thiol Reactive Species 73

4.4.2 Fn EECMs Assemble According to Biomimetic Hallmarks Enabling a Site-specific HA-Conjugation Strategy 78

4.4.3 Thiol Conjugation Strategy Enables Highly Controlled Presentation of Fibrillar Fn and HA in Three-dimensions 83

4.4.4 Fn-HA EECMs Display Tumor-mimetic Morphology and Biochemistry 88

4.4.5 Fn-HA EECMs Allude to Complex Role of Protein-glycan Regulation in Tumor Tissue 91

4.5 Conclusions and Implications 102

Chapter 5 Methods 107

5.1 Publication Information 107

5.2 Deoxycholate Treatment 108
5.3 Proteomics 108
5.4 Materials and SU-8 Fabrication 109
5.5 Protein Coating 109
5.6 Fluid Flow Modeling 110
5.7 Cell Culture 111
5.8 Cell Elongation Imaging 111
5.9 Cell proliferation assay 111
5.10 Fluorescence staining and visualization 112
5.11 Live Cell Migration Assay 112
5.12 Directionality Analysis 113
5.13 Statistics 113
5.14 Decellularization 114
5.15 HA Synthesis Materials 114
5.16 HA Synthesis and Purification 114
5.17 HA-Fn Bioconjugation 115
Chapter 6 Summary and Future Directions 117
6.1 Publication Information 117
6.2 Summary and Lessons Learned 117
6.3 Future Directions for EECMs 119
6.3.1 High Throughput Technological Bridge Systems Using Photolithography 119
6.3.2 Combining Fn Assembly Techniques with 3D printing – Spatial Selectivity of Cell Seeding on EECMs 122
6.3.3 Using Fluidic Devices to Create Micro to Multi-centimeter Constructs 123
6.4 Reflection and Outlook 125
Appendix A 127

SU-8 Scaffold Fabrication Protocol 127

References 132

List of Tables

Table 3.1 A summary of fibronectin-based biomaterials and their characteristics. Documented are the methods of Fn assembly, the ability to control orientation in order to create aligned or non-aligned matrices, the dimensionality (i.e. 2D/3D), overall x-y material scale, fiber diameters, their microstructure, and the type of substrate (i.e., free standing, suspended, or adhered to a surface/2D material). If a material is noted as 2.5D that indicates that the Fn network is relatively thin but are suspended or freestanding in such a way that differs from a conventional 2D substrate. n.r. – not reported, FS – free standing; Sus. – suspended, Adh. – adhered to a 2D substrate 42

Table 3.2 Top: SEM of a SU-8 TPS. Reported in the table are target values versus measured. Measured values came from images taken in DPBS, representing the geometry in situ during the coating process. Height was measured using contact profilometry in a dry state. Data reported as average ± standard deviation. 67

List of Figures

Figure 1.1 Illustration of extracellular influences on cell fate and critical hallmarks to consider when defining engineered systems 22

Figure 2.1 Characterization of Fn EECM stability and degradability using classic descriptions and model cell lines. A: fFn networks remain intact after deoxycholate treatment. (Left) Fn (green) deposited by hydrodynamically induced fibrillogenesis onto a tessellated scaffold. (Right) Fn (green) deposited by hydrodynamically induced fibrillogenesis onto a tessellated scaffold after 1% deoxycholate treatment. The scale bar in (A) is 50 μm. B: illustration of well plate format (24-well) with EECMs attached to steel frames for use in cell culture. C: Representative images of MCF7 and MDA-MB-231s grown on Fn EECMs. D: Normalized metabolic activity to quantify proliferation on EECMs..... 31

Figure 2.2 EECM stability during culture with NIH-3T3s. CLSM MIP of an aEECM prior to cell seeding (0 d) and approaching cell saturation (4 d), where cells can be observed in the differential interference contrast (DIC) image..... 32

Figure 2.3 Hydrodynamically induced fibrillogenesis of fibronectin results in fFn that is recognized by IST-9 antibody. A: graphical scheme of experimental procedure. B, C, D (left two columns): non-woven PLGA nano/micro-fiber mats with Fn statically adsorbed. E,F,G: Fn fibrils following hydrodynamic fibrillogenesis across PLGA TPS. Grayscale images in both left and right groups are DIC images (left) corresponding to colored fluorescent image (right). B: Non-specific Fn polyclonal Ab (pAb) (green) staining of Fn statically adsorbed on PLGA fibers. C: Fn-3 antibody staining (purple) of Fn adsorbed on PLGA fibers. D: Specifc mAb (IST9) staining to identify EDA-Fn (orange) for Fn adsorbed on PLGA fibers. E: pAb for Fn (green) on fFn EECM. F: Fn-3 Ab (purple) on fFn EECM. G: IST-9 staining for EDA-Fn on fFn EECMs (orange) (right). Both the Fn-3 and IST-9 antibody only stain positive on fFn networks but not conformally deposited Fn. All scale bars 100 mm 33

Figure 2.4 Proteomics analysis confirms presence of EDA sequence in fibronectin sourced for fFn EECMs. Two peptides unique to the alternatively spliced domain A (EDA) sequence were identified in the soluble fibronectin sourced for fFn network formation. Mass spectrometry results are shown for tryptic EDA peptides A-B: N-terminus labelled as b ion and Cterminus labelled as y ion. C: Sequence coverage map of fibronectin where yellow highlight indicates amino acid detection. The amino acid sequence highlighted by the red boxes indicate the EDA portion. At least 71% sequence coverage was reported. Sequence coverage may be greater than 71% and as high as 82%, if variable regions susceptible to modification during analysis are included..... 34

Figure 2.5 Fibronectin and collagen co-assembly in EECMs. A: fFn EECM with FITC-COL / FN. SHG imaging of native COL/FN (right column). Below is image quantification demonstrating control over mass ratio. B: fFn EECM with native Fn and COL-I. SHG imaging of native COL/Fn. In collaboration with J. Buschhaus, Luker Lab Scale bars: 100μm 36

Figure 3.1 Polymer scaffold geometry and orientation induces fibril alignment during hydrodynamically-induced fibrillogenesis. A: SEMs of TPSs with rectangular pore geometries made from SU-8 via photolithography. Scale bars are 500 μm (architecture) 250 (orientation) μm. B: illustration depicting how TPSs are coated via hydrodynamically induced fibrillogenesis to produce aligned or non-aligned 3D Fn matrices. C: Top-down view of COMSOL model revealing flow profiles when TPS pore direction is perpendicular or parallel to flow direction. Black arrows indicate the direction of fluid flow on the inlet side. Streamlines are shown in black and plotted over the velocity profile which is depicted via color from 0 m s−1to 0.018 m s−1. . 44

Figure 3.2 Time-lapse 2D fluid model to assess flow characterics in microcentrifuge tubes at 1.45 s (8 RPM) used to evaluate the velocity of fluid flow during hydrodynamically-induced fibrillogenesis. Arrows and colors of the arrows (white to red scalar) indicate the direction of flow and velocity, respectively. The two phases (fluid, air) are depicted with the blue to red scalar. 45

Figure 3.3 3D perspectives of the fluid flow profile across perpendicular (A) and parallel (B) oriented TPSs. Black arrows indicate fluid flow direction on the inlet side of the model. Streamlines are shown in black while velocities are represented by color..... 46

Figure 3.4 Precisely aligned 3D fibronectin networks across the tissue length scale. A,B: CLSM MIPs with SEMs of polymer scaffolds overlaid in the upper right-hand corner to illustrate the orientation of polymer pores with respect the 0° flow direction. Left column: aEECM. Right column: naEECM. Scale bars are 500 μm. C,D: directionality histograms of CLSM MIPs for aEECM and nEECM, respectively. Gaussian fits are overlaid in black. FWHM are reported to indicate narrowness of the distribution, as well an alignment parameter AP which indicates increases in aligned fibrils with higher values. E: summation analysis of histogram data from C,D to assess the amount of features within different angle bins. The circular diagrams to the right of the graph graphically represent the boundaries of the bin (black lines), and the 0 – 180º line (dashed blue line). F: volume render of an aEECM (two coatings). The volume boundaries in the image are 193.633 μm (x,y) and 62.725 μm (z). The Holm-Sidak Multiple t-test was used to assess significance. *$P \leq 0.05$. 47

Figure 3.5 Image of MCF7 cells (magenta) cultured in an Fn EECM (green) demonstrates that cells integrate in the three-dimensional volume within EECMs. The center image is a 2-photon confocal MIP projected onto the xy plane. The right image image is an yz orthogonal slice and the bottom image is an xz orthogonal slice. Slice locations are demonstrated with red lines. A Gaussian blur filter, sigma = 1.0, and gamma correction of 0.6 was applied to both channels for display purposes. Scale bar = 100 μm and applies to all three views. 49

Figure 3.6 Visual representation displaying the relative imaging length scales assessed throughout the manuscript. This demonstrates the achievement of fibril alignment from the multi-millimeter “tissue” length scale down to the submicron, “subcellular” length scale.

Imaging studies performed at the “cellular” length scale is a scale in which multiple NIH-3T3 fibroblasts are captured within the same field of view. Approximate ROIs are shown on the tissue and cellular length scales in the white box. These images are not from the same sample but are compiled to illustrate relative scales. 50

Figure 3.7 3D perspectives of the fluid flow profile across perpendicular oriented TPSs of 245 µm (A) and 950 µm gap lengths (B). Black arrows indicate fluid flow direction on the inlet side of the model. Streamlines are shown in black while velocities are represented by color. 51

Figure 3.8 Fn EECMs across TPSs with varying gap length. A,C: 250 µm gap length TPSs. B,D: 950 µm gap length TPSs. A,B: SEMs of the TPSs before coating. C,D: MIPs of the Fn networks after coating. Scale bars = 500 µm..... 52

Figure 3.9 Aligned fibronectin networks influence fibroblast orientation and polarity on the cellular length scale. NIH-3T3s align with fibronectin fibrils on aEECM significantly compared to naEECM. A,D: Confocal MIPs of NIH-3T3s. Green: Fn, red: F-actin , blue: nuclei. A gamma correction of 0.5 was applied to the actin channel for visualization purposes. Scale bars: 50 µm. B,E: Actin directionality analysis histograms. Gaussian fits are overlaid in black. FWHM are reported to indicate narrowness of the distribution, as well an alignment parameter AP which indicates increases in aligned fibrils with higher values. C,F: aspect ratio analysis of actin morphology and nuclear morphology, respectively. G: Binning analysis of histogram data from B,E to assess the fraction of the fibrils falling within different angle bins. The circular diagrams to the right of the graph graphically represent the boundaries of the bin (black lines), and the 0 – 180º line (dashed blue line). H: actin stress fiber analysis of F-actin images displays the number of stress fibers per cell in the y-axis. The Mann-Whitney U and Holm-Sidak Multiple t-test were performed to compare groups and assess statistical significance. *P ≤ 0.05, **P ≤ 0.01, ***P ≤ 0.001..... 54

Figure 3.10 Fibril diameter analysis. A: Fn fibril diameter data generated from image analysis of CLSM MIPs of aEECM and naEECMs in Figure 3.9. Mean (X), mean ± one sample standard deviation ($X \pm s$), and sample sizes (n) are reported in the table below the graph B: shows transformed diameter data, transformed via the equation: $y' = log10yymax$. Skewness and kurtosis are reported to indicate the data are sufficiently normal after transformation. Transformed data were used to generate the summary statistics reported in the table above. 56

Figure 3.11 Normalized cell proliferation. Data generated over the course of 6.5 d using a Tox8, resazurin-based metabolic assay. Data plotted are the fluorescent intensity measurements normalized to the initial time point (13.5 h). Aligned vs non-aligned EECMs were not statistically different at any time point..... 57

Figure 3.12 Aligned fibronectin guides fibroblast motility. Live Cell migration analysis on aEECM (A,B,C), naEECM (D,E,F), and 2D (G,H,I), which reveals significant directionally persistent migration along aligned fibrils compared to non-aligned fibrils and 2D. A,D,G: Representative cell track images are overlaid onto brightfield images (t = 0). Scale bars = 100 µm. The time reference bar indicates increasing time from blue to red. B,E,H: Wind rose plots display the number of cells (length of bar from the origin) and their respective direction from 0°

to 360° in 10° bins. C, F, I: walk plots displaying individual cell paths from their origin as a function of distance in the x-y directions. **J**: box plot of cell persistence time assessed in the primary direction, extracted from the APRW model. K: box plot of cell movement anisotropic index data was calculated from persistence time and speed. L: box plot of cell speed, as determined from the APRW model. The Kruskal-Wallis test and post-hoc analysis via a Dunn's multiple comparisons test were performed to assess statistical significance. *P ≤ 0.05, **P ≤ 0.01, ***P ≤ 0.001 59

Figure 3.13 Fn EECMs facilitate growth of various cell types. A: induced pluripotent stem cells (iPSCs) seeded onto a fibronectin EECM at a concentration of 100,000 cells mL^{-1} (single cell seeding). IPSCs were expanded for 14 d before imaging. B: H9 human embryonic stem cell (hESC) colonies seeded on an EECM. Colonies were gathered using a colony picker, transferred in medium and seeded on fibronectin EECMs for 24 h prior to imaging. The yellow outline marks the initial boundaries of the seeded hESC colony. C: MDA-MB-231 cells were seeded at 75,000 cells mL^{-1} on fibronectin EECMs for 20 h prior to imaging. D: SUM-159 cells on an EECM. Fibronectin EECM scaffolds were placed in cell suspension ($4.0x10^6$ cells mL^{-1}) for 4 hours before being removed, rinsed with DPBS and imaged. All scale bars = 100 µm..... 61

Figure 3.14 Visual representation of quantitative metrics used to describe directionality histograms. The full-width at half maximum (FWHM) is the width of the distribution at the y-value which is halfway from the baseline (y-offset) to the peak of the distribution. The alignment parameter (AP) describes a value where the area under the Gaussian (aligned features) is normalized by the area under the y-offset (non-aligned features). 64

Figure 3.15 Fluid flow characteristics across perpendicularly oriented TPSs at different inlet velocities. 66

Figure 4.1 Defined derivatization of HA enables minimally modified thiol reactive species A: thiol-reactive functionalization of hyaluronic acid. B: 1H NMR spectrum of 40% degree of substitution modification of 15kDa HA confirming successful chemical modification. C: SEC-MALS (620nm laser) demonstrating that molecular weight is not affected by modification strategy. D: illustration depicting site-specific thiol conjugation strategy to produce HA-Fn conjugates that produce fibrillar EECMs via hydrodynamically induced fibrillogenesis. E: Merged CLSM MIP of Fn-HA EECM (15kDa HA) where Fn is depicted in green and HA is depicted in magenta. Contrast and gamma adjustments were applied for display purposes F: SEMs of of Fn EECMs vs Fn-HA EECMs demonstrating fibrillar morphology at higher resolution..... 74

Figure 4.2 ^{1}H NMR spectrum of 14% degree of substitution modification of 2000kDa HA (hmw HA-2PT) and 15kDa (lmw HA-2PT)...... 75

Figure 4.3 Fn EECMs assemble according to biomimetic hallmarks enabling a site-specific HA-conjugation strategy A: CLSM MIPs of nFn EECMs stained for EDA-Fn (yellow), non-specific Fn (green) compared to an isotype control. Quantification was performed using a platereader for the EDA-Fn stain (Ex: 490nm, Em: 530nm).B: brightfield image of nFn hydrodynamic coating that were treated with 70kDa fragment (top) or with nothing (bottom)C: CLSM MIPs of Dylight-488 conjugated nFn that has been untreated (left) or treated with 20mM

reducing agent TCEP (right). Quantification of total coverage was performed on CLSM MIPs and shows dramatic reduction of area coverage for nFn treated with TCEP. D: Image of SDS PAGE gel comparing Fn in tris vs borate buffer, HA-Fn conjugates following thiol specific strategy, nFn treated with 20mM TCEP and Fn treated with beta mercaptoethanol (β-ME). E: CLSM MIPs of HABP stained (magenta) EECMs after incubation at 37 C for 5 d in DPBS comparing different conjugation strategies. +Unfold (+Un) indicates unfolded nFn. "R-HA" denotes modified, thiol reactive HA compared to native HA. 2000kDa HA was used in these studies. Fn EECM were Fn EECMs without any HA treatment used as a negative control. Quantification was performed on MIPs (far right). *P ≤ 0.05, **P ≤ 0.01, ***P ≤ 0.001. 79

Figure 4.4 Evaluation of various nFn products. A: Area coverage analysis based on CLSM MIPs assessed either from from general Fn pAb staining (left) or EDA-Fn specific mAb staining (right). B: brightfield image of TPSs that were hydrodynamically coated with Fn from different vendors. C: Ratiometric platereader analysis of signal from EDA-Fn normalized by general Fn stain. D: SDS-PAGE of Fn products from different vendors to assess the presence of dimeric protein content in the unreduced state vs Sigma Fn treated with β-ME (far left lane). 80

Figure 4.5 A: CLSM MIPs and anlaysis from Figure 4.3, with additional group where Fn EECMs were treated with soluble native HA2000kDa for the duration of the study (5 d) as well as additional unbiased quantification methods using a platereader to validate image quantification. CLSM MIPs of HABP stained EECMs comparing different conjugation strategies (top row). DIC counter images (bottom row) are provided to demonstrate fibrillar EECM was present in each condition. +Unfold (+Un) indicates unfolded nFn. "R-HA" denotes modified, thiol reactive HA compared to native HA. 2000kDa HA was used in these studies. Fn EECM were Fn EECMs without any HA treatment used as a negative control. B: is the same integrated density quantification as Figure 4.3 where Fn EECMs were used to determine the pixel intensity threshold cutoff for analysis. C: Orthogonal quantification using a platereader, assessing just the HABP stain (Ex 490nm/Em 530nm). D: Platereader analysis where EECMs were co-stained with pAb for Fn and HABP/pFn ratios were normalized to nFn +Un +R-HA2000kDa *P ≤ 0.05, **P ≤ 0.01, ***P ≤ 0.001 ****P ≤ 0.0001. 81

Figure 4.6 Characterization of Fn-HA EECMs of different molecular weights compared to Fn EECMs. A: CLSM MIP of Fn-HA EECMs (Fn-15kDa top row, Fn-2000kDa bottom row) where Fn and HA were visualized with fluorescent tags (Dylight 488 and Cy5, respectively). B: Manual fibril diameter analysis of Fn-HA conjugate EECMs compared to pure Fn EECMs. Each group is represented by split histogram, violin plot and box-whisker. C: High resolution 3D volume renders comparing Fn-HA conjugates with different molecular weights. D: Summary of mass loading quantification (top) and fibril diameter analysis (bottom). E: Platereader quantification of EECMs where HABP/aFn pAb ratios were normalized to Fn-HA2000kDa EECMs. *P ≤ 0.05, **P ≤ 0.01, ***P ≤ 0.001 ****P ≤ 0.0001. 84

Figure 4.7 A: linear regressions of sample Fn-HA15kDa and Fn-HA2000kDa EECMs compared to respective 3D gelatin controls with known mass loading used to determine mass ratios of HA in Fn fibrils within EECms. B: CLSM MIPs of EECMs stained withwith aFn pAb (green) and HABP (magenta). These EECMs were used in the platereader quantification from Figure 4.6 E. 86

Figure 4.8 Fn-HA EECMs display tumor-mimetic morphology and biochemistry A: Bulk RNA-seq analysis of breast cancer cell lines (T47D, MCF7) co-cultured with two bone marrow stromal cell lines (HS27a, HS5). Co-cultured breast cancer cells (bold) were compared to stromal cells (bold) in the top 4 rows. Where breastcancer cells co-cultured (bold) were compared to standard monocultured breast cancer cells (bold) in the bottom 4 rows. B: CLSM MIPs of Fn-HA2000kDa EECM stained with EDA-Fn (yellow) co-stained with HABP (magenta) in the top row compared to MCF7/HS5 co-cultures subjected to de-cellularization (2nd row), fixed MCF7/HS5 co-cultures (3rd row) with imaging controls of Fn only EECMs and de-cellularized co-cultures treated with hyaluronidase in the bottom row. 89

Figure 4.9 MCF7 cells grown on Fn-HA EECMs, Fn EECMs and TCPS (2D) in 2% (v/v) FBS were characterized to assess phenotype and epithelial/mesenchymal tumorigenic characteristics. A: representative brightfield images of MCF7s on different conditions after6 d before being assayed in all other panels. B: viability assessed by flow cytometry for DAPI negative MCF7s. C: Spheroid formation assay in methyl cellulose containing MEBM assessed after 15 d in sphere culture. D: Scratch wound assay following 4.5 d of regrowth with linear regressions (solid colored lines) with error for fits (corresponding dotted lines). E: Dye retention assay using CTFR dye to quantify non-proliferating cells denoted CTFR+ with flow cytometry. F: Phenotyping by flow cytometry to quantify populations of CD44+/- and CD24 +/- cells. G: Phenotyping by flow cytometry to quantify dual positive ALDH+ / CD44+ 24- BCSCs. H: Phenotyping by flow cytometry to quantify CD44+ 24- that are in the CTFR+ subpopulation. I: Regrowth curves of MCF7s that were CTFR + or CTFR low that were replated into 96 well TCPS plates growth in full, 10% FBS medium where regrowth kinetics were are summarized in J. Values with ** here indicate fitted values reported outside of time course and i.d. represents insufficient data for fitted values during the time course assessed. *P ≤ 0.05, **P ≤ 0.01, ***P ≤ 0.001 ****P ≤ 0.0001. 93

Figure 4.10 D2.OR cells grown on Fn-HA EECMs, Fn EECMs and TCPS (2D) in 2% (v/v) FBS were characterized to assess epithelial/mesenchymal tumorigenic characteristics. B,C: also include D2.ORs grown in full serum (10% FBS), TCPS coated with Fn or Fn-HA conjugates (2D + groups), as well as D2.ORs grown in non-methyl cellulose containing MEBM (suspension). A: representative brightfield images of D2.OR on different conditions after 5 d before being assayed in all other studies with D2.ORs. B: viability assessed by flow cytometry for DAPI negative D2.OR cells. C: Spheroid formation assay in methyl cellulose containing MEBM assessed after 15 d of sphere culture. D: Scratch wound assay following 3 d of regrowth with linear regressions (solid colored lines) with error for fits (corresponding dotted lines). *P ≤ 0.05..... 95

Figure 4.11 D2.OR cells grown on Fn-HA EECMs, Fn EECMs and TCPS (2D), TCPS coated with Fn or Fn-HA conjugates (2D + groups), in 2% (v/v) FBS compared with cells grown in full serum (2D 10% FBS), and non-methyl cellulose containing MEBM suspension culture to assess conditions that promote CTFR+ populations. A: Illustration of experimental work flow. B: CTFR+ cells assessed by flow cytometry. C: Spheroid formation assay in methyl cellulose containing MEBM assessed after 15 d of sphere culture for CTFR+ cells compared to CTFR low cells. D: Representative histograms of CTFR + or low cells to show relative population distributions as a function of culture substrate. E: CTFR+ cells from mammosphere culture that were filtered and replated on TCPS in 10% FBS. F: Representative

brightfield images of regrowth assay in E. *P ≤ 0.05, **P ≤ 0.01, ***P ≤ 0.001 ****P ≤ 0.0001. 97

Figure 4.12 D2.OR cells grown on Fn-HA EECMs, Fn EECMs and TCPS (2D), in 2% (v/v) FBS for 5 d injected into NODscid mice to assess in vivo tumor growth and overall survival. A: Illustration of experimental work flow B: Comprehensive imaging of all mice in the study. Some mice do not appear in later images because they excluded due to procedure-related death. C: In vivo growth dynamics over the first 50 d. D: Doubling time (d) for growth dynamics assessed via non-linear of log10 from C. E: Number of mice excluded from each group because they died due to surgical procedures. F: Survival curve where at this point in the study, no mice have died due to tumor burden..... 101

Figure 6.1 A: SU-8 scaffold manufacturing process. B: SU-8 pore geometries and free volume % 120

Figure 6.2 Controlled cell seeding utilizing an aqueous two-phase system of dextran and PEG. A: Proof of concept experiment with 3D bioprinter to deposit cells in a controlled geometry. B: Confocal MIPs showing that cells can be controlled in a x-y area and z-depth on EECMs..... 122

Figure 6.3 Fluidic devices to as a new approach for EECM production. A: Overall workflow using standard 24-well format sized EECMs. B: EECM coating across micropillar. Above image illustrates 3 PDMS devices that fit into a 96-well plate. Bottom image illustrates zoomed image with EECM coating across micropillars. C: concept sketches for scale-up approach of EECMs 124

Abstract

The extracellular matrix (ECM) is a complex amalgam of proteins and polysaccharides that actively influences cell fate via biochemical and biophysical cues. Fibronectin (Fn) is the bedrock of many native interstitial ECM, existing as a fibrillar protein network that sequesters cell signaling factors and ECM macromolecules and serves an indispensable role in ECM assembly. Despite its ubiquity in mammalian biology, it remained an outstanding challenge to recapitulate critical aspects of Fn in native tissue such as its fibrillar morphology with defined, native bioactivity in a scalable, three-dimensional construct. Our lab recently pioneered the creation of 3D fibrillar Fn networks suspended across hyper-porous polymer scaffolds on the millimeter length scale. This is achieved by shearing a Fn solution across a polymeric scaffold at the solution/air interface, which promotes the formation of robust 3D networks through hydrodynamic processes.

Native Fn fibrillogensis occurs through Fn-Fn interactions following integrin mediated stretching of solute Fn by cells. First, I investigated *in vitro* hydrodynamic assembly looking toward hallmarks of cell-based Fn fibrillogenesis for comparison. I found that hydrodynamically induced fibrillogenesis revealed domains of Fn that were only conformationally active in a fibrillar state and not when statically adsorbed onto a synthetic surface. Furthermore, the engineered Fn networks exhibited other notable hallmarks of cell-assembled fibronectin including stability, co-assembly with collagen-I, tissue-mimetic mechanical properties, cell-like fibrillar morphology, and native-requisites for assembly. These native like constructs are referred to as engineered extracellular matrices (EECMs).

Second, I demonstrated that the fluid shear-interface can be engineered during fibril assembly to tailor flow profiles, enabling the creation of precisely aligned or non-aligned EECMs (aEECMs and naEECMs, respectively). The aEECMs significantly influenced fibroblast fate by guiding cell orientation, increasing nuclear and cytoplasmic aspect ratio and promoting a dramatic increase in directionally persistent cell motility.

Third, by taking advantage of Fn's conformational sensitivity, I employed a site-specific conjugation strategy to create well defined glycan-Fn conjugates using hyaluronan (HA). I demonstrated these to be tumor-mimetic and to maintain relevant bioactivity as demonstrated with domain specific Fn mAbs as well as a link-module based HA binding protein stain. Fn-HA EECMs were leveraged to study tumor cell regulation and appeared to uncover a unique molecular weight dependent cooperative and antagonist role of HA in the presence of conformationally active, fibrillar Fn.

Finally, I reflect on collaborative pursuits and side projects to look toward future applications of EECMs where there is huge potential in possible industrial collaborations and new opportunities for the creation of advanced composites. EECMs are readily compatible with conventional cell culture techniques, various analysis modalities and show great promise as they are practical, definable, scalable and highly efficacious in a broad array of applications.

To date, EECMs have been shown to successfully facilitate bone regeneration, reliably expand patient tumor cells *ex vivo*, serve as a defined substrate for stem-cell engineered heart/brain organoids, and govern tumor cell phenotype – all whilst having great translational promise. These EECMs are continuing to be leveraged to address challenging problems in tissue regeneration and tumor microenvironment engineering, where they elucidate the broader value of engineered, proteinaceous biomaterials with defined heterogeneity.

Chapter 1 Introduction

1.1 Publication Information

Parts of work in this chapter are published as: Anke Steier,* Ayşe J. Muñiz,* Dylan Neale,* Joerg Lahann. "Emerging Trends in Information-Driven Engineering of Complex Biological Systems." *Advanced Materials.* 31(26). 2019. DOI: 10.1002/adma.201806898 [1] * = authors share equal contribution.

1.2 The Problem at Hand

1.2.1 The Global Burden of Cancer and Impact of the Microenvironment

The probability of an individual being diagnosed with some type of cancer in their lifetime is nearly 40%. [2] There are ~1,700 cancer-deaths in the US each day. For women, breast cancer has the highest incident rate of new diagnoses, totaling over 200,000 and accounts for more than 40,000 deaths each year [2]. The five-year survival rate of breast cancer plummets to 23% when distant metastases are observed, which indicates advanced disease.[2] Metastasis is responsible for 90% of all cancer deaths. [3] Metastatic progression is governed by microenvironmental factors, [4,5] where studies into tumor tissue remodeling have helped to understand disease progression,[6,7] and could thereby improve preclinical model systems.

1.2.2 The Inefficiencies and Complexities of Preclinical Drug Screening

Some estimate that a single cancer therapeutic costs ~$1 billion to develop due to high risk, where more than 80% of preclinical oncology candidates do not make it through clinical

translation.[8] Many attribute this huge number of failed drug-candidates to poor preclinical efficacy prediction arising from insufficient preclinical models [9]. For cancer therapeutics, the classic model is that of an immortalized cell line grown on a 2D substrate. In the 1990s, 60 cell lines cultured *in vitro* were employed as a means to advance promising drug candidates to xenograft models and eventually clinical trials; however, the initial *in vitro* models had very low predictive power of effective the therapies.[10] Cell lines grown on 2D substrates are insufficient for multiple reasons: 1) cell lines have undergone significant genetic and transcriptome changes 2) they no longer represent the tumor heterogeneity found in the primary tissue source and 3) they lack various stromal aspects of the tumor microenvironment that impact drug response [10]. Patient derived xenografts (PDXs) offer an attractive solution because they maintain heterogeneity; [9] however, given their cost, labor and often poor engraftment efficiency, it is difficult to employ them in a high-throughput means to screen many preclinical drug candidates. Although, with incredible investment, Novartis demonstrated the use of PDXs on a grand scale for preclinical drug screening application after amassing over one-thousand PDXs. [9]

To make matters more complex, once effective therapies have been translated to the clinic, patient to patient variability in drug response occurs as cancers are heterogeneous diseases with numerous subtypes.[11] Patient variability has made cancer a very attractive pathology for employing personalized health, which aims to provide care specific for an individual. Toward this goal, the dramatic decrease in gene sequencing costs has given rise to an increase patient tumor sequencing for individualized molecular characterization [12]. This has led to initiatives that connect genetic and transcriptomic profiling of patients to drug response, so that more effective therapy regimens can be prescribed.[12,13] Especially important to personalized treatment is the *ex vivo* expansion of primary patient tumors.

Rapid and reliable e*x vivo* expansion of primary patient tumors on an *in vitro* platform that maintains clonal and transcriptomic heterogeneity would be a powerful platform for personalized drug screening or developing individualized immunotherapies. This distant goal is hampered by great difficulty in maintaining viable primary patient cells, let alone recapitulating heterogeneity, where 2D substrates are demonstrated to be woefully insufficient. To lower this barrier, 3D substrates offer a potential solution.[14–16] Given the vast amount of literature demonstrating 3D environments influence cell phenotype and drug resistance, it is reasonable that *defined 3D in vitro substrates aimed at maintaining cellular heterogeneity can be intelligently designed for drug screening with the eventual goal of personalized medicine.*

1.2.3 The Need for 3D In Vitro Models

Over the last decade, there has been an explosion of investment into 3D cell culture systems to study human pathobiology and physiology to improve drug screening, investigate fundamental biological mechanisms, or move closer to regenerative medicine goals. In the 1980s Mina Bissell's group published pioneering work surrounding breast cells in the 3D microenvironment [17,18]. In this and later work, her group showed that mammary cells derived from lactating mice would lose milk secretion capabilities when grown on 2D substrates, but this could be recovered when grown on 3D ECM gels. Despite the belief at the time that ECM was merely structural, their studies demonstrated that the ECM had a very active role in modulating cell phenotype. Using protein derived gels, they showed that the malignant phenotype of tumor cells could be reverted to a more normal one through treatment with an integrin β1 blocking antibody [19]. Additionally, HER2+ tumor cells' sensitivity to targeted therapies could be increased through the disruption of β1 mediated integrin binding [16]. Collectively, Bissell's group demonstrated the phenotype of a tumor cell is critically regulated by the ECM in which it

resides. [19–22] This catalyzed research to model complexity observed *in vivo*, where animal models serve as a standard tool for preclinical research.

Animal models replicate many aspects of human pathobiology, but they are not without limitation. PDXs capture cellular heterogeneity and aspects of biological complexity [23]. On the other hand, they are time and labor intensive, can take 1-4 months to utilize for studies [24], and are hampered by low grafting efficiency. Additionally, mouse-strains used for xenografts lack intact immune systems which is of key importance to immune oncology. Additionally, *in vivo* models are difficult to employ as a means of decoupling the various interacting microenvironmental factors.

In spite of years of research on the 3D tissue environment, 2D substrates are still widely used due to ease, predictability and reproducibility.[25] Yet, 2D *in vitro* substrates such as treated glass or tissue culture polystyrene (TCPS) are mechanically and chemically irrelevant to human physiology. They facilitate monolayer culture, but this approach gives rise to aberrant phenotypes and clonal selection not representative of their *in situ* predecessors. To increase the biological relevance of 2D substrates, it is standard practice to adsorb different ECM components onto these surfaces. While this might help to improve cell attachment, these processes do not recapitulate the native structure of those ECM components found *in situ.*

In oncology drug development, prediction of off-target toxicity is as important as efficacy. In the last decade, there has been an explosion of investigative toxicology work to develop and validate micro-physiological (tissue engineering systems) platforms to improve preclinical predictions and mitigate the burden associated with animal models.[26,27] Tissue engineered models representative of normal heart, intestine, brain, and liver are of great value as these organs are most commonly implicated in clinical safety failure.[28]

In the current landscape, most systems are based off of self-assembling cell organoids, (a substrate independent approach) that can be hampered by high variability and poor usability. Advances in biomaterial/substrate based tissue engineering continues to demonstrate the translational potential of these systems in recapitulating tissue complexities.[29] Beyond the distant goal of regrowing entire organs or eliminating animal models, there is a role for biomaterial-based constructs to incrementally advance humanized-tissue constructs for drug discovery. *As an interim approach, immortalized cells can be utilized to rapidly prototype 3D substrates with a focus on specific phenotypic or functional heterogeneity induced by engineered biomaterials.*

1.2.4 Clinical Translation and Regulatory Considerations

Ultimately, for a tissue scaffold to be clinically translatable it has to (i) demonstrate efficacy and validation in a tissue application, (ii) meet rigorous standards for safety, (iii) be commercially manufactured according to Current Good Manufacturing Practices (CGMP) emphasizing precisely defined formulation, and (iv) be scalable with economic viability. Many acellular tissue scaffolds have been successful in the clinic; however, these challenges pose significant hurdles for cell-based therapies leading to fewer successes [30]. Cell-therapy challenges in tissue engineering have been outlined extensively[31]. Regulatory pathways may change for acellular compared to cell-based scaffolds, depending on the country, market of interest and intended medical application. In the United States, cell free scaffolds may be treated as medical devices and regulated by the FDA's Center for Devices and Radiological Health (CDRH). If a tissue scaffold is cell-laden, then it may be characterized as a biologic and regulated by the FDA's Center for Biologics Development and Research (CBER). Cell based systems are subject to additional scrutiny for various reasons, including increased safety concerns and the need to translate varying academic research practices into strictly controlled manufacturing processes

that adhere to CGMP, which stresses the importance of control from raw materials all the way through reliably generating a consistent, characterized product at a commercial scale with excellent quality control[30–32].

For instance, the U.S. Food and Drug Administration (FDA) utilizes the International Organization for Standardization (ISO) standards to assess risk and biocompatibility (ISO 10993 standards). It is critical to note that the FDA regulates devices, not materials; hence, for regulatory agencies and researchers, all considerations of the appropriateness of a material is application dependent. Additionally, the comprehensive approach necessary for assessing safety and biocompatibility of a medical device seeking regulatory approval is challenging to achieve for academic researchers; however, some of the subcategorized tests laid out in the FDA guidelines may be useful in directing academic studies and help to solidify good research practices at the onset of ideation and discovery to ensure translational potential of a biomaterial/tissue engineering construct.

1.3 The Moving Target: Tissue Complexity and Heterogeneity

1.3.1 The Foundation of Tissue: The Extracellular Matrix

At the foundation of tissue structure and remodeling is the extracellular matrix (ECM), a complex milieu of bio-macromolecules that influences cell behavior through its composition and physical properties. ECM provides a three dimensional microenvironment for cells of structural and functional proteins, proteoglycans and glycoproteins[33]. Various tissues have unique compositions, conformations and architectures in their normal state, as well as unique signatures when diseased[34,35]. Yet, there are numerous proteins (*e.g.*, fibronectin, collagen, laminin, fibrinogen, vitronectin, thrombospondin, elastin, tenascin, and osteopontin) which are found in the ECM[35–38]. For example, laminin is abundant in the basement membrane of tissue which

possess a more sheet like structure, whereas interstitial matrices of tissues are chiefly made of fibrillar proteins like collagens I, III and fibronectin[39,40]. ECM macromolecules provides structural support and mechanical integrity of the local microenvironment, has attachment sites for cell surface receptors.[41] ECM can act as a reservoir for latent signaling factors that can be released via degradation and can influence cell processes such as migration and proliferation[33]. Additionally, cells actively remodel their local microenvironment by exerting forces on the matrix, secreting new proteins or degrading proteins through matrix metalloproteases (MMPs), which in turn leads to changes in the proliferation, migration and adhesion and creates a complex dynamic reciprocity between cells and the ECM.[42]

1.3.2 Tissue Remodeling in Breast Cancer

The ECM of the tumor microenvironment is also comprised of various proteins, proteoglycans and glycans.[39,43–45] Physical properties like stiffness, architecture, and composition are also important for tumor progression and have shown to be modulators of tumor cell phenotype [20,46–48]. In a process known as desmoplasia, healthy mammary tissue is remodeled, and this mammographically dense, characteristically fibrous ECM is a well-validated risk factor.[49] On the protein level, this remodeling includes deposition of aligned, fibrillar collagens, deemed "tumor associated collagen signatures (TACS)" with validated correlations to poor patient prognosis.[6] These aligned collagen fibers presumably act as highways for invasive carcinoma cells and can even facilitate metastatic phenotypes.[50–52] While collagen is a well-characterized protein in desmoplasia, seemingly correlated but less studied signatures implicate fibronectin (Fn) and hyaluronan (HA) as well (*the basis of Chapter 4 of this dissertation)*. Fn-rich stromal cell secretions guide tumor cell orientation and motility, and excessive accumulation correlates with poor prognosis.[53–55] Interestingly, breast tissue of high-risk, obese individuals has

implicated both Fn and collagen remodeling in desmoplasia.[56] Increased deposition of HA has also been correlated with the invasive front of tumors and poor prognosis, but remains an elusive ECM component in desmoplasia due to its many complexities in tumor biology.[57–61]

Notably, the establishment of TACS (mid 2000s to early 2010s) correlates with a time in which collagen biomaterials were established, enabling widespread investigation of the topic with these collagen materials. Additionally, the seminal paper was based on a label-free, *in situ* imaging technique that captures characteristic oscillations from asymmetric molecules (like assembled collagen fibrils)[7,62] but is not established for Fn or HA. *Therefore, given the multi-variant structure and composition of remodeled tumorigenic breast tissue, there is a need for 3D cell culture models that enable controlled presentation of native Fn and HA in addition to collagen to investigate this dynamic progression.* The following sections (1.4 to 1.6) will extensively overview biomaterials and tissue engineering approaches with a broad focus to underscore these less-studied, but likely important, tumor-associated ECM components.

1.4 Biomaterial Candidates for Engineered Tissue Systems

There is a plethora of materials used in the micromanufacturing of bio-integrative systems with various *in vitro* or *in vivo* applications. These materials are comprised of metals, ceramics, macromolecules, or composites thereof. Apart from polymers and naturally derived materials, ceramic and metal materials have a long and successful history in dental and orthopedic applications.[63–65] Furthermore, there are many applications of biomaterials as medical devices that have been discussed elsewhere[66,67]. In contrast, this subsection will focus on emerging trends in the employment of macromolecular materials in tissue engineering with a specific focus on challenges associated with their validation and clinical translation. Naturally occurring biomacromolecules are employed as biomaterials and are primarily comprised of

polysaccharides (glycans) and proteins. They generally feature physiologically relevant compositions, biocompatibility, abundant availability or bio-inductive properties[68,69]. Synthetic macromolecules used in biomaterials applications are generally comprised of synthetic polymers, such a polyesters, polyurethanes, hydrogels or acrylate functionalized polymers. Synthetic materials allow for more precisely controlled physical properties such as chemical composition, stiffness, degradability and architecture.[68,70]

1.4.1 Synthetic Materials

Polyesters are biodegradable, biocompatible, and have a long history of use in various *in vivo* applications, such as sutures. Common polyester biomaterials are poly(lactic acid) (PLA), poly(lactic-*co*-glycolic acid) (PLGA), poly(ε-caprolactone) (PCL), and poly(lactide-*co*-caprolactone) (PLCL). These polymers are frequently electrospun to create fibrous mats used for tissue engineering[71–73]. While electrospun mats are common in tissue engineering, there are subtler biological implications, namely the potential for protein fouling on implanted scaffolds to initiate an adverse immune response that can be addressed by modifying the surface of fibers with non-fouling coatings[74]. Our lab has leveraged the chemical functionality of polyesters to create electrospun bi-phasic fibers of PLGA derivatives to direct the attachment of cells on microfibers[75]. Polyesters are also favored for their inherent degradability, which occurs through acid or base catalyzed hydrolysis of the ester backbone. For PLGA this results in the release of metabolites, *i.e.*, glycolic acid and lactic acid, which can be cleared by the host. The degradation rate can be controlled by the ratio of lactic acid and glycolic acid blocks, as well as blending PLGA with other polymer derivatives[76,77].

Given that polyesters are thermoplastic, they can easily be incorporated into melt extrusion or filament based 3D printing systems[78–80]. Generally, using these techniques larger

fibers (>100 μm) are produced, which may not be desired for certain tissue engineering applications since features would ideally be subcellular (<20 μm). Wunner *et al*. developed a melt-electrospinning technique to create porous scaffolds comprised of 20 μm diameter fibers[81]. Our lab has reported an electrospinning-based jet writing technique that allows for 3D printing of scaffolds comprised of very fine PLGA fibers (≤10 μm diameter) that were highly successful in repairing a cranial defects in mice[82]. Furthermore, polyesters are amenable to other manufacturing techniques such as microsphere sintering, solvent casting, and phase separation[83]. Other efforts involved similar techniques in combination with a sacrificial template technique to create porous PLGA scaffolds with multi-length scale features for spinal cord injury repair[84]. Beyond polyester materials, high resolution 3D printing of polyelectrolyte solutions can be used to create tissue scaffold structures. These inks are combinations of polyanions like poly(acrylic acid) (PAA) and polycations like poly(ethylenimine) (PEI), or poly(allylamine hydrochloride) (PAH) that can be written into structures with filament sizes as small as 1μm[85,86]. Additionally, light-based polymerization of synthetic polymers is attractive for the manufacturing of complex materials systems because of its potential for ultra-fine resolution and spatiotemporal control. Various acrylates or acrylate-modified polymers are used for their advantageous photopolymerization. Furthermore, commercially available photoresist like OrmoComp® has been used in conjunction with multi-photon polymerization to create ≤1 μm sized features which can be selectively functionalized to guide cell attachment[87]. This material is a hybrid organic/inorganic molecule comprised of a silicon based component and photopolymerizable component[88].

Generally, photopolymerization chemistries rely on a photoinitiator that forms radicals upon illumination, which polymerizes a monomer that possesses multifunctional crosslinkers[89].

Various additives, including other polymers, can be added to tune solution properties critical for 3D printing[89]. Photopolymerization techniques are widely applied to hydrogels and other polymers for tissue engineering applications[89,90]. These polymer networks make up a large class of water-laden polymer networks that are typically biocompatible and have physiological stiffnesses similar to many tissues. Hydrogels can be crosslinked *via* covalent bonds (chemical hydrogels) or non-covalent (physical hydrogels) molecular interactions[90]. PEG is a ubiquitous hydrogel in tissue engineering that is generally bio-inert, yet amenable to dramatic chemical modifications to create a diverse array of functional PEG derivatives[91]. PEG can be functionalized to be photo-reactive, with PEG di-acrylates (PEGDA) and PEG methacrylates (PEGMA) being the most common candidates[90]. When 3D printing hydrogels, there are many considerations ranging from fluid properties, nozzle design and the choice of crosslinking method (physical vs. chemical) to solution properties, such as shear-thinning/thickening, viscosity, and time to gelation. Gaining deeper control over these solution properties, especially those occurring dynamically during gelation/crosslinking is key for the future of 3D printing hydrogels[90]. High-resolution hydrogel structures have been demonstrated by Richter *et al.*, where 1 μm sized PEGDA structures were created to engineer protein-repellant portions of the aforementioned microstructures[87].

Outside of photopolymerization and 3D printing, PEG can be formed into monolithic gels using other crosslinking methods such as enzymatic crosslinking of functionalized PEGs. These gels can contain relevant cell binding motifs and biodegradabable linkages to create biochemically relevant material surfaces that have been shown to be dramatically influence cell behavior[92–94]. Advances have been made to improve encapsulation and spatial localization of single cells in functionalized biodegradable PEG microspheres with the potential to study single-

cell behavior in controlled 3D niches[95]. Additionally, PEG has been demonstrated to be incredibly versatile and amenable to modification with various glycosaminoglycans (GAGs) to produce GAG composites with tunable properties, which offers a potential route to the critical role of these polysaccharides in ECM biology[96]. Other bio-inert hydrogels used in tissue engineering applications include poly(2-hydroxy ethyl methacrylate) (PHEMA), poly(acrylamide) (PA), and poly(N-isopropyl acrylamide) (PNIPAAm) and have been discussed elsewhere[97]. While hydrogels may give rise to precise control over physical parameters like stiffness and degradability, many synthetic hydrogels lack physiologically relevant architectural motifs, such as fibril structures, which in part gives rise to interest in utilizing naturally-derived materials[70].

1.4.2 Naturally Derived Materials

Protein-based biomaterials include, for example, collagen, fibrin, laminin, fibronectin and elastin. Examples of polysaccharide-based biomaterials include alginate, chondroitin sulfate, heparin sulfate, chitosan, and hyaluronic acid. Virtually all of these materials, either alone or in combination with another natural/synthetic material, have been processed into tissue scaffolds using electrospinning[98–101]. While traditional electrospun tissue scaffolds recapitulate the fibril structure of the ECM, they tend to be dense, relatively thin, difficult to handle, and are difficult to produce with higher order, organized architecture. Other traditional manufacturing techniques such as freeze drying, phase separation and gas foaming techniques have been used with proteinaceous materials like gelatin and collagen to create porous scaffolds[102–105]. Some of these scaffolds may display ideal levels of porosity, but still lack precise control over microscale features and their hierarchal organization.

Furthermore, many of these biomaterials, like alginate and collagen, naturally form hydrogels that can be incorporated into 3D printing techniques. These systems tend to be more cell-compatible than synthetic 3D printing solutions; however, high resolution 3D printed structures using naturally derived materials is an outstanding challenge. Nevertheless, advances have been made in 3D printing of collagen scaffolds; however, these scaffolds have relatively large printed features (>100 μm) comprised of smaller collagen fibrils[106]. Collagen is widely used because of its innate propensity to auto-polymerize *in vitro* and form hydrogels comprised of physiological relevant fibril architecture. This simultaneously poses a drawback, because subtle changes in solution properties like temperature or concentration can alter the properties of the resultant collagen hydrogels, and concentrations in which collagen gels assembled *in vitro* (>=1mg/mL) are much higher than is physiologically relevant.

The potential benefits of naturally derived materials in tissue engineering may include their relative abundance, their biochemical relevance, their biocompatibility, their inherent degradability, and their bio-inductive capacity. However, many of these materials are not mechanically robust and require secondary crosslinking to stabilize them prior to cellularization. Furthermore, as a result of various phenomenological assembly processes of different naturally derived materials, they generally lack orthogonal control over physical properties such as stiffness, ligand density, and architecture[107].

1.5 The State of the Art: Approaches and Limitations

1.5.1 Polymeric Scaffolds and Synthetic Hydrogels

Due to their durability and cell compatibility, hydrogels are used as a protein replacement, or addition, to provide a supportive cell environment[108]. Through its coordinated

control, physical properties such as density and structure can be tuned to investigate cell behavior. Chemical modification of the bioactivity as well as the cell behavior can be influenced and makes it a promising and diverse material to investigate[109]. Hydrogel-based biomaterials can be spatially controlled by bioprinting or photo-patterning[110,111].

There are a huge number of synthetic systems that have been leveraged to study tumor phenomena, including 3D printed polymer scaffolds, microfabricated devices comprised of poly(dimethyl siloxane) (PDMS), electrospun polymer fiber mats, and synthetic hydrogels [112,113]. While synthetic systems provide a well-defined means to the impact of isolated materials properties, they generally lack relevant biological composition. Changes in composition have a profound impact on cell morphology, behavior and motility [14,20]. Furthermore, while synthetic systems like PEG hydrogels provide a customizable platform to effectively control stiffness, they lack relevant fibril architecture and are not inherently degradable. *Cell binding and degradability are important features to recapitulate in vitro, so degradable peptide motifs will be incorporated into synthetic systems. However, they may never match the complexity of native proteins. Given the important role of full length, native proteins in governing tumor cell behavior and drug response, synthetic systems may be too reductionistic in approach.* Some microfluidic models offer great promise to isolate and control specific tissue properties; however, they are currently hindered by the fact that many are largely 2D culture substrates that lack relevant 3D ECM structures.[112,113]

1.5.2 High Resolution Manufacturing – Two Photon Polymerization

Synthetic polymers and naturally-derived proteins are being explored for their potential in 2-photon polymerization (2PP). Some naturally derived materials are more biologically active than others. For instance, bovine serum albumin (BSA) is a natural material used in 2PP, but it

lacks relevance as a biomaterial for studying cell-ECM interactions. Ovsianikov *et al.* generated scaffolds composed of a methacrylate-modified gelatin (GelMod) for the expansion of adipose-derived stem cells [114]. Su *et al.* reported on a series of 2PP printed structures composed of a mixture of laminin/BSA in the presence of Rose Bengal dye for studying stem cell migration [115]. Collagen-I was also implemented in 2PP with high spatial resolution[116]. *A critical outstanding question for all of these materials is whether they retain the biologically relevant protein configurations following the multiphoton crosslinking process. Additionally, their throughput is currently a limiting factor, but this approach is ripe for technological improvement.*

1.5.3 Bioprinting and Natural Hydrogels

Given the limitations of synthetic systems, naturally derived 3D substrates are commonly used. In fact, much of Mina Bissell's previously discussed work was performed either in collagen gels or laminin rich gels like Matrigel. Matrigel is a commercially available protein matrix derived from mouse sarcoma secretions that has been widely used in the cancer research space. However, its composition is heterogeneous, it has little utility for the specific isolation of individual protein components and is subject to great batch-to-batch variability [117]. Many other groups have also investigated culture on ECM derived hydrogels, like collagen and gelatin scaffolds [44,45]; however, these systems do not allow for modulation of stiffness and architecture without changing protein concentration or introducing crosslinking chemistry. In either case, the fundamental impact of the protein can be skewed. Hence, while these naturally derived materials are of biologically relevant composition, they generally lack the ability to tune other material properties in an orthogonal manner. Additionally, while collagen is a key component of the pathological progression of tumorigenic breast tissue, it is only one component. And as previously outlined, other components like Fn and HA also play key roles in tumor progression.

Furthermore, bulk encapsulation of cells into a hydrogel is a common strategy for both synthetic and natural scaffolds that may be too dense for a post-production seeding strategy. Modern approaches allow for selective deposition of bioinks containing cells or cell aggregates in a process referred to as "bioprinting"[118]. This is typically achieved via droplet- or extrusion-based printing. In both cases, either the printhead or stage are controlled and translate over xy and z directions. Droplet printing requires that the polymer or prepolymer solution have gelation kinetics that match the deposition speed, which can limit the library of materials available for this technique. Extrusion-based printing passes polymer or pre-polymer material through a nozzle in a continuous ejection method to maintain contact with the stage and is typically slower than droplet printing. In either case, the solutions may be subject to additional thermal, mechanical, or light treatment.

Cell-hydrogel printing of defined 3D structures can have advantages over seeding on acellular scaffolds, such as controlled cell placement, high seeding efficiencies, and control over cell-matrix properties. However, many limitations plague current systems, such as low printing resolutions, lengthy solution optimization procedures, and creating large 3D structures that do not collapse from their own weight. Several strategies for overcoming these limitations have been investigated, such as including sacrificial support structures, and rapid crosslinking to facilitate larger build volumes[119 97,118,120–123]. Exciting emerging techniques focus on incorporating aspects of tissue heterogeneity that are found in native tissue, via deposition of multiple materials or compartments sequentially or simultaneously. Layer-by-layer deposition of scaffold support materials and cell-laden bioinks was achieved using a multi-head 3D printing system to print large-scale proof-of-concept architectures resembling tooth, kidney, ear, and skin[119,124]. This system, known as the integrated composite tissues/organs building system and

the integrated tissue and organ printer (ITOP) system are two examples of integrated systems for printing heterogeneous solutions. ITOP demonstrated a proof-of-concept printing of an anatomical defect of large tissue structures by incorporating micro-channels to facilitate nutrient diffusion and combining hydrogels and synthetic polymers for imparting mechanical strength[125]. *Currently, 3D bioprinting techniques do not utilize Fn as a conformationally active, fibrillar ECM due to Fn's complex, domain-interaction dependent native assembly (a topic of ongoing investigation). Work presented in this dissertation supports Fn's importance as a biomaterial as well as technological improvements that inform future pursuits toward this goal.*

1.5.4 Cell-assemblies: Spheroids and Organoids

Spheroid culture is a technique employed to improve biological relevance *in vitro*, which forces cell-cell interactions through some substrate independent culture method (hanging droplet or non-adherent surface coatings). As long ago as 1971, Sutherland et al. published the significance of spheroids as an *in vitro* tumor model, and their popularity has grown once more.[126,127] This method increases cell-cell interactions, allows for cellular co-culture and for cells to produce their own ECM. Spheroid cultures can be amenable to high-throughput screening, but are generally difficult to control, especially in academic labs relying mostly on manual cell-culture procedures. Given the self-assembled nature of spheroids, there is little control over spheroid size, which can lead to substantial nutrient gradients. Additionally, not all cells can be grown in this manner. *Spheroid cultures require substantial investment to optimize culture procedures, and some cells may only form loosely bound cell clusters. Given the difficulty in perpetually expanding primary patient tumor cells, this dramatically limits the clinical utility of spheroid cultures, but they are used as a benchmarking tool in this dissertation.*

1.5.5 Cell Secretions and Decellularized Tissues

Another technique employed in tissue engineering is to produce complex, native growth platforms from cell secretions by removing the cellular components using detergents and ion-gradients. These biochemically and structurally complex tissue scaffolds reflect native environments and utilize methodologies that can be extended to the organ-level. For instance, Ott *et al*. successfully decellularized a rat heart, which gave rise to perfusion-decellularization of whole organs[128]. Since then, companies like Miromatrix Medical Inc. have scaled this to larger, human-relevant sized organs[129].

Cell secreted matrices from relevant stromal cells (CAFs / adipose stroma / bone marrow stromal cells) are also employed in tumor microenvironment modeling [53,54,56]. While these matrices are highly relevant to *in vivo* structures, they lack control over material properties, are slow to produce, are undefined compositionally, and are fragile/difficult to handle. Their compositions can be understood through extensive proteomics and glycomics, but are defined by the cell and not easily be controlled at the onset [130]. This of great concern when considering clinical translation, as such undefined substrates may impart unwanted impurities. *Since cell secreted matrices are physiologically relevant, they are therefore technologically relevant to the studies in this dissertation and serve as a control to benchmark engineered ECMs to native-ECM.*

1.6 Defining the target: Biomaterial Characterization, Benchmarking, and Validation

1.6.1 Biomaterials characterization and its challenges

Biomaterials systems that aim to recapitulate the hierarchal biological features found *in vivo* become increasingly difficult to characterize. Beyond biocompatibility, characterizing

material properties like topology and stiffness in a translationally validated context becomes very difficult as well. There are some standard characterization methods such as those put forth by the American Society for Testing and Materials (ASTM) for biomaterials systems (F2150-13 and STP1173); however, complex composite materials, especially macromolecular systems, may not strictly adhere to the requisites of those tests[131,132]. Yet, as previously discussed, it is well accepted that cell behavior largely hinges on these inherent material properties (physical and biochemical). This underscores the need to approach the characterization of 3D biomaterials with standards and good practices in mind.

Surface topography is known to influence cell behavior, as has been shown with various well-defined engineered 2D surfaces[133]. However, nano-scale topography under physiological conditions in 3D is very difficult to assess *in situ* considering the hydrated state of many biomaterials. Liquid phase atomic force microscopy (AFM) can be applied on relatively flat surfaces; however, many biomaterials have higher order, microscale topography that precludes the use of AFM-based assessment of nano-topography. Future advancements in environmental scanning electron microscopy (ESEM) or cryo-SEM techniques may address some of these shortcomings. Additionally, advancements in ultra-high resolution fluorescent imaging technologies is helping to shed light on focal adhesion dynamics in 3D systems[134]. *For the work in this dissertation, fluorescent microscopy and silicification techniques (Brinker, J and colleagues) to preserve fibrillar structure for standard SEM were sufficient to study topography.*

Characterizing and engineering the biochemical composition of a tissue is also a non-trivial because tissues are compositionally diverse owing to the hundreds of different proteins and polysaccharides that comprise a single tissue[135]. Often, there is a gap in knowledge about the complete composition of a target tissue and most importantly, which of the proteins are critical to

facilitate the tissue's primary function at the cellular level. This gap in knowledge gave rise to a significant effort from a Swedish-based program in 2003 known as the Human Protein Atlas (HPA)[136]. The HPA has set out to map every protein from the cellular to the organ level with a multi-omics approach using transcriptomics, antibody-imaging, and mass spectrometry proteomics[137,138]. Efforts like these will give engineers a target to aim for, so that scaffolds and materials can be more intelligently designed. *However, for the work in this dissertation, histological studies of breast tumors going back ~40 years in some cases was sufficient to guide approaches, but future studies would benefit from an omics-approach.*

1.6.2 Functional Benchmarking and Tissue Characterization

Establishing functional benchmarks for *in vitro* systems against native tissues is non-trivial, yet key to the success of any *in vitro* technology to ensure that new approaches can be scaled and validated. For instance, primary hepatocyte spheroids led to the ability to maintain viable, metabolically active, functional hepatocytes and translationally relevant cultures for up 5 weeks which is not possible to do using conventional 2D culture methods [139]. In 2017, AstraZeneca and Genentech used primary hepatocyte spheroids to demonstrate an improvement in hepatotoxicity prediction power of this 3D model compared to 2D methods of culturing hepatocytes [140]. In addition to potential strides in preclinical drug safety assessment, the knowledge gained from understanding how the 3D microenvironment of a liver spheroid improves primary hepatocyte viability and function could potentially inform the next steps to recreating larger scale functional liver mimics for tissue engineering applications.

In cardiac engineering, readouts for tissue maturation include conduction velocity, force generation, and calcium handling[141,142]. With these benchmarks, Ronaldson-Bouchard *et al*. could clearly demonstrate the state of the art in maturing iPSC derived cardiomyoctes *in vitro*[143]

at that time. These and similar constructs can be used to improve preclinical toxicity assessment, and glean critical information for eventual full scale tissues for implantation.

In stark contrast, tumor tissue engineering is ambiguous because they are vastly heterogeneous and by definition are abnormal. Hence, the benchmarks of "normal," "adult," "fetal," that can sometimes be leveraged guide tissue engineering of healthy tissues are undefined in tumor tissues. It instead makes sense to focus on *ex vivo* expansion of primary cells and the enrichment of invasive phenotypes implicated in metastasis. Recent advancements in immunotherapies has only bolstered the need for *ex vivo* tumor cell growth in order to create personalized medicines, where 2D culture methods fail. As outlined in previous sections, there exists *no universal solution for the reliable expansion of tumor cells, where biomaterial models offer a path forward.*

1.7 A hybrid approach to biomaterials for preclinical modeling

1.7.1 Tissue as Composite Materials

Tissues are composite materials comprised of complex interfaces where ECM proteins and glycans act in concert to direct cell fate with multi-faceted cues that hinge on their material properties. To engineer tissue, multiphasic materials systems are necessary. Given that cells respond sensitively to their microenvironment, it becomes paramount to precisely control proteins/glycans used *in vitro* while considering *how simple is complex enough* (a mantra of tissue engineers). *Toward this, hybrid engineered models utilizing native proteins/glycans suspended across synthetic polymer scaffolds offers an attractive approach to reduce complexity while leveraging control in order to preserve known (and potentially unknown) roles of ECM molecules.*

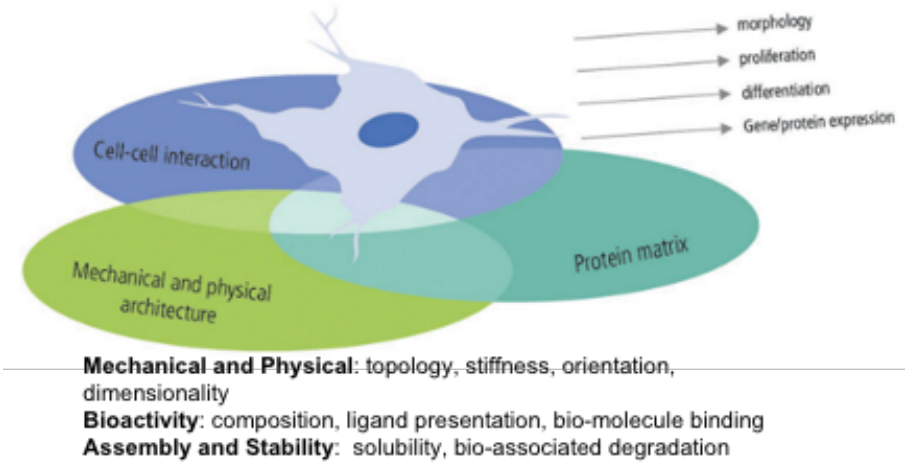

Figure 1.1
Illustration of extracellular influences on cell fate and critical hallmarks to consider when defining engineered systems

Parameters to consider when designing an artificial matrix include composition, morphology, relative amount, fibril density, relative stiffness, the orientation of the protein structures, their biochemical binding characteristics, assembly modalities, their stability, as well as degradability. [144–146] Figure 1.1, illustrates these important hallmarks of tissue heterogeneity.

1.7.2 Leveraging Engineered Extracellular Matrices to Model Native-ECM

Hurdles to translating 3D models include **cost, process scalability**, **ease of handling**, and **reproducibility** with the monumental effort of capturing **physiological relevance**. To address challenges in tissue engineering, our lab has developed a process by which suspended protein matrices can be produced by shearing solutions across hyperporous polymer scaffold. This process was extended to various proteins including Fn, collagen-I, and laminin. It was demonstrated that **engineered extracellular matrices (EECMs)** have great promise in stem cell engineering and tumor microenvironment engineering with great potential to reliably expand patient derived tumor cells scaffolds.[82,147]

In studying pure Fn, collagen and laminin EECMs, it became clear that *Fn is an elusive biomaterial that has been underexplored relative to other naturally derived materials* with intriguing biological roles in embryonic development, wound healing, and tumorigenesis. Fn is an anchorage, stem-cell niche protein that directs cells through integrin binding. During my dissertation research, myself and others in the lab leveraged Fn's universality to collectively demonstrate that EECMs could be used to culture many cell types – including pluripotent stem cells, mesenchymal stem cells, and tumor cells of various tissue origin. This makes Fn-based EECMs incredibly attractive as a potentially unprecedented, universal solution in biomaterials research.

Furthermore, Fn has been described as an extracellular "glue" that facilitates the assembly of other ECM molecules.[148] Therefore, the notion that fibronectin fibrillogenesis in our system occurs was of great interest to potentially mimic native-ECM assembly modalities. Collectively these engineered Fn networks appeared to have the requisite qualities for translation as a universal solution for preclinical modeling. *Namely, they were **compositionally definable**, potentially **scalable**, convenient to **handle**, and seemingly **native-like** when compared to cell secretions which could enable a single platform for simultaneous efficacy and toxicity modeling.*

1.8 Scope of this Work

Critically, Fn alone is not sufficient to capture native tumor tissue heterogeneity, where multi-component mixtures are necessary (discussed in 1.3.2). *Hence, while Fn EECMs displayed great promise, their translation and application as a preclinical model was inhibited by a limited understanding of their assembly, physiological relevance, physical properties, and scalability.*

*For my dissertation research, I sought to characterize the assembly of this Fn-based material system, expand control over **composition** and **topology**, and employ EECMs as **scalable***

tissue-mimetic *preclinical cell culture models with* ***defined heterogeneity***. To do this, I explored hallmarks of native tissues and leveraged that knowledge to engineer biomimetic ECMs with Fn at their foundation. With rationally designed EECMs, I investigated the bi-directional relationship between tumor cells and their protein-glycan microenvironment. The following is a brief overview of my dissertation chapters.

Chapter 2: explores engineered fibronectin matrices as a platform for ECM mimicry. **Bioactivity**, **stability/degradability**, and **mechanical properties** are characterized as they relate cell-derived matrices and breast tumor tissue.

Chapter 3: explores hydrodynamics to control fibrillar **architecture** during fibronectin EECM assembly. **Topography** and **dimensionality** are characterized, and the role of fibronectin **architecture** is explored as a topographical cue for cell orientation and motility.

Chapter 4: explores the **assembly** of Fn EECMs compared to hallmarks of cell-derived matrices. Methodology is developed to expand **biochemical composition** to include critical glycans (hyaluronan) associated with ECM remodeling. Here, I report defined hyaluronic acid-fibronectin matrices that model tumor-associated Fn-HA rich stroma. These EECMs are leveraged to understand the influence of HA and Fn on metastatic potential of breast tumor cells.

Chapter 5: outlines methodology used in the studies throughout the dissertation.

Chapter 6: Summarizes the work presented in the dissertation and lays out promising preliminary studies that serve as the basis for future work to improve applications of EECMs. Here photolithography was employed as an established process to improve polymeric scaffold **scalability** enabling new geometries used to explore **dimensionality** in angiogenesis, as well as novel opportunities to model tumor-blood vessel dynamics. Then approaches for combining 3D printing technologies and EECMs are demonstrated. These would enable defined **cell-cell/cell-**

ECM interactions in 3D tissue models. Finally, improvements to EECM **reproducibility** and **scalability** using 3D printing and soft-lithography is demonstrated. This would enable clinical applications requiring large scale constructs as well as high throughput micro-tissues.

Chapter 2 Engineered Fibrillar Fibronectin and its Characterization

2.1 Publication Information

Parts of the work presented in this chapter are published as:

S. Jordahl, L. Solorio, Dylan B. Neale, Sean McDermott, Jacob H. Jordahl, Alexandra Fox, Christopher Dunlay, Annie Xiao, Martha Brown, Max Wicha, Gary D. Luker, and Joerg Lahann. "Engineered Fibrillar Fibronectin Networks as Three-Dimensional Tissue Scaffolds." *Advanced Materials*. 31(46). 2019. DOI: 10.1002/adma.201904580 [147]

And

Dylan B. Neale, Ayşe J. Muñiz, Michael S. Jones, Do Hoon Kim, Johanna M. Buschhaus, Brock A. Humphries, William Y. Wang, Brendon M. Baker, Jeffery E. Raymond, Luis Solorio, Gary D. Luker, Joerg Lahann "Aligned Networks of Engineered Fibrillar Fibronectin Guide Cellular Orientation and Motility." *Small Structures.* 2(6). 2021. DOI: 10.1002/sstr.202000137 [149]

And

Anke Steier,* Ayşe J. Muñiz,* Dylan Neale,* Joerg Lahann. "Emerging Trends in Information-Driven Engineering of Complex Biological Systems." *Advanced Materials.* 31(26). 2019. DOI: 10.1002/adma.201806898.[1] * = authors share equal contribution.

2.2 Abstract

Adhesive proteins, and ubiquitously Fn, are used functionally as adsorbed coatings in order to improve attachment and create a more supportive cell environment when using synthetic material substrates either in 2D or 3D. However, adsorbed protein coatings are deposited in a

manner which is structurally and functionally distinct from fibrillar protein networks naturally deposited by cells that constitute native-ECM. While primary amino acid sequence is associated with differences in protein bioactivity, Fn bioactivity is highly sensitive to the physical conformation in which it is presented in an engineered system. Furthermore, Fn is foundational to ECM assembly and implicated in hallmarks of tissue development in all stages of mammalian development, as well as pathogenesis. Hallmarks of cell-assembled matrices are well defined using cell-secretion models; however, engineered biomaterials have historically failed to recapitulate hallmarks of cell-derived Fn assembly. Our lab developed a hydrodynamic methodology to produce insoluble fibrillar Fn matrices which served as 3D cell culture substrates and appeared to mimic that of native cell assembled Fn assembly. While these Fn EECMs proved incredibly useful in tumor cell and stem cell culture, fundamental characterization of these materials was lacking. In this chapter the mechanical properties, degradability, stability, and bioactivity of engineered Fn matrices (Fn-EECMs) are characterized against published literature to benchmark Fn EECMs to native-ECM. It was found that Fn adsorption onto surfaces does not promote assembly of Fn that facilitates binding of certain type III domains. Furthermore, Fn EECMs were found to be stable following classically defined characteristics of cell-secreted ECM with mechanical properties analogous to breast tumor tissue.

2.3 Introduction

2.3.1 Fibronectin, a Foundational ECM Molecule

The ECM is a complex amalgam of biomacromolecules comprised of hundreds of proteins and glycans. Central to tissue genesis, ECM composition and structure transform during healthy and pathobiological processes to characteristically impact function.[1,135,150,151]. Fn is at the foundation of fibrillar ECM assembly and is ubiquitous and indispensable for various processes

in mammalian biology. A mechanosensitive protein, fibronectin exists in a compact state when solubilized such as in blood plasma, and in various stretched states such as fibrillar fibronectin (fFn) in ECM.[152,153] It presents mostly as a large (~440 kDa) dimer in blood plasma and insoluble multimers in tissues.[148,154] Cell-mediated Fn fibrillogenesis is a complex process that is believed to primarily occur through integrin binding of the solute dimeric protein followed by traction force-driven stretching that reveals conformationally active type III domains. These cryptic, type III domains bind additional solute dimers *via* the 70 kDa N-terminus, leading to the formation of insoluble fibrillar networks.[153,155,156] Despite years of study, a comprehensive understanding of the intricacies of native Fn assembly and how each region of the type I, II, and III Fn domains and how they interact with one another or cells to govern fibril formation is still a topic of ongoing research. [157–160]

2.3.2 Protein Adsorption on Surfaces

A common technique for creating an attachment surface for cells on synthetic material scaffolds involves physisorption of proteins. Thereby, the protein needs to undergo a change in conformation to adsorb on the surface. Solution conditions such as concentration, solvent and substrate properties dominate the morphology characteristics of the adsorbed protein layer[144–146]. This stochastic adhesion may lead to denaturation or inaccessibility of binding sides[145]. *In vivo*, cells form protein matrices, especially fibrillar fibronectin under mechanical tension by stretching the protein leading to exposed self-association sites. To mimic this process *in vitro,* various approaches ranging from stirring, mechanically pulling over electrical forces, to the use of active denaturants, have been investigated[161–164].

2.3.3 Biomaterial Mechanical Characterization

The stiffness of a material directs cell fate, which is well accepted using 2D models but becomes increasingly complex to assess in 3D systems. Depending on the inherent properties and size of a biomaterial, the characterization of stiffness may involve rheological techniques, unconstrained compression testing, tensile testing, contact model guided indentation (nanoscale to macroscale) or via ultrasound elastography[165–169]. In all cases, the underlying assumptions and limitations of the model and method chosen should be carefully considered, which may highlight the need for new models to be adapted for particular biomaterial systems. This is especially important when biomaterials *in vitro* are compared to the native, *in vivo*, tissue which often cannot be done directly considering different methodologies needed for each setting. Stringent adherence to good practices, as well as differences in methodologies and test conditions are critical to address when interpreting and comparing the results of mechanical testing[170]. Furthermore, any bulk material properties offer little information as to the cell-scale heterogeneity of mechanical properties, especially as the cells engage in a dynamic modulation of their 3D biomaterial environment through physical manipulation and chemical degradation.

2.3.4 Fn Biomaterials

Despite its prevalence in mammalian biology, Fn's adoption as a 3D biomaterial has been limited, in part, due to the difficulty of understanding and controlling its assembly into insoluble fibrillar networks. Early work utilized solution-denaturants and reducing agents to assemble insoluble fibronectin materials.[171,172] Solution extraction combined with fluid-forces produced large, dense, mats of oriented fibronectin via shearing through a syringe or on spinning impellers.[104,173–175] Recently, a solvent-based rotary spinning technique led to large-scale (centimeter-length), force-induced nanofiber Fn mats that were used in wound healing.[176] Material surfaces can also be used to promote the assembly of insoluble fibrils.[162,177–179] Notable examples

include the demonstration of surface-detachable nanotextiles with precise control over x-y plane arrangement but with limited thickness (1 - 10 nm).[178] Forces generated from the expansion of lipid monolayers in contact with physiological buffers can be used to assemble Fn.[180] Other techniques utilize force at a liquid-air interface to promote assembly, where micron-scale Fn fibrils can be drawn out of concentrated Fn droplets.[173,181,182] Aggregation of Fn at the air-solution interface can be combined with droplet-shearing across micro-engineered surfaces to create suspended fibrils across small gap lengths (< 10 μm).[183,184] Critically, these techniques require manual manipulation to orient fibrils[173,181,182] with intrinsic length scale limitations that preclude formation of millimeter-length fibrillar networks with interconnected 3-dimensionality.[173,181–184]

2.4 Results and Discussion

2.4.1 Fn EECM Stability, Degradability and Bioactivity Compared to Cell Secretions

Fibronectin was historically differentiated by its source: cellular or plasma, which was then correlated to distinct isoforms but were generally defined by their physical presentation.[185] Generally, cellular Fn was generated by cells in culture, wherein insoluble fibrillar matrices could be produced and studied. In contrast, plasma Fn, isolated from blood plasma secreted mostly by hepatocytes, was in a soluble form. For our processes, we use commercially available fibronectin isolated from blood plasma, where this solute protein could be sheared at the air-solution interface across a hyperporous polymer membrane to produce arrays of insoluble networks. And while these fibrillar Fn networks produced (EECMs) displayed notable morphological similarities to matrix deposited by human mammary fibroblasts (work conducted by Jordahl, S. for this publication)[147], their stability, degradability and bioactivity to validate this had not been explored.

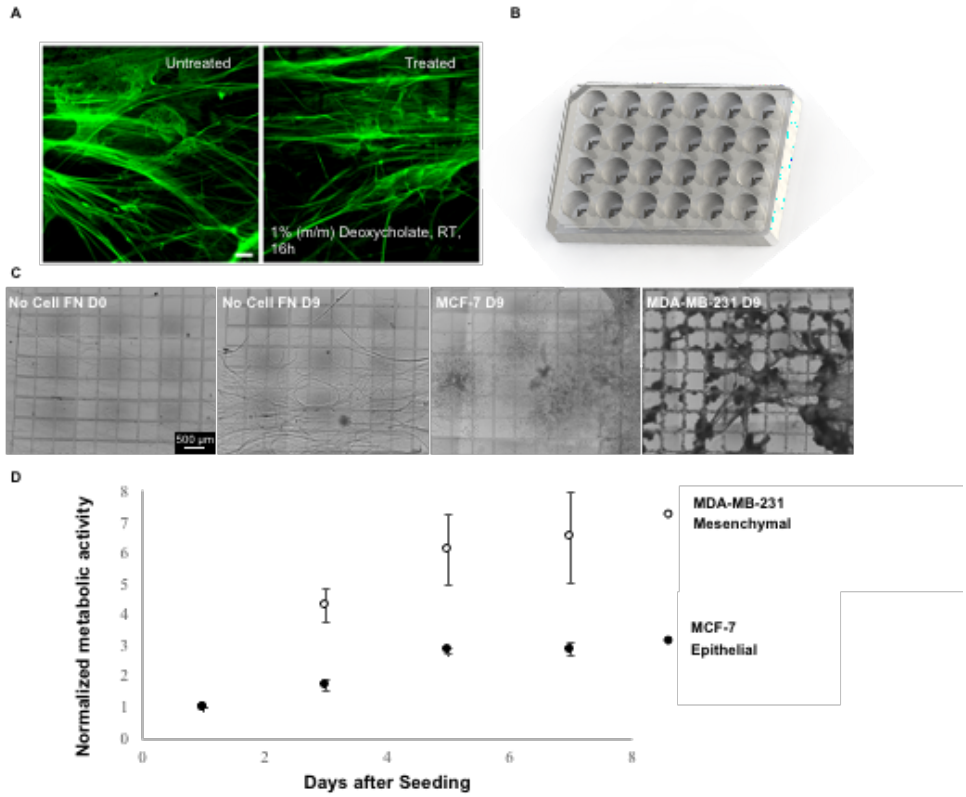

Figure 2.1
Characterization of Fn EECM stability and degradability using classic descriptions and model cell lines*. A: fFn networks remain intact after deoxycholate treatment. (Left) Fn (green) deposited by hydrodynamically induced fibrillogenesis onto a tessellated scaffold. (Right) Fn (green) deposited by hydrodynamically induced fibrillogenesis onto a tessellated scaffold after 1% deoxycholate treatment. The scale bar in (A) is 50 µm. B: illustration of well plate format (24-well) with EECMs attached to steel frames for use in cell culture. C: Representative images of MCF7 and MDA-MB-231s grown on Fn EECMs. D: Normalized metabolic activity to quantify proliferation on EECMs*

Cell secreted Fn matrices in culture were classically defined as being deoxycholate insoluble[186] because adsorbed Fn or aggregated Fn would dissolve when treated with this mild detergent. In contrast, "cellular" fibronectin would resist dissolution, which we now know to be a function of dimeric protein unfolded and strong, Fn-Fn intermolecular interactions that form assembled multimeric structures. Applying this classic description, I treated Fn EECMs with 1% deoxycholate overnight at RT and observed no changes, Figure 2.1 A.

To further probe, stability of EECMs in a biologically relevant context, MCF7s and MDA-MB-231s were used, as MCF7s are an ER+, luminal line that are known to be quite

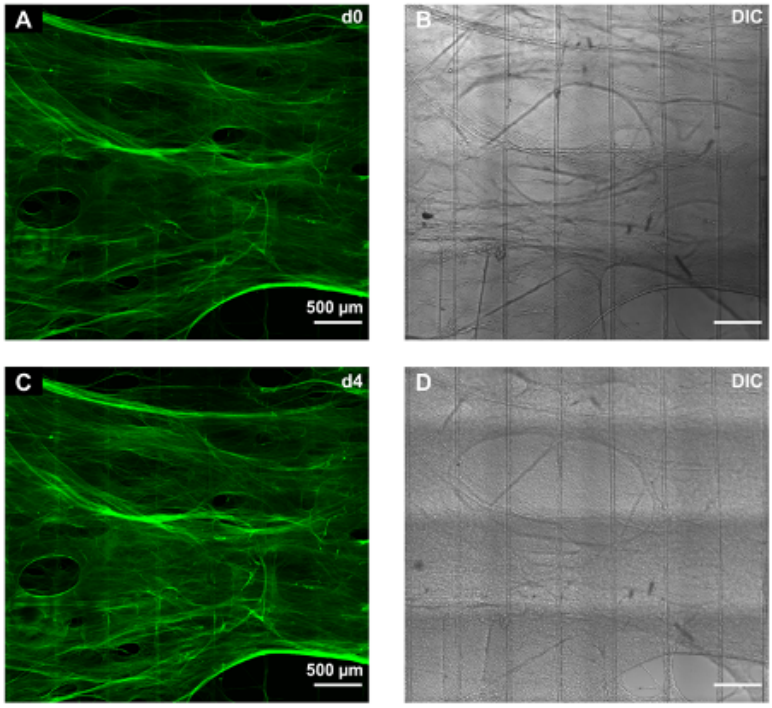

Figure 2.2
EECM stability during culture with NIH-3T3s*. CLSM MIP of an aEECM prior to cell seeding (0 d) and approaching cell saturation (4 d), where cells can be observed in the differential interference contrast (DIC) image.*

epithelial and not aggressive *in vivo*. In contrast, MDA-MB-231s are aggressive and will spontaneously metastasize *in vivo.* Figure 2.1 C shows representative brightfield images over the growth time course, where proliferation was quantified (Figure 2.1 D). This shows that both cell lines reached saturation on the EECMs around d 7, where by d 9 (Figure 2.1 C) brightfield images show that the more aggressive MDA-MB-231s significantly degraded away the matrix, likely as a function of matrix-metalloprotease (MMP) secretion. Below, in Figure 2.2, during culture with NIH-3T3 (mouse fibroblast, non-tumor cell line), confocal images illustrate with greater resolution the remarkable stability of these Fn EECMs during cell culture conditions. Collectively, these data highlights that while assembled, stable constructs for cell culture, Fn EECMs are still able to be degraded by cells and engage in ECM reciprocity, which is an important hallmark of biomaterials systems.[1]

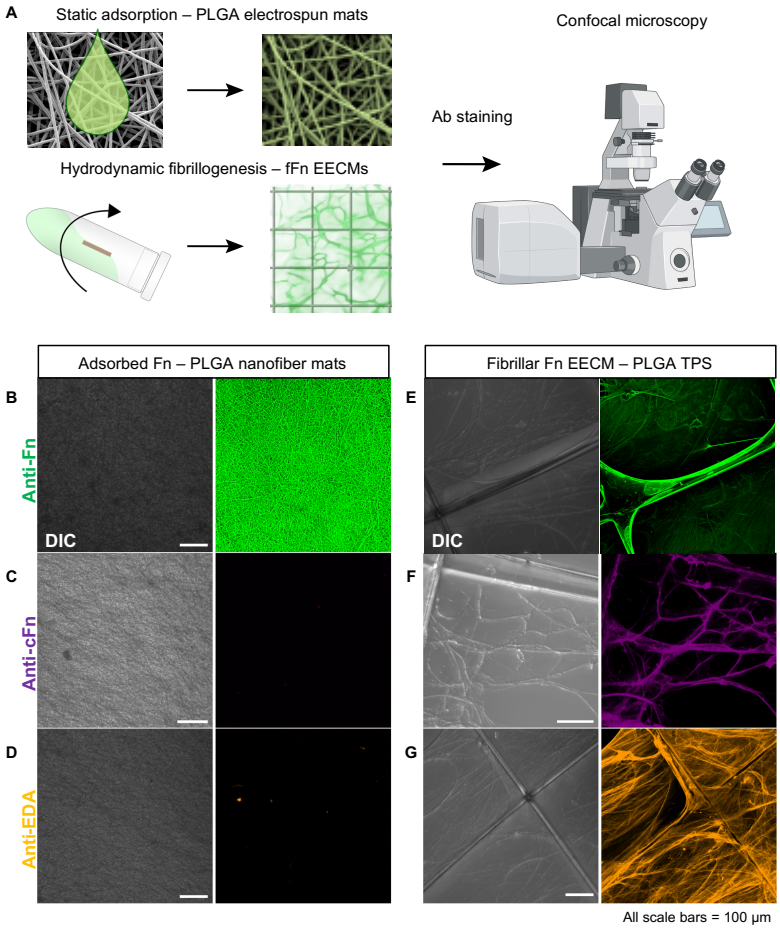

Figure 2.3
Hydrodynamically induced fibrillogenesis of fibronectin results in fFn that is recognized by IST-9 antibody. *A: graphical scheme of experimental procedure. B, C, D (left two columns): non-woven PLGA nano/micro-fiber mats with Fn statically adsorbed. E,F,G: Fn fibrils following hydrodynamic fibrillogenesis across PLGA TPS. Grayscale images in both left and right groups are DIC images (left) corresponding to colored fluorescent image (right). B: Non-specific Fn polyclonal Ab (pAb) (green) staining of Fn statically adsorbed on PLGA fibers. C: Fn-3 antibody staining (purple) of Fn adsorbed on PLGA fibers. D: Specifc mAb (IST9) staining to identify EDA-Fn (orange) for Fn adsorbed on PLGA fibers. E: pAb for Fn (green) on fFn EECM. F: Fn-3 Ab (purple) on fFn EECM. G: IST-9 staining for EDA-Fn on fFn EECMs (orange) (right). Both the Fn-3 and IST-9 antibody only stain positive on fFn networks but not conformally deposited Fn. All scale bars 100 mm*

Critical to Fn's bioactivity are mechanically sensitive type-III domains that lack disulfide stabilization and are comprised of seven stranded ß-barrels sensitive to mechanical deformation. Interactions between these conformationally sensitive ("cryptic") type-III domains and type-I domains were identified as key interactions in Fn assembly.[185] The two cellular Fn isoforms are alternatively spliced type-III domains known as extracellular domain A and B (EDA/EDB or EIIIA/EIIIB).[185]

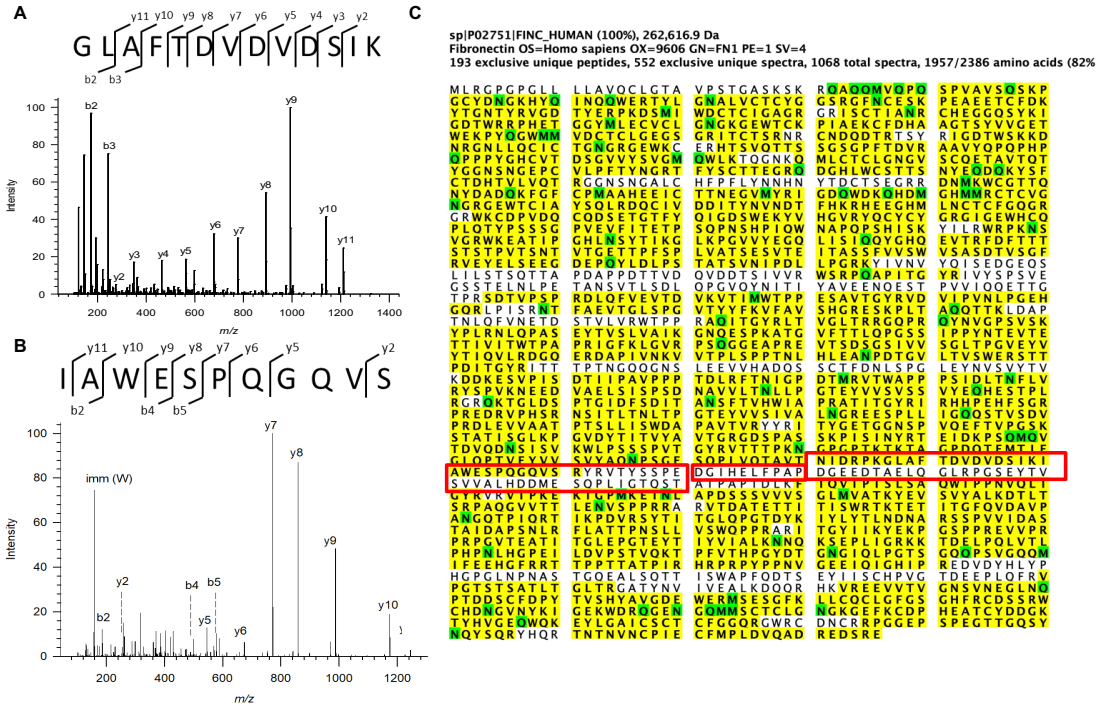

Figure 2.4

Proteomics analysis confirms presence of EDA sequence in fibronectin sourced for fFn EECMs. *Two peptides unique to the alternatively spliced domain A (EDA) sequence were identified in the soluble fibronectin sourced for fFn network formation. Mass spectrometry results are shown for tryptic EDA peptides A-B: N-terminus labelled as b ion and Cterminus labelled as y ion. C: Sequence coverage map of fibronectin where yellow highlight indicates amino acid detection. The amino acid sequence highlighted by the red boxes indicate the EDA portion. At least 71% sequence coverage was reported. Sequence coverage may be greater than 71% and as high as 82%, if variable regions susceptible to modification during analysis are included*

To assess the presence and conformational sensitivity of these type-III domains, fibrillar Fn EECMs were compared to Fn statically deposited onto non-woven mats (a chemically identical polymeric scaffold of randomly deposited PLGA fibers). Those were then stained with a general anti-Fn antibody as well as two “cellular Fn” antibodies, outlined in Figure 2.3 A. Fibrillar Fn but not conformally deposited Fn, stained positively with an Fn-3 antibody indicating exposed cellular fibronectin after hydrodynamic fibrillogenesis. This resembled the staining of Fn deposited by human mammary fibroblasts.[147] In contrast, statically adsorbed Fn on either tessellated scaffolds or tissue culture polystyrene (TCPS) was not recognized by the Fn-3 antibody[147] For further validation, an IST-9 antibody was used since its specificity to the

alternatively spliced domain A (EDA), a cellular fibronectin variant within the type III region of fibronectin, is well documented.[187–189]

When directly comparing engineered fFn networks to adsorbed Fn, we found that the Fn-3 and IST-9 antibodies only recognized the fFn networks and not the Fn conformally deposited onto non-woven mats (Figure 2.3). To definitively confirm the presence of EDA(+) Fn in our protein source, liquid chromatography mass spectrometry-based (LC-MS) proteomics was performed. As expected, the main constituent was Fn with 71 to 82% sequence coverage (Figure 2.4). Annotated MS/MS spectra for tryptic EDA peptides GLAFTDVDVDSIK and IAWESPQGQVSR are shown in Figure 2.4 A and 2.4 B, respectively. These EDA fragments are expected to be identified after trypsin digestion and indeed were identified with nearly complete sequencing, confirming the presence of EDA(+) Fn in our protein source. Although, plasma Fn isoforms are the main constituent of Fn in blood plasma, previous studies have reported that small fractions of cellular Fn can circulate in the blood of healthy patients.[190] We note that the role of the EDA domain in Fn biology is a topic of ongoing investigation. While this variant is not believed to be a requisite for fibrillogenesis,[191]some studies have shown it plays an important role by leading to more robust fibrillar networks secreted by cells.[192]Additionally, while some report recombinant EDA(+) Fn coated onto a surface may enhance cell migration,[193]other studies have suggested that knockdown of EDA-Fn secretion impedes cell motility even on Fn coated substrates.[194]Missirlis et al. discuss potentially conflicting results researchers have reported with respect to the role of EDA-Fn in cell motility.

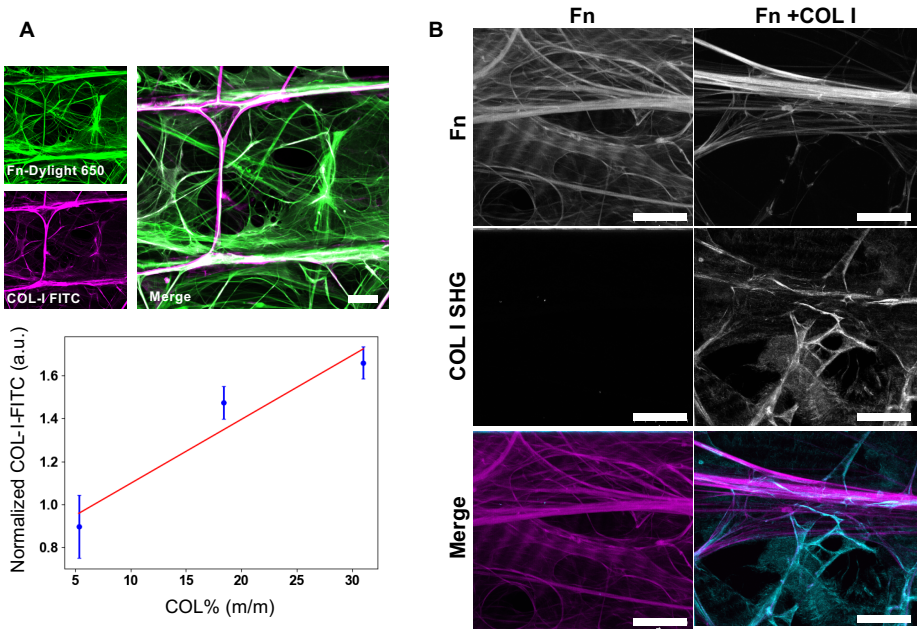

Figure 2.5
Fibronectin and collagen co-assembly in EECMs*. A: fFn EECM with FITC-COL / FN. SHG imaging of native COL/FN (right column). Below is image quantification demonstrating control over mass ratio. B: fFn EECM with native Fn and COL-I. SHG imaging of native COL/Fn. In collaboration with J. Buschhaus, Luker Lab Scale bars: 100μm*

2.4.2 Fn-Collagen EECMs and Fn EECM Mechanical Properties

Fn is a known promiscuous binder of growth factors and other ECM macromolecules and even contributes to their assembly.[160,185] In pulse chase experiments, it was shown that fibrillar collagen stabilization in cell secreted networks required fibronectin.[195] Furthermore, collagen-I self-assembly into the gels typically used by researchers (discussed in the Ch.1 Introduction) occurs at concentrations higher than is physiologically relevant (>1 mg/mL), where Paten et al. remarked the co-assembly of collagen with Fn in vitro at 0.5 mg/mL as indicating unique Fn-collagen interactions.[160] Taking this as a baseline, I investigated the assembly of Fn EECMs with collagen-I (COL I) present. Typically, Fn EECMs are produced from 100ug of the protein in a total of 900uL of DPBS. Prior to coating, I added ~50ug, ~20ug, and ~6ug of FITC labeled

COL-I to 100ug of Fn in a total of 900uL DPBS, Figure 2.5 A. At ~33% m/m (~0.06mg/mL), confocal images show strong signal from the COL-I co-localizing with Fn. After performing image quantification, I demonstrate that the relative intensity of COL-I/Fn correlates well with the mass fraction in the mixture. Since this experiment showed promise, 33% m/m COL-I / Fn EECMs were produced using an unlabeled collagen isolated from rats. Second harmonic generation (SHG) was used to image the unlabeled COL-I because this technique is widely used as a label-free, imaging technique for assembled collagens *in vivo*.[62] SHG occurs when the electric field of incident light is sufficiently strong to deform asymmetric molecules. The subsequent anisotropy generates an oscillating field at twice the frequency (half the wavelength). This signal is strong in assembled collagens due to the asymmetric crystalline nature of their triple helices. Notably, Fn does not exhibit the same phenomena, so a fluorescently tagged dye was used to visualize Fn. SHG, displayed in Figure 2.5 B, confirmed that the 33% m/m COL-I scaffolds indeed displayed imaging signatures of assembled collagen. This occurred at ~10-fold lower concentrations than the most relevant similar report of cell-free assembled matrices,[160] and further validates the native-like bioactivity of Fn EECMs used by our lab. Furthermore, it technologically enables future, assembled Fn/COL EECMs to be employed as defined, multi-component mixtures to model TACS (outlined in 1.3.2).

Finally, to establish a baseline for defining the mechanical characteristics of these EECMs, I devised a way to coat EECMs over a substrate with a cylindrical opening such that the geometries would match a thin-film contact mechanics model developed and published by Baker et al. that has been validated to characterize the mechanical properties of geometrically similar, thin electrospun mats.[168,196] Force-distance curves were gathered using a CellScale Microsquisher, the model was fit to the data using a least squares regression with the force as the

fitted parameter to determine the elastic modulus. Poisson's ratio was assumed to be 0.5. These preliminary studies place pure Fn EECMs at ~27 ± 17.9 kPa, with a thickness of 54.1 ± 9.6 μm (n = 4). This confirms that the range of Fn EECMs is within the 10s of kPa range reported for breast tissue and other pathogenic tissue models, where Seo et al. reported a modulus range of 9 – 25kPa for cell secreted matrices used as models for breast tumors.[56]

2.5 Conclusions and Implications

Collectively, these data provide strong evidence that Fn EECMs display many traits of native-like cell assembled Fn ECM. They are incredibly stable in cell culture conditions and easy to handle making them practical to use. Furthermore, they display binding via antibodies in a manner that suggests that EDA(+) Fn within our protein source is physically exposed only after hydrodynamic fibrillogenesis, and is not available for antibody binding when then the Fn is conformally adsorbed onto a surface. The mechanosensitivity of the EDA domain is not well known according to leading experts in the field;[148] hence, it is reasonable that changes in Fn-EDA binding activity may occur when Fn is presented in a fibrillar state compared to a conformal surface coating, which has not been directly investigated to our knowledge for the EDA domain. Making this one of the first reports implying EDA as a mechanosensitive domain following fibrollogenesis. This finding warrants further investigation given the potentially conflicting results reported for the EDA domain. Furthermore, these many unknowns underscore the need for a native-like fibrillar Fn cell culture platform.

Toward assembly, we postulate that our Fn fibril production and characterization results are consistent with a mechanism where interfacial shearing induces mechanical deformation of solute Fn that extends the protein, enabling self-polymerization and fiber formation. This is analogous to the mechanically induced unfolding of the fibronectin molecule during cell-driven

as well as previously reported shear-driven fibrillogenesis, outlined in the introduction. In contrast to the widely used conformal Fn pre-coatings, hydrodynamically induced fibrillogenesis not only results in a stable, fibrillar matrix readily applicable to 3D cell culture, but also provides access to ECM mimicries with well-defined characteristics.

Chapter 3 Aligned Networks of Engineered Fibrillar Fibronectin Guide Cellular Orientation and Motility

3.1 Publication Information

The work in this chapter is published as:

Dylan B. Neale, Ayşe J. Muñiz, Michael S. Jones, Do Hoon Kim, Johanna M. Buschhaus, Brock A. Humphries, William Y. Wang, Brendon M. Baker, Jeffery E. Raymond, Luis Solorio, Gary D. Luker, Joerg Lahann "Aligned Networks of Engineered Fibrillar Fibronectin Guide Cellular Orientation and Motility." *Small Structures.* 2(6). 2021. DOI: 10.1002/sstr.202000137 [149]

3.2 Abstract

The ECM influences biological processes associated with tissue development and disease progression. However, robust cell-free techniques to control fiber alignment of naturally derived ECM proteins, such as fibronectin, remain elusive. It is demonstrated that controlled hydrodynamics of fibronectin solutions at the air/fluid interface of porous tessellated polymer scaffolds (TPSs) generates suspended 3D fibrillar networks with alignment across multiple length scales (< 1 μm, 1 μm - 20 μm, extended to > 1 mm). The direction of the fluid flow and the architecture of the polymeric supports influence protein solution flow profiles and, subsequently, the alignment of insoluble fibronectin fibrils. Aligned networks of fibrillar fibronectin characteristically alter fibroblast phenotype, indicated by increased directional orientation, enhanced nuclear and cytoskeletal polarity, and highly anisotropic and persistent cell motility when compared to nonaligned 3D networks and 2D substrates. Engineered extracellular

matrices (EECMs) establish a critically needed tool for both fundamental and applied cell biology studies, with potential applications in diverse areas such as cancer biology and regenerative medicine.

3.3 Introduction

Aligned architecture is ubiquitous in ECM across various niches including soft tissue, skeletal muscle, cardiac tissue, and pathogenic tumor tissue.[197–200] On the macroscale, alignment guides load bearing in tendons, facilitates force transmission in muscle, and promotes healthy cardiac processes[151,199–201], while in cancer is correlated with poor prognosis.[6,7] In skin, local regions of anisotropic ECM fibers with long range isotropy are characteristic of normal structure and mechanical stability, while the deposition of dense, highly aligned ECM is associated with aberrant scar tissue.[176,202,203] On the cellular scale, ECM anisotropy has nuanced influences in wound healing, electrical signal propagation, angiogenesis, and remodeled pathogenic tissue, [50,143,204–207] where the complex origin-effect relationship of aligned ECM is just beginning to be understood using 2D culture models.[208] This manifests a need for engineered 3D protein structures with tunable alignment to serve as robust *in vitro* models and help elucidate the complex role of ECM organization.

Emerging studies into the architecture of ECM typically use synthetic materials, collagen gels, cell-secreted matrices or adsorbed protein layers deposited onto 2D substrates to model fibrillar structures.[53,194,209–211] Cell-secreted matrices model native fibrillar microenvironments, but these are complex amalgams of various deposited proteins and soluble factors.[130] Collagen gels are a prevalent biomaterial, where there exists several methods to create aligned networks *in vitro* including shear flow, magnetic fields, and mechanical strain.[210,212–216] Equivalent methods do not exist for other highly relevant ECM proteins, namely fibronectin (Fn). Mounting evidence

suggests that Fn has a significant role in governing cell orientation and motility.[154,194,211,217] Additionally, cancer associated fibroblasts secrete aligned Fn, among other macromolecules, which has been shown to promote the migratory behavior of tumor cells *in vitro*.[53,54] Below is a summary of fibronectin biomaterials and their microstructural control.

Table 3.1
A summary of fibronectin-based biomaterials and their characteristics. *Documented are the methods of Fn assembly, the ability to control orientation in order to create aligned or non-aligned matrices, the dimensionality (i.e. 2D/3D), overall x-y material scale, fiber diameters, their microstructure, and the type of substrate (i.e., free standing, suspended, or adhered to a surface/2D material). If a material is noted as 2.5D that indicates that the Fn network is relatively thin but are suspended or freestanding in such a way that differs from a conventional 2D substrate. n.r. – not reported, FS – free standing; Sus. – suspended, Adh. – adhered to a 2D substrate*

Method	Alignment (length scale)	Dimensionality	Overall area or length	Fiber diameter	Microstructure	Type of substrate	Ref.
solution		n.r.	cm^2	10 ± 2.8 nm	n.r.	FS	[171,218]
shearing via impellers and syringes	yes, mm	3D	cm^2	2-7 µm	Dense mats with tubular pores	FS	[104,173,175]
lipid monolayer expansion	no	n.r.	μm^2	"few" µm	Fibrillar networks	n.r.	[180]
manually drawn from droplets	yes, mm	2D	mm	0.2-10 µm	Branched fibrillar networks	Adh.	[173,219]
manually drawn from droplets	yes, cm	1D	cm	2 - 5 µm	single fibers	Sus.	[181,182,220]
shearing across micropillars	yes, <10 µm *gaps*	2.5D	cm^2	Single fibers: 20 - 160 nm fiber bundles: ~1-2 µm	Single fibers or fiber bundles bridging micropillars with <10 µm gaps	Sus.	[183,184]
rotary jet spinning	yes, <200 µm	3D	cm^2	457 ± 138 nm	Fibrillar networks	FS	[176]
surface-induced	no	2D	cm^2	≤10 µm	Fibrillar networks	Adh.	[162,179,221]
surface-induced	yes, mm	2.5D	mm^2	3.7 ± 1.0 µm	User-defined patterns	Adh., Sus., FS	[177,178]

Recently, our group demonstrated creation of millimeter-scale suspended 3D fibrillar Fn networks compatible with conventional cell culture and analysis modalities were achieved which was extensively characterized in Chapter 2.[147] Critically, these constructs lacked precise control of fiber alignment.

Here, control over the degree of alignment of 3D fibrillar Fn networks suspended across porous polymer support structures without the use of solution denaturants or solvents is demonstrated. These engineered extracellular matrices (EECMs) display cell relevant 3-dimensionality (~50 – 70 μm), suspension over large gap lengths (245 – 950 μm) and coverage over large areas (~25 mm^2). Further proposed is a process whereby fibril assembly at the air-solution interface is guided by flow profiles that can be tailored through physical interactions between the solution and polymeric support scaffold. This novel system is applied to study the influence of Fn fiber directionality on fibroblast morphology and motility. This work establishes a cell-free technique to model 3D fibrillar networks of Fn with controlled orientation using the purified protein. To our knowledge, this constitutes the first report of such a Fn-based system.

3.4 Results and Discussion

3.4.1 Polymer Scaffold Geometry and Orientation Induces Fibril Alignment During Hydrodynamically-induced Fibrillogenesis

We explored the hypothesis that tailored fluid flow profiles across the tessellated polymer support structures at the air/fluid interface will influence directional orientation of the fibril architecture during hydrodynamically-induced fibrillogenesis. Polymer scaffolds, comprised of SU-8, were engineered using photolithography to contain extended rectangular pores with varying gap lengths of 248 μm ± 3.2 μm, 497 μm ± 5 μm, and 946 μm ± 2.6 μm, and with strut widths of 36 μm ± 0.7 μm (Table 3.2). Scaffolds were engineered to be thin (112 μm ± 1.7 μm)

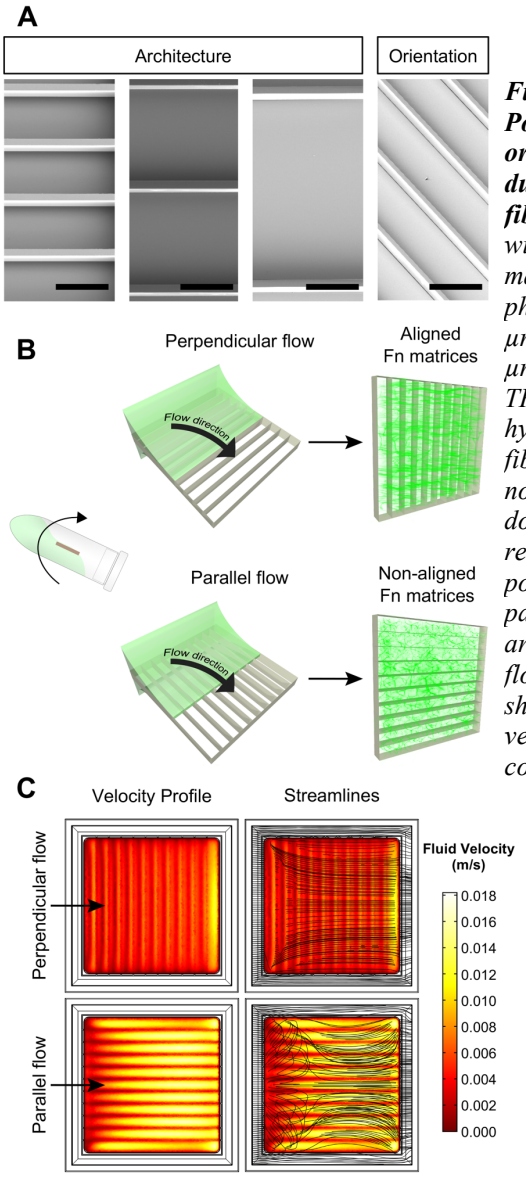

Figure 3.1
Polymer scaffold geometry and orientation induces fibril alignment during hydrodynamically-induced fibrillogenesis*. A: SEMs of TPSs with rectangular pore geometries made from SU-8 via photolithography. Scale bars are 500 µm (architecture) 250 (orientation) µm. B: illustration depicting how TPSs are coated via hydrodynamically induced fibrillogenesis to produce aligned or non-aligned 3D Fn matrices. C: Top-down view of COMSOL model revealing flow profiles when TPS pore direction is perpendicular or parallel to flow direction. Black arrows indicate the direction of fluid flow on the inlet side. Streamlines are shown in black and plotted over the velocity profile which is depicted via color from 0 m s−1to 0.018 m s−1.*

in order to avoid limits in nutrient/oxygen diffusion, allow for efficient imaging, and provide sufficient free volume to be filled in by the suspended Fn networks (~3.77 mm^3). These rectangular pores (~0.25/0.5/0.95 mm by ~5.8 mm) were tessellated across a length of ~5.8 mm, and act as a highly porous, free-standing support structure for the suspended 3D fibrillar Fn networks. While SU-8 is not considered a bio-absorbable polymer, it has been demonstrated to have *in vitro* and *in vivo* utility as a biomaterial.[55,222,223] Therefore, it was used in this model

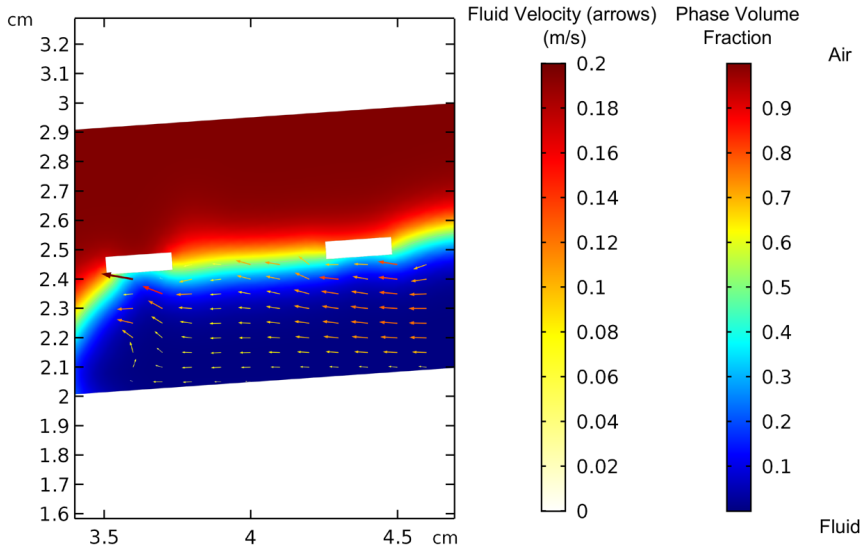

Figure 3.2
Time-lapse 2D fluid model to assess flow characterics in microcentrifuge tubes at 1.45 s (8 RPM) used to evaluate the velocity of fluid flow during hydrodynamically-induced fibrillogenesis. *Arrows and colors of the arrows (white to red scalar) indicate the direction of flow and velocity, respectively. The two phases (fluid, air) are depicted with the blue to red scalar.*

system to allow for high fidelity to intended scaffold geometries, rapid fabrication, and mechanical robustness. Polymer scaffolds with pores of varying gap length are depicted in SEMs (Figure 3.1A, Table 3.2). As indicated in Figure 3.1B, the Fn networks are 3D fibrillar networks suspended across a highly porous scaffold comprised of tessellated rectangular pores. These scaffolds are herein referred to as tessellated polymer scaffolds (TPSs). Using fluid modeling (COMSOL Multiphysics), we compared the flow characteristics across TPSs with pores oriented perpendicular or parallel to the inlet flow direction; (see SI of published manuscript**)** for a wireframe diagram to reference the scaffold geometry with respect to the flow direction. To inform the 3D model design, a two-phase, time-lapse 2D model was generated, (Figure 3.2). With perpendicularly orientated pores, the flow was slower and resulted in generally straighter streamlines across the entire length of the TPS (Figure 3.1C). The streamlines also exhibited a slightly periodic nature with some recombining flow profiles from pore to pore (Figure 3.3). When the fluid flow direction is parallel to the long axes of the pores, the flow tended to be faster

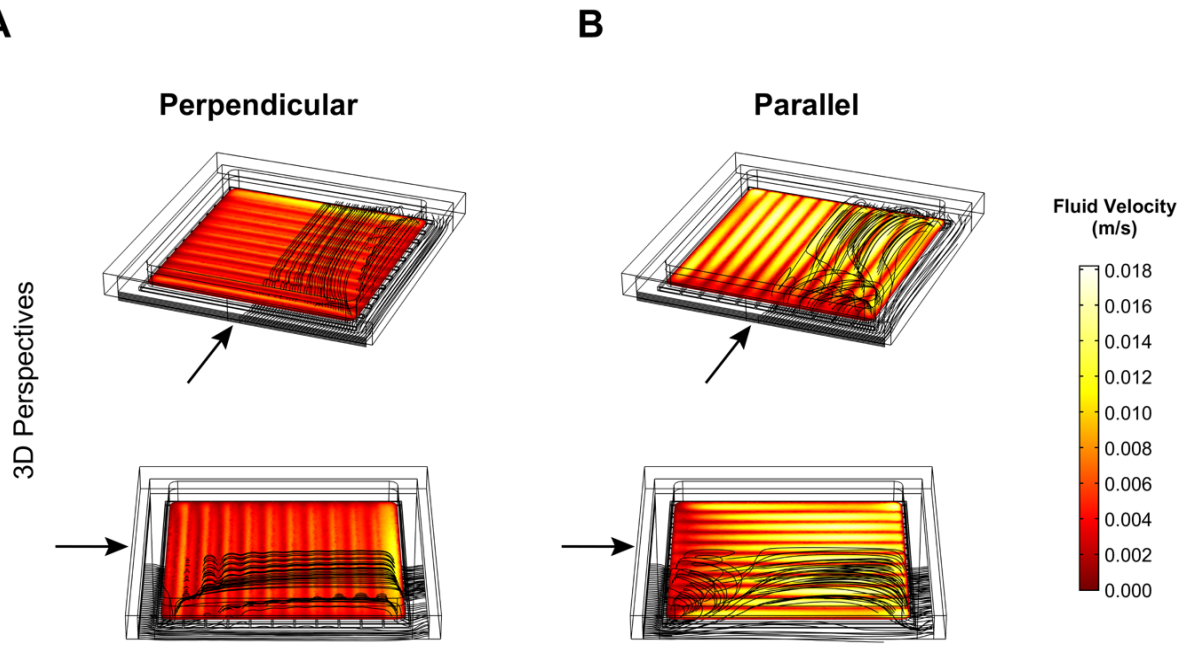

Figure 3.3
3D perspectives of the fluid flow profile across perpendicular (A) and parallel (B) oriented TPSs*. Black arrows indicate fluid flow direction on the inlet side of the model. Streamlines are shown in black while velocities are represented by color*

with more vortices, which leads to warped streamlines across the length of the entire scaffold (Figure 3.1C, Figure 3.3). The modeling suggests that TPSs with perpendicularly oriented pores lead to a more coherently aligned fluid flow field across the length of the scaffold. Collectively, the modeling data suggest fluid flow profiles can be guided during hydrodynamically-induced fibrillogensis as a function of interactions between the supporting TPS and the protein solution. If fibril assembly follows fluid flow profiles, hydrodynamically-induced fibrillogenesis perpendicular to the long axis of the TPS pores would give rise to aligned Fn fibril architecture, represented schematically in Figure 3.1 B. Conversely, if the fluid is directed such that the flow is parallel to the long axis of the pores, the fibrillar networks would be more disorganized and less oriented (Figure 3.1B). Throughout this manuscript, alignment refers to individual fibrils within a network of Fn that share a common directionality axis, where the axis of alignment is defined as the 0° - 180° horizontal line. In aligned engineered extracellular matrices (aEECM),

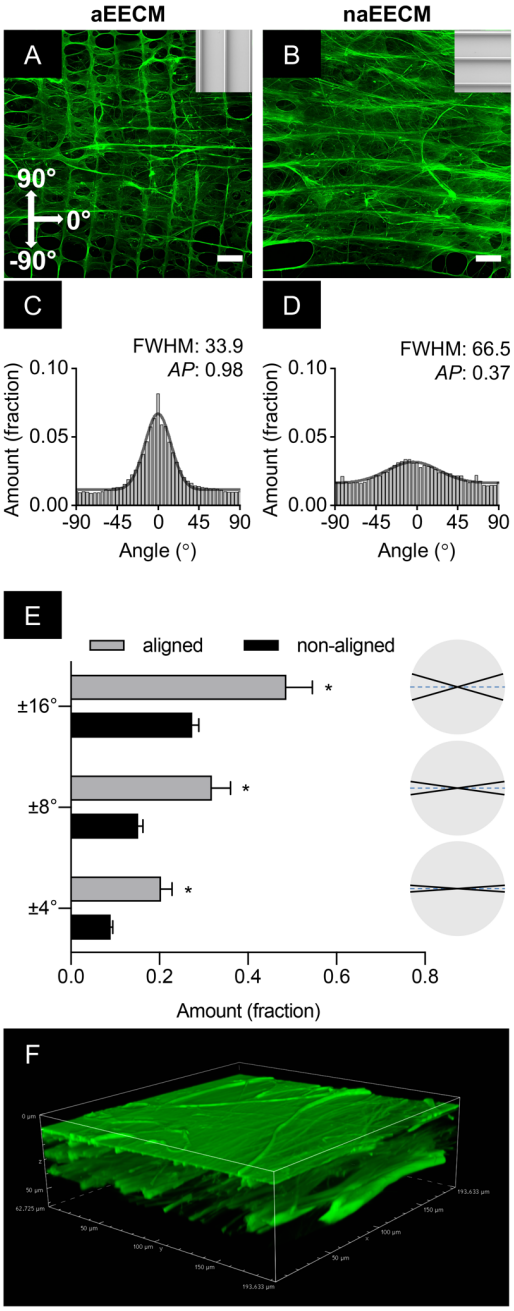

Figure 3.4
Precisely aligned 3D fibronectin networks across the tissue length scale*. A,B: CLSM MIPs with SEMs of polymer scaffolds overlaid in the upper right-hand corner to illustrate the orientation of polymer pores with respect the 0° flow direction. Left column: aEECM. Right column: naEECM. Scale bars are 500 µm. C,D: directionality histograms of CLSM MIPs for aEECM and nEECM, respectively. Gaussian fits are overlaid in black. FWHM are reported to indicate narrowness of the distribution, as well an alignment parameter AP which indicates increases in aligned fibrils with higher values. E: summation analysis of histogram data from C,D to assess the amount of features within different angle bins. The circular diagrams to the right of the graph graphically represent the boundaries of the bin (black lines), and the 0 – 180° line (dashed blue line). F: volume render of an aEECM (two coatings). The volume boundaries in the image are 193.633 µm (x,y) and 62.725 µm (z). The Holm-Sidak Multiple t-test was used to assess significance. *P ≤ 0.05.*

the fibrils share a directional axis, whereas significantly fewer of the fibrils in non-aligned engineered extracellular matrices (naEECM) share a common axis and lack overall organization.

3.4.2 Precisely aligned 3D fibronectin networks across the tissue length scale

TPSs were coated with Fn at a concentration of 111 µg mL^{-1} via rotation at 8 RPM following the procedure schematically represented in Figure 3.1 B**,** described in the *Experimental* section

and previously reported.[147] With this technique, fibrillogenesis does not occur in the absence of fluid flow (i.e., 0 RPM). [147] We postulate the mechanism of fibril assembly occurs by a force-induced process at the solution/air interface across the TPS, which is likely similar to the fiber drawing/droplet shearing processes previously reported [173,181,183]. Additionally, these fibrillar Fn materials are insoluble to an overnight treatment in 1% deoxycholate, further indicating that they are assembled, multimeric Fn networks.[147] SEMs of the TPS pores are overlaid in the upper right-hand corner of the maximum intensity projections (MIPs) to indicate the orientation of the TPS pores at the time of hydrodynamically-induced fibrillogenesis with respect to the 0° fluid flow direction (Figure 3.4A,B). These MIPs, captured *via* confocal laser scanning microscopy (CLSM), demonstrate that when TPS pores were oriented with the long axis perpendicular to the flow direction, the resultant fibronectin matrices were highly aligned (aEECMs), as confirmed by CLSM MIPs shown in Figure 3.4A. Given the large area of the scaffolds (~5.8 mm x ~5.8 mm)

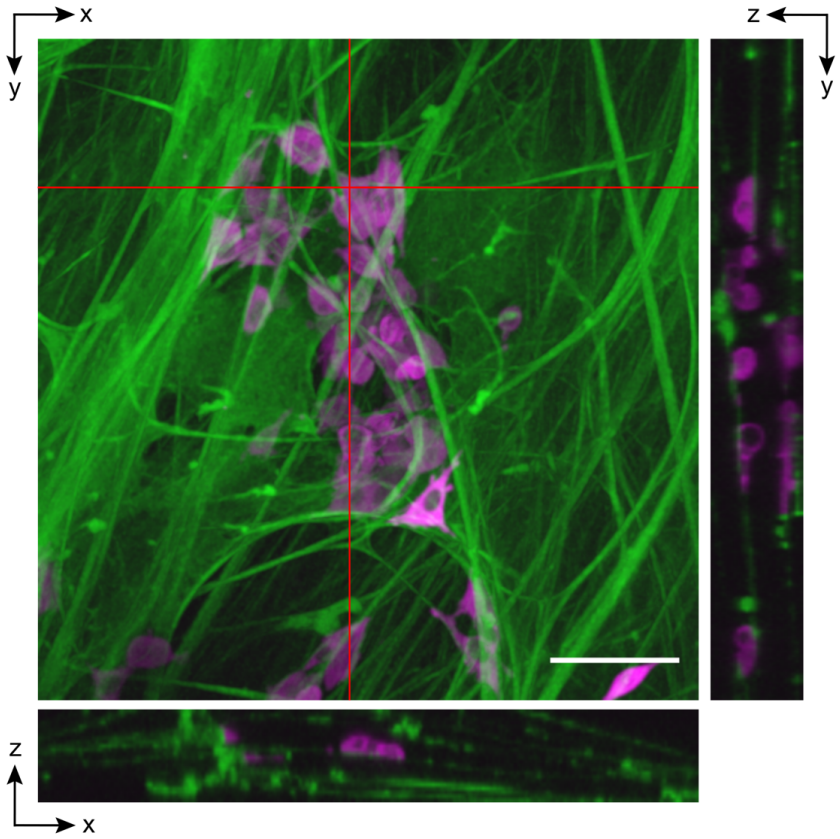

Figure 3.5
Image of MCF7 cells (magenta) cultured in an Fn EECM (green) demonstrates that cells integrate in the three-dimensional volume within EECMs. *The center image is a 2-photon confocal MIP projected onto the xy plane. The right image image is an yz orthogonal slice and the bottom image is an xz orthogonal slice. Slice locations are demonstrated with red lines. A Gaussian blur filter, sigma = 1.0, and gamma correction of 0.6 was applied to both channels for display purposes. Scale bar = 100 µm and applies to all three views.*

and thin scaffold height (~0.11 mm), the resulting suspended Fn matrices' directional orientation (aligned or non-aligned) was predominantly observed in the x-y plane and not along the z-axis planes. Throughout the manuscript MIPs of confocal images are used for display purposes. To elucidate the 3-dimensionality at the cellular-length scale, both a volume render of an EECM (Figure 3.4) and a confocal image with an MIP in the center and orthogonal views along the z-axis planes are provided to demonstrate ~50-70 µm of fibrillar Fn EECM depth, where Figure 3.5 also demonstrates an EECM with cells integrating throughout the volume. These images demonstrate the EECMs are a relatively porous collection of interconnected fibrillar elements

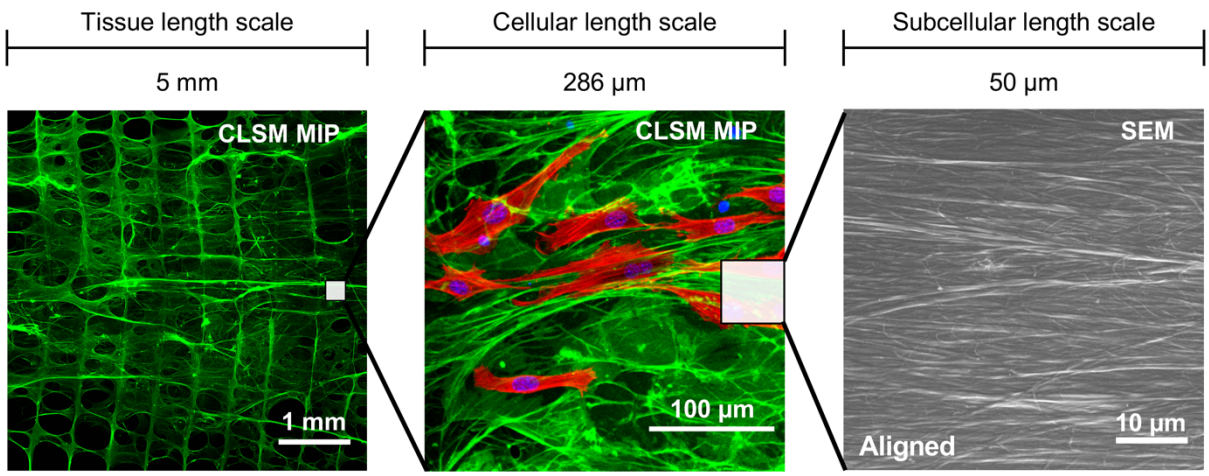

Figure 3.6
Visual representation displaying the relative imaging length scales assessed throughout the manuscript. *This demonstrates the achievement of fibril alignment from the multi-millimeter "tissue" length scale down to the submicron, "subcellular" length scale. Imaging studies performed at the "cellular" length scale is a scale in which multiple NIH-3T3 fibroblasts are captured within the same field of view. Approximate ROIs are shown on the tissue and cellular length scales in the white box. These images are not from the same sample but are compiled to illustrate relative scales.*

with cell-relevant 3-dimensionality. This is markedly different from other technologies employed in this space, which are often gel-based systems that encapsulate and physically constrain cells within a volume of material.[224] Given the wide range of mammalian cell size (~10 to 100 µm in diameter), as well as tissue length scales (~100 µm to centimeters), Figure 3.6 defines the relative "tissue," "cellular" and "subcellular" length scales when describing features and elements used in this manuscript.

COMSOL modeling predicted that at an inlet velocity of 0.15 m s^{-1}, lower gap lengths would lead to higher fluidic alignment (Figure 3.7A,B). Optimal gap length is likely a tradeoff between ideal flow conditions and Fn's proclivity to self-assemble and align over that length. Our model was designed to investigate the former, and thus it is expected that optimal experimental conditions would deviate based on Fn's self-assembly.

Critically, as gap length (pore size) decreases, porosity also decreases. A 500 µm gap length was chosen for the following studies because it led to highly aligned EECMs, with a higher

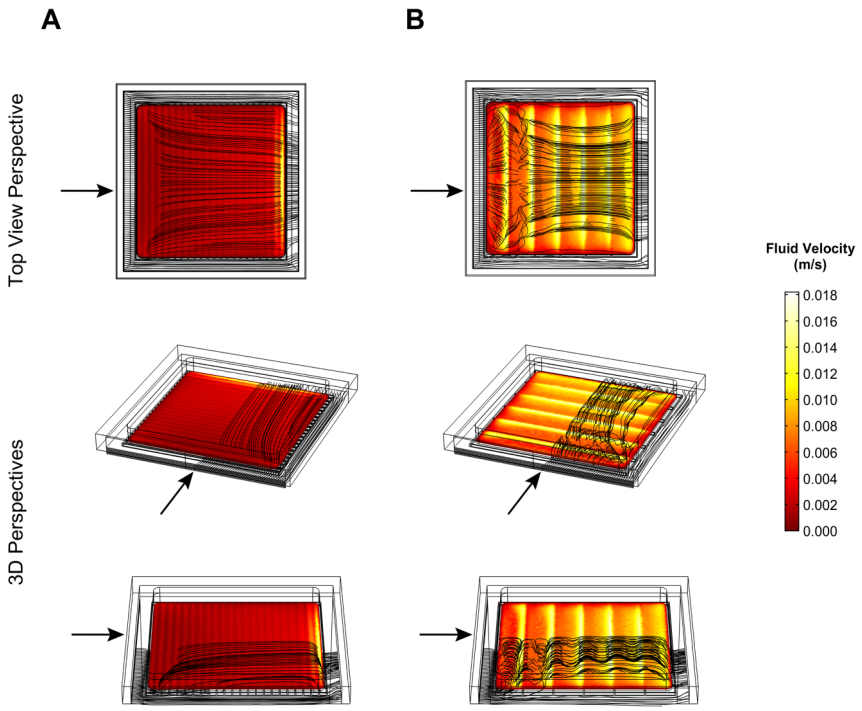

Figure 3.7
3D perspectives of the fluid flow profile across perpendicular oriented TPSs of 245 µm (A) and 950 µm gap lengths (B). *Black arrows indicate fluid flow direction on the inlet side of the model. Streamlines are shown in black while velocities are represented by color.*

porosity (~94%) compared to the 245 µm gap length (~88%) (Table S1), indicating a minimization of the amount of synthetic material present in the composite structure post-fibrillogenesis. Additionally, aEECMs produced from gap lengths of 950 µm were less aligned compared to 500 µm gap lengths, demonstrated qualitatively by CLSM MIPs and reflected in the modeling data (Figure 3.4A,B; 3.7A,B; 3.8C,D). In Figure 3.4C,D, the orientation of fibrils and larger fibrillar bundles was assessed along the tissue length scale via large ROIs. These data represent the orientation of fibrils around the axis of alignment (0°), where the y-axis displays the normalized power spectra resulting from a Fast Fourier Transform (FFT). This spectrum represents a convolution of both the number and intensity of the assessed fibers (Figure 3.4C,D). Gaussian distributions were fit to the data and the full width at half max values (FWHM) indicate narrowness of the distributions. Additionally, the area underneath the Gaussian curve were

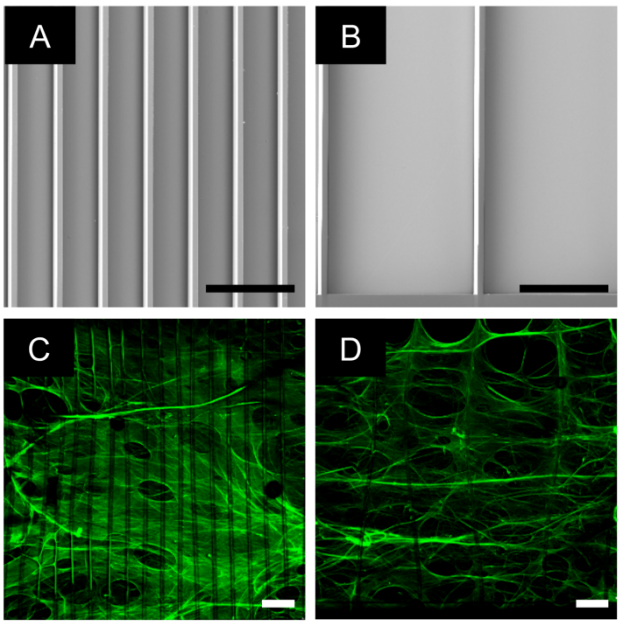

Figure 3.8
Fn EECMs across TPSs with varying gap length. *A,C: 250 µm gap length TPSs. B,D: 950 µm gap length TPSs. A,B: SEMs of the TPSs before coating. C,D: MIPs of the Fn networks after coating. Scale bars = 500 µm*

normalized by the area underneath the y-offset to define an alignment parameter (*AP*), wherein a higher value represents a higher degree of fibril alignment, see Figure 3.14. For TPSs with a 500 µm gap length and pores oriented parallel to fluid flow (0°), naEECMs were formed as demonstrated qualitatively (Figure 3.4B), whereas when TPS pores were perpendicular to flow (90°), fibrils were more highly aligned (Figure 3.4A**)**. Quantitative analysis revealed a FWHM of 66.5 and an *AP* of 0.37 (Figure 3.4D) for naEECM, compared to a FWHM of 33.9 and an *AP* of 0.98 in the aEECM group (Figure 3.4C). Additional analysis of the directionality data (Figure 3.4C,D) presents the summation of feature intensity of the normalized power spectra in directionality bins (±4°, ±8°, ±16°) for aEECMs compared to naEECMs (represented in Figure 3.4E). Expanded data with higher bins are reported in SI of published manuscript. The directionality groups are represented graphically to the right of the figure for each respective subset. This analysis reveals that 20.4% of continuous features in the aEECMs fall into the

narrow group of ±4° around the axis of alignment, compared to only 8.9% in the naEECMs. Additionally, nearly half of assessed features in aEECMs (48.6%) fall within the ±16°, compared to 27.4% in the naEECMs. Differences in means between naEECMs and aEECMs at ≤ ±33°, displayed in Figure 3.4E were statistically significant. The differences observed at > ±33° were not statistically significant. This analysis further elucidates that pore architecture during the coating process influences the flow profiles, and subsequently the orientation of the insoluble fibronectin fibrils. Higher-magnification SEMs confirm the presence of submicron fibrillar elements, as well as their aligned directional orientation at this length scale (Figure 3.6). This also points toward a probable likelihood of EECMs inducing topographically mediated cell-phenomena.

These EECMs are suspended across large gap lengths (245 – 950 μm) that span multiple millimeters, as demonstrated in Figure 3.4A,B, which is achieved using aqueous buffers and does not rely on the use of solution denaturants or solvents.[104,171–174,176] This marks an improvement over past reports of oriented fibrils across ~4 μm gap lengths.[183,184] Additionally, these EECM constructs are a robust free-standing composite material that is easily handleable. Table 3.1 overviews the characteristics of other fibrillar Fn biomaterials, as they compare to EECMs. The ROIs for directionality analysis at the tissue length scale are large, see *Experimental Methods*. Importantly, the perceived degree of alignment of an interconnected fibrillar network can be impacted by the length scale of observation, where areas larger than the length of entanglements appear more randomly oriented.[224]

Collectively, these data demonstrate that control over the polymer-Fn solution fluid interface enables a precise, cell-free method to create engineered fibrillar Fn networks with controlled

fibrillar alignment of subcellular features to larger fibrillar elements across the several millimeters.

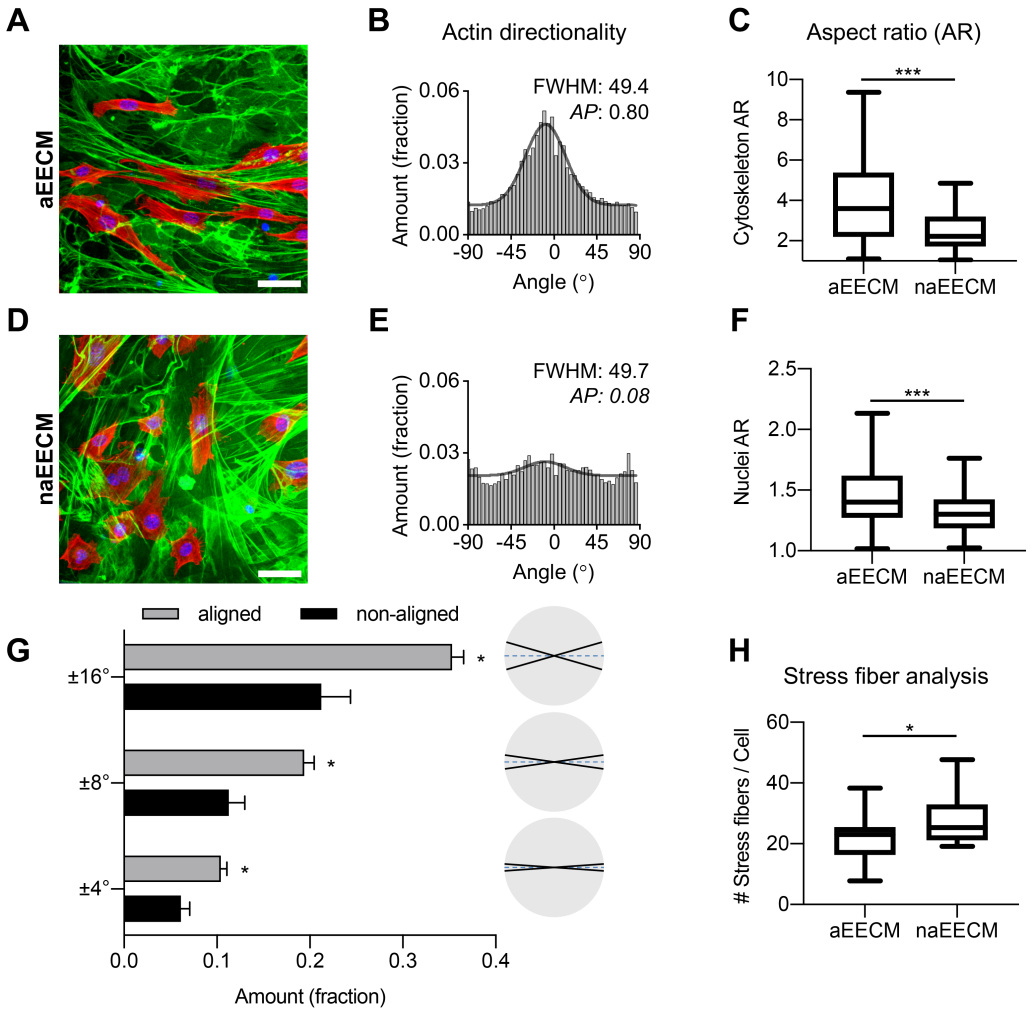

Figure 3.9

Aligned fibronectin networks influence fibroblast orientation and polarity on the cellular length scale. *NIH-3T3s align with fibronectin fibrils on aEECM significantly compared to naEECM. A,D: Confocal MIPs of NIH-3T3s. Green: Fn, red: F-actin , blue: nuclei. A gamma correction of 0.5 was applied to the actin channel for visualization purposes. Scale bars: 50 µm. B,E: Actin directionality analysis histograms. Gaussian fits are overlaid in black. FWHM are reported to indicate narrowness of the distribution, as well an alignment parameter AP which indicates increases in aligned fibrils with higher values. C,F: aspect ratio analysis of actin morphology and nuclear morphology, respectively. G: Binning analysis of histogram data from B,E to assess the fraction of the fibrils falling within different angle bins. The circular diagrams to the right of the graph graphically represent the boundaries of the bin (black lines), and the 0 – 180° line (dashed blue line). H: actin stress fiber analysis of F-actin images displays the number of stress fibers per cell in the y-axis. The Mann-Whitney U and Holm-Sidak Multiple t-test were performed to compare groups and assess statistical significance. *P ≤ 0.05, **P ≤ 0.01, ***P ≤ 0.001*

3.4.3 Aligned Fibronectin Networks Influence Fibroblast Orientation and Polarity

To evaluate the topographical impact of the EECMs at the cellular length scale, CLSM imaging of individual cells was performed at higher magnification. To evaluate changes in contact guidance in response to the topography of the Fn EECM, NIH-3T3 fibroblasts were cultured for 24 h. F-actin staining revealed fibroblasts cultured on the aEECMs were more elongated compared to naEECMs (Figure 3.9A,D). Analysis of cell directionality based on the F-actin staining at the cellular length scale reveals a similar FWHM (49.4) on aEECMs (Figure 3.9B) compared to the naEECMs (FWHM 49.7) Figure 3.9E; however, the *AP* values were separated by a 10-fold margin: 0.80 and 0.08. Additional summation of the features of the F-actin directionality of cells seeded on aEECMs (Figure 3.9G), revealed 19.4% within ±8° of the directionality axis, and 35.3% within ±16°, compared to 11.3% and 21.2% for those cells seeded on naEECMs, respectively. Mirroring the analysis on the Fn networks, significantly higher amounts of F-actin features ≤ ±16° for cells seeded on aEECMs compared to naEECMs (published manuscript SI). The CLSM MIPs shown in Figure 3.9A,D confirm an excellent correlation between fibrillar alignment and cell directionality for aEECMs. Additionally, the aspect ratios of both cell nuclei and their cytoskeletons significantly increased when seeded on aEECMs compared to EECMs Figure 3.9C,F. F-actin channels of CLSM MIPs were analyzed using a previously published MATLAB script to identify and quantify the presence of actin stress fibers (SFs), where representative analysis images are shown in **(**see published manuscript SI**)**.[225] A significantly higher number of SFs was observed in cells seeded on naEECMs (Figure 3.9H), which may indicate that cells seeded on aEECMs are migrating more than those seeded on naEECMs. Evidence suggests SFs are more prominent and in higher number in stationary cells, as migrating cells have to continuously break and reform their adhesions sites.[226,227]

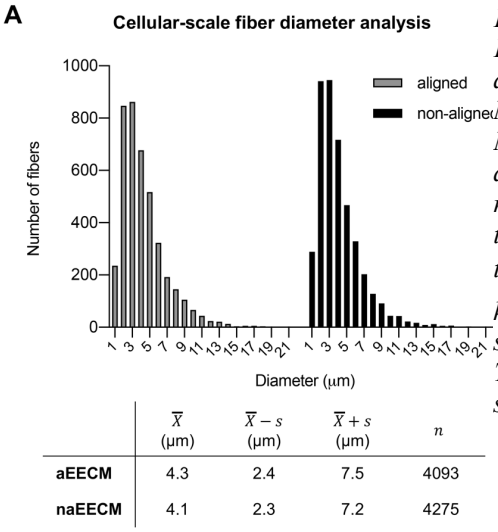

	$\overline{X}$ (μm)	$\overline{X}-s$ (μm)	$\overline{X}+s$ (μm)	n
aEECM	4.3	2.4	7.5	4093
naEECM	4.1	2.3	7.2	4275

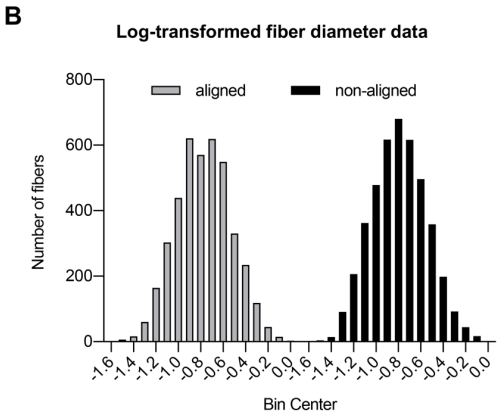

Transformed Distributions	*Skewness*	*Kurtosis*
aEECM	0.04752	- 0.2666
naEECM	0.1172	- 0.2735

Figure 3.10
Fibril diameter analysis. *A: Fn fibril diameter data generated from image analysis of CLSM MIPs of aEECM and naEECMs in Figure 3.9. Mean (X), mean ± one sample standard deviation (X ± s), and sample sizes (n) are reported in the table below the graph B: shows transformed diameter data, transformed via the equation:* $y' = log_{10}\frac{y}{y_{max}}$. *Skewness and kurtosis are reported to indicate the data are sufficiently normal after transformation. Transformed data were used to generate the summary statistics reported in the table above.*

To further characterize EECMs at the cellular length scale, fibril diameters (Figure 3.10) of the Fn channel of CLSM images were assessed using a previously published open source software (GTFiber2, GitHub).[228] Examples of segmented images are provided in published manuscript SI**.** These data revealed very similar, right-skewed distributions for both aEECMs and naEECMs with a mean of 4.3 μm and 4.1 μm, respectively. The range between the – 1 standard deviation and the + 1 standard deviation was 2.4 μm – 7.5 μm for aEECM and 2.3 μm – 7.2 μm for naEECM.

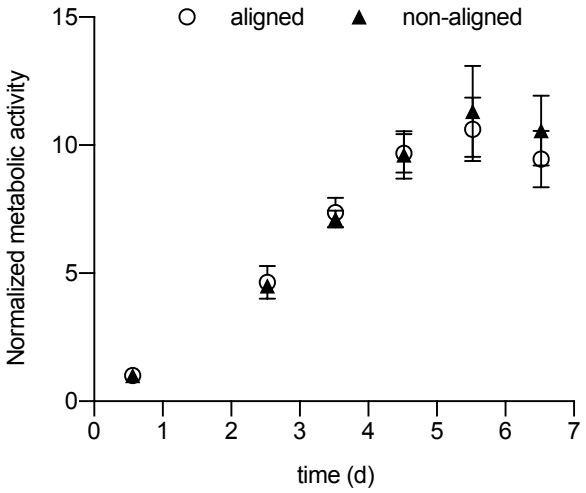

Figure 3.11
Normalized cell proliferation. *Data generated over the course of 6.5 d using a Tox8, resazurin-based metabolic assay. Data plotted are the fluorescent intensity measurements normalized to the initial time point (13.5 h). Aligned vs non-aligned EECMs were not statistically different at any time point.*

To determine whether EECM topography impacts cell growth, proliferation on aEECMs and naEECMs was assessed over 6.5 days. The rate of proliferation was very similar and not significantly different for all time points, Figure 3.11. Cell saturation on the EECMs occurred at 5.5d, where 360,000 ± 62,000 and 391,000 ± 13,000 cells were estimated on naEECMs and aEECMs, respectively. Furthermore, EECMs are remarkably stable in cell culture conditions, as shown by imaging of an aEECM over 4 days of cell culture (Figure 2.2). Figure 2.2 indicates no appreciable differences in the fibrillar Fn network integrity despite nearly complete cell coverage, which is displayed in the differential interference contrast (DIC) counter image.

Collectively, the data presented in Figure 3.9 support the notion that fibroblasts respond to the topography of EECMs, wherein fibril alignment does not impact proliferation rate, but over short periods of time causes a significant increase in cell alignment, an increase in cytoskeletal/nuclear elongation, as well as a decrease in actin SFs. Recent work where Fn was adsorbed onto a 2D surface using microcontact printing, revealed that alignment of contact printed lines of solute Fn

had a substantial impact on cell morphology, polarization and migration.[211] In 3D fibrillar Fn networks, alignment also substantially impacted the polarization and orientation of cells.

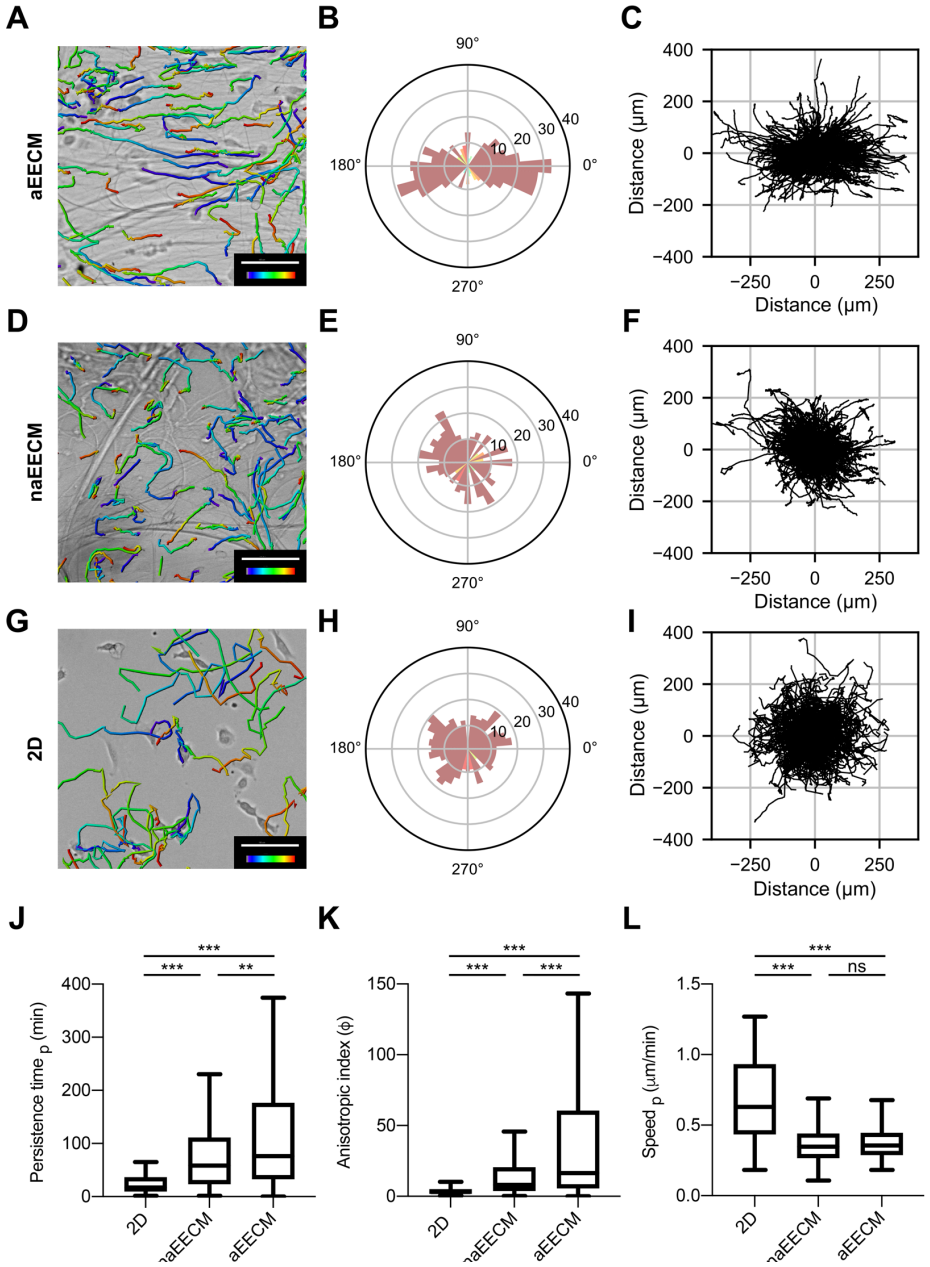

Figure 3.12

Aligned fibronectin guides fibroblast motility. *Live Cell migration analysis on aEECM (A,B,C), naEECM (D,E,F), and 2D (G,H,I), which reveals significant directionally persistent migration along aligned fibrils compared to non-aligned fibrils and 2D. A,D,G: Representative cell track images are overlaid onto brightfield images (t = 0). Scale bars = 100 µm. The time reference bar indicates increasing time from blue to red. B,E,H: Wind rose plots display the number of cells (length of bar from the origin) and their respective direction from 0° to 360° in 10° bins. C, F, I: walk plots displaying individual cell paths from their origin as a function of distance in the x-y directions.* ***J****: box plot of cell persistence time assessed in the primary direction, extracted from the APRW model. K: box plot of cell movement anisotropic index data was calculated from persistence time and speed. L: box plot of cell speed, as determined from the APRW model. The Kruskal-Wallis test and post-hoc analysis via a Dunn's multiple comparisons test were performed to assess statistical significance. *P ≤ 0.05, **P ≤ 0.01, ***P ≤ 0.001*

3.4.4 Aligned Fibronectin Guides Fibroblast Motility

To further elucidate the influence of Fn architecture on fibroblast motility, time lapse microscopy studies were performed. To quantify cell motility in 3D suspended Fn EECMs, time-lapse fluorescent microscopy was performed on NIH-3T3 fibroblasts containing a H2B-RFP nuclear reporter in an incubator chamber over 20 h with 20 min imaging intervals. Spontaneous migration occurs on EECMs of different topographical alignment in the absence of chemotactic gradients and other external cues. The data generated from the nuclei tracking analysis were then fit to the anisotropic persistent random walk (APRW) model published by Wu *et al*. to quantify metrics of anisotropic index, persistence time and speed in the primary (p) and non-primary (np) directions.[229] Qualitatively, cells migrated straighter and displaced further on aEECMs as seen in representative images of migration tracks overlaid on a brightfield image of the initial frame (Figure 3.12A,D,G). The wind-rose plots shown in Figure 3.12B,E,H quantitatively indicate that a larger population of migratory cells displaced in the direction of the axis of alignment (0° - 180° line). These findings are corroborated by cell tracks plotted as walk plots (Figure 3.12C,F,I). Critically, the metrics generated *via* the APRW model suggest a significant increase in directionally persistent cell migration on aEECMs compared to naEECMs and 2D control substrates (Figure 3.12J,K). Both persistence time and anisotropic migration were increased in the 3D system compared to 2D, confirming findings by Wu *et al*. and underlining the importance of studying cell phenomena like directionally persistent cell migration in 3D systems.[230] As expected, most of the cells on 2D surfaces had lower persistence time with a third quartile value of 37 min (~2 intervals) for the distribution (Figure 3.12J). In stark contrast, also shown in Figure 3.12J, persistence times of cells seeded on naEECMs revealed a third quartile of 111 min (~5.5 intervals) while the third quartile of the persistence time distribution of cells seeded on aEECMs was 177 min (~9 intervals) Figure 3.12J. The distinct differences in fibroblast motility

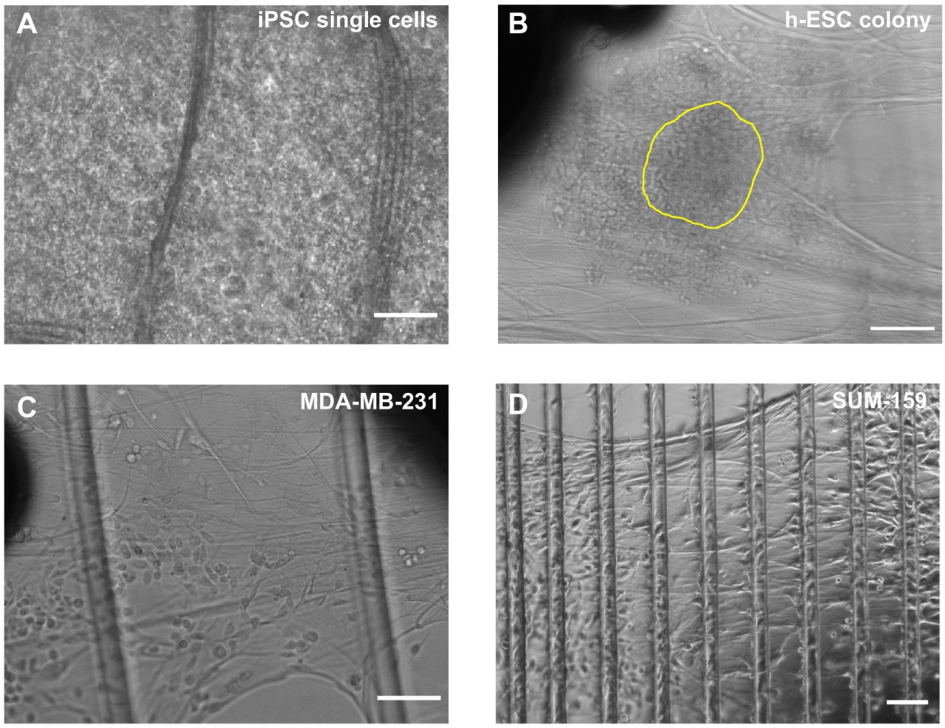

Figure 3.13
Fn EECMs facilitate growth of various cell types. *A: induced pluripotent stem cells (iPSCs) seeded onto a fibronectin EECM at a concentration of 100,000 cells mL^{-1} (single cell seeding). IPSCs were expanded for 14 d before imaging. B: H9 human embryonic stem cell (hESC) colonies seeded on an EECM. Colonies were gathered using a colony picker, transferred in medium and seeded on fibronectin EECMs for 24 h prior to imaging. The yellow outline marks the initial boundaries of the seeded hESC colony. C: MDA-MB-231 cells were seeded at 75,000 cells mL^{-1} on fibronectin EECMs for 20 h prior to imaging. D: SUM-159 cells on an EECM. Fibronectin EECM scaffolds were placed in cell suspension ($4.0x10^6$ cells mL^{-1}) for 4 hours before being removed, rinsed with DPBS and imaged. All scale bars = 100 µm.*

on 2D substrates, naEECMs and aEECMs are also reflected in the anisotropic indices of the primary cell direction, where the third quartiles were 5.1, 20.6, and 60.7, respectively (Figure 3.12K). The anisotropic index values on aEECMs are substantially higher than a previous report of primary mouse fibroblasts assessed in a 2D scratch wound assay, which was 2.4.[231] Values of speed were higher on 2D compared to 3D, Figure 3.12L, which is consistent with reports from Wu *et al*. Interestingly, cell speed was not significantly different between aEECM and naEECM Figure 3.12L. While studies of cell-secreted matrices point to Fn as a key player in anisotropic cell migration, the findings in this manuscript demonstrate the ability to model these migratory

phenomena and point to aligned fibrillar Fn as playing a key role in directionally persistent cell migration.

To evaluate suitability of EECMs to be applied in other biological contexts, a proof-of-concept study was performed to assess the attachment and/or expansion of pluripotent stem cells and breast cancer cell lines, Figure 3.13**.** EECMs facilitated the attachment, rapid flattening and expansion of human embryonic stem cell colonies, as well as the attachment of single induced pluripotent stem cells (iPSCs) that were reliably expanded to confluence over 14 days. Furthermore, EECMs facilitate the attachment and growth of various cancer cell lines (MDA-MB-231s, SUM-159s, MCF7s) Figure 3.13, 3.5, as well as primary patient tumor cells.[147]

Cell migration processes are critical in embryogenesis, wound healing, as well as cancer metastasis,[232,233]but are inherently different in 3D environments compared to 2D due to the fact that cells access environmentally mediated motility modes.[196,224] While anisotropic cell migration induced from chemotactic and mechanical gradients has been well studied, topographically mediated migration is less understood and predominately studied in engineered 2D systems.[234–236] Using adsorbed Fn on 2D surfaces, certain domains have been implicated in directing persistent cell migration,[194,217] while our findings underscore alignment of Fn networks as a major factor of directionally persistent migration in the absence of other known external cues.

Considering the importance of directional motility in wound healing, embryogenesis, as well as tumor progression, these Fn EECMs provide a novel 3D platform for future studies to better understand the role Fn has in governing cell migration in various tissue contexts.

3.4.5 Supplemental Discussion and Figures

1. *A brief discussion of the interpretation of FFT spectral analysis*:

The artificial bins represent intensity residuals when features in the more aligned (closer to 0 degree) and less aligned (closer to ± 90°) are removed. As an example: a bin at 18° (16° - 20° binning) is the difference between the intensity of 0 to +20° and 0 to +16°. The intensity of the spectra in each of these bins is an assessment of the intensity of feature alignment that gets redirected off axis, and not a direct count of parallel and perpendicular features. Therefore, the data is more analogous to elastic scattering techniques (x-ray; electron) than a true count-based analysis. The spectra from +90 to -90° is half of the spectra that could be obtained, where the second half of the spectra is merely a reflection of the first half; therefore, only +90° to -90° spectra are reported.

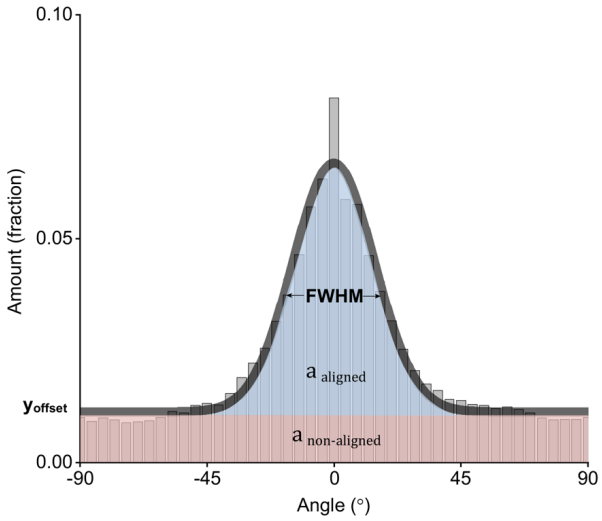

$$AP = \frac{a_{aligned}}{a_{non-aligned}}$$

Figure 3.14
Visual representation of quantitative metrics used to describe directionality histograms*. The full-width at half maximum (FWHM) is the width of the distribution at the y-value which is halfway from the baseline (y-offset) to the peak of the distribution. The alignment parameter (AP) describes a value where the area under the Gaussian (aligned features) is normalized by the area under the y-offset (non-aligned features).*

2. A brief discussion of the alignment parameter:

The alignment parameter (*AP*) is defined as the area under the Gaussian curve, normalized by the area under the y-offset, see Figure 3.14 for a graphical representation.

$$\textit{Equation 1: } AP = \frac{a_{aligned}}{a_{non-aligned}}$$

Perfectly aligned fibrils would be a narrow distribution with no y-offset, and completely random fibrils would be flat distribution with no curve. Both the full width at half maximum (FWHM) and *AP* are considered in describing the characteristics of the data.

3. Equations used in assessing motility data:

The diffusivity in either direction is calculated from the speed (S) and persistence time (P), Equation 2.

$$\textit{Equation 2}: D = \frac{S^2 P}{4}$$

The anisotropic index (ϕ) is the diffusivity (*D*) along the primary (p) axis divided by diffusivity along the non-primary (np) axis, Equation 3.

$$\textit{Equation 3}: \phi = \frac{D_p}{D_{np}} = \frac{{S_p}^2 P_p}{{S_{np}}^2 P_{np}}$$

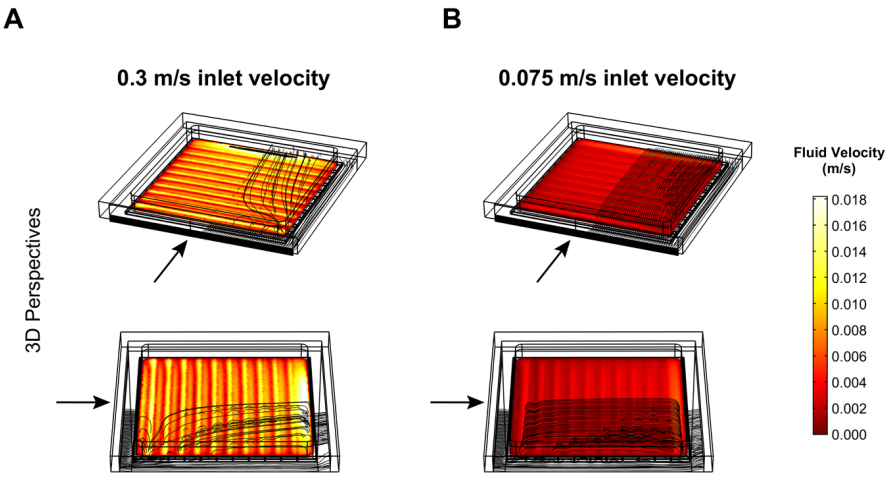

Figure 3.15
Fluid flow characteristics across perpendicularly oriented TPSs at different inlet velocities.

4. A brief discussion of fluid flow rates:

8 RPM was found through qualitative inspection of the 2D COMSOL model to produce fluid flows of ~0.15m/s (see published manuscript SI). This value was employed as the inlet velocity of the 3D model. At this flow rate, fluid flow streamlines were found to be coherently aligned across the length of the tessellated polymer scaffold (TPS). At half of this rate (0.075m/s) there was not a substantial improvement in fluid flow profiles, through qualitative inspection (Figure 3.15). Furthermore, at lower rotational velocities, the number of fluid-scaffold contacts would be decreased during the coating process. At higher flow rates (0.3m/s) vortices are observed (Figure 3.15).

Table 3.2
Top: SEM of a SU-8 TPS. Reported in the table are target values versus measured. Measured values came from images taken in DPBS, representing the geometry in situ during the coating process. Height was measured using contact profilometry in a dry state. Data reported as average ± standard deviation.

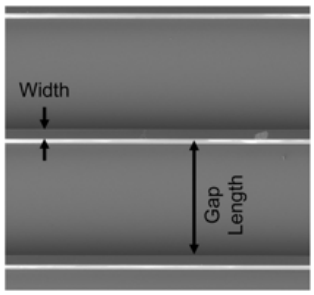

	Rectangle 245	Rectangle 500	Rectangle 950	SU-8 Spin Height
Gap Length Target (μm)	245	500	950	n/a
Gap Length Measured (μm)	248 ± 3.2	497 ± 5.0	946 ± 2.6	n/a
Width Target (μm)	35	35	35	n/a
Width Measured (μm)	35 ± 1.2	36 ± 0.7	35 ± 1.6	n/a
Approximate Free Volume (%)	88	94	97	n/a
Height Target (μm)				110
Height Measured (μm)				112 ± 1.7

3.5 Conclusions and Implications

Controlled hydrodynamics of a Fn solution over TPSs induces protein fibrillogenesis, wherein alignment of 3D fibrillar Fn networks can be modulated by engineering the direction of the fluid profiles, in the absence of solution denaturants or solvents. Collectively, these data demonstrate Fn fibril alignment as a major ECM factor in directing cell orientation, where engineered fibrillar Fn networks induce fibroblast polarity and serve as contact guidance “highways” that cause a dramatic increase in directionally persistent motility. Building off of previous literature in 2D model systems, these results were gathered using a 3D *in vitro* system composed of purified

fibronectin. While engineered 2D and 2.5D systems provide remarkable control over the presentation of topographical information for studying cell migration, in tissues the role of ECM topography is inextricably linked to composition. Hence, 3D protein-based *in vitro* models offer an attractive option for decoupling these matrix properties; however, controlling the assembly and structure of proteinaceous materials is a significant challenge where oriented EECMs constitute an advancement. This is especially important in the context of Fn because it is a known mechanosensitive protein with conformationally active binding domains, and future work would benefit from utilizing EECMs to decouple Fn-specific cues.

The potential utility of these constructs in tissue engineering is widespread given they are easily handleable, well-plate compatible, porous, optically translucent and compositionally defined. They allow for efficient cell seeding, recovery and imaging. These characteristics make them compatible with many conventional cell analysis and imaging modalities as is demonstrated in this manuscript as well as our previous work.[147] Future work would benefit from extending the concepts outlined in this manuscript to create aligned Fn matrices with biodegradable polymers *via* the utilization of advanced 3D printing techniques such as 3D jet-writing or melt-electrospinning as the supporting scaffold in order to access *in vivo* application spaces.[81,82]

This novel technology provides a critical link between biologically derived and synthetic biomaterials and will enable a broad range of studies on ECM-driven cell phenomena in aligned matrices. With further work, these hydrodynamically-induced fibrillar networks may lead to novel *in vitro* models for studying ECM-mediated phenomena in healthy and diseased tissue states.

Chapter 4 Hyaluronan Decorated Fibrillar Fibronectin Constructs Modulate Metastatic Potential in Breast Tumor Cells

4.1 Publication Information

Studies are ongoing at the time of writing this chapter. Interpretation of results is subject to change as future studies conclude and the manuscript undergoes peer review. The work presented in this chapter is in preparation for publication in the following form: Dylan B. Neale, Mirella Wawryszyn, Grace Bushnell, Johanna Buschhaus, Malini Mukherji, Do Hoon Kim, Sebastian Spann, Carlo Botha, Ayse Muniz, Adrian Shimpi, Claudia Fischbach, Jeffery E. Raymond, Burkhard Luy, Manfred Wilhelm, Gary D. Luker, Max Wicha, Joerg Lahann. "Hyaluronic acid decorated fibrillar fibronectin constructs modulate metastatic potential in breast tumor cells." *In preparation*

4.2 Abstract

Despite many reviews that indicate substantial knowledge regarding HA and its influence on tumor progression, hallmarks of tumor cell behavior that govern metastasis and recurrence are underexplored in the context of ECM mediated regulation of tumor cells. Given the complex nature of native HA synthesis/degradation, concatenation to other signaling networks, and the difficulty in characterizing hyaluronan, cell-based models make it challenging to isolate the role of HA in tumor tissue. Additionally, biomaterial-based approaches to study tumor-associated HA utilize hydrogels that are not physiologically representative of tissue morphology, dimensionality, and ECM complexity. Hence, whether the overexpression and deposition of

hyaluronan into tissues is itself a regulator of tumor cell fate or just a by-product of aberrant metabolism is an outstanding ambiguity. To address this, rational design guided from accumulated literature regarding HA and Fn stability, assembly, and biochemistry was leveraged to produce native-like engineered ECMs. This methodology leads to remarkable control over EECM fibrillar topography and HA mass ratio. Fn-HA EECMs further display morphological and biochemical similarity to a cell-derived tumor associated system. Then Fn EECMs decorated with high (2000kDa) and low molecular weight (15kDa) HA-Fn EECMs were employed to study the effect HA accumulation in primary tumor tissues has on epigenetically regulating the metastatic potential of breast tumor cells.

4.3 Introduction

The ECM is an astonishingly complex web of macromolecules that act on one another in reciprocity with cells to govern tissue development. Studies into the matrisome fixate on the proteome (proteins) with rising attention given to the glycome (glycans), yet in tissue these disparate molecules interweave making their biological function inextricably bound. Two ECM components at the foundation of vertebrate biology are Fn and HA (commonly "hyaluronan," "hyaluronic acid" or "hyaluronate"). Fn is essential for life demarcating vertebrate biology and HA synthase 2 (HAS2) expression is critical in developing embryos.[237,238] Both have roles in embryonic development, wound healing, and fibrotic remodeling in cancer progression where accumulation of excess HA and Fn in tumors is associated with poor patient prognosis in breast cancer.[55,239–241]

HA is a linear, non-sulfated, negatively charged glycosaminoglycan synthesized at the surface of cells whose extracellular presentation is controlled by transmembrane synthesis enzymes (HAS1, HAS2, HAS3) and six known degradation enzymes (hyaluronidases).[238,242]

Critical to its biological role, HA presents in fluids, acts as a lubricious water-laden semisolid in connective tissue and is heavily implicated in tumor progression in various tissue-types.[238,243,244] HA's incorporation into tissue niches like cartilage is relatively well defined [238,242] and proteoglycan-HA cable structures are identified as immune cell modulators,[242] but HA's many-faced roles in the tumor microenvironment remains unclear.[243,245]

Qualitatively, "high" molecular weight is described as "healthy" whereas "low" molecular weight or "fragmented" HA is "diseased/inflamed," yet there are many caveats and exceptions to this assertion.[61,243,246,247] For instance, naked mole rats, whose cultured cells secrete ultrahigh molecular weight HA (6,000kDa – 12,000kDa HA) are peculiarly resistant to developing cancer with unusually long lifespans.[248] Comparatively, ~300kDa up to 2,000kDa is generally regarded as the high-end of HA molecular mass with other reports up to 6,000kDa in human physiology.[238,246,249] Despite conflicting reports, certainly these large polymeric HA molecules are simultaneously degraded in solution and tissues leading to fragments. Soluble fragmented oligomeric HA has been shown to promote angiogenesis and stimulate matrix metalloproteases (critical for tumor progression), yet when delivered to tumor xenografts inhibited tumor growth[243,250,251]. Fuchs et al demonstrated oligomeric HAs inhibited angiogenesis in a CD44/CXCR4/CXCL12 dependent manner.[252] In colorectal cancer patients most HA analyzed in tumor tissue fluids was of higher molecular weight, but oligomeric HA of 6-25 disaccharides (~2.4k – 10k) was detected in a subset of tumors that was not present in healthy tissues and correlated with lymph node invasion/metastases. While soluble HA is well studied, the role of tissue bound HA is more elusive.

In an insoluble state, HA forms a robust pericellular coating and accumulates significantly in remodeled, fibrillar tumor tissue.[57,240,244,253] Overexpressing hyaluronidase to

combat this and may inhibit growth in breast and colon cancer but stimulated metastasis in prostate cancer.[243] Clinical approaches to deliver hyaluronidases may be helpful in improving the delivery of adjuvant therapies and useful in cosmetic procedures, but their clinical adoption is limited by unclear in vivo mechanisms and concerning toxicity profiles.[253–256] CD44, a cell membrane protein and HA-binding protein (HABP) is heavily implicated in cancer progression and a biomarker for highly tumorigenic, stem-like cancer cells.[257,258] CD44 has served as a target for direct disruption HA binding with concerning efficacy and side effects.[60] Recently soluble HA was implicated as a carrier of iron via CD44-mediated endocytosis preserving epithelial to mesenchymal (EMT)/cancer stem cell (CSC) phenotypes.[259] Interestingly, expression of HAS2, thought to encode for high Mw HA, is heavily implicated in invasive/metastatic breast cancer[260] and oligomers of 3-9 disaccharide units (~1.8kDa – 3.5 kDa) can outcompete polymeric HA binding [60,261] attenuating signaling to prevent tumorigenic outcomes.[60] Therefore, conflictingly, higher molecular weight HA-tumor cell binding seems to be implicated as a necessary component of tumorigenesis with outstanding postulates about whether high molecular weight-HA prevents invasive/EMT-phenotypes[259] or arises to enhance EMT, migration and invasion.[244] Lengths of tissue bound HA that promote differential tumor cell phenotype are underexplored creating a dire need for engineered systems to faithfully recapitulate tumor-ECM heterogeneity to dissect the complexities of HA in tumor stroma.

Fibronectin (Fn) expression is commonly used as a marker for EMT and has been implicated in promoting stemness and metastatic spread in breast cancer cells.[147,259] To directly probe whether stromal bound HA would enhance or perturb invasive/metastatic phenotypes in a Mw dependent manner, we conjugated minimally modified HA to native Fn (nFn) isolated from blood plasma to engineer three-dimensional (3D) tumor-mimetic tissue scaffolds. These

engineered extracellular matrices present with native morphology, biochemistry and afford well controlled physical properties. Remarkably, after only 5-6 days of culture on Fn-HA EECMs, EECMs impart lasting phenotypic changes that are correlated with metastasis and recurrence that are in the process of being compared to in vivo studies. To our knowledge, this constitutes the first report assessing the direct role of HA Mw and Fn in stromal tissue as an epigenetic regulator of tumor metastasis.

4.4 Results and Discussion

4.4.1 Defined Derivatization of HA Enables Minimally Modified Thiol Reactive Species

Hyaluronic acid's simple linear structure is made up of disaccharide repeat units of linked D-glucuronic acid and N-acetyl-D-glucosamine (GlcNAc), Figure 4.1A. As a result, its biological role is largely influenced by differential molecular weight defining physical properties and binding mechanisms to other biomolecules and cell surfaces.[245,246,262] HA is notoriously difficult to isolate, stabilize, and accurately characterize[246,262,263] contributing to the discrepancies that mar the understanding of HA's biological role, especially in pathogenesis. Furthermore, complex bioregulation of HA synthesis and degradation makes using cell or tissue-based in vitro models challenging to control HA presentation. Engineered technologies offer an attractive approach; however, HA is most commonly formed into hydrogels lacking tumor relevant fibrillar morphology and dimensionality[264]. Other approaches include conjugation to proteinaceous materials using non-specific amide chemistry or simple steric intercalation techniques, both potentially lead to ambiguous modifications to HA-binding.[265,266] Pre-modification strategies of HA to make it reactive offers a measured path forward where quality control measures can be employed.[267–269]

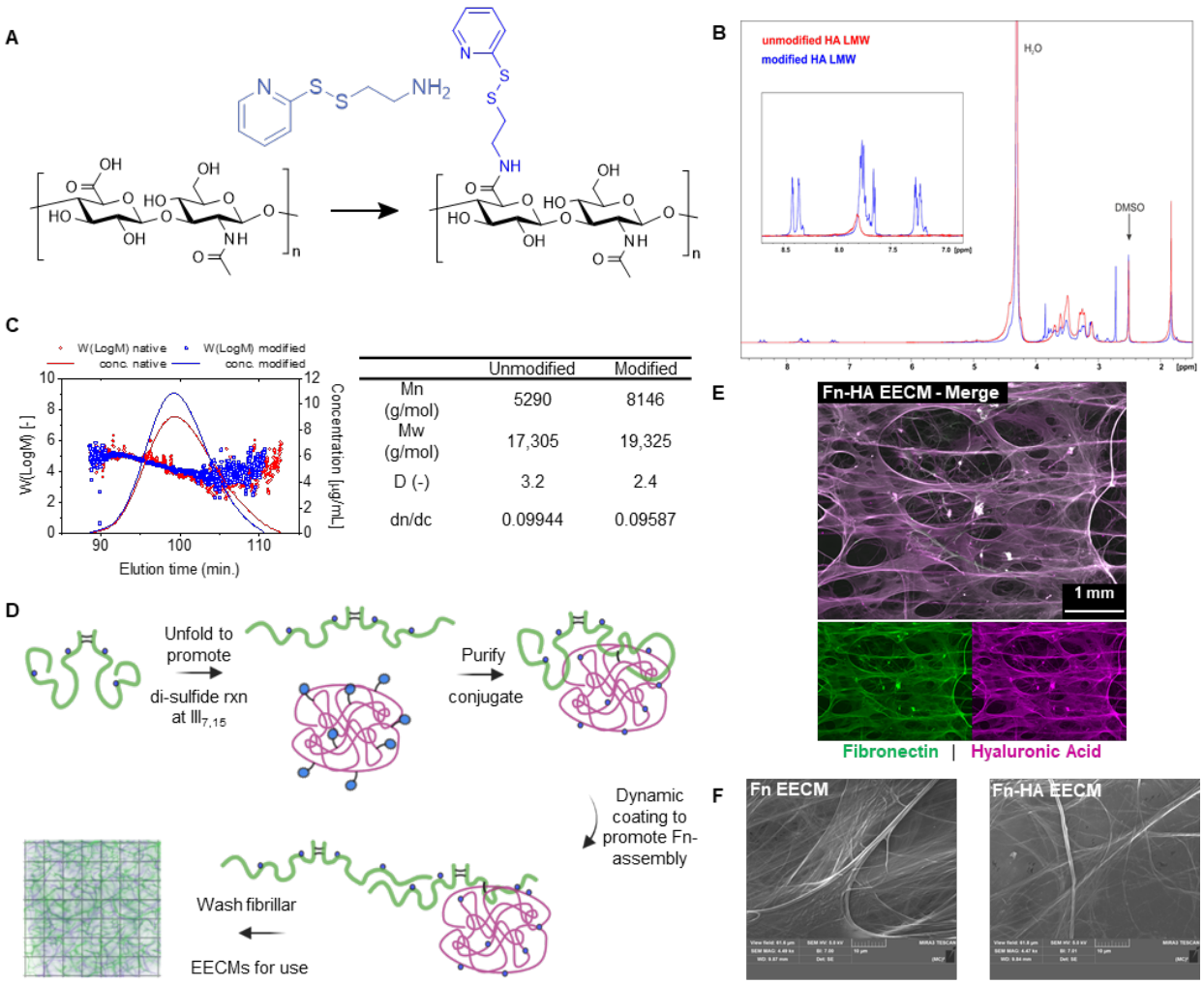

Figure 4.1
Defined derivatization of HA enables minimally modified thiol reactive species A: thiol-reactive functionalization of hyaluronic acid. *B: 1H NMR spectrum of 40% degree of substitution modification of 15kDa HA confirming successful chemical modification. C: SEC-MALS (620nm laser) demonstrating that molecular weight is not affected by modification strategy. D: illustration depicting site-specific thiol conjugation strategy to produce HA-Fn conjugates that produce fibrillar EECMs via hydrodynamically induced fibrillogenesis. E: Merged CLSM MIP of Fn-HA EECM (15kDa HA) where Fn is depicted in green and HA is depicted in magenta. Contrast and gamma adjustments were applied for display purposes F: SEMs of of Fn EECMs vs Fn-HA EECMs demonstrating fibrillar morphology at higher resolution.*

A thiol reactive strategy was employed with (S)-2-Pyridylthio cysteamine (2PT) used as the functional linker-moiety shown in Figure 4.1A. ^{1}H NMR spectra of highly modified (40% degree of substitution) vs unmodified HA show the methyl peak of the N acetyl moiety from the GlcNAc subunit at 1.9 ppm appears as a sharp singlet for both (Figure 4.1B). In contrast, the multiplets at 7.2-8.4 ppm indicate the attachment of the thio-pyridyl group confirming the

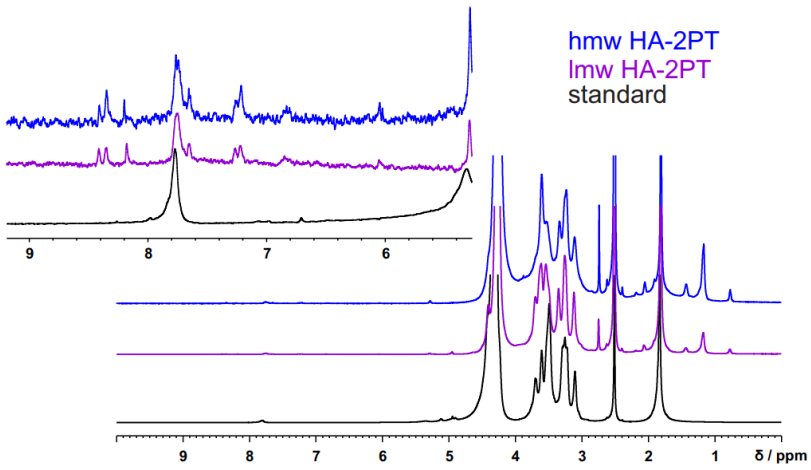

Figure 4.2
^{1}H NMR spectrum of 14% degree of substitution modification of 2000kDa HA (hmw HA-2PT) and 15kDa (lmw HA-2PT).

modification strategy was successful. Size exclusion chromatography multi-angle laser light scattering (SEC-MALLS) was employed to obtain absolute measures of molecular weight, see Figure 4.1C, according to previously published method developed by Botha et al.[270]. For SEC standard calibration of the modified and pure HA, the dn/dc values were determined in a concentration range of 0.3–2.1 g/L (with 0.3 g/L increments). Compounds in DMSO/H_2O mixture 6/4 (v/v) with 0.05 M LiBr was applied at an operating temperature of 40 °C, where a RI detector was utilized with a flow rate of 0.3 mL/min. With the physical correlation between the intensity of the scattered light and the dn/dc value for its concentration, the MW can be determined after an approximation for larger particles above the 10 nm range. SEC elution curves indicate similar distributions with ~20min elution times and similar peak maxima, Figure 4.1C. The data summarized in the adjacent table (Figure 4.1C) display minor shifts in the weight average molecular weight (Mw ~17.3 kg/mol vs ~19.3 kg/mol) following chemical derivatization. The dispersity index (D) decreases for the 2PT modified group, likely due to purification following the reaction. We can therefore conclude that the synthesis approach was successful, and no polymer chain degradation or crosslinking/polymerization has occurred. HA

of this length is herein referred to as “15k” per the manufacturer’s label. Given the promising characterization at higher degrees of substitution (40%, theoretical), a lower degree of substitution of 2PT modification (14%, theoretical) was chosen as critical HA-binding literature has been based on 8-mer HA (4 disaccharide subunits)[271,272]. This degree of substitution would preserve a total of ~33 disaccharide subunits per molecule (15k g/mol) statistically preserving many unmodified multi-unit blocks. ^{1}H NMR confirmed successful modification of both “15k” (15k g/mol) and “2000k” (2000k g/mol) HA at lower degrees of substitution, Figure 4.2. These lengths were chosen to model high molecular weight HA in tissue (2000k), as well as the fragmented-tissue bound remains (15k) to create 3D tissue scaffolds co-expressed with native Fn as a tumor-mimetic environment.

Native, dimeric Fn (nFn) has two free thiols per monomer buried conformationally in solution (“cryptic”) at type-III domains 7 and 15 that can be leveraged for site-specific conjugation following unfolding of the protein.[171,181,273] The protein can then be refolded following modification and used to initiate *in vitro* fibril assembly by drawing fibers or assembled by cells in culture, as Vogel and colleagues demonstrated.[181,273,274] An approach adapted from these techniques was employed (illustrated in Figure 4.1D) to promote Fn unfolding in 4 M guanidine hydrochloride (Gdn) in a slightly basic buffer (0.05 M sodium borate, pH 8.5) to promote cleaving of the N-heterocycle with the thiol-terminus of Fn’s cysteine in $FnIII_7$ and $FnIII_{15}$ leading to di-sulfide linked Fn-HA conjugates. The conjugation mixtures were purified using dialysis. Hydrodynamic fibrillogenesis, previously published by our lab, [147,149] was employed to create 3D EECMs for cell culture. Shown in a CLSM MIP, Figure 4.1E, these EECMs are able to cover multi-millimeter areas and have fibrillar morphology. SEMs

display fibrillar morphology of Fn and Fn-HA EECMs at higher resolution, Figure 4.1F. Additional characterization is presented in the following sections.

4.4.2 Fn EECMs Assemble According to Biomimetic Hallmarks Enabling a Site-specific HA-Conjugation Strategy

Fn is a mechanosensitive protein with conformationally active domains whose ECM assembly is dependent on dimeric protein unfolding inducing intermolecular binding that produces insoluble multimeric fibrillar structures.[153,155] Details of specific domain interactions is a topic of ongoing investigation, but in vitro processes are thought to leverage this native phenomena to produce assembled-Fn biomaterials, overviewed elsewhere. [149,152,159,220] Among the many bio-active Fn domains, the cellular fibronectin splice variant containing the extracellular domain A (EDA or EIIIA) has been implicated in sustaining CD44+ colon cancer cells, and breast cancer cells grown on Fn-EECMs that stain positive for EDA-Fn following fibril assembly promoted CSCs, though the role of the EDA domain has apparently conflicting reports in need of clarity.[147,185,275] Figure 4.3A demonstrates positive staining of EDA-Fn compared to an isotype control indicating bio-active Fn domains, which we previously showed are not conformationally available when adsorbed onto either 2D surfaces or polymeric fibers.[147]

To assess assembly of Fn EECMs, nFn solutions were treated with 70kDa proteolytic Fn fragments, which contain the 70kDa N-terminus (FnI_{1-9} , $FnII_{1-2}$) implicated in the FnI-FnIII interactions required for assembly and historically used to block cell-mediated nFn assembly.[155] The 70kDa fragment was added in nFn solution used to produce EECMs at 0.176 mg/mL (~5 molar excess) immediately prior to initiating hydrodynamic fibrillogenesis. Figure 4.3B shows that fibril formation was perturbed, indicating that FnI-FnIII interactions are involved in EECM fibrillogenesis. Furthermore, disulfide reducing agents are commonly used to aid protein-based thiol chemistry; however, dimeric nFn is disulfide linked at the C-terminus and the dimeric form of the protein has been reported as a requisite for native assembly.[155,185] Previously used for

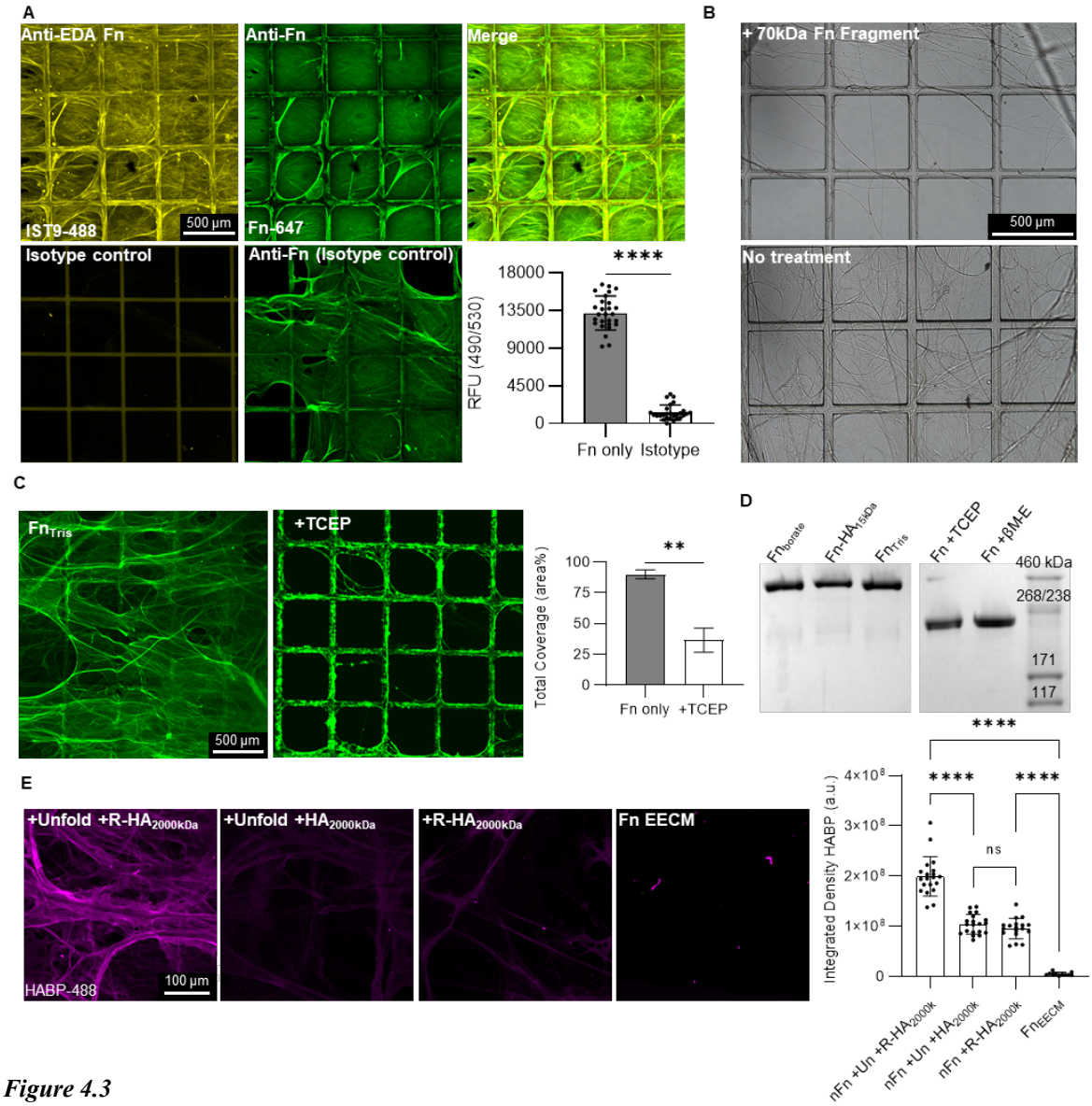

Figure 4.3
Fn EECMs assemble according to biomimetic hallmarks enabling a site-specific HA-conjugation strategy *A: CLSM MIPs of nFn EECMs stained for EDA-Fn (yellow), non-specific Fn (green) compared to an isotype control. Quantification was performed using a platereader for the EDA-Fn stain (Ex: 490nm, Em: 530nm).B: brightfield image of nFn hydrodynamic coating that were treated with 70kDa fragment (top) or with nothing (bottom)C: CLSM MIPs of Dylight-488 conjugated nFn that has been untreated (left) or treated with 20mM reducing agent TCEP (right). Quantification of total coverage was performed on CLSM MIPs and shows dramatic reduction of area coverage for nFn treated with TCEP. D: Image of SDS PAGE gel comparing Fn in tris vs borate buffer, HA-Fn conjugates following thiol specific strategy, nFn treated with 20mM TCEP and Fn treated with beta mercaptoethanol (β-ME). E: CLSM MIPs of HABP stained (magenta) EECMs after incubation at 37 C for 5 d in DPBS comparing different conjugation strategies. +Unfold (+Un) indicates unfolded nFn. "R-HA" denotes modified, thiol reactive HA compared to native HA. 2000kDa HA was used in these studies. Fn EECM were Fn EECMs without any HA treatment used as a negative control. Quantification was performed on MIPs (far right). *P ≤ 0.05, **P ≤ 0.01, ***P ≤ 0.001.*

synthesis of HA-Fn hydrogels,[276] 20mM tris(2-carboxyethyl)phosphine (TCEP) at RT was added to nFn solutions for 15min prior to the EECM coating process (2 h coating). Treatment with

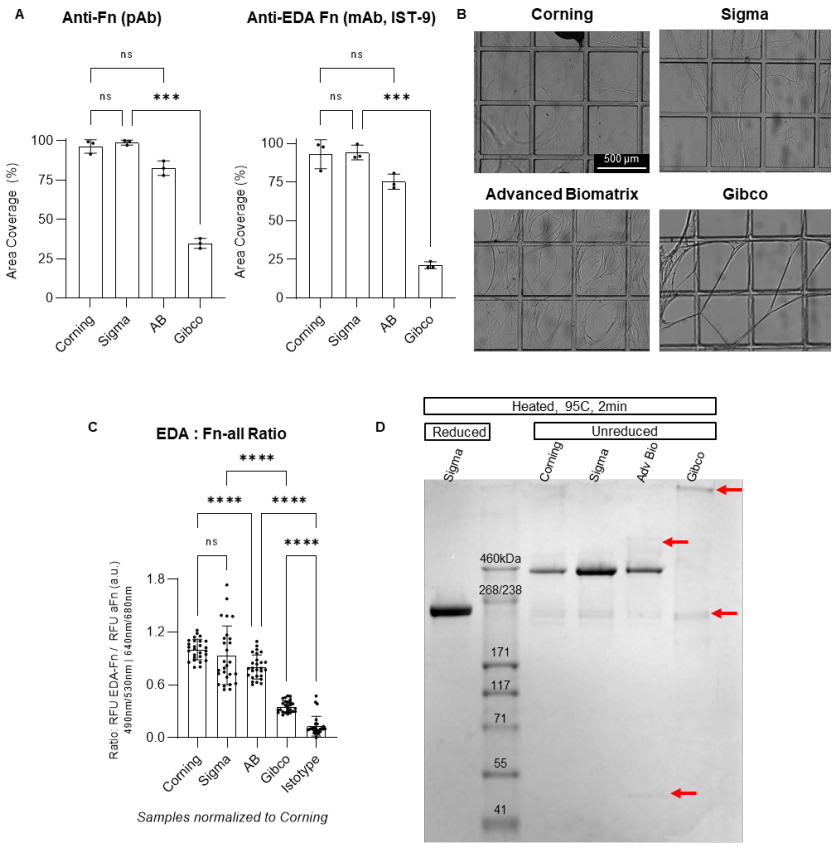

Figure 4.4

Evaluation of various nFn products. *A: Area coverage analysis based on CLSM MIPs assessed either from from general Fn pAb staining (left) or EDA-Fn specific mAb staining (right). B: brightfield image of TPSs that were hydrodynamically coated with Fn from different vendors. C: Ratiometric platereader analysis of signal from EDA-Fn normalized by general Fn stain. D: SDS-PAGE of Fn products from different vendors to assess the presence of dimeric protein content in the unreduced state vs Sigma Fn treated with β-ME (far left lane).*

TCEP critically ablated the formation of fibrillar EECMs indicated by representative CLSM MIPs and area coverage image quantification, Figure 4.3C. Furthermore, SDS-PAGE, Figure 4.3D, confirmed that this treatment reduced nFn to its monomeric form but did not significantly fragment it further. Other commercially available nFn sources were assessed for both the presence of dimer as well as EDA-antibody binding, Figure 4.4, further correlating the dimeric protein with fibril formation. Additionally, the SDS-PAGE of Fn-HA15k conjugates (Figure 4.3D) shows preservation of the dimeric protein after the bioconjugation method outlined in Figure 4.1D (prior to fibril assembly).

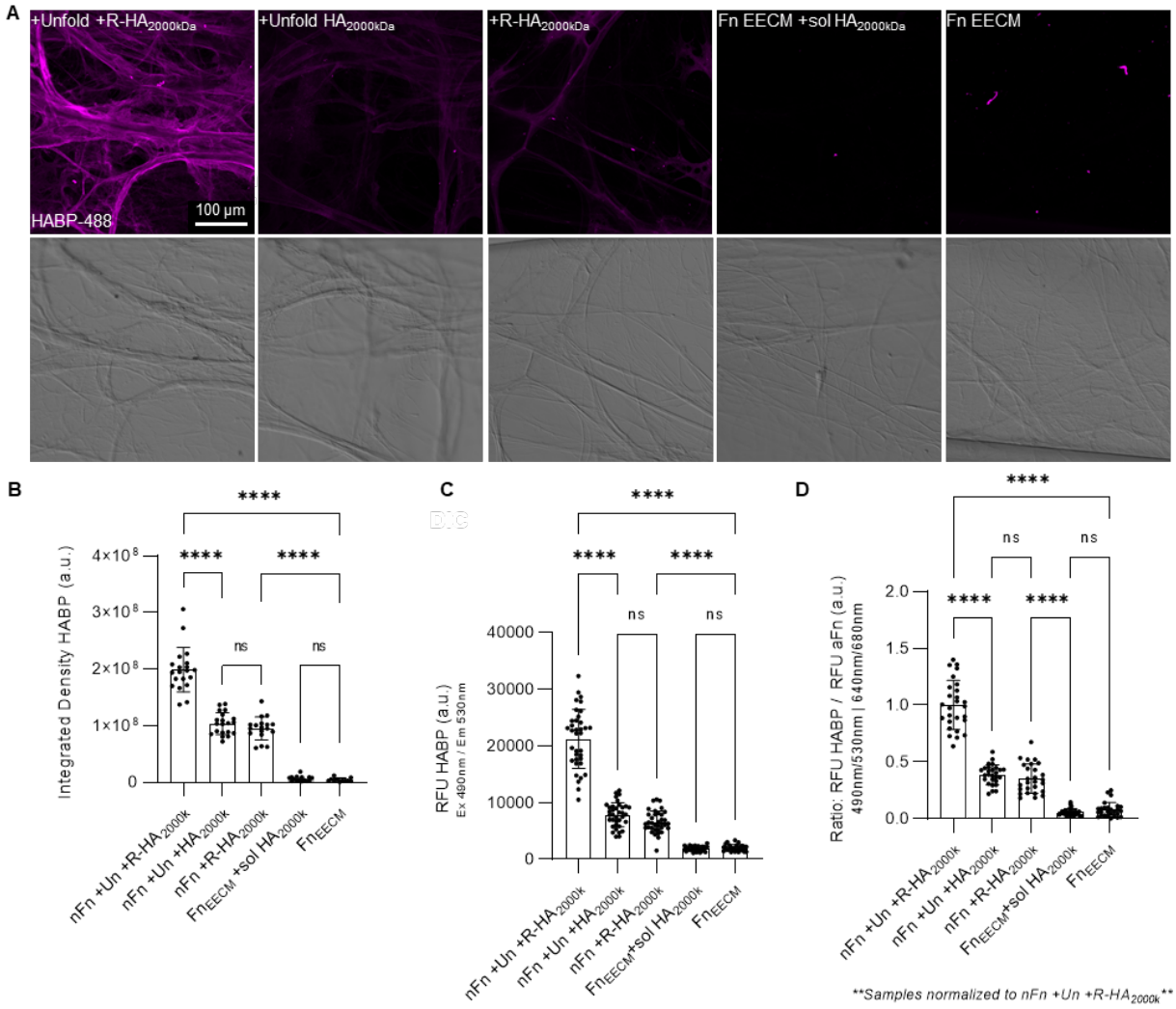

Figure 4.5
*A: CLSM MIPs and anlaysis from Figure 4.3, with additional group where Fn EECMs were treated with soluble native HA2000kDa for the duration of the study (5 d) as well as additional unbiased quantification methods using a platereader to validate image quantification. CLSM MIPs of HABP stained EECMs comparing different conjugation strategies (top row). DIC counter images (bottom row) are provided to demonstrate fibrillar EECM was present in each condition. +Unfold (+Un) indicates unfolded nFn. "R-HA" denotes modified, thiol reactive HA compared to native HA. 2000kDa HA was used in these studies. Fn EECM were Fn EECMs without any HA treatment used as a negative control. B: is the same integrated density quantification as Figure 4.3 where Fn EECMs were used to determine the pixel intensity threshold cutoff for analysis. C: Orthogonal quantification using a platereader, assessing just the HABP stain (Ex 490nm/Em 530nm). D: Platereader analysis where EECMs were co-stained with pAb for Fn and HABP/pFn ratios were normalized to nFn +Un +R-HA2000kDa *P ≤ 0.05, **P ≤ 0.01, ***P ≤ 0.001 ****P ≤ 0.0001.*

To validate the proposed bioconjugation method and assess bound HA stability in cell culture conditions, nFn was treated with Gdn to unfold the protein and exposed to 2PT modified HA-2000k (R-HA$_{2000kDa}$) and formed into EECMs via hydrodynamic fibrillogenesis, Figure

4.3E. This was compared to unfolded Fn treated with unmodified HA and folded Fn with R-HA. Fn EECMs that were not exposed to any HA were used as a control. All EECMs were incubated at 37 C for 5 d in DPBS before a biotinylated HA-binding protein (HABP) probe was used to visualize and quantify the incorporation of HA via image analysis. All groups successfully formed fibrillar EECMs, but more HA in the unfolded/R-HA group was incorporated compared to either other group of nFn treated with HA. Figure 4.5 includes DIC counter images displaying similar amounts of fibrillar EECM in each group. Orthogonal quantification was performed using a platereader to assess fluorescence intensity of the HABP stain alone as well as the HABP/Fn ratios after co-staining with a non-specific polyclonal anti-Fn polyclonal antibody (pAb). Relative values are similar and statistical interpretation from all methods is identical, which suggests the methodology used here and throughout the chapter are robust. Furthermore, Fn EECMs treated with soluble, unmodified HA over the same 5 d time course, showed no difference compared to untreated Fn EECMs implying that fibrillar Fn does not sequester HA from solution in cell culture conditions. Additionally, the similarity of unfolded/native HA and folded Fn/R-HA, indicates that although HA is incorporated, it may be due to non-specific binding or steric intercalation of this very large molecule. Critically, other systems relying on intercalation of unmodified HA and ionic interactions for stabilization precludes stable incorporation of low Mw HA (6.4 kDa),[266] which may indicate those systems are acting as delivery platforms for soluble HA rather than presenting HA in a tissue-relevant, surface bound form. Additionally, while there are some reports of Fn binding HA,[242] this approach is not supported by our data. Finally, the HABP probe used suggests that minimally modified HA incorporated into Fn EECMs still possesses requisite structure to bind via Link-module (primary binding domain of such probes), discussed further in the following section.

4.4.3 Thiol Conjugation Strategy Enables Highly Controlled Presentation of Fibrillar Fn and HA in Three-dimensions

Critical to the biological questions pursued, incorporation of 2000kDa and 15kDa HA into EECMs must be achieved with similar physical characteristics for downstream cell studies. Figure 4.6 summarizes physical characterization of the Fn-HA EECMs compared to Fn alone. For the remaining studies in this chapter, all EECMs were produced across polymeric scaffolds with large rectangular pores coated with parallel fluid flow such that the resulting fibrils lack orientation using methodology previously reported.[149] CLSM MIPs of large area scans of Fn-HA EECMs show that regardless of molecular weight, large multi-millimeter areas can be achieved with similar, non-oriented fibrillar morphology (Figure 4.6A). Because of the importance of topology in cell-biology and tissue engineered systems,[70,277] high-resolution confocal images were analyzed to determine fibril diameter. Fn, Fn-HA15k, and Fn-HA2000k EECMs all display remarkably similar, narrow distributions of fibril diameter, Figure 4.6B. Furthermore, Figure 4.6C displays 3D renders of ~70 μm x 70 μm areas dwith ~20 μm of z-depth. Figure 4.6D summarizes fibril diameter distributions and mass loading. All groups have ~ 1 μm diameters with 95% ranges from ~ 0.6 μm to 4 μm and skewed distributions tending toward slightly larger diameters. Diameter distribution summaries display exceedingly small changes between all groups. Collectively, these data illustrate the physical nature of EECMs: coherent sheets comprised of fibrils with ~1 μm diameters are interconnected in a porous manner throughout the ~100 μm of polymer scaffold z-depth across ~5 mm x 5 mm areas. Cells can then be seeded throughout EECMs simply by pipetting a solution over them. By comparison, other engineered technologies rely on modified/naturally derived hydrogels which physically encapsulate cells or only facilitate cells sitting atop the substrate.[265,266,278,279] Physical constraints in these systems

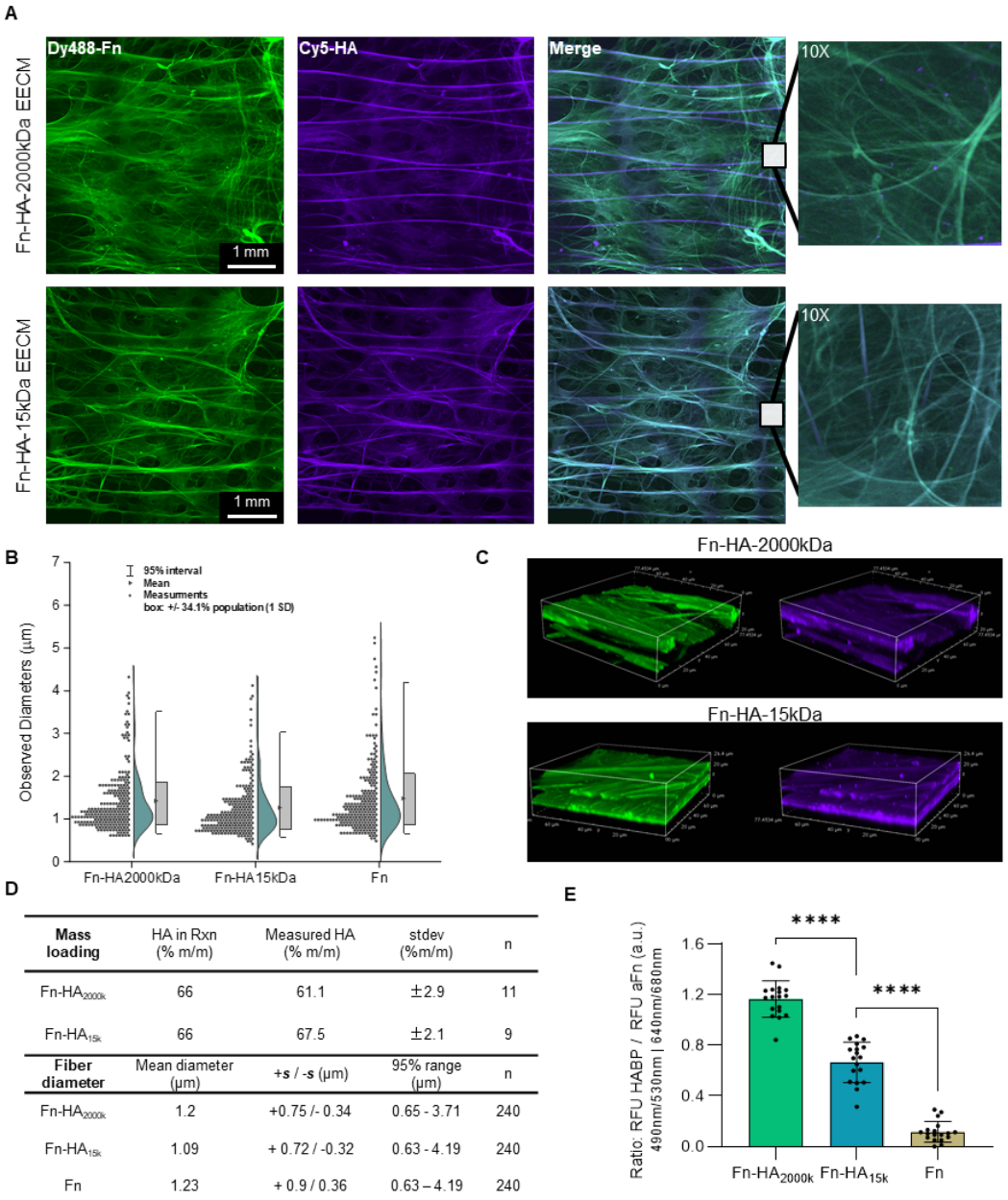

Mass loading	HA in Rxn (% m/m)	Measured HA (% m/m)	stdev (%m/m)	n
Fn-HA$_{2000k}$	66	61.1	±2.9	11
Fn-HA$_{15k}$	66	67.5	±2.1	9
Fiber diameter	Mean diameter (µm)	+***s*** / -***s*** (µm)	95% range (µm)	n
Fn-HA$_{2000k}$	1.2	+0.75 / - 0.34	0.65 - 3.71	240
Fn-HA$_{15k}$	1.09	+ 0.72 / -0.32	0.63 - 4.19	240
Fn	1.23	+ 0.9 / 0.36	0.63 – 4.19	240

Figure 4.6
Characterization of Fn-HA EECMs of different molecular weights compared to Fn EECMs*. A: CLSM MIP of Fn-HA EECMs (Fn-15kDa top row, Fn-2000kDa bottom row) where Fn and HA were visualized with fluorescent tags (Dylight 488 and Cy5, respectively). B: Manual fibril diameter analysis of Fn-HA conjugate EECMs compared to pure Fn EECMs. Each group is represented by split histogram, violin plot and box-whisker. C: High resolution 3D volume renders comparing Fn-HA conjugates with different molecular weights. D: Summary of mass loading quantification (top) and fibril diameter analysis (bottom). E: Platereader quantification of EECMs where HABP/aFn pAb ratios were normalized to Fn-HA2000kDa EECMs. *P ≤ 0.05, **P ≤ 0.01, ***P ≤ 0.001 ****P ≤ 0.0001.*

may in and of itself play a role in the observations of growth modulation/phenotype. This shortcoming is overcome by employing porous EECMs.

Furthermore, relative amount between 15kDa and 2000kDa HA within EECMs is another critical parameter to control. To quantify mass loading R-HA was simultaneously tagged with a Cy5 dye and Fn was labeled with a Dylight 488 dye. Fn EECMs and control samples were imaged using confocal microscopy. Control samples with known ratios of Fn-Dylight488 and HA-Cy5 were loaded into 4% m/m gelatin as a 3D matrix. To construct 3-point calibration curves, linear regressions were fit to intensity ratios of Fn-Dylight 488 and HA-Cy5 vs mass ratio, Figure 4.7. HA loading was calculated from Fn/HA EECM intensity ratios (imaged identically to the control cohort) using the linear fit equation. The mass loading data summarized in Figure 4.6D highlights similar loading for both molecular weights; 61.1 ± 2.9 % (m/m) for HA-2000kDa compared to 67.5 ± 2.1 % (m/m) for HA-15kDa. Additionally, loading of both HA lengths in the fibrillar EECMs closely reflect the original reaction mixture (66% HA in Fn m/m) indicating the bioconjugation process is remarkably well controlled despite the ~130-fold difference in HA-length. Finally, knowing that loading of both HA lengths was similar, Fn-HA EECMs were co-stained with HABP and an anti-Fn pAb to assess the binding affinity of HABP. The biotinylated-HABP used derived from bovine nasal cartilage, reports binding to HA >2kDa and is composed of proteoglycans binding primarily through via the Link-module. HABPs that can be classified as Link-module binding include aggrecan, versican, hyaluronectin and CD44.[60,238,243,280] Other important receptors including RHAMM bind through the B(X7)B motif,[281] which would not be reflective of the data presented here. In Figure 4.6E, platereader quantification of the HABP/aFn ratio shows that despite equal mass loading, HA-2000k within EECMs has a higher binding affinity for a Link-module based probe. CLSM MIPs of these stained samples are shown in Figure 4.7. Large, polymeric HA has been implicated in

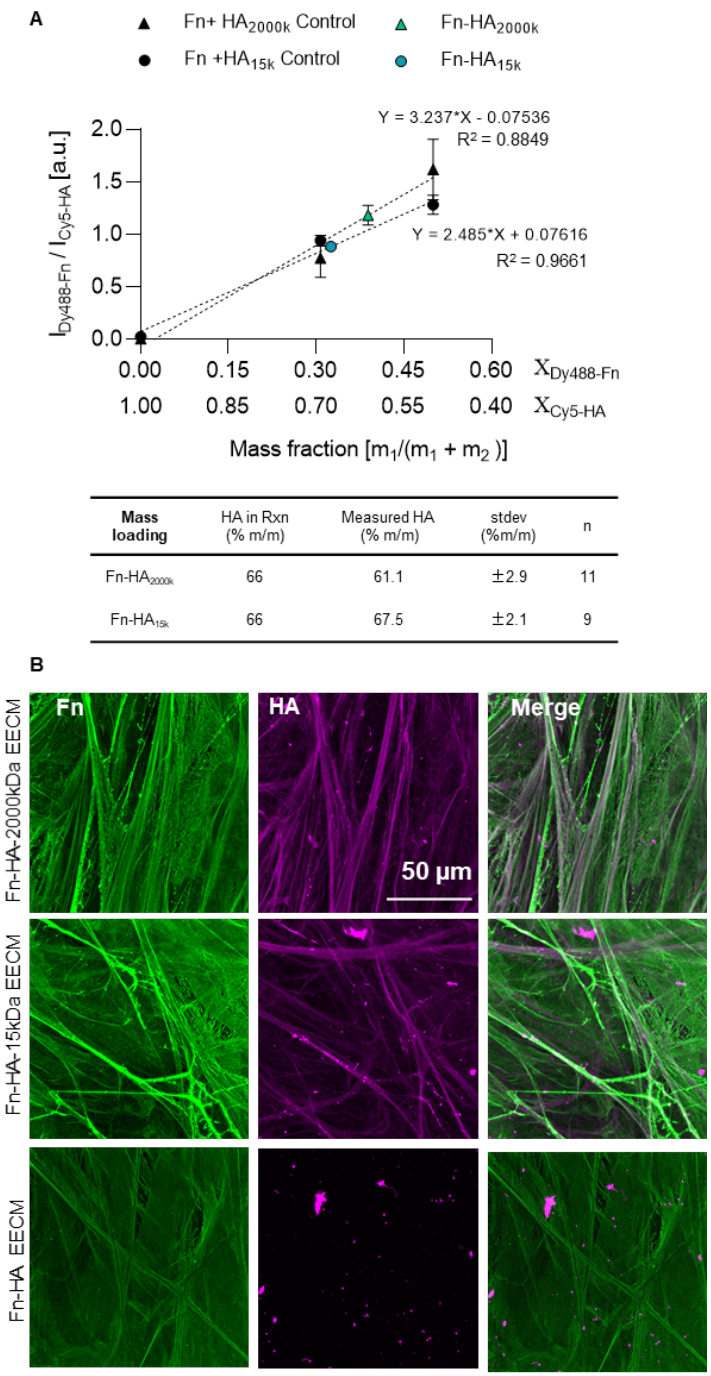

Mass loading	HA in Rxn (% m/m)	Measured HA (% m/m)	stdev (%m/m)	n
Fn-HA$_{2000k}$	66	61.1	±2.9	11
Fn-HA$_{15k}$	66	67.5	±2.1	9

Figure 4.7
A: linear regressions of sample Fn-HA15kDa and Fn-HA2000kDa EECMs compared to respective 3D gelatin controls with known mass loading used to determine mass ratios of HA in Fn fibrils within EECms. B: CLSM MIPs of EECMs stained withwith aFn pAb (green) and HABP (magenta). These EECMs were used in the platereader quantification from Figure 4.6 E.

multi-valent interactions with HABPs potentially explaining CD44 clustering at cell membranes,

and underpin why sandwich-like ELISA underestimate lower Mw HA bound on surfaces

(<150kDa) potentially due to perturbing the flexibility necessary to adopt loop conformations for HABP binding.[246,282–284] Hence, HABP affinity for the HA integrated into Fn EECMs reflects reported literature, where these differences may play a role in modulating cell behavior.

4.4.4 Fn-HA EECMs Display Tumor-mimetic Morphology and Biochemistry

Laminin and collagen IV compose the normal epithelium basement membrane, where escape from this and exposure to fibrotic ECM appeared to confer phenotypic advantages that lead to dissemination of tumor cells.[285–287] Seminal work by Mina Bissel's group shed light on the importance of the ECM in malignancies and Paolo Provenzano/Patricia Keeley paved the way for mechanistic and prognostic understanding of collagen reorganization in breast tumor stroma.[6,7,19,288] It is clear that intratumoral cellular and ECM heterogeneity is correlated with poor prognosis and is implicated in facilitating metastatic dissemination of tumor cells.[287,289] Disseminating tumor cells commonly home to the bone marrow as a site for metastasis and recurrence, where cells secrete high levels of HA as a normal component of this tissue niche.[5,290–292] Stromal cells are implicated as the architects of tumor ECM, and bone-marrow derived mesenchymal stem cells (BM-MSCs) are known to be recruited to the primary tumor and contribute to metastatic spread.[293]

To compare our engineered system to a heterogenous environment reflective of intratumoral heterogeneity, a co-culture model comprised of tumor-cells (T47Ds or MCF7s) and bone-marrow cells (HS27a or HS5) was utilized to investigate the role of ECM heterogeneity. HS27a and HS5 bone marrow stromal cells are used as analogues for BM-MSCs in cancer research, where HS5s have been verified as representative analogues for primary MSCs.[294] Furthermore, this co-culture system previously revealed that a greater fraction of tumor cells co-cultured with BM-MSCs resided in a quiescent state with increased metastatic potential.[295] Bulk RNA sequencing revealed that both HS27a and HS5s in co-culture generally expressed higher levels of HAS2 than MCF7s/T47Ds in the correlated co-culture, Figure 4.8A. Interestingly, HS5s

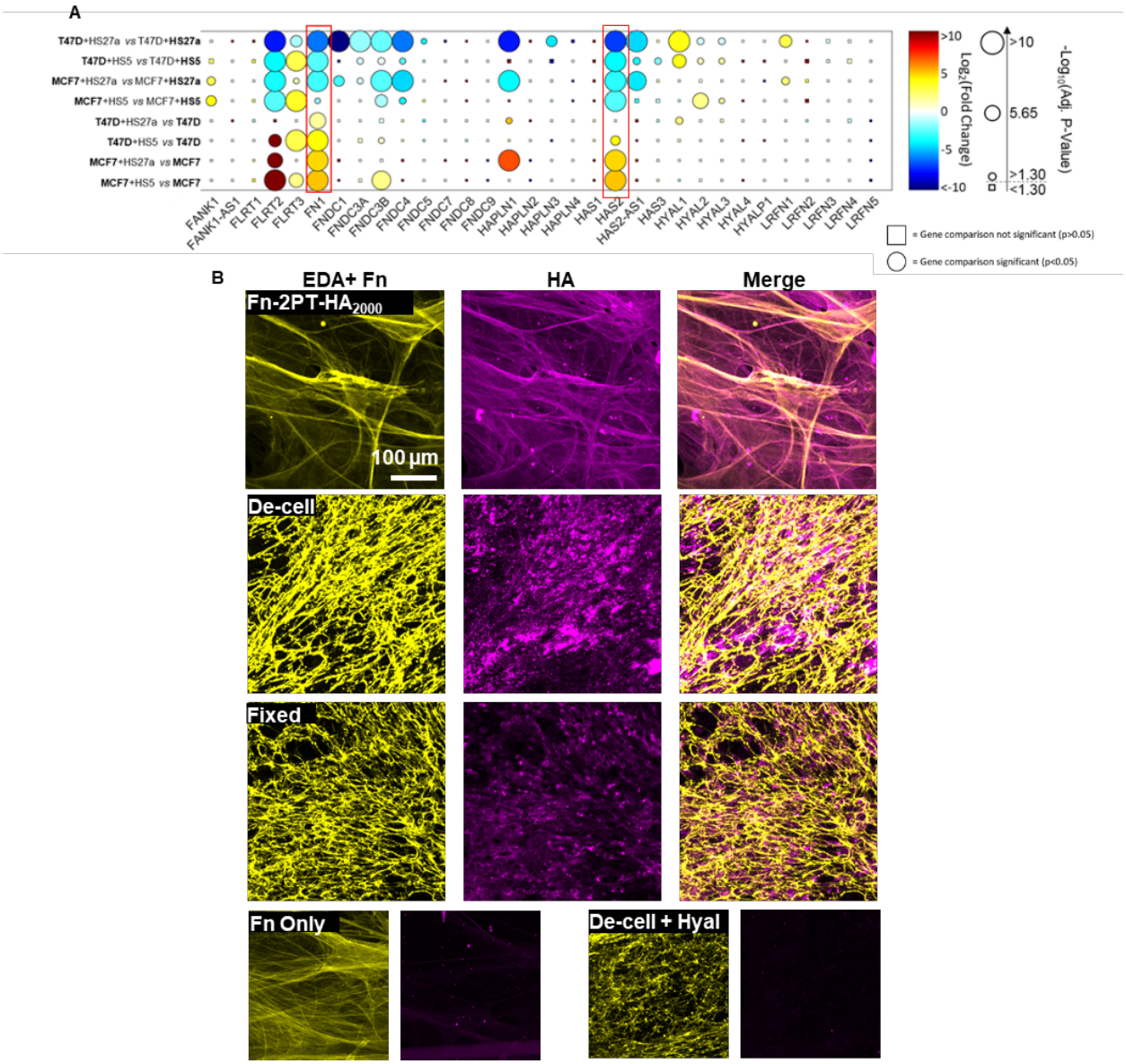

Figure 4.8
Fn-HA EECMs display tumor-mimetic morphology and biochemistry *A: Bulk RNA-seq analysis of breast cancer cell lines (T47D, MCF7) co-cultured with two bone marrow stromal cell lines (HS27a, HS5). Co-cultured breast cancer cells (bold) were compared to stromal cells (bold) in the top 4 rows. Where breastcancer cells co-cultured (bold) were compared to standard monocultured breast cancer cells (bold) in the bottom 4 rows. B: CLSM MIPs of Fn-HA2000kDa EECM stained with EDA-Fn (yellow) co-stained with HABP (magenta) in the top row compared to MCF7/HS5 co-cultures subjected to de-cellularization (2nd row), fixed MCF7/HS5 co-cultures (3rd row) with imaging controls of Fn only EECMs and de-cellularized co-cultures treated with hyaluronidase in the bottom row.*

had less significant changes in expression of FN1 in co-culture compared to MCF7s in the respective co-culture. Additionally, MCF7s in co-culture with HS5 and HS27a had a marked increase in the expression of both HAS2 and FN1 compared to MCF7s in monoculture. To

investigate these transcriptional signatures at the protein level, co-cultures of MCF7s/HS5s were fixed and decellularized to assess their stability and compared to EECMs, Figure 4.8B. Co-cultures showed substantial deposition of fibrillar, EDA+ Fn as well as HA, with clear co-localization of fibrillar EDA-Fn with HA. Additionally, much of the HA remained intact following decellularization indicating that it was insoluble/tissue bound. Finally, Fn-HA EECMs display similar fibrillar morphology to cell secretions where much of the HA and Fn signal co-localizes (displayed in merge channel) with distinct regions and nodes similar to the co-cultures.

HAS2 expression in breast tumor cells has been correlated with invasive phenotypes and reported as encoding for high Mw HA (>1,000kDa).[260,296] Furthermore, in breast cancer upregulation of FN1 expression is reported alongside EMT/CSC-enrichment in HA-related investigations,[259,297,298] but FN1 expression is used as a marker for EMT and not investigated extracellularly. In lung and other tissues, deposition of Fn and HA have been correlated with fibrotic remodeling but the significance underpinning their co-secretion is elusive.[299,300] In the context of breast cancer the dual presentation of HA and Fn as fibrotic extracellular components capable of influencing cell fate warrants further investigation.

4.4.5 Fn-HA EECMs Allude to Complex Role of Protein-glycan Regulation in Tumor Tissue

With Fn-HA EECMs established as well controlled, tumor-mimetic microenvironments, we explored the hypothesis that HA present in the tumor stroma would epigenetically regulate cell phenotype and influence metastatic potential of tumor cells. Toward this, MCF7s were grown in low FBS (2% v/v) on EECMs (Fn, Fn-HA2000k, Fn-HA15k) and compared to TCPS (2D) in 2% v/v FBS as well as standard (10% v/v FBS). Figure 4.9A shows in bright field after 6 d that cells were approaching confluence without any obvious changes in growth dynamics or morphology indicative of unhealthy cells. This was supported by viability measurements where all groups were similar and above 70%, Figure 4.9B. Interestingly, MCF7s primed on different environments displayed differential sphere formation capacity which would generally indicate upregulation of tumor-initiating stem phenotypes, shown in Figure 4.9C. Here Fn EECMs significantly upregulated sphere formation, assessed at 15 d, compared to 2D. Fn-HA2000k EECMs where not different than 2D, yet MCF7s primed on Fn-HA15k EECMs were significantly above 2D and similar to Fn EECMs. MCF7s cultured on different conditions were then replated into 96 well plates and allowed to proliferate for 4.5 d before assessing scratch wound kinetics to assess invasive/migratory phenotypic changes, which revealed no striking differences in the epithelial MCF7 cell line Figure 4.9D.

To investigate the role of various growth environments on proliferation and stemness, a dye retention assay with Cell Trace Far Red (CTFR) was performed using flow cytometry. This assay stratifies proliferating and non-proliferating cells because lower dye signal arises from a greater number of cell divisions. Dye retention assays have also been used to identify breast CSCs and normal mammary stem cells.[301–303] This revealed that despite robust growth on EECMs observed under brightfield microscopy during the 6 d of growth (Figure 4.9A), there

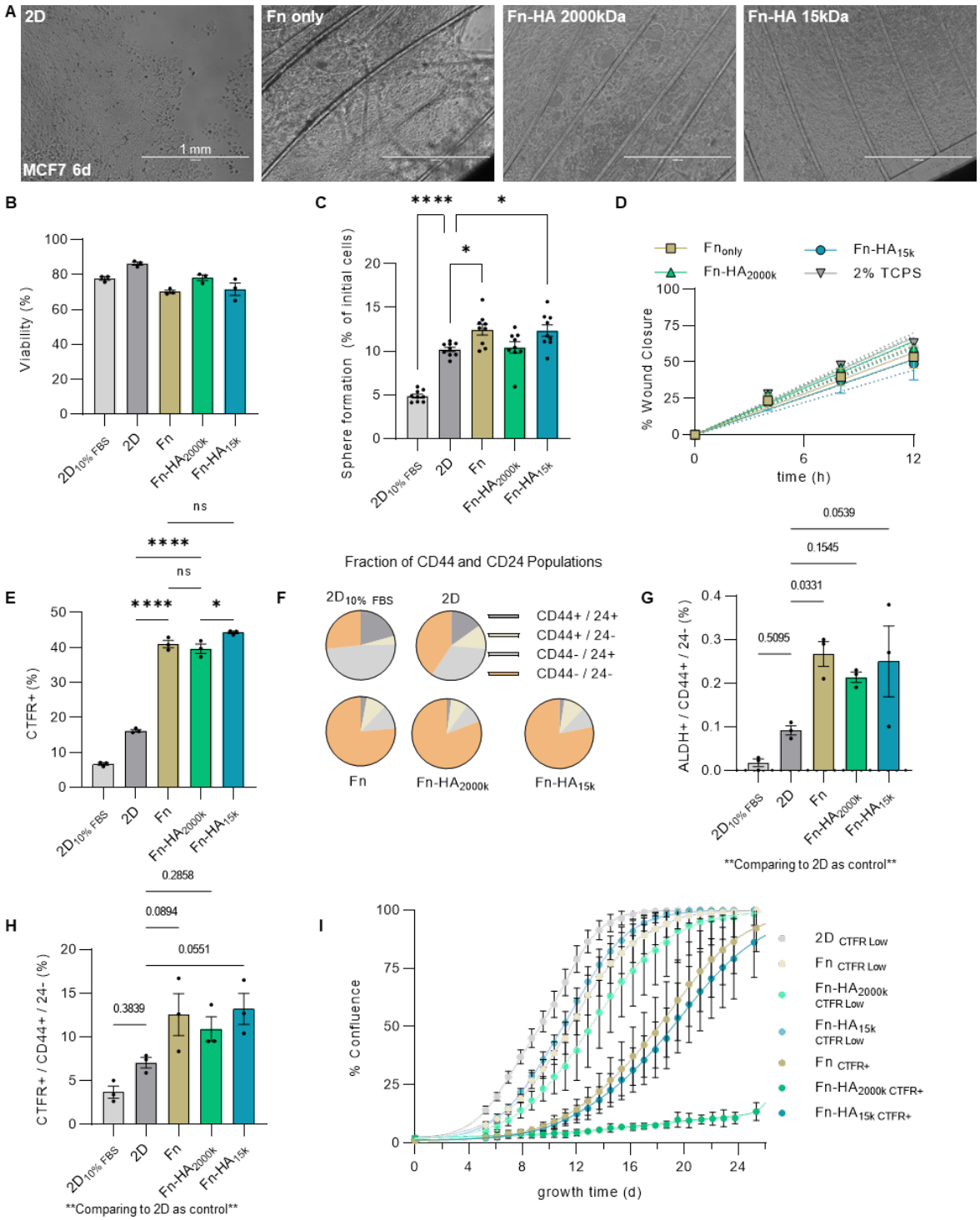

J

Re-growth kinetics	Max growth rate [%conf. / d]	t,5% [d]	t,50% [d]	t, 95% [d]
2D CTFR Low	10.9	3.1	9.3	14.5
Fn CTFR Low	10.0	3.7	11.5	19.1
Fn-HA2000k CTFR Low	8.6	4.8	13.1	21.5
Fn-HA15 CTFR Low	10.1	4.2	11.0	17.2

Re-growth kinetics	Max growth rate [%conf. / d]	t,5% [d]	t,50% [d]	t, 95% [d]
Fn CTFR(+)	7.7	8.4	18.2	*26.5***
Fn-HA2000k CTFR(+)	0.6	12.7	i.d.	i.d.
Fn-HA15 CTFR(+)	7.2	8.8	19.2	*28.7***

were substantial populations of high dye retaining (CTFR+) cells on the 3D environments

Figure 4.9
MCF7 cells grown on Fn-HA EECMs, Fn EECMs and TCPS (2D) in 2% (v/v) FBS were characterized to assess phenotype and epithelial/mesenchymal tumorigenic characteristics. *A: representative brightfield images of MCF7s on different conditions after6 d before being assayed in all other panels. B: viability assessed by flow cytometry for DAPI negative MCF7s. C: Spheroid formation assay in methyl cellulose containing MEBM assessed after 15 d in sphere culture. D: Scratch wound assay following 4.5 d of regrowth with linear regressions (solid colored lines) with error for fits (corresponding dotted lines). E: Dye retention assay using CTFR dye to quantify non-proliferating cells denoted CTFR+ with flow cytometry. F: Phenotyping by flow cytometry to quantify populations of CD44+/- and CD24 +/- cells. G: Phenotyping by flow cytometry to quantify dual positive ALDH+ / CD44+ 24- BCSCs. H: Phenotyping by flow cytometry to quantify CD44+ 24- that are in the CTFR+ subpopulation. I: Regrowth curves of MCF7s that were CTFR + or CTFR low that were replated into 96 well TCPS plates growth in full, 10% FBS medium where regrowth kinetics were are summarized in J. Values with ** here indicate fitted values reported outside of time course and i.d. represents insufficient data for fitted values during the time course assessed. *$P \leq 0.05$, **$P \leq 0.01$, ***$P \leq 0.001$ ****$P \leq 0.0001$.*

compared to 2D Figure 4.9E. Here FN-HA15k EECMs had a nominal, but statistically significant increase over Fn-HA2000k EECMs.

Next we investigated, CD44+/CD24- and ALDH+ which are used to denote breast CSCs subpopulations that are more mesenchymal and epithelial, respectively.[304–307] These markers were assayed alongside CTFR via flow cytometry. Surprisingly, CD44+ populations did not change across 3D groups, but CD24 was significantly decreased following culture on all EECMs compared to 2D, Figure 4.9F. Neither mesenchymal-CSC (CD44+/24-) nor epithelial-CSC (ALDH+) populations differed across MCF7s grown on 2D or 3D EECMs in low serum. Interestingly, dual-positive CD44+/24-/ALDH+ populations were higher on Fn and Fn-HA15k ($p = 0.0331$, $p = 0.0539$, respectively) than was Fn-HA2000k ($p = 0.1545$) when compared to 2D (Figure 4.9G). Because of the dramatic increase in dye retention, the intersection of CTFR+/CD44+/24- populations was assessed which displayed similar trends. When compared to 2D, Fn ($p = 0.0894$) and Fn-HA15k ($p = 0.0551$) were approaching significance, but Fn-HA2000k (0.2858) was not significant.

Next to evaluate whether growth characteristics were altered by the initial growth substrate, CTFR+ cells were sorted from CTFR low cells and replated on standard TCPS 96 well plates and grown in full serum (10% v/v) media, Figure 4.9I. Growth kinetics were

determined by non-linear fits and summarized in Figure 4.9J. These data showed that of CTFR low groups, 2D regrowth was fastest (10.9 %conf / d, $t_{50\%}$ = 9.3 d), followed by Fn-HA15k and Fn EECMs (10.1 %conf / d, $t_{50\%}$ = 11.0 d | 10.0 %conf / d, $t_{50\%}$ = 11.5 d, respectively) and then Fn-HA2000k (8.6 %conf / d, $t_{50\%}$ = 13.1 d). Not surprisingly, CTFR+ cells grew slower than the CTFR low counterparts, but intriguingly CTFR+ MCF7s primed on Fn-HA2000k samples displayed little growth over the time course assessed.

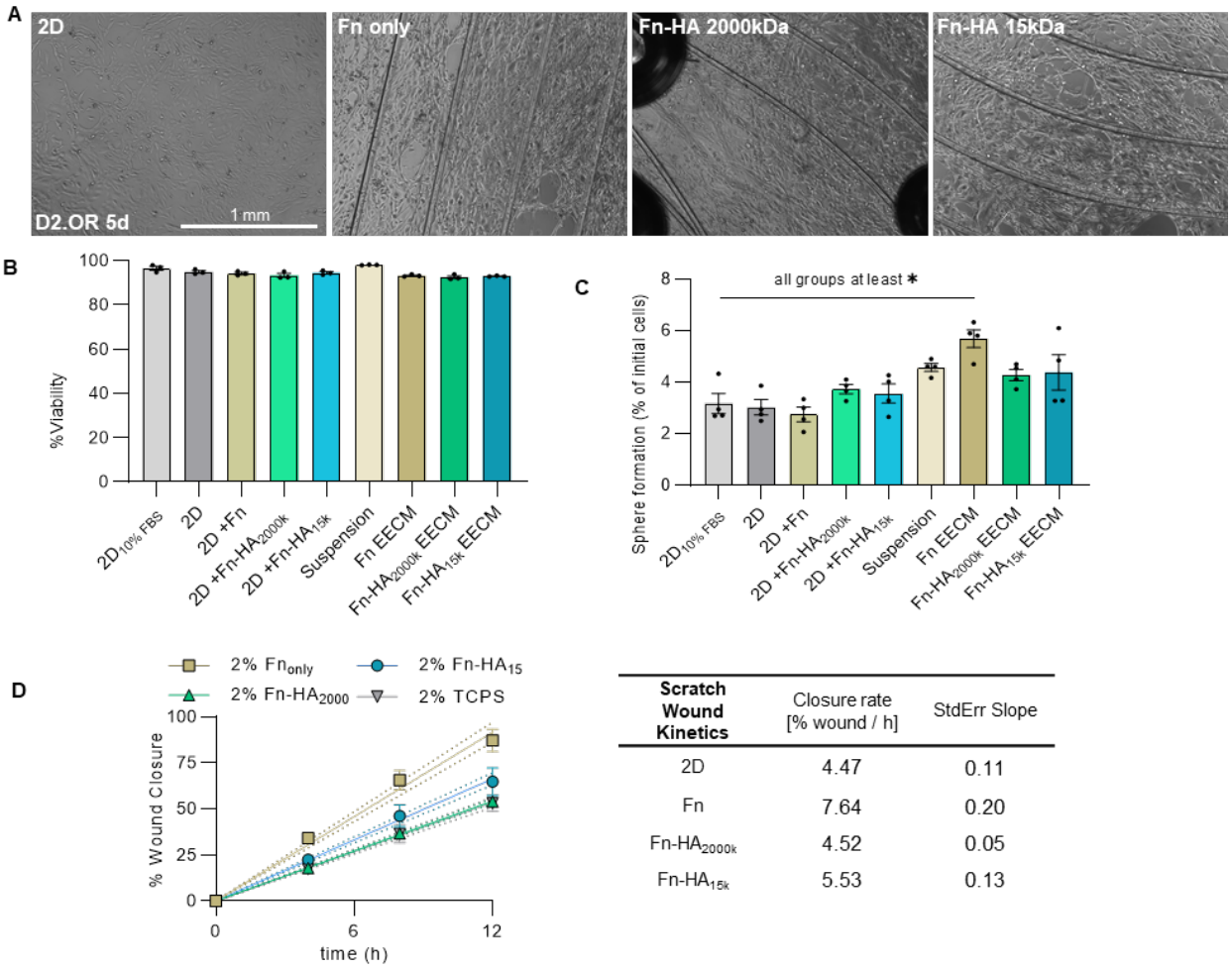

Scratch Wound Kinetics	Closure rate [% wound / h]	StdErr Slope
2D	4.47	0.11
Fn	7.64	0.20
Fn-HA$_{2000k}$	4.52	0.05
Fn-HA$_{15k}$	5.53	0.13

Figure 4.10
D2.OR cells grown on Fn-HA EECMs, Fn EECMs and TCPS (2D) in 2% (v/v) FBS were characterized to assess epithelial/mesenchymal tumorigenic characteristics. *B,C: also include D2.ORs grown in full serum (10% FBS), TCPS coated with Fn or Fn-HA conjugates (2D + groups), as well as D2.ORs grown in non-methyl cellulose containing MEBM (suspension). A: representative brightfield images of D2.OR on different conditions after 5 d before being assayed in all other studies with D2.ORs. B: viability assessed by flow cytometry for DAPI negative D2.OR cells. C: Spheroid formation assay in methyl cellulose containing MEBM assessed after 15 d of sphere culture. D: Scratch wound assay following 3 d of regrowth with linear regressions (solid colored lines) with error for fits (corresponding dotted lines). *P ≤ 0.05.*

Given the interesting changes in dye-retention, regrowth and phenotype with MCF7s, D2.OR cells were grown on the different environments as this cell line has been characterized as modeling metastatic recurrence *in vivo* but not *in vitro* unless grown on a 2.5D environment (atop Matrigel).[308] Similar to MCF7s, D2.ORs displayed attachment and slow proliferation in low serum conditions, Figure 4.10. All groups had high viability after culture for 5 d on all

substrates (>90 %), Figure 4.10B. Additional 2D control groups included TCPS (2D) coated with Fn, Fn-HA2000k, and Fn-HA15k to explore the role of conformation of the protein-glycan conjugates. Cells grown in mammosphere media (suspension) were used as a 3D control because mammosphere culture is reported to enrich for stem-cells as well as non-proliferating cores. Interestingly, only Fn EECMs showed significant increases in sphere formation compared to all 2D groups, and not any 3D groups Figure 4.10C. Suspension culture was statistically significantly higher than 2D+Fn but not any other groups. Notably, Fn and Fn-HA conjugates coated on 2D surfaces did not impact sphere formation. Furthermore, scratch wound assay showed differences in wound closure kinetics following 3d of regrowth on TCPS before beginning the assay, Figure 4.10D. D2.ORs primed on Fn displayed the fastest wound closure (7.64 % wound / h), followed by Fn-HA15k (5.53 % wound / h) and finally Fn-2000k and 2D (4.52 % wound / h | 4.47 % wound / h, respectively).

To characterize growth characteristics, the dye retention assay was again utilized, displayed graphically in Figure 4.11A. With D2.ORs, 3D EECM conditions again supported substantial increases in CTFR+ populations compared to all 2D groups (Figure 4.11B). Furthermore, both Fn-HA EECMs displayed significantly higher dye-retention than either suspension culture or Fn EECMs. Fn-HA15k again showed a nominal, but not statistically significant increase in CTFR+ populations compared to Fn-HA2000k. Fn and Fn-HA conjugates coated on 2D surfaces did not impact dye retention compared to other 2D samples. High dye retaining cells were sorted from the lower dye retention (CTFR+ vs CTFR low) and assessed via sphere formation assay, Figure 4.11C with sorting gates represented in Figure 4.11D. Unexpectedly, high dye retaining cells, especially those primed on Fn-HA EECMs, had a marked decrease in sphere formation efficiency compared to their low dye retaining correlates.

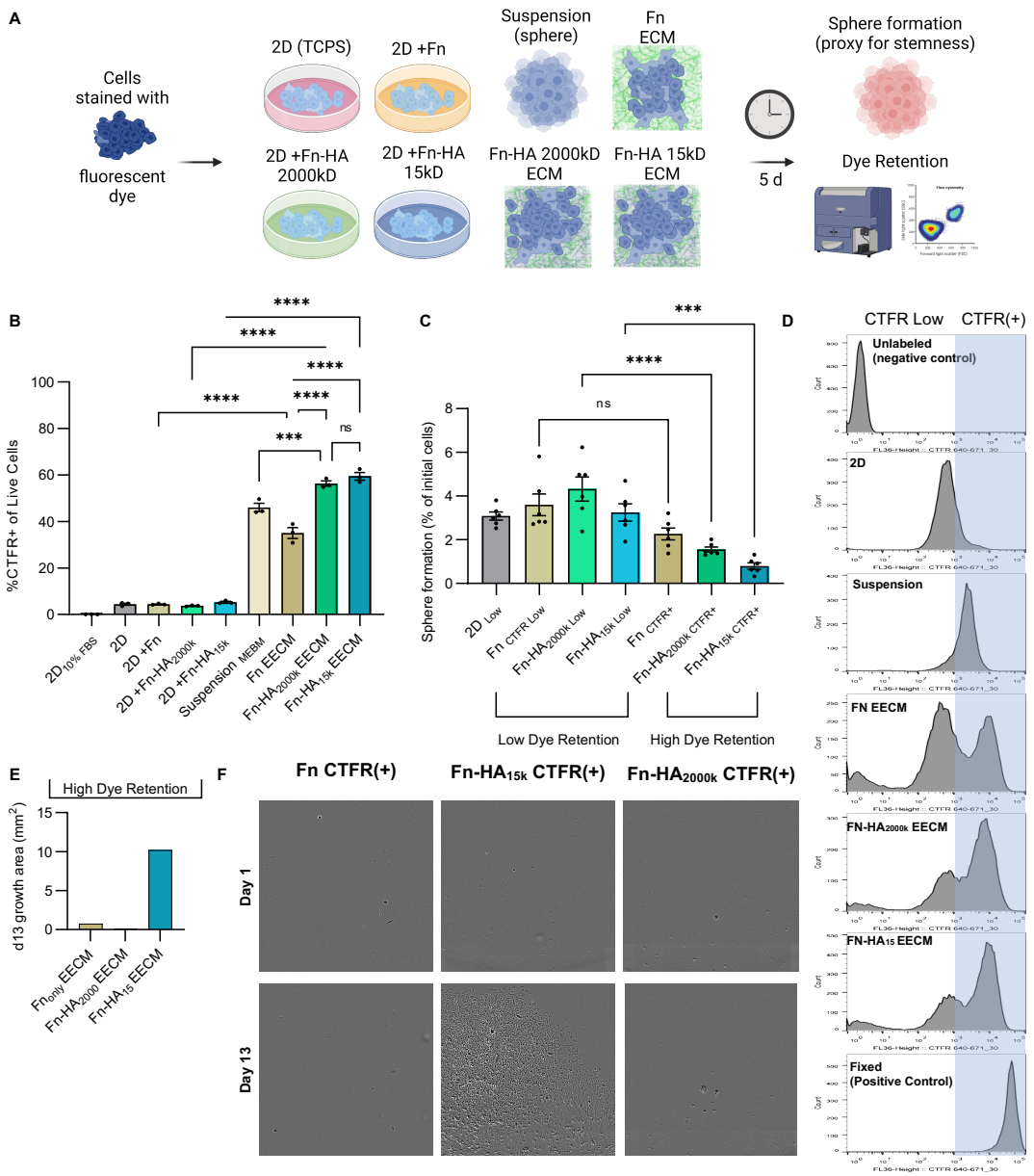

Figure 4.11
D2.OR cells grown on Fn-HA EECMs, Fn EECMs and TCPS (2D), TCPS coated with Fn or Fn-HA conjugates (2D + groups), in 2% (v/v) FBS compared with cells grown in full serum (2D 10% FBS), and non-methyl cellulose containing MEBM suspension culture to assess conditions that promote CTFR+ populations. *A: Illustration of experimental work flow. B: CTFR+ cells assessed by flow cytometry. C: Spheroid formation assay in methyl cellulose containing MEBM assessed after 15 d of sphere culture for CTFR+ cells compared to CTFR low cells. D: Representative histograms of CTFR + or low cells to show relative population distributions as a function of culture substrate. E: CTFR+ cells from mammosphere culture that were filtered and replated on TCPS in 10% FBS. F: Representative brightfield images of regrowth assay in E. *P ≤ 0.05, **P ≤ 0.01, ***P ≤ 0.001 ****P ≤ 0.0001.*

Histograms of the CTFR signal shows that when cultured on 2D or in suspension culture, D2.ORs have a singular distribution of dividing cells (Figure 4.11D). These distributions shift

down from the positive control differentially, indicating a change in proliferative rate, which was unsurprisingly faster for 2D than suspension. Remarkably, when grown on EECMs, three distinct proliferative populations are observed. The highest dye retaining peak likely indicates a quiescent population that had divided at least once, as the peak maxima are lower than the positive control but interestingly slightly higher than suspension culture. There is then a moderately proliferating bulk that aligns with 2D, as well as a highly proliferative population that has lost all dye (aligned with unlabeled control). The quiescent CTFR+ group is upregulated in both Fn-HA EECMs compared to Fn EECMs. Critically, these tri-modal growth populations were not observed for any of the 2D groups coated with Fn or Fn-HA conjugates. This indicates that conformationally active, fibrillar fibronectin promotes markedly heterogeneous growth where the presence of HA facilitates more quiescent cells. During the sphere formation assay, cells in the CTFR+ groups sorted from EECMs (Figure 4.11C) appeared to reside in a single-cell, quiescent state instead of forming spheres. These cells were filtered from spheroids using a 35 μm flow tube and replated onto TCPS 96 well plates and cultured in standard media (DMEM, 10% FBS). Strikingly, D2.ORs primed on Fn-HA15k EECMs for 6 d that resided in a single-cell state during 18 d in non-adherent, serum free mammosphere culture were able to re-activate on TCPS in 10% FBS and displayed substantial growth not seen by those cells primed on either Fn or Fn-HA2000k EECMs.

Notably, the lack of differences in growth populations in 2D+Fn-HA (15k/2000k) indicates that HA alone in these models is not sufficient to direct growth kinetics, and is instead catalyzed by the presence of conformationally active fibrillar Fn. The significance of fibrillar Fn and not 3D culture alone is supported, as D2.ORs grown in suspension did not give rise to multi-modal growth populations. Finally, the lack of differences in sphere formation of D2.ORs

cultured on Fn/Fn-HA coated 2D substrates (Figure 4.10C) all collectively support the notion that conformational activity of fibrillar Fn is key to both the stem phenotype and differential growth kinetics observed across two cell lines and various assays. We previously showed that Fn coated on 2D surfaces did not display active binding for cellular Fn mAbs,[147] which indicates conformationally sensitive type-III domains are exposed in the fibrillar form and may, in part, explain this finding. Interestingly, Barney et al. reported cells capable of entering long term *in vitro* dormancy were those that organized fibrillar-Fn rich ECMs and had heterogeneous populations of proliferating/non-proliferating cells. [309] This finding is consistent with the observations reported here that fibrillar Fn itself plays a key role in producing quiescent/highly proliferative cells. Toward the differences in sphere formation for CTFR+ cells, Cicalese et al. proposed a model in which CSCs may divide symmetrically to produce two additional stem cells with increasing asymmetric divisions to produce progenitors overtime which would lead to CSCs with different levels of dye retention.[301] Even though high dye retaining D2.ORs had lower sphere formation, it is possible that while not sphere forming, the high dye retaining D2.ORs from Fn-HA15k environments adopted a phenotype whereby long-term survival advantages are conferred but not captured *in vitro* by the mammosphere assay.

Therefore, to vet significance of these *in vitro* findings and directly probe the metastatic colonization of cells primed on different environments, intracardiac injections were performed using NODscid mice and D2.ORs engineered with a click beetle green (CBG) luminescence reporter. Dissemination and growth kinetics are being assessed using Bioluminescence imaging (BLI), shown schematically in Figure 4.12A, and overall survival will be reported. BLI up to day 50 shows similar trends to *in vitro* studies for the 3D groups in that Fn and Fn-15k EECMs have similar, faster overall doubling times (36.03 d and 36.43 d, respectively) compared to Fn-2000k (66.82 d). At this point in time, cells primed on 2D regressed indicated by a negative doubling time. Notably, interesting phenomena have been observed qualitatively by inspection such as D2.ORs primed on Fn EECMs that colonized the lower body (likely bone metastases) in at least one case are regressing over the first 50 d (mouse #1 in Fn group), which does not appear to be the case in Fn-HA 15k or Fn-HA 2000k. Though it is too early to draw conclusions, as this assay is expected to take up to 100+ d, because D2.ORs are less aggressive *in vivo* than other cell lines more commonly studied *in vivo* (i.e. MDA-MB-231). This makes them an ideal candidate for resolving differences in metastatic phenotype conferred by in vitro culture on EECMs.

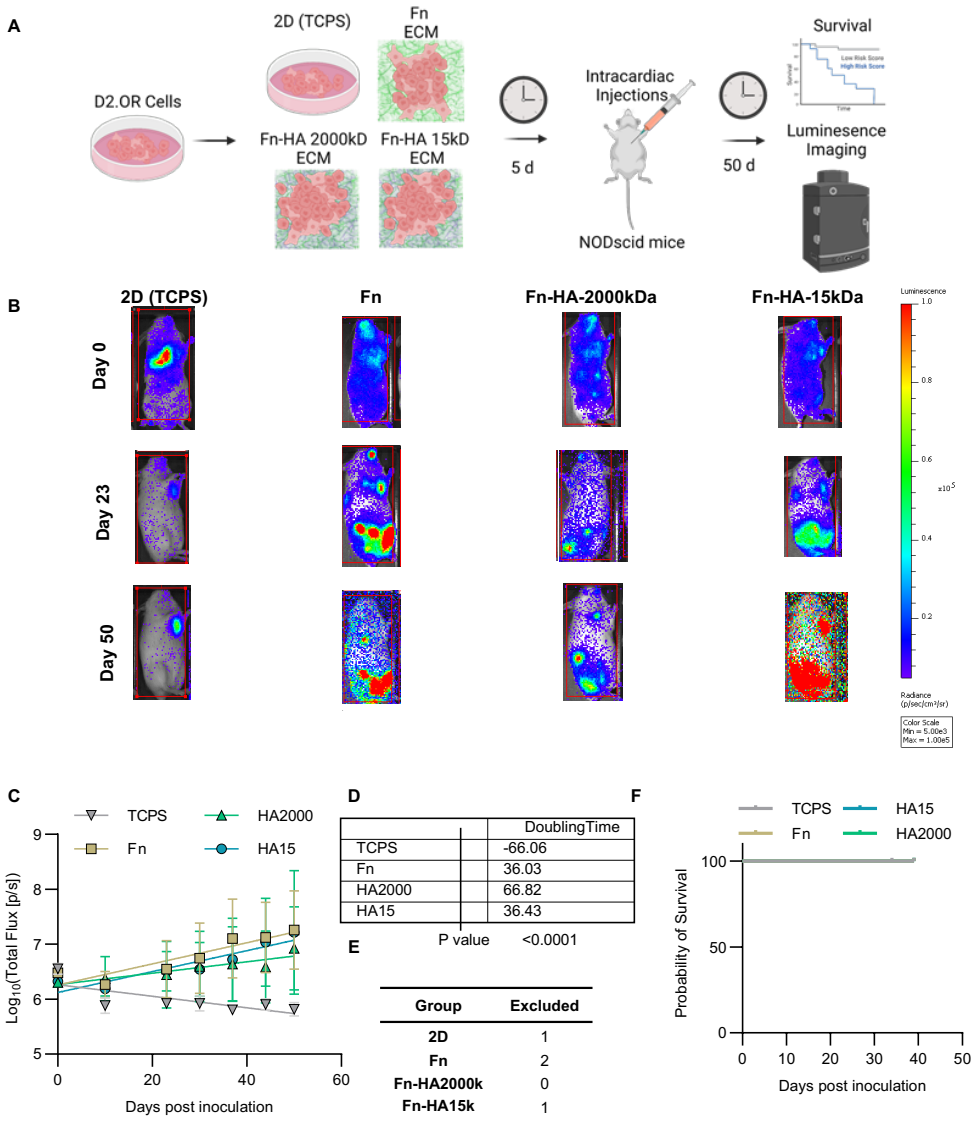

Figure 4.12
D2.OR cells grown on Fn-HA EECMs, Fn EECMs and TCPS (2D), in 2% (v/v) FBS for 5 d injected into NODscid mice to assess in vivo tumor growth and overall survival. *A: Illustration of experimental work flow B: Comprehensive imaging of all mice in the study. Some mice do not appear in later images because they excluded due to procedure-related death. C: In vivo growth dynamics over the first 50 d. D: Doubling time (d) for growth dynamics assessed via non-linear of log10 from C. E: Number of mice excluded from each group because they died due to surgical procedures. F: Survival curve where at this point in the study, no mice have died due to tumor burden.*

Collectively, Fn influenced cells to display hallmarks of stemness upregulation *in vitro* as noted by functional sphere formation assays and phenotyping. Furthermore, Fn consistently caused upregulation of dye retaining populations, which has been indicative of CSC enrichment. While the presence of high Mw (2000kDa) HA seemed to perturb these functional phenotypes, it

did not completely reverse them. Additionally, fibrillar Fn clearly impacts growth dynamics as assessed by dye retention, regrowth assays and metastatic growth *in vivo* wherein high Mw HA (2000kDa) leads to overall slower proliferating cells or cells that cannot reactivate in standard culture conditions, while low Mw 15kDa HA facilitates recovery of growth. Collectively, these data imply that fibrillar Fn induces bipotent CSCs implicated in metastasis as well as heterogeneous growth populations, while co-presentation of low Mw HA may confer additional phenotypic advantages of long-term survival implicated in metastasis/recurrence.

4.5 Conclusions and Implications

Here we report stable, fibrillar Fn/HA mimics that are representative of tumor-associated ECM produced by employing a controlled disulfide conjugation strategy by target free thiols at $FnIII_{7,15}$ with minimally modified HA. Fn fibril assembly can be induced with hydrodynamic fibrillogenesis and is apparently not reliant on domain interactions or disulfide bonds involving $FnIII_{7,15}$. We employed rigorous characterization to ensure the Mw of the commercially available HA was as reported and remained unmodified following chemical derivatization. A minimal substitution rate was chosen to statistically preserve many HA-binding subunit blocks. We demonstrate that Fn EECM assembly followed established characteristics from cell secretion models in that the dimeric protein was critical and assembly was perturbed by treatment with the 70kDa N-terminal fragment.[155] The bioconjugation methodology developed to produce Fn-HA EECM conjugates is remarkably well controlled for both high (2000kDa) and low (15kDa) HA, despite very large differences in length. This was demonstrated by confirming HA presentation in fibrillar ECM substrates reflected the original reaction mixture even after purification and fibril assembly. The physical characteristics of Fn EECMs or Fn-HA EECMs are well controlled where they are all porous, 3D, have narrow (~1 μm – 4 μm) fibril diameter distributions and are

able to cover large areas and facilitate unconstrained cell growth throughout the constructs. Furthermore, Fn-HA EECMs display binding by a Link-module probe in a Mw dependent manner reflective of literature reports where high Mw HA had substantially increased binding compared to low Mw HA.

To validate the clinical motivation, a co-culture model reflecting BM-MSC recruitment to the primary tumor demonstrated increased deposition of tissue bound HA and Fn at the transcriptional and protein level. Fn-HA EECMs were then demonstrated as biochemically and morphologically similar to the secreted ECM of tumor cell/MSC co-cultures but are produced with definable, purified components compared to the diverse mixtures that constitute cell-secreted ECMs. Tumor-mimetic EECMs were then employed to assess epigenetic regulation of tumor cells grown in Fn, High Mw HA-rich and low Mw HA-rich environments. We found significant increases in sphere formation efficiency of MC7s primed on Fn and Fn-HA15k EECMs indicating upregulation of CSCs. Additionally, the trends in sphere formation, did not correlate with CD24 status, CD44+/24-, or ALDH+ populations but instead correlated with dye retention (CTFR+), CTFR+/CD44+/24-, and ALDH+/CD44+/24- populations. Bipotent breast CSCs are thought to have greater metastatic potential and may be a more reliable marker to transcend subtype/cell line differences.[305,310] Compelling single cell lineage tracing in pancreatic cancer has revealed EMT extremes are less metastatic than EMT hybrids, which is consistent with the proposed model for breast CSCs existing on this epithelial to mesenchymal spectrum.[305,311] Additionally, MCF7 growth dynamics were modified following only 6 days of growth where Fn-HA15k and Fn EECMs showed faster regrowth than Fn-HA2000k, and CTFR+ MC7s grown on Fn-HA2000k did not grow after nearly 4 weeks of culture.

Fibrillar fibronectin also induced higher sphere formation in D2.ORs, which was not seen when the protein and protein-glycan conjugates were coated onto TCPS. For this more mesenchymal cell line, fibrillar Fn also induced a stark increase in scratch wound closure after cell populations proliferated for 3 d indicating inherited phenotypic changes. High Mw HA appeared to repress this phenotype while low Mw HA allowed for partial recovery of this invasive/migratory phenotype. Most interestingly, conformationally active, fibrillar fibronectin induced disparate growth populations comprised of some entering quiescence, moderately proliferating cells, and rapidly proliferating cells. This was not observed when this cell line was grown on 2D or even when grown in 3D spheroids. The presence of high and low Mw HA facilitated more cells entering a quiescent state, where those cells grown in the presence of low Mw HA may have a greater capacity for survival/reactivation. Thus far, up to day 50 whole-body *in vivo* growth kinetics of D2.ORs reflect the influence on growth observed *in vitro* with MCF7s whereby cells primed on Fn and Fn-HA15k are growing more rapidly than HA-2000k.

Taken together, the cell studies support the notion that fibrillar Fn induces bipotent CSC phenotypes, as well as growth phenotypes that are implicated in metastasis/recurrence. These changes conferred inherited functional differences in cells reflected by downstream assays performed days (scratch), weeks (sphere formation/regrowth) or months (intracardiac injections) following priming of tumor cells for only 5-6 days on different environments. Furthermore, unique growth characteristics observed with growth on fibrillar Fn reasonably agree with a recent report that fibrillar Fn is involved in the entrance of dormancy, but our studies were not taken out to the long culture times employed by Barney et al,[309] but instead indicate potential entrance into quiescence. Also critical to interpretation, even at a ~2:1 mass ratio (HA:Fn) high Mw HA generally suppressed bipotent phenotypes induced by Fn *in vitro*, but it was not

sufficient to completely reverse these phenotypes in all cases. Interestingly, these data imply conflicting roles of high Mw HA and fibrillar Fn and potentially cooperative roles once the glycan has been degraded away to where only low Mw fragmented HA remains, and fibrillar Fn appears to be the catalyst. At the time of writing, final conclusions cannot be drawn as this work is still partially in progress. The story will become more clear following conclusions of animal studies, as their complexity simply cannot be recapitulated *in vitro*. For instance, natural killer (NK) cells present in the mouse model chosen may play part in tumor cell regression/recurrence. Therefore, it remains to be seen whether high Mw HA continues to repress the phenotypes that appeared to be induced by fibrillar Fn. Finally, transcriptional analysis would be helpful to map out the vast signaling networks that may be influenced and add credence to the functional phenotypes observed and would support future studies into the mechanisms of the interesting phenotypes reported here.

The role of HA in tissue biology is one of incredibly disparate reports ranging anywhere from 117kDa to 6,000kDa being described as "high" where others define 100-1000kDa as lower/intermediate.[238,246,262,279] This is of course is context dependent, but there exist discrepancies of reports within the same tissue systems, which is especially misleading for those beginning research in the field, especially in the pathogenic tissue contexts. From HA's discovery in vitreous fluid in 1934, to the few studies in the 1970s implicating it in embryonic development, it was not until the 1990s and early 2000s that heavy investigation began into its role the tumor microenvironment.[238,244] Hence, the comparative baseline for modeling these pathogenic tissue systems is being amassed and can be aided by engineered technologies. While our understanding of soluble HA, particularly oligomeric fragments, in tumor progression has grown more advanced, there is likely much to learn of the role of HA in proteinaceous fibrotic

tissues. Expanded understanding of *in vitro* and *in vivo* tumor cell regulation utilizing precisely defined engineered models offer a valuable path forward toward clarifying seemingly disparate reports.

Ultimately, proteins and glycans are complex molecules whose tertiary/quaternary structure define their presentation and thereby their function. Cells do not simply bind fragmented peptide domains or glycan fragments when engaging intact tissues. Therefore, this should not be overlooked when engineering biomaterials, as it may have unintended consequences in modeling native tissue biology; defining the level of complexity needed is at the crux of employing reductionistic models. While HA hydrogels have a well-established and undeniable benefit in regenerative engineering,[312] their use as models for pathogenesis is currently limited due to a lack of tumor tissue-relevant mimicry. A distinct departure from previously reported systems, these engineered fibrillar Fn constructs decorated with HA of defined length fill this unmet need and can be used to further elucidate HA's complex role in the tumor microenvironment. The studies presented here imply that Fn and HA may have simultaneous cooperative and conflicting roles in a Mw dependent manner that are important in regulating tumor cell fate to confer survival and facilitate metastasis. With further investigation of the Fn and HA constructs reported here, there is opportunity to expand our fundamental knowledge of tumor progression and rapidly manufacture reproducible, defined 3D models. With additional findings, there is potential to employ implantable HA constructs clinically to repress invasive phenotypes, to improve drug screening by enriching metastatic phenotypes, or to improve patient cell expansion *ex vivo*.

Chapter 5 Methods

5.1 Publication Information

Parts of the work presented in this chapter are published as:

S. Jordahl, L. Solorio, Dylan B. Neale, Sean McDermott, Jacob H. Jordahl, Alexandra Fox, Christopher Dunlay, Annie Xiao, Martha Brown, Max Wicha, Gary D. Luker, and Joerg Lahann. "Engineered Fibrillar Fibronectin Networks as Three-Dimensional Tissue Scaffolds." *Advanced Materials*. 31(46). 2019. DOI: 10.1002/adma.201904580 [147]

And

Dylan B. Neale, Ayşe J. Muñiz, Michael S. Jones, Do Hoon Kim, Johanna M. Buschhaus, Brock A. Humphries, William Y. Wang, Brendon M. Baker, Jeffery E. Raymond, Luis Solorio, Gary D. Luker, Joerg Lahann "Aligned Networks of Engineered Fibrillar Fibronectin Guide Cellular Orientation and Motility." *Small Structures.* 2(6). 2021. DOI: 10.1002/sstr.202000137 [149]

Other parts of work presented in this chapter are in preparation for publication in the following form: Dylan B. Neale, Mirella Wawryszyn, Grace Bushnell, Johanna Buschhaus, Malini Mukherji, Do Hoon Kim, Sebastian Spann, Carlo Botha, Ayse Muniz, Adrian Shimpi, Claudia Fischbach, Jeffery E. Raymond, Burkhard Luy, Manfred Wilhelm, Gary D. Luker, Max Wicha, Joerg Lahann. "Hyaluronic acid decorated fibrillar fibronectin constructs modulate metastatic potential in breast tumor cells." *In preparation*

5.2 Deoxycholate Treatment

Fn EECMs that were subjected to deoxycholate treatment were submerged in 1% deoxycholate solution overnight on an orbital shaker. Fn EECMs that were left untreated for comparison to deoxycholate exposure were also rotated overnight in water on the orbital shaker. These Fn EECMs were prepared using fluorescent Fn that was first conjugated to DyLight-650 (antibody labeling kit following manufacturer instructions, Thermofisher Scientific).

5.3 Proteomics

Lyophilized fibronectin (Corning) was dissolved in DPBS as described above. The protein concentration was determined by Qubit fluorometry (Invitrogen). 10µg of the sample was processed by SDS-PAGE using a 10% Bis-Tris NuPage mini-gel with the MOPS buffer system. The mobility region was excised and processed by in-gel digestion using a robot (ProGest, DigiLab) using the following procedure: washed with 25mM ammonium bicarbonate followed by acetonitrile, reduced with 10mM dithiothreitol at 60°C followed by alkylation with 50mM iodoacetamide at RT, digested with sequencing grade trypsin (Promega) at 37°C for 4h, and quenched with formic acid. Then the supernatant was analyzed directly without further processing. Half of the gel digest was analyzed by nano LC-MS/MS with a Waters NanoAcquity HPLC system interfaced to a ThermoFisher Q Exactive. Peptides were loaded on a trapping column and eluted over a 75µm analytical column at 350nL/min; both columns were packed with Luna C18 resin (Phenomenex). The mass spectrometer was operated in data-dependent mode, with the Orbitrap operating at 70,000 FWHM and 17,500 FWHM for MS and MS/MS respectively. The fifteen most abundant ions were selected for MS/MS. Data were searched using a local copy of Mascot (Matrix Science) with the following parameters: Enzyme: Trypsin/P; Database: SwissProt Human (concatenated forward and reverse plus common contaminants); Fixed modification:

Carbamidomethyl (C); Variable modifications: none; mass values: monoisotopic; peptide mass tolerance: 10 ppm; fragment mass tolerance: 0.02 Da; maximum. missed cleavages: 2. Mascot dat-files were parsed into Scaffold (Proteome Software) for validation, filtering and to create a non-redundant protein list. Data were filtered using 1% protein and peptide FDR and requiring at least two unique peptides per protein.

5.4 Materials and SU-8 Fabrication

Polymer scaffolds were made of SU-8 2050 (Kayaku Advanced Materials) using a photolithography lift-off procedure described in Appendix A[55,313]. Briefly, three layers of OmniCoat (Kayaku Advanced Materials) were spun onto 4-inch silicon wafers and transferred to a hot plate at 200°C for 1 min after each coating. SU-8 2050 was spun to the desired thickness, allowed to degas overnight, before UV curing per the manufacturer's recommendations. Following lift-off in SU-8 developer (Kayaku Advanced Materials), scaffolds were extensively rinsed (7-10 times) with fresh isopropyl alcohol and allowed to dry for at least 1 week before use in cell culture. SU-8 scaffolds were then attached to custom stainless-steel frames before the applying the protein coating.

5.5 Protein Coating

Polymer scaffolds were coated with human fibronectin (Corning) that was diluted to a concentration of 111 μg mL^{-1} in calcium/magnesium free Dulbecco's phosphate buffered saline (DPBS) for 2 h, as described previously.[147] Briefly, TPSs were suspended with the center of the scaffold at the solution/air interface, and with the steel-frame/scaffold construct centered on the long-axis of a low-binding microcentrifuge tube (Biotix). The TPSs were then gently sheared in

an Eberbach EL655.I Incubator tumbler (Eberbach Corp., Belleville, MI, USA) at 8 rotations per minute (RPM) and 30°C.

For assembly blocking experiments, 70kDa Fn fragment was added to native dimeric Fn (0.176 mg/mL 70kDa fragment/0.106 mg/mL in 0.9mL with DPBS as a solvent) before assessing the formation of fibrillar EECMs via hydrodynamic fibrillogenesis. Brightfield images were gathered to assess fibril network formation.

5.6 Fluid Flow Modeling

COMSOL 5.3a was used in order to simulate fluid flow during the fibronectin coating process. Solidworks 2018 SP 4.0 was used to create a dimensionally accurate CAD model of the SU-8 scaffolds mounted on a frame with a cuboidal inlet/outlet (with a cross-sectional area matching that of the centrifuge tube) underneath the scaffold (illustrated in published manuscript SI). The polymer scaffold was drawn dimensionally accurate: the struts were 35 μm wide with gap lengths of 245 μm, 500 μm, and 950 μm. The 3D model was approximated as steady state, laminar flow. The SU-8 polymer was modeled as nylon and the dilute fibronectin solution as water from COMSOL's material library. The scaffold material was treated as a no-slip boundary, and the air-liquid interface was treated as a slip-boundary. A separate, 2D, time-dependent COMSOL model consisting of an air and liquid phase in a tube (geometrically similar to the microcentrifuge tube used for the hydrodynamically-induced coating), at an angular velocity of 8 RPM was used and to elucidate the velocity at the inlet of the 3D model (see published manuscript SI and Figure 3.2). Based on this 2D model, an inlet velocity of 0.15 m s^{-1} was used in the 3D model. COMSOL's streamlines and velocity slice analysis functions were used to create the plots of flow behaviors around the scaffolds shown throughout Chapter 3.

5.7 Cell Culture

NIH-3T3s were cultured in high-glucose Dulbecco's Modified Eagle Medium (DMEM) with 10% (v/v) fetal bovine serum (FBS). D2.OR and MCF7s (Chapter 4) were grown in DMEM with 2% (v/v) FBS on EECMs / 2D (Chapter 4). For regrowth assays (Chapter 4), cells were grown in DMEM with 10% FBS (v/v). All cells were tested and confirmed negative for mycoplasma using a Lonza MycoAlert™ kit (Lonza) in accordance with the manufacturer recommendations.

5.8 Cell Elongation Imaging

100,000 unlabeled NIH-3T3 fibroblasts were seeded on the aligned versus non-aligned Fn matrices in a 100 μL droplet for 1h at 37°C in an ultra-low adhesion 24-well plate (Corning Inc, Corning, NY, USA). They were then topped off with 1 mL of fresh culture medium and allowed to spread for 24 h. They were then fixed overnight at room temperature in 4% paraformaldehyde, then washed three times with DPBS and prepared for staining. Cytoskeleton aspect ratio values represent the cell length divided by cell width. Nuclear aspect ratio values were generated using ImageJ to fit an ellipse (long axis divided by the short axis). EECMs (aligned vs non-aligned) were produced in triplicate. 7 ROIs within each EECM was assessed for a total of 42 multi-channel images.

5.9 Cell proliferation assay

100,000 NIH-3T3s were seeded in 1mL of complete media on EECMs. A resazurin-based assay, Tox8 (Sigma-Aldrich, St. Louis, MO, USA), was employed to assess metabolic activity. Cells were incubated with 10% (v/v) Tox8 reagent in complete media for 1h. The supernatant was removed, spun at 800 xg for 5 min to pellet any potential detached cells, and the

fluorescent intensity was measured (excitation 560 nm, emission 590 nm) using a Molecular Devices SpectraMax M5e plate reader (Molecular Devices). Measurements were normalized to the initial timepoint at 13.5 h. To estimate the cell number on the scaffolds, a serial dilution of a known number of cells were seeded onto 24-well plates, allowed to attach for 5 h, then treated with the same Tox8 protocol. A linear regression was fit to the data ($R^2 = 0.9938$) in order to correlate the fluorescence intensity values to cell number using Graphpad Prism (v 8.4.3).

5.10 Fluorescence staining and visualization

In order to visualize the fibronectin for directionality analysis, unmodified Fn was blended with Dylight-650 or Dylight488 conjugated Fn. The dye used was an NHS-ester prepared in accordance with manufacturer recommendations (ThermoFisher Scientific). In the cell spreading assay, nuclei were stained with Hoechst 33342 (ThermoFisher Scientific), and actin with Alexa Fluor™ 488 phalloidin (ThermoFisher Scientific). Stains used for EECMs were one of the following: anti-Fn pAb (Sigma-Aldrich, F3648), anti-EDA-Fn mAb (Abcam, ab6328), biotinylated-hyaluronic acid binding protein (b-HABP, Millipore, 385911).

5.11 Live Cell Migration Assay

NIH-3T3 were engineered with a H2B-RFP reporter to visualize the nuclei for live cell tracking. Images were taken using an Olympus-IX83 with a humidified live cell incubator, at a temperature of 37°C with 5% CO_2. Cells were seeded at 50,000 in 1 mL of complete media and allowed to attach for 1 h before acclimating to microscope incubator for 1 h and imaged for 20 h. Image sets were processed using Imaris (Bitplane) to render cell position over time by tracking cell nuclei. Each trace set was manually inspected to ensure the traces were accurately representing cell motility. Hence, given the imaging modality, the cell migration patterns are 2D

projections of migration within the 3D EECMs. Data was then fit to the APRW model where persistence (P) and speed (S) along the primary (p) and non-primary (np) directions was calculated on a single-cell basis.

5.12 Directionality Analysis

The directionality of both Fn fibrils across the tissue length scale and actin staining at the cellular length scale were analyzed using the Directionality plugin in Fiji (ImageJ) with the Fourier components method on CLSM MIPs. The "amount" represents the relative fraction of intensity in a given angle bin normalized by all the power spectrum intensity. Notably, with this methodology, intensity associated with the off-axis events include the width of well aligned features and should not be taken as a pure count of unaligned fiber (i.e. intensity is feature intensity-based, not count-based). When assessing Fn fibrils at the tissue length scale, 9-10 Regions of interest (ROIs) with an average size of ~1,300,000 μm^2 were chosen within SU-8 gap length across the length of the scaffold and accrued over 3 replicates. Using OriginPro (v. 2019, OriginLab Corp.), a Gaussian distribution was fit to the histograms and the full width at half max (FWHM) values were reported as an indication of how wide or narrow the distributions were. Additionally, an alignment parameter (AP) was defined as being the area under the Gaussian curve, normalized by the area under the y-offset. See Chapter 3.4.5 for further details and Figure 3.14 for a graphical representation.

5.13 Statistics

Three or more replicates were used to generate the data throughout the dissertation unless otherwise noted. For statistical analyses either custom Python script or Graphpad Prism were used. The Shapiro-Wilks Test or others were used to determine whether the data follow a normal

distribution. Equal variance was assessed using Levene's test or others. When comparing three or more groups, if the data are not normal or do not have equal variance between groups, then the Kruskal-Wallis H-test followed by post-hoc analysis was performed to assess levels of statistical significance among the groups. For comparing two groups, the Mann-Whitney U Test was performed if the data were non-parametric and a T-test if data were parametric or the Holm-Sidak Multiple t-test.

5.14 Decellularization

Cells were removed from HS5/MC7 co-cultures according to Lu et al.[314] Samples were washed with phosphate buffered saline (PBS), then deionized (DI) water, and immersed in a solution of 0.1% Triton X 100 with 1.5 m KCl in 50 x 10^{-3} m Tris buffer on a slow moving shaker for 4-6 hours at on ice. Samples were washed in 10 x 10^{-3} m Tris buffer, followed by DI water for one hour each. Samples were not fixed then co-stained with anti-EDA-Fn and b-HABP.

5.15 HA Synthesis Materials

HA, with the molecular weights of 8-15 kDa and 1750-2000 kDa were purchased from Contipro. Dowex ® 50W-X8, 4-Methylmorpholin (NMM) and 2-chloro-4,6-dimethoxy-1,3,5-triazine (CDMT) were purchased from VWR. (S)-2-Pyridylthio cysteamine hydrochloride from abcr and the Cy-5 Amine (CAS 1807529-70-9) from Abcam.

5.16 HA Synthesis and Purification

The reaction procedure was adapted from Bergmann et al.[267] and modified for our purposes. The carboxylic acid moiety was derivatized as it follows: Hyaluronic acid sodium salt was dissolved in MilliQ water (5 mg/mL, pH 6.85) and mixed with Dowex H+. The mixture was stirred firmly at room temperature for 1 h, then filtered by tangential flow filtration, the solution

(pH 2.85) was freeze-dried to obtain hyaluronic acid protonated form. Hyaluronic acid (0.158 g, 0.415 mmol, 1.00 equiv.) was dissolved in 150 mL of MilliQ water in a round-bottomed flask followed by the dropwise addition of 50 mL of acetonitrile while stirring. To the solution was added 0.01470 g (0.0159 mL, 0.145 mmol, 0.350 equiv) 4-methylmorpholine (NMM). The solution was then cooled down to 4 °C, and 0.0137 g (0.0785 mmol, 0.189 equiv) of 2-chloro-4,6-dimethoxy-1,3,5-triazine, was added and stirred at room temperature for 1 h. Subsequently, the solution was mixed with the respective amines. In order to obtain HA-2PT-Cy5, 0.0137 g (0.0619 mmol, 0.149 equiv) of (S)-2-Pyridylthio cysteamine hydrochloride (2PT) and were added and 0.0109 g (0.0166 mmol, 0.0400 equiv.) Cy-5 amine were stirred for 20 h at room temperature. To only obtain non-labeled HA-2PT (i.e. “modified HA,” “R-HA”), the same reaction procedure was executed despite leaving out the Cy-5 amine. Finally, Dowex saturated sodium form was added to the reaction mixture, stirred for 30 mins and then filtered through tangential flow filtration (TFF) purification from Repligen, with 3 kDa cutoff hollow fiber mPES MidiKros® filter modules for the purification of 8-15 kDa modified HA and 300 kDa cutoffs for the 1750-2000 kDa HA. After was freeze-drying and lyophilization HA-2PT and HA-2PT-Cy5 were obtained (yields).

5.17 HA-Fn Bioconjugation

Dimeric, plasma derived Fn (Corning or Sigma) was dialyzed into 0.05M borate (pH 8.5) at a starting concentration of 2.5mg/mL, typically resulting in ~2mg/mL Fn in borate. 2PT-modified-HA was dissolved at 10mg/mL in 0.05M borate buffer. Borate buffer and 8 M Gdn was added such that the resultant mixture was 4 M Gdn, ~1.4 mg/mL 2PT-HA and ~ 0.7mg/mL Fn for a conjugation reaction. In series for the conjugation reaction: Fn (in borate) was diluted with additional borate buffer, then Gdn was added for 10min, followed by 2PT-HA. Argon gas was

then sprayed in the top of the microcentrifuge tube (reaction vessel) through a sterile filter, and the reactions were gently rocked at 30 C for 18 h. Reaction mixtures were then isolated with a syringe and dialyzed with Slide-a-lyzer (Thermoscientific) cassettes with cutoffs lower than each molecular weight (10k for 2000kDa, and 3.5k for 15kDa). Fn concentration in the resultant mixture using A280 measurements and using a calibration curve accumulated over time across multiple lots of product.

Chapter 6 Summary and Future Directions

6.1 Publication Information

Parts of work presented in the chapter is published as:

Anke Steier,* Ayşe J. Muñiz,* Dylan Neale,* Joerg Lahann. "Emerging Trends in Information-Driven Engineering of Complex Biological Systems." *Advanced Materials.* 31(26). 2019. DOI: 10.1002/adma.201806898.[1] * = authors share equal contribution.

And

Ariel A Szklanny, Dylan B Neale, Joerg Lahann, Shulamit Levenberg. "Stepwise Cell Seeding on Tessellated Scaffolds to Study Sprouting Blood Vessels." *Journal of Visualized Experiments*. (167). 2021. DOI:10.3791/61995 [313]

6.2 Summary and Lessons Learned

3D tissue engineered systems have made undeniable contributions to fundamental biology, regenerative engineering, and investigative toxicology. Consequently, there are numerous organoid, lab-on-a-chip, and 3D bioprinting companies charging forward with a vast network of academic researchers fortifying the foundation. Yet, in spite of frequent reports in the field, many systems are too labor intensive, unreliable, or costly to ever realize practical translation despite the sensation surrounding them. With this pragmatic mindset, engineered protein substrates resonated with me as having great potential when I first started my Ph.D. In complete duality, I identified subtleties often overlooked in biomaterials research. Having

bestowed upon myself two macromolecules (fibronectin and hyaluronan) with long and winding histories, complex roles in biology, and expansive reaches into many healthy and diseased tissue systems, I took a step backward and focused my efforts. I targeted cell-ECM-interactions in native-like environments through engineered fibronectin with a focus on the tumor microenvironment but broad applicability to various regenerative engineering applications. The work presented here makes strides toward unpacking native-ECM environments and points toward solutions that might inform their control for future bio-manufacturing processes.

Furthermore, it advances the foundation of Fn-based biomaterials and demonstrates their general value. Specifically, I have worked to validate methods that our hydrodynamic method, which is similar to fiber drawing (Vogel and colleagues) or droplet coatings (Spatz and colleagues), displays key functional characteristics of native, cell-assembled fibronectin but on a grander scale with the potential to achieve industrial processes. My studies aligned these engineered matrices with native tissues from a mechanical, assembly modality, and a biochemical perspective.

I then put forward attainable approaches to control fibrillar architecture utilizing native fibronectin, which is generally an elusive biomaterial to work with. I demonstrated aligned fibronectin structures had profound impacts on cell orientation and migration patterns. This not only highlighted fibronectin as a critically important protein to study in 3D environments, as opposed to the 2D adsorption models generally used, but delivers a practical model for researchers to utilize moving forward. Exciting work from our lab has shown great promise building upon these studies to apply similar substrates in cardiac tissue engineering, where ECM alignment is crucial to tissue function.

Finally, I leveraged the foundation built by my previous studies with this material system and incorporated hyaluronan into engineered 3D fibrillar fibronectin constructs. After learning the hard way that some commercially available hyaluronan was not even within the order of magnitude as advertised, I took a deeper dive into my bioconjugation processes. This led to a robust bioengineered substrate exemplified by a high degree of control over fibronectin and hyaluronan co-presentation. These two components are repeatedly implicated in breast cancer tumorigenesis, yet, to the best of my knowledge, have not been explored together from an extracellular perspective. Utilizing this new model, my preliminary studies indicate a complex, molecular weight dependent role of hyaluronan that is initiated by conformationally active fibronectin. In the next section, I overview a few of my many pursuits over the years that I find promising for the next generation.

6.3 Future Directions for EECMs

6.3.1 High Throughput Technological Bridge Systems Using Photolithography

Throughout many of the studies in my dissertation research, photolithography was employed to create precisely defined 3D polymeric scaffolds. These were then utilized as a high-throughput co-culture system to study the formation of organized and repeatable vessel networks in a 3D environment by our collaborators (Levenberg Lab).[315] Szklanny et al, developed a two-step seeding protocol showing that vessels within the system react to the scaffold topography, presenting distinctive sprouting behaviors depending on the compartment geometry in which the vessels were templated.

The creation of functional vasculature *in vitro* is a grand challenge in tissue engineering, which only recently (after the publication of this methods paper) has seen significant advancement.[29] Previously, a great amount of work has been carried out to study vascular

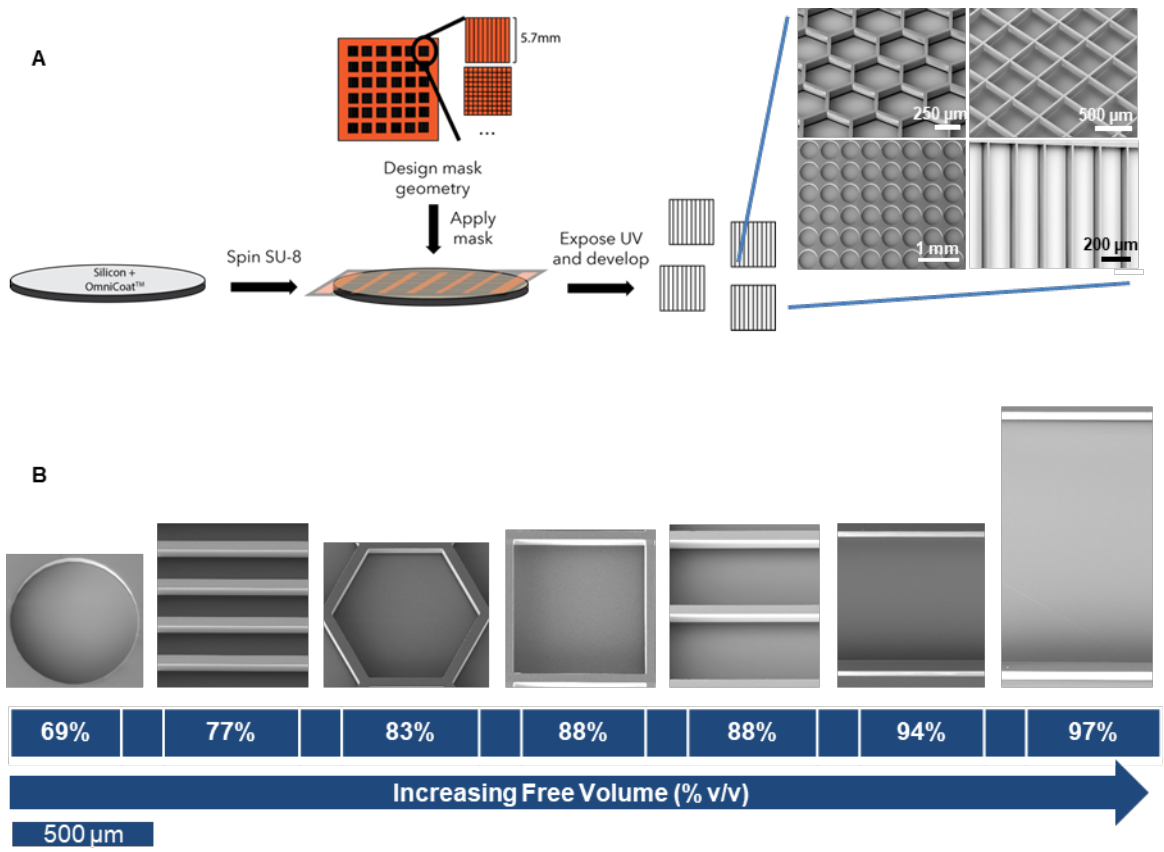

Figure 6.1
A: SU-8 scaffold manufacturing process. B: SU-8 pore geometries and free volume %

development, including co-culturing the cells on hydrogels[316], hydrogels-scaffold combinations[11,12], 2D platforms, and microfluidic devices[319]. Hydrogels lack mechanical integrity and are readily distorted by cell-mediated forces[320], while 2D and microfluidic platforms are often not reflective of native tissue environments that are a requisite to translational findings[15,16]. Understanding how newly sprouting vessels react to their surrounding environment can provide critical insight that might allow for the fabrication of engineered environments with the capability of guiding the vessel development in a predictable manner.

Hence, understanding vascular formation phenomena is especially critical to keep pace with the rapid emergence of submicron-to-micron scale fabrication techniques, such as stereolithography, digital projection lithography, continuous liquid interface production, 3D

melt-electro jetwriting, solution based 3D electro jet writing, and emerging bioprinting techniques[1,82,323,324]. Aligning control of these micromanufacturing techniques with a deepened understanding of vascular biology is key to the creation of an appropriate engineered vasculature for a target tissue.

Figure 6.1 illustrates the process for the production of SU-8 TPSs along with various compartment geometries and their relative free volume. These SU-8 TPSs with rectangular pore geometries were utilized to explore physical fluidic interactions between TPSs and protein solutions that enabled highly aligned Fn EECMs (Chapter 3) for studying spontaneous cell motility processes.

By utilizing 3D scaffolds with tessellated compartment geometries, and a two-step seeding technique, highly organized vascular networks grew in a platform that was easy monitor with conventional fluorescence confocal microscopy. The tessellated geometries provide a high throughput system with individual units containing vessels that respond to their local environment. Hence, this approach, and the use of these photolithographed structures offers a technological bridge to rapidly prototype geometries in 3D with high precision. Information gleaned from these studies can inform the design of 3D printed structures, where throughput is critically limited compared to lithographic processes.

This high throughput, compartmentalized micro-vessel array could be used to rapidly screen drug candidates or interfaced with proteinaceous EECMs to enable complex co-cultures. This approach would give rise to novel, high throughput devices to study tumor-blood vessel interactions – a key step in tumor cell metastasis. Additionally, these findings would guide the design of more complex 3D printed systems; hence, such constructs act as a technological bridge

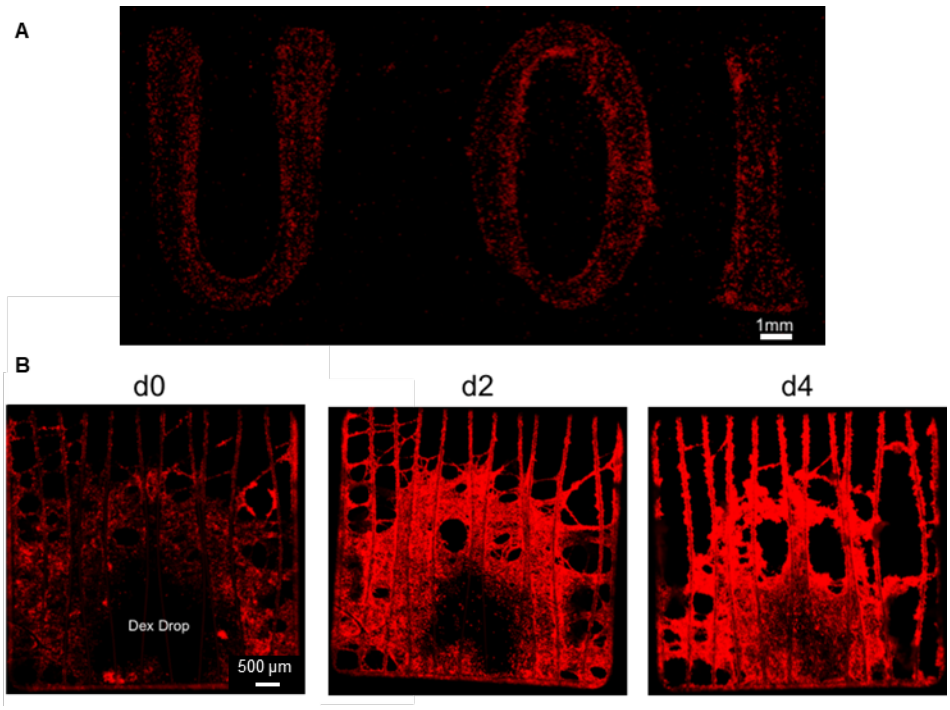

Figure 6.2
Controlled cell seeding utilizing an aqueous two-phase system of dextran and PEG. *A: Proof of concept experiment with 3D bioprinter to deposit cells in a controlled geometry. B: Confocal MIPs showing that cells can be controlled in a x-y area and z-depth on EECMs*

to inform decisions in throughput limiting micro-manufactured systems. The method for producing these TPSs is outlined in Appendix A and published, as mentioned in 6.1.[313]

6.3.2 Combining Fn Assembly Techniques with 3D printing – Spatial Selectivity of Cell Seeding on EECMs

While EECMs have been demonstrated as remarkable native-like fibrillar 3D structures, the ability to deposit cells in a controlled manner was never achieved. Controlling cell-cell interactions at defined protein structure interfaces is key to future achievement in tissue engineering with proteinaceous biomaterials. Here I leveraged an aqueous two-phase system comprised of 12.8% w/w dextran (500kDa) and 6.4% polyethylene glycol (PEG, 35kDa). At these high concentrations, these two aqueously miscible materials partially phase separate giving rise to their utility as cell-friendly patterning tools.[325] I utilized this system to perform

preliminary studies where I confirmed their utility to pattern cells on a classic 2D substrate according to the previous reports (Figure 6.2 A). I then expanded this to 3D EECMs where I created a cell-exclusion zone using a cell-free dextran phase (the denser component), followed by a cell-laden solution (mCh-MDA-MB-231s) in the PEG-phase, Figure 6.2 B. Cells were seeded overnight before EECMs were washed with culture media and imaged using CLSM over a 4 d time course. It was clear that cells were excluded before subsequently migrating into the exclusion area. Here I demonstrate that despite 3D, fibrillar morphology, this aqueous cell-patterning system has promise to be combined with defined protein structures and 3D bioprinting to study defined cell-cell/cell-ECM interfaces

6.3.3 Using Fluidic Devices to Create Micro to Multi-centimeter Constructs

The goal of this work was to utilize well established, translational processes to design devices to coat EECMs in a substrate independent fashion with greater precision and reproducibility than the inherited, manual process. If successful, this would enable high throughput assessment of cell responses by creating microscale constructs, as well as multi-centimeter EECMs that could be utilized to greatly expand the number of cells that a single EECM device can facilitate or to dramatically increase throughput of studies in a way that has hampered projects in the lab. More broadly, large scale structures would be very attractive in the rapid and reliable expansion of patient cells, where *ex vivo* culture of primary patient tumors is a monumental challenge for the development of cancer immunotherapies. Toward the motivation for micro-systems, engineered fibronectin constructs showed great promise as cardiac engineering scaffolds from differentiated iPSCs; however, their throughput and constraint to stainless steel frames limited functional readouts. Hence, well defined, micro-EECMs systems across flexible PDMS posts could enable pursuits requiring experimental scale that was

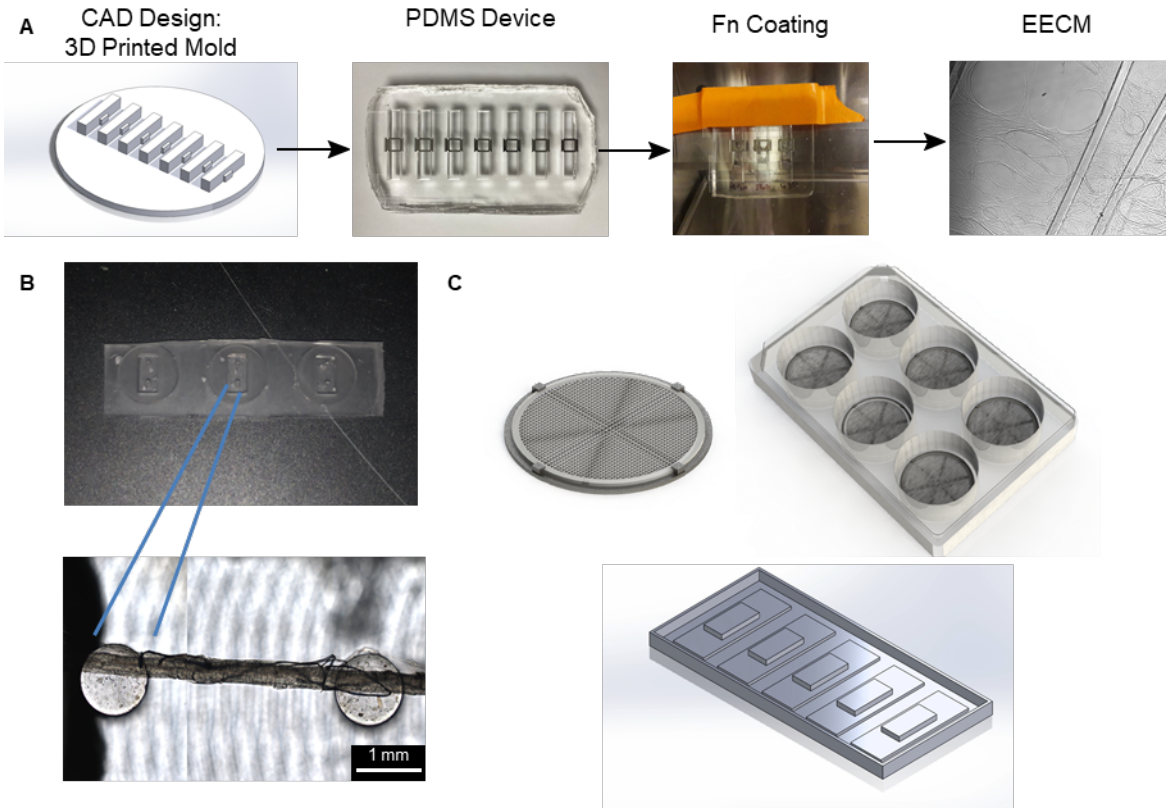

Figure 6.3
Fluidic devices to as a new approach for EECM production*. A: Overall workflow using standard 24-well format sized EECMs. B: EECM coating across micropillar. Above image illustrates 3 PDMS devices that fit into a 96-well plate. Bottom image illustrates zoomed image with EECM coating across micropillars. C: concept sketches for scale-up approach of EECMs*

previously unachievable due to practical production limitations. Preliminary experiments demonstrated that well controlled processes can be achieved by the workflow (outlined in Figure 6.3 A) utilizing 3D printed and soft-lithography as well-established processes. Additionally, micro scale EECM structures were produced across micropillars on a 96-well footprint, Figure 6.3 B. Finally, progress has been made toward achieving large scale constructs, as ex vivo patient cell expansion remains an outstanding challenge. Concepts are outlined in Figure 6.3 C and serve as the basis for a potential industry funding project to expand primary patient tumor cells *ex vivo*.

6.4 Reflection and Outlook

Fibronectin has been an exciting and challenging protein to work with as a bioengineer. While literature was exploding in the 1980s and 1990s, the topic started to simmer on various fronts. Useful domain specific antibodies that were once commercially available are now obscurities that may be lost forever in the depths of cryo-freezers. In the field of natural biomaterials, I suspect fibronectin's slip into the background was in large part due to the practical utility of other materials like collagen, alginate, fibrin being more accessible. Fortunately, researchers like Mosher, Vogel, Parker, Smith, and Spatz (and others) continued exploring Fn's utility as a biomaterial. Over the time of my Ph.D., it has been exciting to be a part of the development of fibronectin materials.

Information-assisted manufacturing of complex functional tissues with various cell types is now on the horizon. Future challenges are to implement the vast amounts of available information about cell-signaling networks, tissue biology, and bio-interfacial interactions to create defined, engineered products that are economically viable. High-throughput techniques based on experimental design and omics-guided material design and biological characterization will play an important role in building an intelligent infrastructure for imitating native tissue. Due to the emerging trend of using information-driven design and CAD-based micromanufacturing techniques, different structures and scaffold sizes can be produced with high-precision using mostly synthetic materials. However, recapitulating native protein matrix design and cell assemblies remains an outstanding challenge. Since Fn does not auto-assemble the way other bio-inks do, it will be quite interesting to see how and if it is incorporated into the current bioprinting pipeline to leverage this bio-inductive, native material. Since it assembles via

fluidic processes, it has the potential to be incorporated into microfluidic systems, which marks a unique technological path forward toward its adaption into the broader biotechnology pipeline.

Excitingly, fabrication of thick artificial tissues is now being realized. Further progress in integrating functional microscale tissue elements that recapitulate organ processes like filtration, transport with various cell types and complex structures will hinge on the combination of advancement in bio-printing/additive manufacturing, tissue biology and bio-omics. Very promising advancements in tissue engineering recently, include functional vasculature *in vitro*, cell culture-based meat alternatives, plant-based meat alternatives, various micro-physiological systems to improve clinical drug toxicity prediction, and tissue engineered models for studying immune-interactions amongst many other achievements. These are incredibly exciting times for multi-disciplinary, bioengineering teams pursuing complex problems that had eluded scientific achievement for years. The solutions are now at our fingertips and it is with great anticipation that I, in lockstep with many amazing people, will continue to these technologies forward.

Appendix A

SU-8 Scaffold Fabrication Protocol

This work is published as: Ariel A Szklanny, Dylan B Neale, Joerg Lahann, Shulamit Levenberg. "Stepwise Cell Seeding on Tessellated Scaffolds to Study Sprouting Blood Vessels." Journal of Visualized Experiments. (167). 2021. DOI:10.3791/61995 [313]

1. Tessellated scaffold fabrication

1.1. Prepare scaffolds using a photolithography technique with the selected geometry of interest.

1.1.1 Before spin coating, clean the silicon wafer. This can be done with plasma cleaning or a solvent cleaning technique. If plasma cleaning, follow the standard operating procedure of your instrument for operational details. In either case, ensure the wafer is free of defects/contamination. Spray with compressed nitrogen gas and inspect the wafer to ensure it is free of debris before spin-coating. This wafer will serve as the substrate in which the scaffolds are created.

NOTE: For best results start with a fresh wafer. Wafers can be re-used but should be cleaned and free of old photoresist, surface defects and debris. Be sure to never touch the surface of the wafer, except toward the outer edge where you do not have any design features. It is helpful to use wafer-tweezers when handling. Silicon wafers vary in size, and what size wafer used will be depend on the equipment you have access to.

1.1.2. Center a silicon wafer onto the spin-coater chuck using a guide. Briefly spin the wafer to ensure it has been properly centered on the chuck, adjust as necessary until properly centered. This must be done every time a wafer is placed on the spin-coater. Dispense 1-4mL of the lift-off reagent onto the wafer (this will depend on the size of the wafer). Approximately 2mL of lift-off reagent works well for a 4-inch wafer. Set spin-coater spread speed at 500 RPM for 5 seconds, and the spin-speed to 1000 RPM for 30 seconds, then spin the lift-off reagent. Inspect the wafer to ensure it has an even coating across the wafer. Any debris left on the wafer will be very obvious at this point. Any scaffolds in that area will likely be unable. After spin coating, transfer to a hot plate and bake for 1 minute at 200º C.

1.1.3. Repeat the previous step two more times for a total of three coatings.

1.1.4. Spin-coat the Omnicoat-coated silicon wafer with SU-8 2050 photoresist until obtaining a thickness of approximately 100 μm.

1.1.4.1. Dispense 1 mL of resist for every 25 mm of substrate diameter.

NOTE: Be careful to avoid bubbles while pouring the resist. For SU-8 2050, pouring approximately a 2-inch diameter circle, when using a 4-inch silicon wafer works well.

1.1.4.2. Spin-coat the SU-8 2050. Spread at a speed of 500 RPM for 5 seconds, followed by a spin speed between 1700 to 1800 RPM to achieve approximately 100 μm thickness.

1.1.4.3. Optional: after spinning, the spin coated wafers can be left to de-gas overnight on a level surface protected from light prior to the pre-bake. This may help to rid the resist of any bubbles and allow defects to level out.

NOTE: The actual thickness of the resist and the resultant scaffolds can vary with user error and equipment parameters. Therefore, the thickness of the scaffolds should be verified later, in 1.7. Modify spin coating procedures accordingly to achieve the desired thickness.

1.1.5. Prior to exposure, pre-bake the wafers at 65°C for 10 min then 95°C for 40-50 min. Prior to exposure, test the surface of the resist by pressing on the edge with a pair of tweezers to ensure that it is no longer tacky/viscous. It is helpful to pull the wafer off of the hot plate and allow it to cool for a 30sec-1min before assessing the tackiness.

NOTE: Slow temperature ramp times (heating and cooling) may help to prevent warping of the scaffolds.

1.2. Expose the photoresist to UV light (350-400 nm) through a photomask with an exposure energy of 215-240 mJ/cm2 for a resist thickness of 85 – 110 μm. Refer to photoresist manufacturer guidelines for recommended exposure energy-thickness correlations. Ensure your exposure is properly calibrated such that the energy is verified. Adjust your exposure time as necessary to achieve desired exposure energy. Furthermore, mask aligners may allow for different exposure modes, i.e. vacuum contact, hard contact, soft contact, and proximity contact (specific terms may vary). Generally, these will impact resolution and feature alignment. The authors typically used a “hard contact” mode; however, with the large feature sizes (>30 μm), it is unlikely to significantly impact the results. If you desire very small features or to do multiple layers, where alignment will matter, then you will need to consider exposure modes and mask aligner procedures more carefully. Be sure to consider the height of the resist when adjusting the thickness value. Refer to the standard operating procedures of your mask-aligner for operation details.

NOTE: the design of the photomask will determine the scaffolds size, compartment geometry, and number of scaffolds obtained per batch. The use of a hard glass or quartz photomask will yield the highest resolution; however, a soft polymer transparent film photomask generally can

be used for these large feature sizes (>10 μm). The use of a film-photomask may lead to topographical features along the z-axis of the scaffold pores as a result of poorer feature resolution. This could potentially have an influence on cell-behavior. Verify the desired resolution and consult with whomever is producing the photomask before deciding because this will change depending on how the photomasks are produced.

1.3. Bake the wafer immediately after UV exposure at 65ºC for 2-5 minutes and then at 95ºC for 8-10 minutes.

1.4. Develop the scaffolds to remove undeveloped resist.

1.4.1. Immerse the scaffolds using a low volume of SU-8 developer solution for 7-10 minutes to dissolve any undeveloped resist.

1.4.2. Rinse with isopropyl alcohol (IPA).

1.4.3. Dry wafer with compressed nitrogen.

NOTE: Be careful during step 1.4 to not cause premature release of the scaffolds. Low volumes of developer and gentle handling are necessary to achieve this.

1.6. Following development, hard bake the wafers at 150°C for 15 min.

NOTE: After hard bake, turning off the hotplate to allow the wafers to cool very slowly may be advantageous in preventing warping/curling of the final scaffolds.

1.7. Optional: Following the hard bake, and prior to lift-off is the most advantageous time to assess scaffold thickness since the scaffolds should still be gently adhered to the surface of the wafer. For this procedure, contact profilometry works well; however, any appropriate method could be employed.

1.8. Lift the scaffolds off the wafer.

1.8.1. Submerging the scaffolds in SU-8 developer should cause them to immediately lift off the wafer. If scaffolds do not lift off, gently push the scaffolds with a pair of wafer-tweezers.

1.8.2. Remove excess developer.

1.8.3. Transfer the scaffolds into new container and submerge in isopropyl alcohol. Rinse in IPA for a minimum of 6 times to ensure all developer has been removed.

1.9. Air dry the scaffolds for a minimum of a week before use.

References

(1) Steier, A.; Muñiz, A.; Neale, D.; Lahann, J. Emerging Trends in Information-Driven Engineering of Complex Biological Systems. *Adv. Mater.* **2019**, *31* (26), 1806898. https://doi.org/10.1002/adma.201806898.

(2) Siegel, R. L.; Miller, K. D.; Jemal, A. Cancer Statistics, 2018. *CA. Cancer J. Clin.* **2018**, *68* (1), 7–30. https://doi.org/10.3322/caac.21442.

(3) Mehlen, P.; Puisieux, A. Metastasis: A Question of Life or Death. *Nat. Rev. Cancer* **2006**, *6* (6), 449–458. https://doi.org/10.1038/nrc1886.

(4) Psaila, B.; Lyden, D. The Metastatic Niche: Adapting the Foreign Soil. *Nat. Rev. Cancer* **2009**, *9* (4), 285–293. https://doi.org/10.1038/nrc2621.

(5) Fidler, I. J. The Pathogenesis of Cancer Metastasis: The "seed and Soil" Hypothesis Revisited. *Nat. Rev. Cancer* **2003**, *3* (June), 453–458. https://doi.org/10.1038/nrc1098.

(6) Conklin, M. W.; Eickhoff, J. C.; Riching, K. M.; Pehlke, C. A.; Eliceiri, K. W.; Provenzano, P. P.; Friedl, A.; Keely, P. J. Aligned Collagen Is a Prognostic Signature for Survival in Human Breast Carcinoma. *Am. J. Pathol.* **2011**, *178* (3), 1221–1232. https://doi.org/10.1016/j.ajpath.2010.11.076.

(7) Provenzano, P. P.; Eliceiri, K. W.; Campbell, J. M.; Inman, D. R.; White, J. G.; Keely, P. J. Collagen Reorganization at the Tumor-Stromal Interface Facilitates Local Invasion. *BMC Med.* **2006**, *4* (1), 38. https://doi.org/10.1186/1741-7015-4-38.

(8) DiMasi, J. A.; Reichert, J. M.; Feldman, L.; Malins, A. Clinical Approval Success Rates for Investigational Cancer Drugs. *Clin. Pharmacol. Ther.* **2013**, *94* (3), 329–335. https://doi.org/10.1038/clpt.2013.117.

(9) Gao, H.; Korn, J. M.; Ferretti, S.; Monahan, J. E.; Wang, Y.; Singh, M.; Zhang, C.; Schnell, C.; Yang, G.; Zhang, Y.; Balbin, O. A.; Barbe, S.; Cai, H.; Casey, F.; Chatterjee, S.; Chiang, D. Y.; Chuai, S.; Cogan, S. M.; Collins, S. D.; Dammassa, E.; Ebel, N.; Embry, M.; Green, J.; Kauffmann, A.; Kowal, C.; Leary, R. J.; Lehar, J.; Liang, Y.; Loo, A.; Lorenzana, E.; Robert McDonald, E.; McLaughlin, M. E.; Merkin, J.; Meyer, R.; Naylor, T. L.; Patawaran, M.; Reddy, A.; Röelli, C.; Ruddy, D. A.; Salangsang, F.; Santacroce, F.; Singh, A. P.; Tang, Y.; Tinetto, W.; Tobler, S.; Velazquez, R.; Venkatesan, K.; Von Arx, F.; Wang, H. Q.; Wang, Z.; Wiesmann, M.; Wyss, D.; Xu, F.; Bitter, H.; Atadja, P.; Lees, E.; Hofmann, F.; Li, E.; Keen, N.; Cozens, R.; Jensen, M. R.; Pryer, N. K.; Williams, J. A.; Sellers, W. R. High-Throughput Screening Using Patient-Derived Tumor Xenografts to Predict Clinical Trial Drug Response. *Nat. Med.* **2015**, *21* (11), 1318–1325. https://doi.org/10.1038/nm.3954.

(10) Wilding, J. L.; Bodmer, W. F. Cancer Cell Lines for Drug Discovery and Development. *Cancer Res.* **2014**, *74* (9), 2377–2384. https://doi.org/10.1158/0008-5472.CAN-13-2971.

(11) Rivenbark, A. G.; O'Connor, S. M.; Coleman, W. B. Molecular and Cellular Heterogeneity in Breast Cancer. *Am. J. Pathol.* **2013**, *183* (4), 1113–1124. https://doi.org/10.1016/j.ajpath.2013.08.002.

(12) Chin, L.; Andersen, J. N.; Futreal, P. A. Cancer Genomics: From Discovery Science to Personalized Medicine. *Nat. Med.* **2011**, *17* (3), 297–303. https://doi.org/10.1038/nm.2323.
(13) Tsimberidou, A.-M.; Iskander, N. G.; Hong, D. S.; Wheler, J. J.; Falchook, G. S.; Fu, S.; Piha-Paul, S.; Naing, A.; Janku, F.; Luthra, R.; Ye, Y.; Wen, S.; Berry, D.; Kurzrock, R. Personalized Medicine in a Phase I Clinical Trials Program: The MD Anderson Cancer Center Initiative. *Clin. Cancer Res.* **2012**, *18* (22), 6373–6383. https://doi.org/10.1158/1078-0432.CCR-12-1627.
(14) Correia, A. L.; Bissell, M. J. The Tumor Microenvironment Is a Dominant Force in Multidrug Resistance. *Drug Resist. Updat.* **2012**, *15* (1–2), 39–49. https://doi.org/10.1016/j.drup.2012.01.006.
(15) Miller, B. E.; Miller, F. R.; Heppner, G. H. Factors Affecting Growth and Drug Sensitivity of Mouse Mammary Tumor Lines in Collagen Gel Cultures. *Cancer Res.* **1985**, *45* (September), 4200–4205.
(16) Weigelt, B.; Lo, A. T.; Park, C. C.; Gray, J. W.; Bissell, M. J. HER2 Signaling Pathway Activation and Response of Breast Cancer Cells to HER2-Targeting Agents Is Dependent Strongly on the 3D Microenvironment. *Breast Cancer Res. Treat.* **2010**, *122* (1), 35–43. https://doi.org/10.1007/s10549-009-0502-2.
(17) Lee, Eva, Parry Gordon, B. M. Modulation of Secreted Proteins of Mouse Mammary Epithelial Cells by the Collagenous Substrata. *J. Cell Biol.* **1984**, *98* (1), 146–155. https://doi.org/10.1083/jcb.98.1.146.
(18) Lee, E. Y.; Lee, W. H.; Kaetzel, C. S.; Parry, G.; Bissell, M. J. Interaction of Mouse Mammary Epithelial Cells with Collagen Substrata: Regulation of Casein Gene Expression and Secretion. *Proc. Natl. Acad. Sci.* **1985**, *82* (5), 1419–1423. https://doi.org/10.1073/pnas.82.5.1419.
(19) Weaver, V. M.; Petersen, O. W.; Wang, F.; Larabell, C. A.; Briand, P.; Damsky, C.; Bissell, M. J. Reversion of the Malignant Phenotype of Human Breast Cells in Three-Dimensional Culture and In Vivo by Integrin Blocking Antibodies. *J. Cell Biol.* **1997**, *137* (1), 231–245.
(20) Bissell, M. J.; Hines, W. C. Why Don't We Get More Cancer? A Proposed Role of the Microenvironment in Restraining Cancer Progression. *Nat. Med.* **2011**, *17* (3), 320–329. https://doi.org/10.1038/nm.2328.
(21) Weaver, V. M.; Howlett, A. R.; Langton-Webster, B.; Petersen, O. W.; Bissell, M. J. The Development of a Functionally Relevant Cell Culture Model of Progressive Human Breast Cancer. *Semin. Cancer Biol.* **1995**, *6* (3), 175–184. https://doi.org/10.1006/SCBI.1995.0021.
(22) Rizki, A.; Weaver, V. M.; Lee, S.-Y.; Rozenberg, G. I.; Chin, K.; Myers, C. A.; Bascom, J. L.; Mott, J. D.; Semeiks, J. R.; Grate, L. R.; Mian, I. S.; Borowsky, A. D.; Jensen, R. A.; Idowu, M. O.; Chen, F.; Chen, D. J.; Petersen, O. W.; Gray, J. W.; Bissell, M. J. A Human Breast Cell Model of Preinvasive to Invasive Transition. *Cancer Res.* **2008**, *68* (5), 1378–1387. https://doi.org/10.1158/0008-5472.CAN-07-2225.
(23) Choi, S.; Lin, D.; Gout, P. W.; Collins, C. C.; Xu, Y.; Wang, Y. Lessons from Patient-Derived Xenografts for Better in Vitro Modeling of Human Cancer. *Adv. Drug Deliv. Rev.* **2014**, *79–80*, 222–237. https://doi.org/10.1016/j.addr.2014.09.009.
(24) Morton, C. L.; Houghton, P. J. Establishment of Human Tumor Xenografts in Immunodeficient Mice. *Nat. Protoc.* **2007**, *2* (2), 247–250.

https://doi.org/10.1038/nprot.2007.25.
(25) Hutmacher, D. W. Biomaterials Offer Cancer Research the Third Dimension. *Nat. Mater.* **2010**, *9* (2), 90–93. https://doi.org/10.1038/nmat2619.
(26) Dehne, E.-M.; Winter, A.; Marx, U. Microphysiological Systems in the Evaluation of Hematotoxicities during Drug Development. *Curr. Opin. Toxicol.* **2019**, *17*, 18–22. https://doi.org/10.1016/j.cotox.2019.09.008.
(27) Peterson, N. C.; Mahalingaiah, P. K.; Fullerton, A.; Di Piazza, M. Application of Microphysiological Systems in Biopharmaceutical Research and Development. *Lab Chip* **2020**, *20* (4), 697–708. https://doi.org/10.1039/C9LC00962K.
(28) Cook, D.; Brown, D.; Alexander, R.; March, R.; Morgan, P.; Satterthwaite, G.; Pangalos, M. N. Lessons Learned from the Fate of AstraZeneca's Drug Pipeline: A Five-Dimensional Framework. *Nat. Rev. Drug Discov.* **2014**, *13* (6), 419–431. https://doi.org/10.1038/nrd4309.
(29) Szklanny, A. A.; Machour, M.; Redenski, I.; Chochola, V.; Goldfracht, I.; Kaplan, B.; Epshtein, M.; Simaan Yameen, H.; Merdler, U.; Feinberg, A.; Seliktar, D.; Korin, N.; Jaroš, J.; Levenberg, S. 3D Bioprinting of Engineered Tissue Flaps with Hierarchical Vessel Networks (VesselNet) for Direct Host-To-Implant Perfusion. *Adv. Mater.* **2021**, *33* (42), 2102661. https://doi.org/10.1002/adma.202102661.
(30) Kirouac, D. C.; Zandstra, P. W. The Systematic Production of Cells for Cell Therapies. *Cell Stem Cell* **2008**, *3* (4), 369–381. https://doi.org/10.1016/j.stem.2008.09.001.
(31) Almela, T.; Brook, I. M.; Moharamzadeh, K. The Significance of Cell-Related Challenges in the Clinical Application of Tissue Engineering. *J. Biomed. Mater. Res. Part A* **2016**, *104* (12), 3157–3163. https://doi.org/10.1002/jbm.a.35856.
(32) Serra, M.; Brito, C.; Correia, C.; Alves, P. M. Process Engineering of Human Pluripotent Stem Cells for Clinical Application. *Trends Biotechnol.* **2012**, *30* (6), 350–359. https://doi.org/10.1016/j.tibtech.2012.03.003.
(33) Badylak, S. F. The Extracellular Matrix as a Scaffold for Tissue Reconstruction. *Semin. Cell Dev. Biol.* **2002**, *13* (5), 377–383. https://doi.org/10.1016/S1084952102000940.
(34) Frantz, C.; Stewart, K.; Sci, V. W.-J. C.; 2010, undefined. The Extracellular Matrix at a Glance. *jcs.biologists.org*.
(35) Rouslahti, E.; Pierschbacher, M. D. New Perspectives in Cell Adhesion:RGD and Integrins. *Science (80-.).* **1987**, *238*, 491–497. https://doi.org/10.1126/science.2821619.
(36) Kielty, C. M.; Sherratt, M. J.; Shuttleworth, C. A. Elastic Fibres. *J. Cell Sci.* **2002**, *115* (Pt 14), 2817–2828. https://doi.org/10.1111/j.1468-2494.2010.00574.x.
(37) Rowe, S. L.; Stegemann, J. P. Interpenetrating Collagen-Fibrin Composite Matrices with Varying Protein Contents and Ratios. *Biomacromolecules* **2006**, *7* (11), 2942–2948. https://doi.org/10.1021/bm0602233.
(38) Ricard-Blum, S.; Ruggiero, F. The Collagen Superfamily: From the Extracellular Matrix to the Cell Membrane. *Pathologie Biologie*. 2005, pp 430–442. https://doi.org/10.1016/j.patbio.2004.12.024.
(39) Lu, P.; Weaver, V. M.; Werb, Z. The Extracellular Matrix: A Dynamic Niche in Cancer Progression. *J. Cell Biol.* **2012**, *196* (4), 395–406. https://doi.org/10.1083/jcb.201102147.
(40) Oskarsson, T. Extracellular Matrix Components in Breast Cancer Progression and Metastasis. *The Breast* **2013**, *22*, S66–S72. https://doi.org/10.1016/j.breast.2013.07.012.
(41) Rijal, G.; Li, W. Native-Mimicking in Vitro Microenvironment: An Elusive and Seductive Future for Tumor Modeling and Tissue Engineering. *J. Biol. Eng.* **2018**, *12* (1), 20.

https://doi.org/10.1186/s13036-018-0114-7.
(42) Petreaca, M.; Martins-Green, M. Cell–Extracellular Matrix Interactions in Repair and Regeneration. *Princ. Regen. Med.* **2019**, 15–35. https://doi.org/10.1016/B978-0-12-809880-6.00002-3.
(43) Balkwill, F. R.; Capasso, M.; Hagemann, T. The Tumor Microenvironment at a Glance. *J. Cell Sci.* **2012**, *125* (23), 5591–5596. https://doi.org/10.1242/jcs.116392.
(44) Shin, C. S.; Kwak, B.; Han, B.; Park, K. Development of an in Vitro 3D Tumor Model to Study Therapeutic Efficiency of an Anticancer Drug. *Mol. Pharm.* **2013**, *10* (6), 2167–2175. https://doi.org/10.1021/mp300595a.
(45) Hirt, C.; Papadimitropoulos, A.; Muraro, M. G.; Mele, V.; Panopoulos, E.; Cremonesi, E.; Ivanek, R.; Schultz-Thater, E.; Droeser, R. A.; Mengus, C.; Heberer, M.; Oertli, D.; Iezzi, G.; Zajac, P.; Eppenberger-Castori, S.; Tornillo, L.; Terracciano, L.; Martin, I.; Spagnoli, G. C. Bioreactor-Engineered Cancer Tissue-like Structures Mimic Phenotypes, Gene Expression Profiles and Drug Resistance Patterns Observed "in Vivo". *Biomaterials* **2015**, *62*, 138–146. https://doi.org/10.1016/j.biomaterials.2015.05.037.
(46) Wei, S. C.; Yang, J. Forcing through Tumor Metastasis: The Interplay between Tissue Rigidity and Epithelial–Mesenchymal Transition. *Trends Cell Biol.* **2016**, *26* (2), 111–120. https://doi.org/10.1016/J.TCB.2015.09.009.
(47) Wu, M.; Swartz, M. A. Modeling Tumor Microenvironments in Vitro. *J. Biomech. Eng.* **2014**, *136* (2), 021011. https://doi.org/10.1115/1.4026447.
(48) Chaudhuri, O.; Koshy, S. T.; Branco da Cunha, C.; Shin, J.-W.; Verbeke, C. S.; Allison, K. H.; Mooney, D. J. Extracellular Matrix Stiffness and Composition Jointly Regulate the Induction of Malignant Phenotypes in Mammary Epithelium. *Nat. Mater.* **2014**, *13* (10), 970–978. https://doi.org/10.1038/nmat4009.
(49) Boyd, N. F.; Dite, G. S.; Stone, J.; Gunasekara, A.; English, D. R.; McCredie, M. R. E.; Giles, G. G.; Tritchler, D.; Chiarelli, A.; Yaffe, M. J.; Hopper, J. L. Heritability of Mammographic Density, a Risk Factor for Breast Cancer. *N. Engl. J. Med.* **2002**, *347* (12), 886–894. https://doi.org/10.1056/NEJMoa013390.
(50) Gilkes, D. M.; Semenza, G. L.; Wirtz, D. Hypoxia and the Extracellular Matrix: Drivers of Tumour Metastasis. *Nat. Rev. Cancer* **2014**, *14* (6), 430–439. https://doi.org/10.1038/nrc3726.
(51) Zhang, K.; Corsa, C. A.; Ponik, S. M.; Prior, J. L.; Piwnica-Worms, D.; Eliceiri, K. W.; Keely, P. J.; Longmore, G. D. The Collagen Receptor Discoidin Domain Receptor 2 Stabilizes SNAIL1 to Facilitate Breast Cancer Metastasis. *Nat. Cell Biol.* **2013**, *15* (6), 677–687. https://doi.org/10.1038/ncb2743.
(52) Corsa, C. A. S.; Brenot, A.; Grither, W. R.; Van Hove, S.; Loza, A. J.; Zhang, K.; Ponik, S. M.; Liu, Y.; DeNardo, D. G.; Eliceiri, K. W.; Keely, P. J.; Longmore, G. D. The Action of Discoidin Domain Receptor 2 in Basal Tumor Cells and Stromal Cancer-Associated Fibroblasts Is Critical for Breast Cancer Metastasis. *Cell Rep.* **2016**, *15* (11), 2510–2523. https://doi.org/10.1016/j.celrep.2016.05.033.
(53) Stanisavljevic, J.; Loubat-Casanovas, J.; Herrera, M.; Luque, T.; Pena, R.; Lluch, A.; Albanell, J.; Bonilla, F.; Rovira, A.; Pena, C.; Navajas, D.; Rojo, F.; Garcia de Herreros, A.; Baulida, J. Snail1-Expressing Fibroblasts in the Tumor Microenvironment Display Mechanical Properties That Support Metastasis. *Cancer Res.* **2015**, *75* (2), 284–295. https://doi.org/10.1158/0008-5472.CAN-14-1903.
(54) Erdogan, B.; Ao, M.; White, L. M.; Means, A. L.; Brewer, B. M.; Yang, L.; Washington,

M. K.; Shi, C.; Franco, O. E.; Weaver, A. M.; Hayward, S. W.; Li, D.; Webb, D. J. Cancer-Associated Fibroblasts Promote Directional Cancer Cell Migration by Aligning Fibronectin. *J. Cell Biol.* **2017**, *216* (11), 3799–3816. https://doi.org/10.1083/jcb.201704053.

(55) Shinde, A.; Libring, S.; Alpsoy, A.; Abdullah, A.; Schaber, J. A.; Solorio, L.; Wendt, M. K. Autocrine Fibronectin Inhibits Breast Cancer Metastasis. *Mol. Cancer Res.* **2018**, *16* (10), 1579–1589. https://doi.org/10.1158/1541-7786.MCR-18-0151.

(56) Seo, B. R.; Bhardwaj, P.; Choi, S.; Gonzalez, J.; Andresen Eguiluz, R. C.; Wang, K.; Mohanan, S.; Morris, P. G.; Du, B.; Zhou, X. K.; Vahdat, L. T.; Verma, A.; Elemento, O.; Hudis, C. A.; Williams, R. M.; Gourdon, D.; Dannenberg, A. J.; Fischbach, C. Obesity-Dependent Changes in Interstitial ECM Mechanics Promote Breast Tumorigenesis. *Sci. Transl. Med.* **2015**, *7* (301), 301ra130-301ra130. https://doi.org/10.1126/scitranslmed.3010467.

(57) Bertrand, P.; Girard, N.; Delpech, B.; Duval, C.; D'Anjou, J.; Dauce, J. P. Hyaluronan (Hyaluronic Acid) and Hyaluronectin in the Extracellular Matrix of Human Breast Carcinomas: Comparison between Invasive and Non-Invasive Areas. *Int. J. Cancer* **1992**, *52* (1), 1–6. https://doi.org/10.1002/ijc.2910520102.

(58) Itano, N.; Kimata, K. Altered Hyaluronan Biosynthesis in Cancer Progression. In *Hyaluronan in Cancer Biology*; Elsevier, 2009; pp 171–185. https://doi.org/10.1016/B978-012374178-3.10010-9.

(59) Toole, B. P.; Wight, T. N.; Tammi, M. I. Hyaluronan-Cell Interactions in Cancer and Vascular Disease. *J. Biol. Chem.* **2002**, *277* (7), 4593–4596. https://doi.org/10.1074/jbc.R100039200.

(60) Toole, B. P. Hyaluronan-CD44 Interactions in Cancer: Paradoxes and Possibilities. *Clin. Cancer Res.* **2009**, *15* (24), 7462–7468. https://doi.org/10.1158/1078-0432.CCR-09-0479.

(61) Schwertfeger, K. L.; Cowman, M. K.; Telmer, P. G.; Turley, E. A.; McCarthy, J. B. Hyaluronan, Inflammation, and Breast Cancer Progression. *Front. Immunol.* **2015**, *6*, 236. https://doi.org/10.3389/fimmu.2015.00236.

(62) Cox, G.; Kable, E. Second-Harmonic Imaging of Collagen. **2006**, *319* (1), 15–35. https://doi.org/10.1007/978-1-59259-993-6_2.

(63) Navarro, M.; Michiardi, A.; Castano, O.; Planell, J. A. Biomaterials in Orthopaedics. *J. R. Soc. Interface* **2008**, *5* (27), 1137–1158. https://doi.org/10.1098/rsif.2008.0151.

(64) Brydone, A. S.; Meek, D.; Maclaine, S. Bone Grafting, Orthopaedic Biomaterials, and the Clinical Need for Bone Engineering. *Proc. Inst. Mech. Eng. Part H J. Eng. Med.* **2010**, *224* (12), 1329–1343. https://doi.org/10.1243/09544119JEIM770.

(65) Lemons, J. E.; Misch-Dietsh, F.; McCracken, M. S. Biomaterials for Dental Implants. In *Dental Implant Prosthetics*; Elsevier, 2015; pp 66–94. https://doi.org/10.1016/B978-0-323-07845-0.00004-X.

(66) Hoffman, A. S.; Engineering, C.; Schoen, F. J.; Lemons, J. E. Biomaterials Science An Introduction to Materials in Medicine, 3rd Edition. In *Biomaterials Science An Introduction to Materials in Medicine*; Ratner, B. D., Hoffman, A. S., Schoen, F. J., Lemons, J. E., Eds.; Elsevier, 2013.

(67) Davis, J. R. Overview of Biomaterials and Their Use in Medical Devices. In *Handbook of Materials for Medical Devices*; Davis, J. R., Ed.; ASM International, 2003; pp 1–11.

(68) Jammalamadaka, U.; Tappa, K. Recent Advances in Biomaterials for 3D Printing and Tissue Engineering. *J. Funct. Biomater.* **2018**, *9* (1), 22.

https://doi.org/10.3390/jfb9010022.
(69) *Biological Interactions on Materials Surfaces*; Puleo, D. A., Bizios, R., Eds.; Springer US: New York, NY, 2009. https://doi.org/10.1007/978-0-387-98161-1.
(70) Lutolf, M. P.; Hubbell, J. A. Synthetic Biomaterials as Instructive Extracellular Microenvironments for Morphogenesis in Tissue Engineering. *Nat. Biotechnol.* **2005**, *23* (1), 47–55. https://doi.org/10.1038/nbt1055.
(71) Jin, L.; Wang, T.; Zhu, M.-L.; Leach, M. K.; Naim, Y. I.; Corey, J. M.; Feng, Z.-Q.; Jiang, Q. Electrospun Fibers and Tissue Engineering. *J. Biomed. Nanotechnol.* **2012**, *8* (1), 1–9. https://doi.org/10.1166/jbn.2012.1360.
(72) Khorshidi, S.; Solouk, A.; Mirzadeh, H.; Mazinani, S.; Lagaron, J. M.; Sharifi, S.; Ramakrishna, S. A Review of Key Challenges of Electrospun Scaffolds for Tissue-Engineering Applications. *J. Tissue Eng. Regen. Med.* **2016**, *10* (9), 715–738. https://doi.org/10.1002/term.1978.
(73) Di Martino, A.; Liverani, L.; Rainer, A.; Salvatore, G.; Trombetta, M.; Denaro, V. Electrospun Scaffolds for Bone Tissue Engineering. *Musculoskelet. Surg.* **2011**, *95* (2), 69–80. https://doi.org/10.1007/s12306-011-0097-8.
(74) Kostina, N. Y.; Pop-Georgievski, O.; Bachmann, M.; Neykova, N.; Bruns, M.; Michálek, J.; Bastmeyer, M.; Rodriguez-Emmenegger, C. Non-Fouling Biodegradable Poly(ϵ-Caprolactone) Nanofibers for Tissue Engineering. *Macromol. Biosci.* **2016**, *16* (1), 83–94. https://doi.org/10.1002/mabi.201500252.
(75) Mandal, S.; Bhaskar, S.; Lahann, J. Micropatterned Fiber Scaffolds for Spatially Controlled Cell Adhesion. *Macromol. Rapid Commun.* **2009**, *30* (19), 1638–1644. https://doi.org/10.1002/marc.200900340.
(76) Mundargi, R. C.; Babu, V. R.; Rangaswamy, V.; Patel, P.; Aminabhavi, T. M. Nano/Micro Technologies for Delivering Macromolecular Therapeutics Using Poly(d,l-Lactide-Co-Glycolide) and Its Derivatives. *J. Control. Release* **2008**, *125* (3), 193–209. https://doi.org/10.1016/j.jconrel.2007.09.013.
(77) Kim, K.; Yu, M.; Zong, X.; Chiu, J.; Fang, D.; Seo, Y.-S.; Hsiao, B. S.; Chu, B.; Hadjiargyrou, M. Control of Degradation Rate and Hydrophilicity in Electrospun Non-Woven Poly(d,l-Lactide) Nanofiber Scaffolds for Biomedical Applications. *Biomaterials* **2003**, *24* (27), 4977–4985. https://doi.org/10.1016/S0142-9612(03)00407-1.
(78) Mellor, L. F.; Huebner, P.; Cai, S.; Mohiti-Asli, M.; Taylor, M. A.; Spang, J.; Shirwaiker, R. A.; Loboa, E. G. Fabrication and Evaluation of Electrospun, 3D-Bioplotted, and Combination of Electrospun/3D-Bioplotted Scaffolds for Tissue Engineering Applications. *Biomed Res. Int.* **2017**, *2017*, 1–9. https://doi.org/10.1155/2017/6956794.
(79) Giordano, R. A.; Wu, B. M.; Borland, S. W.; Cima, L. G.; Sachs, E. M.; Cima, M. J. Mechanical Properties of Dense Polylactic Acid Structures Fabricated by Three Dimensional Printing. *J. Biomater. Sci. Polym. Ed.* **1997**, *8* (1), 63–75. https://doi.org/10.1163/156856297X00588.
(80) Pfister, A.; Landers, R.; Laib, A.; Hübner, U.; Schmelzeisen, R.; Mülhaupt, R. Biofunctional Rapid Prototyping for Tissue-Engineering Applications: 3D Bioplotting versus 3D Printing. *J. Polym. Sci. Part A Polym. Chem.* **2004**, *42* (3), 624–638. https://doi.org/10.1002/pola.10807.
(81) Wunner, F. M.; Wille, M.-L.; Noonan, T. G.; Bas, O.; Dalton, P. D.; De-Juan-Pardo, E. M.; Hutmacher, D. W. Melt Electrospinning Writing of Highly Ordered Large Volume Scaffold Architectures. *Adv. Mater.* **2018**, *30* (20), 1706570.

https://doi.org/10.1002/adma.201706570.
(82) Jordahl, J. H.; Solorio, L.; Sun, H.; Ramcharan, S.; Teeple, C. B.; Haley, H. R.; Lee, K. J.; Eyster, T. W.; Luker, G. D.; Krebsbach, P. H.; Lahann, J. 3D Jet Writing: Functional Microtissues Based on Tessellated Scaffold Architectures. *Adv. Mater.* **2018**, *30* (14), 1707196. https://doi.org/10.1002/adma.201707196.
(83) Rezwan, K.; Chen, Q. Z.; Blaker, J. J.; Boccaccini, A. R. Biodegradable and Bioactive Porous Polymer/Inorganic Composite Scaffolds for Bone Tissue Engineering. *Biomaterials* **2006**, *27* (18), 3413–3431. https://doi.org/10.1016/j.biomaterials.2006.01.039.
(84) Thomas, A. M.; Kubilius, M. B.; Holland, S. J.; Seidlits, S. K.; Boehler, R. M.; Anderson, A. J.; Cummings, B. J.; Shea, L. D. Channel Density and Porosity of Degradable Bridging Scaffolds on Axon Growth after Spinal Injury. *Biomaterials* **2013**, *34* (9), 2213–2220. https://doi.org/10.1016/j.biomaterials.2012.12.002.
(85) Gratson, G. M.; Xu, M.; Lewis, J. A. Microperiodic Structures: Direct Writing of Three-Dimensional Webs. *Nature* **2004**, *428* (6981), 386–386. https://doi.org/10.1038/428386a.
(86) Lewis, J. A. Direct Ink Writing of 3D Functional Materials. *Adv. Funct. Mater.* **2006**, *16* (17), 2193–2204. https://doi.org/10.1002/adfm.200600434.
(87) Richter, B.; Hahn, V.; Bertels, S.; Claus, T. K.; Wegener, M.; Delaittre, G.; Barner-Kowollik, C.; Bastmeyer, M. Guiding Cell Attachment in 3D Microscaffolds Selectively Functionalized with Two Distinct Adhesion Proteins. *Adv. Mater.* **2017**, *29* (5), 1604342. https://doi.org/10.1002/adma.201604342.
(88) Žukauskas, A.; Batavičiūtė, G.; Ščiuka, M.; Jukna, T.; Melninkaitis, A.; Malinauskas, M. Characterization of Photopolymers Used in Laser 3D Micro/Nanolithography by Means of Laser-Induced Damage Threshold (LIDT). *Opt. Mater. Express* **2014**, *4* (8), 1601. https://doi.org/10.1364/OME.4.001601.
(89) Torgersen, J.; Qin, X. H.; Li, Z.; Ovsianikov, A.; Liska, R.; Stampfl, J. Hydrogels for Two-Photon Polymerization: A Toolbox for Mimicking the Extracellular Matrix. *Adv. Funct. Mater.* **2013**, *23* (36), 4542–4554. https://doi.org/10.1002/adfm.201203880.
(90) Jungst, T.; Smolan, W.; Schacht, K.; Scheibel, T.; Groll, J. Strategies and Molecular Design Criteria for 3D Printable Hydrogels. *Chem. Rev.* **2016**, *116* (3), 1496–1539. https://doi.org/10.1021/acs.chemrev.5b00303.
(91) DeForest, C. A.; Anseth, K. S. Advances in Bioactive Hydrogels to Probe and Direct Cell Fate. *Annu. Rev. Chem. Biomol. Eng.* **2012**, *3* (1), 421–444. https://doi.org/10.1146/annurev-chembioeng-062011-080945.
(92) Gjorevski, N.; Sachs, N.; Manfrin, A.; Giger, S.; Bragina, M. E.; Ordóñez-Morán, P.; Clevers, H.; Lutolf, M. P. Designer Matrices for Intestinal Stem Cell and Organoid Culture. *Nature* **2016**, *539* (7630), 560–564. https://doi.org/10.1038/nature20168.
(93) Caiazzo, M.; Okawa, Y.; Ranga, A.; Piersigilli, A.; Tabata, Y.; Lutolf, M. P. Defined Three-Dimensional Microenvironments Boost Induction of Pluripotency. *Nat. Mater.* **2016**, *15* (3), 344–352. https://doi.org/10.1038/nmat4536.
(94) Ehrbar, M.; Rizzi, S. C.; Schoenmakers, R. G.; San Miguel, B.; Hubbell, J. A.; Weber, F. E.; Lutolf, M. P. Biomolecular Hydrogels Formed and Degraded via Site-Specific Enzymatic Reactions. *Biomacromolecules* **2007**, *8* (10), 3000–3007. https://doi.org/10.1021/bm070228f.
(95) Lienemann, P. S.; Rossow, T.; Mao, A. S.; Vallmajo-Martin, Q.; Ehrbar, M.; Mooney, D. J. Single Cell-Laden Protease-Sensitive Microniches for Long-Term Culture in 3D. *Lab*

Chip **2017**, *17* (4), 727–737. https://doi.org/10.1039/C6LC01444E.
(96) Freudenberg, U.; Liang, Y.; Kiick, K. L.; Werner, C. Glycosaminoglycan-Based Biohybrid Hydrogels: A Sweet and Smart Choice for Multifunctional Biomaterials. *Adv. Mater.* **2016**, *28* (40), 8861–8891. https://doi.org/10.1002/adma.201601908.
(97) Bajaj, P.; Schweller, R. M.; Khademhosseini, A.; West, J. L.; Bashir, R. 3D Biofabrication Strategies for Tissue Engineering and Regenerative Medicine. *Annu. Rev. Biomed. Eng.* **2014**, *16* (1), 247–276. https://doi.org/10.1146/annurev-bioeng-071813-105155.
(98) Espíndola-González, A.; Martínez-Hernández, A. L.; Fernández-Escobar, F.; Castaño, V. M.; Brostow, W.; Datashvili, T.; Velasco-Santos, C. Natural-Synthetic Hybrid Polymers Developed via Electrospinning: The Effect of PET in Chitosan/Starch System. *Int. J. Mol. Sci.* **2011**, *12* (3), 1908–1920. https://doi.org/10.3390/ijms12031908.
(99) Sridhar, R.; Lakshminarayanan, R.; Madhaiyan, K.; Amutha Barathi, V.; Lim, K. H. C.; Ramakrishna, S. Electrosprayed Nanoparticles and Electrospun Nanofibers Based on Natural Materials: Applications in Tissue Regeneration, Drug Delivery and Pharmaceuticals. *Chem. Soc. Rev.* **2015**, *44* (3), 790–814. https://doi.org/10.1039/C4CS00226A.
(100) Ingavle, G. C.; Leach, J. K. Advancements in Electrospinning of Polymeric Nanofibrous Scaffolds for Tissue Engineering. *Tissue Eng. Part B Rev.* **2014**, *20* (4), 277–293. https://doi.org/10.1089/ten.teb.2013.0276.
(101) Sajkiewicz, P.; Kołbuk, D. Electrospinning of Gelatin for Tissue Engineering – Molecular Conformation as One of the Overlooked Problems. *J. Biomater. Sci. Polym. Ed.* **2014**, *25* (18), 2009–2022. https://doi.org/10.1080/09205063.2014.975392.
(102) Liu, X.; Ma, P. X. Phase Separation, Pore Structure, and Properties of Nanofibrous Gelatin Scaffolds. *Biomaterials* **2009**, *30* (25), 4094–4103. https://doi.org/10.1016/j.biomaterials.2009.04.024.
(103) Freyman, T. M.; Yannas, I. V.; Gibson, L. J. Cellular Materials as Porous Scaffolds for Tissue Engineering. *Prog. Mater. Sci.* **2001**, *46* (3–4), 273–282. https://doi.org/10.1016/S0079-6425(00)00018-9.
(104) Ahmed, Z.; Underwood, S.; Brown, R. A. Nerve Guide Material Made from Fibronectin: Assessment of in Vitro Properties. *Tissue Eng.* **2003**, *9* (2), 219–231. https://doi.org/10.1089/107632703764664693.
(105) Phillips, J. B.; King, V. R.; Ward, Z.; Porter, R. A.; Priestley, J. V; Brown, R. A. Fluid Shear in Viscous Fibronectin Gels Allows Aggregation of Fibrous Materials for CNS Tissue Engineering. *Biomaterials* **2004**, *25* (14), 2769–2779. https://doi.org/10.1016/j.biomaterials.2003.09.052.
(106) Lee, J.; Kim, G. 3D Hierarchical Nanofibrous Collagen Scaffold Fabricated Using Fibrillated Collagen and Pluronic F-127 for Regenerating Bone Tissue. *ACS Appl. Mater. Interfaces* **2018**, acsami.8b14088. https://doi.org/10.1021/acsami.8b14088.
(107) Trappmann, B.; Chen, C. S. How Cells Sense Extracellular Matrix Stiffness: A Material's Perspective. *Curr. Opin. Biotechnol.* **2013**, *24* (5), 948–953. https://doi.org/10.1016/j.copbio.2013.03.020.
(108) Raic, A.; Rödling, L.; Kalbacher, H.; Lee-Thedieck, C. Biomimetic Macroporous PEG Hydrogels as 3D Scaffolds for the Multiplication of Human Hematopoietic Stem and Progenitor Cells. *Biomaterials* **2014**, *35* (3), 929–940. https://doi.org/10.1016/j.biomaterials.2013.10.038.
(109) Seliktar, D. Designing Cell-Compatible Hydrogels for Biomedical Applications. *Science*

(80-.). **2012**, *336* (6085), 1124–1128. https://doi.org/10.1126/science.1214804.
(110) Barner-Kowollik, C.; Bastmeyer, M.; Blasco, E.; Delaittre, G.; Müller, P.; Richter, B.; Wegener, M. 3D Laser Micro- and Nanoprinting: Challenges for Chemistry. *Angew. Chemie Int. Ed.* **2017**, *56* (50), 15828–15845. https://doi.org/10.1002/anie.201704695.
(111) Leijten, J.; Seo, J.; Yue, K.; Trujillo-de Santiago, G.; Tamayol, A.; Ruiz-Esparza, G. U.; Shin, S. R.; Sharifi, R.; Noshadi, I.; Álvarez, M. M.; Zhang, Y. S.; Khademhosseini, A. Spatially and Temporally Controlled Hydrogels for Tissue Engineering. *Mater. Sci. Eng. R Reports* **2017**, *119*, 1–35. https://doi.org/10.1016/J.MSER.2017.07.001.
(112) Lee, E.; Song, H.-H. G.; Chen, C. S. Biomimetic On-a-Chip Platforms for Studying Cancer Metastasis. *Curr. Opin. Chem. Eng.* **2016**, *11*, 20–27. https://doi.org/10.1016/j.coche.2015.12.001.
(113) Wang, C.; Tong, X.; Yang, F. Bioengineered 3D Brain Tumor Model To Elucidate the Effects of Matrix Stiffness on Glioblastoma Cell Behavior Using PEG-Based Hydrogels. *Mol. Pharm.* **2014**, *11* (7), 2115–2125. https://doi.org/10.1021/mp5000828.
(114) Ovsianikov, A.; Deiwick, A.; Van Vlierberghe, S.; Pflaum, M.; Wilhelmi, M.; Dubruel, P.; Chichkov, B. Laser Fabrication of 3D Gelatin Scaffolds for the Generation of Bioartificial Tissues. *Materials (Basel).* **2010**, *4* (1), 288–299. https://doi.org/10.3390/ma4010288.
(115) Su, P. J.; Tran, Q. A.; Fong, J. J.; Eliceiri, K. W.; Ogle, B. M.; Campagnola, P. J. Mesenchymal Stem Cell Interactions with 3D ECM Modules Fabricated via Multiphoton Excited Photochemistry. *Biomacromolecules* **2012**, *13* (9), 2917–2925. https://doi.org/10.1021/bm300949k.
(116) Bell, A.; Kofron, M.; Nistor, V. Multiphoton Crosslinking for Biocompatible 3D Printing of Type I Collagen. *Biofabrication* **2015**, *7* (3). https://doi.org/10.1088/1758-5090/7/3/035007.
(117) Hutmacher, D. W.; Loessner, D.; Rizzi, S.; Kaplan, D. L.; Mooney, D. J.; Clements, J. A. Can Tissue Engineering Concepts Advance Tumor Biology Research? *Trends Biotechnol.* **2010**, *28* (3), 125–133. https://doi.org/10.1016/j.tibtech.2009.12.001.
(118) Moroni, L.; Boland, T.; Burdick, J. A.; De Maria, C.; Derby, B.; Forgacs, G.; Groll, J.; Li, Q.; Malda, J.; Mironov, V. A.; Mota, C.; Nakamura, M.; Shu, W.; Takeuchi, S.; Woodfield, T. B. F.; Xu, T.; Yoo, J. J.; Vozzi, G. Biofabrication: A Guide to Technology and Terminology. **2018**. https://doi.org/10.1016/j.tibtech.2017.10.015.
(119) Jung, J. W.; Lee, J.-S. S.; Cho, D.-W. W. Computer-Aided Multiple-Head 3D Printing System for Printing of Heterogeneous Organ/Tissue Constructs. *Sci. Rep.* **2016**, *6* (1), 21685. https://doi.org/10.1038/srep21685.
(120) Gao, G.; Cui, X. Three-Dimensional Bioprinting in Tissue Engineering and Regenerative Medicine. *Biotechnology Letters*. 2016. https://doi.org/10.1007/s10529-015-1975-1.
(121) Huang, Y.; Zhang, X.-F.; Gao, G.; Yonezawa, T.; Cui, X. 3D Bioprinting and the Current Applications in Tissue Engineering. *Biotechnol. J.* **2017**, *1600734*, 1600734. https://doi.org/10.1002/biot.201600734.
(122) Zhang, Y. S.; Oklu, R.; Dokmeci, M. R.; Khademhosseini, A. Three-Dimensional Bioprinting Strategies for Tissue Engineering. *Cold Spring Harb. Perspect. Med.* **2018**, *8* (2), 1–16. https://doi.org/10.1101/cshperspect.a025718.
(123) Moroni, L.; Burdick, J. A.; Highley, C.; Jin Lee, S.; Morimoto, Y.; Takeuchi, S.; Yoo, J. J. Biofabrication Strategies for 3D in Vitro Models and Regenerative Medicine. *Nat. Rev. Mater.* **2018**. https://doi.org/10.1038/s41578-018-0006-y.

(124) Kim, B. S.; Lee, J.-S.; Gao, G.; Cho, D.-W. Direct 3D Cell-Printing of Human Skin with Functional Transwell System. *Biofabrication* **2017**, *9* (2), 025034. https://doi.org/10.1088/1758-5090/aa71c8.
(125) Kang, H.-W.; Lee, S. J.; Ko, I. K.; Kengla, C.; Yoo, J. J.; Atala, A. A 3D Bioprinting System to Produce Human-Scale Tissue Constructs with Structural Integrity. *Nat. Biotechnol.* **2016**, *34* (3), 312–319. https://doi.org/10.1038/nbt.3413.
(126) Sutherland, R. M.; McCredie, J. A.; Inch, W. R. Growth of Multicell Spheroids in Tissue Culture as a Model of Nodular Carcinomas<xref Ref-Type="fn" Rid="FN2">2</Xref>. *JNCI J. Natl. Cancer Inst.* **1971**, *46* (1), 113–120. https://doi.org/10.1093/jnci/46.1.113.
(127) Mehta, G.; Hsiao, A. Y.; Ingram, M.; Luker, G. D.; Takayama, S. Opportunities and Challenges for Use of Tumor Spheroids as Models to Test Drug Delivery and Efficacy. *J. Control. Release* **2012**, *164* (2), 192–204. https://doi.org/10.1016/j.jconrel.2012.04.045.
(128) Ott, H. C.; Matthiesen, T. S.; Goh, S.-K.; Black, L. D.; Kren, S. M.; Netoff, T. I.; Taylor, D. A. Perfusion-Decellularized Matrix: Using Nature's Platform to Engineer a Bioartificial Heart. *Nat. Med.* **2008**, *14* (2), 213–221. https://doi.org/10.1038/nm1684.
(129) Seetapun, D.; Ross, J. J. Eliminating the Organ Transplant Waiting List: The Future with Perfusion Decellularized Organs. *Surgery* **2017**, *161* (6), 1474–1478. https://doi.org/10.1016/j.surg.2016.09.041.
(130) Ragelle, H.; Naba, A.; Larson, B. L.; Zhou, F.; Prijić, M.; Whittaker, C. A.; Del Rosario, A.; Langer, R.; Hynes, R. O.; Anderson, D. G. Comprehensive Proteomic Characterization of Stem Cell-Derived Extracellular Matrices. *Biomaterials* **2017**, *128*, 147–159. https://doi.org/10.1016/j.biomaterials.2017.03.008.
(131) ASTM, A. Standard Guide for Characterization and Testing of Biomaterial Scaffolds Used in Tissue-Engineered Medical Products 1. *Annu. B. ASTM Stand. ASTM Int.* **2002**. https://doi.org/10.1520/F2150-13.
(132) Kambic, H. E.; Yokobori, A. T. *Biomaterials ' Mechanical Properties*; 1994.
(133) Bettinger, C. J.; Langer, R.; Borenstein, J. T. Engineering Substrate Topography at the Micro- and Nanoscale to Control Cell Function. *Angew. Chemie Int. Ed.* **2009**, *48* (30), 5406–5415. https://doi.org/10.1002/anie.200805179.
(134) Chiu, C.-L.; Aguilar, J. S.; Tsai, C. Y.; Wu, G.; Gratton, E.; Digman, M. A. Nanoimaging of Focal Adhesion Dynamics in 3D. *PLoS One* **2014**, *9* (6), e99896. https://doi.org/10.1371/journal.pone.0099896.
(135) Bonnans, C.; Chou, J.; Werb, Z. Remodelling the Extracellular Matrix in Development and Disease. *Nat. Rev. Mol. Cell Biol.* **2014**, *15* (12), 786–801. https://doi.org/10.1038/nrm3904.
(136) The Human Protein Atlas.
(137) Uhlen, M.; Fagerberg, L.; Hallstrom, B. M.; Lindskog, C.; Oksvold, P.; Mardinoglu, A.; Sivertsson, A.; Kampf, C.; Sjostedt, E.; Asplund, A.; Olsson, I.; Edlund, K.; Lundberg, E.; Navani, S.; Szigyarto, C. A.-K.; Odeberg, J.; Djureinovic, D.; Takanen, J. O.; Hober, S.; Alm, T.; Edqvist, P.-H.; Berling, H.; Tegel, H.; Mulder, J.; Rockberg, J.; Nilsson, P.; Schwenk, J. M.; Hamsten, M.; von Feilitzen, K.; Forsberg, M.; Persson, L.; Johansson, F.; Zwahlen, M.; von Heijne, G.; Nielsen, J.; Ponten, F. Tissue-Based Map of the Human Proteome. *Science (80-.).* **2015**, *347* (6220), 1260419–1260419. https://doi.org/10.1126/science.1260419.
(138) Thul, P. J.; Åkesson, L.; Wiking, M.; Mahdessian, D.; Geladaki, A.; Ait Blal, H.; Alm, T.; Asplund, A.; Björk, L.; Breckels, L. M.; Bäckström, A.; Danielsson, F.; Fagerberg, L.;

Fall, J.; Gatto, L.; Gnann, C.; Hober, S.; Hjelmare, M.; Johansson, F.; Lee, S.; Lindskog, C.; Mulder, J.; Mulvey, C. M.; Nilsson, P.; Oksvold, P.; Rockberg, J.; Schutten, R.; Schwenk, J. M.; Sivertsson, Å.; Sjöstedt, E.; Skogs, M.; Stadler, C.; Sullivan, D. P.; Tegel, H.; Winsnes, C.; Zhang, C.; Zwahlen, M.; Mardinoglu, A.; Pontén, F.; von Feilitzen, K.; Lilley, K. S.; Uhlén, M.; Lundberg, E. A Subcellular Map of the Human Proteome. *Science (80-.).* **2017**, *356* (6340), eaal3321. https://doi.org/10.1126/science.aal3321.

(139) Bell, C. C.; Hendriks, D. F. G.; Moro, S. M. L.; Ellis, E.; Walsh, J.; Renblom, A.; Fredriksson Puigvert, L.; Dankers, A. C. A.; Jacobs, F.; Snoeys, J.; Sison-Young, R. L.; Jenkins, R. E.; Nordling, Å.; Mkrtchian, S.; Park, B. K.; Kitteringham, N. R.; Goldring, C. E. P.; Lauschke, V. M.; Ingelman-Sundberg, M. Characterization of Primary Human Hepatocyte Spheroids as a Model System for Drug-Induced Liver Injury, Liver Function and Disease. *Sci. Rep.* **2016**, *6* (1), 25187. https://doi.org/10.1038/srep25187.

(140) Proctor, W. R.; Foster, A. J.; Vogt, J.; Summers, C.; Middleton, B.; Pilling, M. A.; Shienson, D.; Kijanska, M.; Ströbel, S.; Kelm, J. M.; Morgan, P.; Messner, S.; Williams, D. Utility of Spherical Human Liver Microtissues for Prediction of Clinical Drug-Induced Liver Injury. *Arch. Toxicol.* **2017**, *91* (8), 2849–2863. https://doi.org/10.1007/s00204-017-2002-1.

(141) Hirt, M. N.; Hansen, A.; Eschenhagen, T. Cardiac Tissue Engineering : State of the Art. *Circ. Res.* **2014**, *114* (2), 354–367. https://doi.org/10.1161/CIRCRESAHA.114.300522.

(142) Radisic, M.; Sefton, M. V. Cardiac Tissue. In *Principles of Regenerative Medicine*; Elsevier Inc., 2011; pp 877–909. https://doi.org/10.1016/B978-0-12-381422-7.10048-3.

(143) Ronaldson-Bouchard, K.; Ma, S. P.; Yeager, K.; Chen, T.; Song, L.; Sirabella, D.; Morikawa, K.; Teles, D.; Yazawa, M.; Vunjak-Novakovic, G. Advanced Maturation of Human Cardiac Tissue Grown from Pluripotent Stem Cells. *Nature* **2018**, *556* (7700), 239–243. https://doi.org/10.1038/s41586-018-0016-3.

(144) Xu, L. C.; Siedlecki, C. A. Effects of Surface Wettability and Contact Time on Protein Adhesion to Biomaterial Surfaces. *Biomaterials* **2007**, *28* (22), 3273–3283. https://doi.org/10.1016/j.biomaterials.2007.03.032.

(145) Roach, P.; Farrar, D.; Perry, C. C. Interpretation of Protein Adsorption: Surface-Induced Conformational Changes. *J. Am. Chem. Soc.* **2005**, *127* (22), 8168–8173. https://doi.org/10.1021/ja042898o.

(146) Nakanishi, K.; Sakiyama, T.; Imamura, K. On the Adsorption of Proteins on Solid Surfaces, a Common but Very Complicated Phenomenon. *Journal of Bioscience and Bioengineering*. 2001, pp 233–244. https://doi.org/10.1016/S1389-1723(01)80127-4.

(147) Jordahl, S.; Solorio, L.; Neale, D. B.; McDermott, S.; Jordahl, J. H.; Fox, A.; Dunlay, C.; Xiao, A.; Brown, M.; Wicha, M.; Luker, G. D.; Lahann, J. Engineered Fibrillar Fibronectin Networks as Three-Dimensional Tissue Scaffolds. *Adv. Mater.* **2019**, *31* (46), 1904580. https://doi.org/10.1002/adma.201904580.

(148) Zollinger, A. J.; Smith, M. L. Fibronectin, the Extracellular Glue. *Matrix Biology*. Elsevier July 1, 2017, pp 27–37. https://doi.org/10.1016/j.matbio.2016.07.011.

(149) Neale, D. B.; Muñiz, A. J.; Jones, M. S.; Kim, D. H.; Buschhaus, J. M.; Humphries, B. A.; Wang, W. Y.; Baker, B. M.; Raymond, J. E.; Solorio, L.; Luker, G. D.; Lahann, J. Aligned Networks of Engineered Fibrillar Fibronectin Guide Cellular Orientation and Motility. *Small Struct.* **2021**, *2* (6), 2000137. https://doi.org/10.1002/sstr.202000137.

(150) Hynes, R. O.; Naba, A. Overview of the Matrisome--An Inventory of Extracellular Matrix Constituents and Functions. *Cold Spring Harb. Perspect. Biol.* **2012**, *4* (1), a004903–

a004903. https://doi.org/10.1101/cshperspect.a004903.
(151) Mouw, J. K.; Ou, G.; Weaver, V. M. Extracellular Matrix Assembly: A Multiscale Deconstruction. *Nat. Rev. Mol. Cell Biol.* **2014**, *15* (12), 771–785. https://doi.org/10.1038/nrm3902.
(152) To, W. S.; Midwood, K. S. Plasma and Cellular Fibronectin: Distinct and Independent Functions during Tissue Repair. *Fibrogenesis Tissue Repair* **2011**, *4* (1), 21. https://doi.org/10.1186/1755-1536-4-21.
(153) Singh, P.; Carraher, C.; Schwarzbauer, J. E. Assembly of Fibronectin Extracellular Matrix. *Annu. Rev. Cell Dev. Biol.* **2010**, *26* (1), 397–419. https://doi.org/10.1146/annurev-cellbio-100109-104020.
(154) Frantz, C.; Stewart, K. M.; Weaver, V. M. The Extracellular Matrix at a Glance. *J. Cell Sci.* **2010**, *123*, 4195–4200. https://doi.org/10.1242/jcs.023820.
(155) Mao, Y.; Schwarzbauer, J. E. Fibronectin Fibrillogenesis, a Cell-Mediated Matrix Assembly Process. *Matrix Biol.* **2005**, *24* (6), 389–399. https://doi.org/10.1016/j.matbio.2005.06.008.
(156) Wu, C.; Keivenst, V. M.; O'Toole, T. E.; McDonald, J. A.; Ginsberg, M. H. Integrin Activation and Cytoskeletal Interaction Are Essential for the Assembly of a Fibronectin Matrix. *Cell* **1995**, *83* (5), 715–724. https://doi.org/10.1016/0092-8674(95)90184-1.
(157) Lemmon, C. A.; Weinberg, S. H. Multiple Cryptic Binding Sites Are Necessary for Robust Fibronectin Assembly. *Biophys. J.* **2018**, *114* (3), 678a. https://doi.org/10.1016/j.bpj.2017.11.3658.
(158) Früh, S. M.; Schoen, I.; Ries, J.; Vogel, V. Molecular Architecture of Native Fibronectin Fibrils. *Nat. Commun.* **2015**, *6* (1), 1–10. https://doi.org/10.1038/ncomms8275.
(159) Lemmon, C. A.; Weinberg, S. H. Multiple Cryptic Binding Sites Are Necessary for Robust Fibronectin Assembly: An In Silico Study. *Sci. Rep.* **2017**, *7* (1), 18061. https://doi.org/10.1038/s41598-017-18328-4.
(160) Paten, J. A.; Martin, C. L.; Wanis, J. T.; Siadat, S. M.; Figueroa-Navedo, A. M.; Ruberti, J. W.; Deravi, L. F. Molecular Interactions between Collagen and Fibronectin: A Reciprocal Relationship That Regulates De Novo Fibrillogenesis. *Chem* **2019**, *5* (8), 2126–2145. https://doi.org/10.1016/j.chempr.2019.05.011.
(161) Wierzbicka-Patynowski, I.; Schwarzbauer, J. E. The Ins and Outs of Fibronectin Matrix Assembly. *J. Cell Sci.* **2003**, *116* (Pt 16), 3269–3276. https://doi.org/10.1242/jcs.00670.
(162) Pernodet, N.; Rafailovich, M.; Sokolov, J.; Xu, D.; Yang, N.-L.; McLeod, K. Fibronectin Fibrillogenesis on Sulfonated Polystyrene Surfaces. *J. Biomed. Mater. Res.* **2003**, *64A* (4), 684–692. https://doi.org/10.1002/jbm.a.10394.
(163) VUENTO, M.; VARTIO, T.; SARASTE, M.; BONSDORFF, C.-H.; VAHERI, A. Spontaneous and Polyamine-Induced Formation of Filamentous Polymers from Soluble Fibronectin. *Eur. J. Biochem.* **1980**, *105* (1), 33–42. https://doi.org/10.1111/j.1432-1033.1980.tb04471.x.
(164) Peters, D. M. P.; Chen, Y.; Zardi, L.; Brummel, S. Conformation of Fibronectin Fibrils Varies: Discrete Globular Domains of Type III Repeats Detected. *Microsc. Microanal.* **1998**, *4* (4), 385–396. https://doi.org/10.1017/S1431927698980369.
(165) Zuidema, J. M.; Rivet, C. J.; Gilbert, R. J.; Morrison, F. A. A Protocol for Rheological Characterization of Hydrogels for Tissue Engineering Strategies. *J. Biomed. Mater. Res. Part B Appl. Biomater.* **2014**, *102* (5), 1063–1073. https://doi.org/10.1002/jbm.b.33088.
(166) Jeon, O.; Bouhadir, K. H.; Mansour, J. M.; Alsberg, E. Photocrosslinked Alginate

Hydrogels with Tunable Biodegradation Rates and Mechanical Properties. *Biomaterials* **2009**, *30*, 2724–2734. https://doi.org/10.1016/j.biomaterials.2009.01.034.
(167) McKee, C. T.; Last, J. A.; Russell, P.; Murphy, C. J. Indentation Versus Tensile Measurements of Young's Modulus for Soft Biological Tissues. *Tissue Eng. Part B Rev.* **2011**, *17* (3), 155–164. https://doi.org/10.1089/ten.teb.2010.0520.
(168) Baker, B. M.; Trappmann, B.; Wang, W. Y.; Sakar, M. S.; Kim, I. L.; Shenoy, V. B.; Burdick, J. A.; Chen, C. S. Cell-Mediated Fibre Recruitment Drives Extracellular Matrix Mechanosensing in Engineered Fibrillar Microenvironments. *Nat. Mater.* **2015**, *14* (12), 1262–1268. https://doi.org/10.1038/nmat4444.
(169) Gennisson, J.-L.; Deffieux, T.; Fink, M.; Tanter, M. Ultrasound Elastography: Principles and Techniques. *Diagn. Interv. Imaging* **2013**, *94* (5), 487–495. https://doi.org/10.1016/j.diii.2013.01.022.
(170) Standard Guide for Evaluating Computerized Data Acquisition Systems Used to Acquire Data from Universal Testing Machines BT - Standard Guide for Evaluating Computerized Data Acquisition Systems Used to Acquire Data from Universal Testing Machines. ASTM International 2013.
(171) Mosher, D. F.; Johnson, R. B. In Vitro Formation of Disulfide-Bonded Fibronectin Multimers*. *J. Biol. Chem.* **1983**, *258* (10), 6595–6601.
(172) Sakai, K.; Fujii, T.; Hayashi, T. Cell-Free Formation of Disulfide-Bonded Multimer from Isolated Plasma Fibronectin in the Presence of a Low Concentration of SH Reagent under a Physiological Condition. *J. Biochem.* **1994**, *115* (3), 415–421. https://doi.org/10.1093/oxfordjournals.jbchem.a124353.
(173) Ejim, O. S.; Blunn, G. W.; Brown, R. A. Production of Artificial-Orientated Mats and Strands from Plasma Fibronectin: A Morphological Study. *Biomaterials* **1993**, *14* (10), 743–748. https://doi.org/10.1016/0142-9612(93)90038-4.
(174) Brown, R.; Blunn, G.; Ejim, O. Preparation of Orientated Fibrous Mats from Fibronectin: Composition and Stability. *Biomaterials* **1994**, *15* (6), 457–464. https://doi.org/10.1016/0142-9612(94)90225-9.
(175) Underwood, S.; Afoke, A.; Brown, R. A.; MacLeod, A. J.; Shamlou, P. A.; Dunnill, P. Wet Extrusion of Fibronectin-Fibrinogen Cables for Application in Tissue Engineering. *Biotechnol. Bioeng.* **2001**, *73* (4), 295–305. https://doi.org/10.1002/bit.1062.
(176) Chantre, C. O.; Campbell, P. H.; Golecki, H. M.; Buganza, A. T.; Capulli, A. K.; Deravi, L. F.; Dauth, S.; Sheehy, S. P.; Paten, J. A.; Gledhill, K.; Doucet, Y. S.; Abaci, H. E.; Ahn, S.; Pope, B. D.; Ruberti, J. W.; Hoerstrup, S. P.; Christiano, A. M.; Parker, K. K. Production-Scale Fibronectin Nanofibers Promote Wound Closure and Tissue Repair in a Dermal Mouse Model. *Biomaterials* **2018**, *166*, 96–108. https://doi.org/10.1016/j.biomaterials.2018.03.006.
(177) Ahn, S.; Deravi, L. F.; Park, S.-J.; Dabiri, B. E.; Kim, J.-S.; Parker, K. K.; Shin, K. Self-Organizing Large-Scale Extracellular-Matrix Protein Networks. *Adv. Mater.* **2015**, *27* (18), 2838–2845. https://doi.org/10.1002/adma.201405556.
(178) Feinberg, A. W.; Parker, K. K. Surface-Initiated Assembly of Protein Nanofabrics. *Nano Lett.* **2010**, *10* (6), 2184–2191. https://doi.org/10.1021/nl100998p.
(179) Rico, P.; Hernández, J. C. R.; Moratal, D.; Altankov, G.; Pradas, M. M.; Salmerón-Sánchez, M. Substrate-Induced Assembly of Fibronectin into Networks: Influence of Surface Chemistry and Effect on Osteoblast Adhesion. *Tissue Eng. Part A* **2009**, *15* (11), 3271–3281. https://doi.org/10.1089/ten.tea.2009.0141.

(180) Baneyx, G.; Vogel, V. Self-Assembly of Fibronectin into Fibrillar Networks underneath Dipalmitoyl Phosphatidylcholine Monolayers: Role of Lipid Matrix and Tensile Forces. *Proc. Natl. Acad. Sci.* **1999**, *96* (22), 12518–12523. https://doi.org/10.1073/pnas.96.22.12518.
(181) Little, W. C.; Smith, M. L.; Ebneter, U.; Vogel, V. Assay to Mechanically Tune and Optically Probe Fibrillar Fibronectin Conformations from Fully Relaxed to Breakage. *Matrix Biol.* **2008**, *27* (5), 451–461. https://doi.org/10.1016/j.matbio.2008.02.003.
(182) Klotzsch, E.; Smith, M. L.; Kubow, K. E.; Muntwyler, S.; Little, W. C.; Beyeler, F.; Gourdon, D.; Nelson, B. J.; Vogel, V. Fibronectin Forms the Most Extensible Biological Fibers Displaying Switchable Force-Exposed Cryptic Binding Sites. *Proc. Natl. Acad. Sci.* **2009**, *106* (43), 18267–18272. https://doi.org/10.1073/pnas.0907518106.
(183) Ulmer, J.; Geiger, B.; Spatz, J. P. Force-Induced Fibronectin Fibrillogenesis in Vitro. *Soft Matter* **2008**, *4* (10), 1998. https://doi.org/10.1039/b808020h.
(184) Kaiser, P.; Spatz, J. P. Differential Adhesion of Fibroblast and Neuroblastoma Cells on Size- and Geometry-Controlled Nanofibrils of the Extracellular Matrix. *Soft Matter* **2010**, *6* (1), 113–119. https://doi.org/10.1039/B911461K.
(185) Patten, J.; Wang, K. Fibronectin in Development and Wound Healing. *Adv. Drug Deliv. Rev.* **2020**, No. xxxx. https://doi.org/10.1016/j.addr.2020.09.005.
(186) MOSHER, D. F.; FOGERTY, F. J.; CHERNOUSOV, M. A.; BARRY, E. L. R. R. Assembly of Fibronectin into Extracellular Matrix. *Ann. N. Y. Acad. Sci.* **1991**, *614* (1), 167–180. https://doi.org/10.1111/j.1749-6632.1991.tb43701.x.
(187) Liao, Y.-F.; Wieder, K. G.; Classen, J. M.; De Water, L. Van. *Identification of Two Amino Acids within the EIIIA (ED-A) Segment of Fibronectin Constituting the Epitope for Two Function-Blocking Monoclonal Antibodies* Downloaded From*; 1999; Vol. 274.
(188) Carnemolla, B.; Borsi, L.; Zardi, L.; Owens, R. J.; Baralle, F. E. Localization of the Cellular-Fibronectin-Specific Epitope Recognized by the Monoclonal Antibody IST-9 Using Fusion Proteins Expressed in E. Coli. *FEBS Lett.* **1987**, *215* (2), 269–273. https://doi.org/10.1016/0014-5793(87)80160-6.
(189) Borsi, L.; Arnemolla, B. C.; Castellani, P.; Rosellini, C.; Vecchio, D.; Allemanni, G.; Chang, S. E.; Taylor-Papadimitriou, J.; Pande, H.; Zardi, L. *Monoclonal Antibodies in the Analysis of Fibronectin Isoforms Generated by Alternative Splicing of MRNA Precursors in Normal and Transformed Human Cells Materials and Methods Materials*.
(190) Castellanos, M.; Leira, R.; Serena, J.; Blanco, M.; Pedraza, S.; Castillo, J.; Dávalos, A. Plasma Cellular-Fibronectin Concentration Predicts Hemorrhagic Transformation After Thrombolytic Therapy in Acute Ischemic Stroke. **2004**. https://doi.org/10.1161/01.STR.0000131656.47979.39.
(191) Leiss, M.; Beckmann, K.; Girós, A.; Costell, M.; Fässler, R. The Role of Integrin Binding Sites in Fibronectin Matrix Assembly in Vivo. *Curr. Opin. Cell Biol.* **2008**, *20* (5), 502–507. https://doi.org/10.1016/j.ceb.2008.06.001.
(192) Abe, Y.; Bui-Thanh, N.-A.; Ballantyne, C. M.; Burns, A. R. Extra Domain A and Type III Connecting Segment of Fibronectin in Assembly and Cleavage. *Biochem. Biophys. Res. Commun.* **2005**, *338* (3), 1640–1647. https://doi.org/10.1016/j.bbrc.2005.10.134.
(193) Manabe, R.; Oh-e, N.; Maeda, T.; Fukuda, T.; Sekiguchi, K. Modulation of Cell-Adhesive Activity of Fibronectin by the Alternatively Spliced EDA Segment. *J. Cell Biol.* **1997**, *139* (1), 295–307. https://doi.org/10.1083/jcb.139.1.295.
(194) Missirlis, D.; Haraszti, T.; Kessler, H.; Spatz, J. P. Fibronectin Promotes Directional

Persistence in Fibroblast Migration through Interactions with Both Its Cell-Binding and Heparin-Binding Domains. *Sci. Rep.* **2017**, *7* (1), 3711. https://doi.org/10.1038/s41598-017-03701-0.
(195) Sottile, J.; Hocking, D. C. Fibronectin Polymerization Regulates the Composition and Stability of Extracellular Matrix Fibrils and Cell-Matrix Adhesions. *Mol. Biol. Cell* **2002**, *13* (10), 3546–3559. https://doi.org/10.1091/mbc.e02-01-0048.
(196) Wang, W. Y.; Davidson, C. D.; Lin, D.; Baker, B. M. Actomyosin Contractility-Dependent Matrix Stretch and Recoil Induces Rapid Cell Migration. *Nat. Commun.* **2019**, *10* (1), 1186. https://doi.org/10.1038/s41467-019-09121-0.
(197) Wigmore, P. M.; Dunglison, G. F. The Generation of Fiber Diversity during Myogenesis. *Int. J. Dev. Biol.* **1998**, *42* (2), 117–125. https://doi.org/10.1387/IJDB.9551857.
(198) Huang, N. F.; Patel, S.; Thakar, R. G.; Wu, J.; Hsiao, B. S.; Chu, B.; Lee, R. J.; Li, S. Myotube Assembly on Nanofibrous and Micropatterned Polymers. *Nano Lett.* **2006**, *6* (3), 537–542. https://doi.org/10.1021/nl060060o.
(199) LeGrice, I. J.; Smaill, B. H.; Chai, L. Z.; Edgar, S. G.; Gavin, J. B.; Hunter, P. J. Laminar Structure of the Heart: Ventricular Myocyte Arrangement and Connective Tissue Architecture in the Dog. *Am. J. Physiol. Circ. Physiol.* **1995**, *269* (2), H571–H582. https://doi.org/10.1152/ajpheart.1995.269.2.H571.
(200) O'Brien, M. Anatomy of Tendons. In *Tendon Injuries*; Maffulli, N., Renström, P., Leadbetter, W. B., Eds.; Springer-Verlag: London, 2005; pp 3–13. https://doi.org/10.1007/1-84628-050-8_1.
(201) Lieber, R. L. *Skeletal Muscle Structure, Function, and Plasticity*; Julet, T., Ed.; Skeletal muscle structure, function and plasticity: the physiological basis of rehabilitation; Lippincott Williams & Wilkins, 2002.
(202) Ferguson, M. W. J.; O'Kane, S. Scar-Free Healing: From Embryonic Mechanism to Adult Therapeutic Intervention. *Philos. Trans. R. Soc. B Biol. Sci.* **2004**, *359* (1445), 839–850. https://doi.org/10.1098/rstb.2004.1475.
(203) Van Zuijlen, P. P. M.; Ruurda, J. J. B.; Van Veen, H. A.; Van Marle, J.; Van Trier, A. J. M.; Groenevelt, F.; Kreis, R. W.; Middelkoop, E. Collagen Morphology in Human Skin and Scar Tissue: No Adaptations in Response to Mechanical Loading at Joints. *Burns* **2003**, *29* (5), 423–431. https://doi.org/10.1016/S0305-4179(03)00052-4.
(204) Costa, K. D.; Lee, E. J.; Holmes, J. W. Creating Alignment and Anisotropy in Engineered Heart Tissue: Role of Boundary Conditions in a Model Three-Dimensional Culture System. *Tissue Eng.* **2003**, *9* (4), 567–577. https://doi.org/10.1089/107632703768247278.
(205) Chung, C.-Y.; Bien, H.; Entcheva, E. The Role of Cardiac Tissue Alignment in Modulating Electrical Function. *J. Cardiovasc. Electrophysiol.* **2007**, *18* (12), 1323–1329. https://doi.org/10.1111/j.1540-8167.2007.00959.x.
(206) Basan, M.; Elgeti, J.; Hannezo, E.; Rappel, W.-J.; Levine, H. Alignment of Cellular Motility Forces with Tissue Flow as a Mechanism for Efficient Wound Healing. *Proc. Natl. Acad. Sci.* **2013**, *110* (7), 2452–2459. https://doi.org/10.1073/pnas.1219937110.
(207) Bauer, A. L.; Jackson, T. L.; Jiang, Y. Topography of Extracellular Matrix Mediates Vascular Morphogenesis and Migration Speeds in Angiogenesis. *PLoS Comput. Biol.* **2009**, *5* (7), e1000445. https://doi.org/10.1371/journal.pcbi.1000445.
(208) Park, D.; Wershof, E.; Boeing, S.; Labernadie, A.; Jenkins, R. P.; George, S.; Trepat, X.; Bates, P. A.; Sahai, E. Extracellular Matrix Anisotropy Is Determined by TFAP2C-Dependent Regulation of Cell Collisions. *Nat. Mater.* **2020**, *19* (2), 227–238.

https://doi.org/10.1038/s41563-019-0504-3.
(209) Ray, A.; Lee, O.; Win, Z.; Edwards, R. M.; Alford, P. W.; Kim, D.-H.; Provenzano, P. P. Anisotropic Forces from Spatially Constrained Focal Adhesions Mediate Contact Guidance Directed Cell Migration. *Nat. Commun.* **2017**, *8*, 14923. https://doi.org/10.1038/ncomms14923.
(210) Torbet, J.; Malbouyres, M.; Builles, N.; Justin, V.; Roulet, M.; Damour, O.; Oldberg, Å.; Ruggiero, F.; Hulmes, D. J. S. Orthogonal Scaffold of Magnetically Aligned Collagen Lamellae for Corneal Stroma Reconstruction. *Biomaterials* **2007**, *28* (29), 4268–4276. https://doi.org/10.1016/j.biomaterials.2007.05.024.
(211) Wang, W. Y.; Pearson, A. T.; Kutys, M. L.; Choi, C. K.; Wozniak, M. A.; Baker, B. M.; Chen, C. S. Extracellular Matrix Alignment Dictates the Organization of Focal Adhesions and Directs Uniaxial Cell Migration. *APL Bioeng.* **2018**, *2* (4), 046107. https://doi.org/10.1063/1.5052239.
(212) Riching, K. M.; Cox, B. L.; Salick, M. R.; Pehlke, C.; Riching, A. S.; Ponik, S. M.; Bass, B. R.; Crone, W. C.; Jiang, Y.; Weaver, A. M.; Eliceiri, K. W.; Keely, P. J. 3D Collagen Alignment Limits Protrusions to Enhance Breast Cancer Cell Persistence. *Biophys. J.* **2014**, *107* (11), 2546–2558. https://doi.org/10.1016/j.bpj.2014.10.035.
(213) Guo, C.; Kaufman, L. J. Flow and Magnetic Field Induced Collagen Alignment. *Biomaterials* **2007**, *28* (6), 1105–1114. https://doi.org/10.1016/j.biomaterials.2006.10.010.
(214) Saeidi, N.; Sander, E. A.; Ruberti, J. W. Dynamic Shear-Influenced Collagen Self-Assembly. *Biomaterials* **2009**, *30* (34), 6581–6592. https://doi.org/10.1016/j.biomaterials.2009.07.070.
(215) Lanfer, B.; Freudenberg, U.; Zimmermann, R.; Stamov, D.; Körber, V.; Werner, C. Aligned Fibrillar Collagen Matrices Obtained by Shear Flow Deposition. *Biomaterials* **2008**, *29* (28), 3888–3895. https://doi.org/10.1016/j.biomaterials.2008.06.016.
(216) Ray, A.; Slama, Z. M.; Morford, R. K.; Madden, S. A.; Provenzano, P. P. Enhanced Directional Migration of Cancer Stem Cells in 3D Aligned Collagen Matrices. *Biophys. J.* **2017**, *112* (5), 1023–1036. https://doi.org/10.1016/j.bpj.2017.01.007.
(217) Missirlis, D.; Haraszti, T.; Scheele, C. V. C.; Wiegand, T.; Diaz, C.; Neubauer, S.; Rechenmacher, F.; Kessler, H.; Spatz, J. P. Substrate Engagement of Integrins A5β1 and Avβ3 Is Necessary, but Not Sufficient, for High Directional Persistence in Migration on Fibronectin. *Sci. Rep.* **2016**, *6* (1), 23258. https://doi.org/10.1038/srep23258.
(218) Chen, Y.; Zardi, L.; Peters, D. M. P. High-Resolution Cryo-Scanning Electron Microscopy Study of the Macromolecular Structure of Fibronectin Fibrils. *Scanning* **1997**, *19* (5), 349–355. https://doi.org/10.1002/sca.4950190505.
(219) Wojciak-Stothard, B.; Denyer, M.; Mishra, M.; Brown, R. A. Adhesion, Orientation, and Movement of Cells Cultured on Ultrathin Fibronectin Fibers. *Vitr. Cell. Dev. Biol. - Anim.* **1997**, *33* (2), 110–117. https://doi.org/10.1007/s11626-997-0031-4.
(220) Mitsi, M.; Handschin, S.; Gerber, I.; Schwartländer, R.; Klotzsch, E.; Wepf, R.; Vogel, V. The Ultrastructure of Fibronectin Fibers Pulled from a Protein Monolayer at the Air-Liquid Interface and the Mechanism of the Sheet-to-Fiber Transition. *Biomaterials* **2015**, *36*, 66–79. https://doi.org/10.1016/j.biomaterials.2014.08.012.
(221) Ballester-Beltrán, J.; Rico, P.; Moratal, D.; Song, W.; Mano, J. F.; Salmerón-Sánchez, M. Role of Superhydrophobicity in the Biological Activity of Fibronectin at the Cell–Material Interface. *Soft Matter* **2011**, *7* (22), 10803. https://doi.org/10.1039/c1sm06102j.
(222) Nemani, K. V; Moodie, K. L.; Brennick, J. B.; Su, A.; Gimi, B. In Vitro and in Vivo

Evaluation of SU-8 Biocompatibility. *Mater. Sci. Eng. C* **2013**, *33* (7), 4453–4459. https://doi.org/10.1016/j.msec.2013.07.001.
(223) Shinde, A.; Paez, J. S.; Libring, S.; Hopkins, K.; Solorio, L.; Wendt, M. K. Transglutaminase-2 Facilitates Extracellular Vesicle-Mediated Establishment of the Metastatic Niche. *Oncogenesis* **2020**, *9* (2), 16. https://doi.org/10.1038/s41389-020-0204-5.
(224) Wu, P. H.; Gilkes, D. M.; Wirtz, D. The Biophysics of 3D Cell Migration. *Annu. Rev. Biophys.* **2018**, *47*, 549–567. https://doi.org/10.1146/annurev-biophys-070816-033854.
(225) Humphries, B. A.; Buschhaus, J. M.; Chen, Y.-C.; Haley, H. R.; Qyli, T.; Chiang, B.; Shen, N.; Rajendran, S.; Cutter, A.; Cheng, Y.-H.; Chen, Y.-T.; Cong, J.; Spinosa, P. C.; Yoon, E.; Luker, K. E.; Luker, G. D. Plasminogen Activator Inhibitor 1 (PAI1) Promotes Actin Cytoskeleton Reorganization and Glycolytic Metabolism in Triple Negative Breast Cancer. *Mol. Cancer Res.* **2019**, *17* (5), 1142–1154. https://doi.org/10.1158/1541-7786.MCR-18-0836.
(226) Burridge, K.; Wittchen, E. S. The Tension Mounts: Stress Fibers as Force-Generating Mechanotransducers. *J. Cell Biol.* **2013**, *200* (1), 9–19. https://doi.org/10.1083/jcb.201210090.
(227) Pellegrin, S.; Mellor, H. Actin Stress Fibres. *J. Cell Sci.* **2007**, *120* (20), 3491–3499. https://doi.org/10.1242/jcs.018473.
(228) Persson, N. E.; Rafshoon, J.; Naghshpour, K.; Fast, T.; Chu, P.-H.; McBride, M.; Risteen, B.; Grover, M.; Reichmanis, E. High-Throughput Image Analysis of Fibrillar Materials: A Case Study on Polymer Nanofiber Packing, Alignment, and Defects in Organic Field Effect Transistors. *ACS Appl. Mater. Interfaces* **2017**, *9* (41), 36090–36102. https://doi.org/10.1021/acsami.7b10510.
(229) Wu, P.-H.; Giri, A.; Wirtz, D. Statistical Analysis of Cell Migration in 3D Using the Anisotropic Persistent Random Walk Model. *Nat. Protoc.* **2015**, *10* (3), 517–527. https://doi.org/10.1038/nprot.2015.030.
(230) Wu, P.-H.; Giri, A.; Sun, S. X.; Wirtz, D. Three-Dimensional Cell Migration Does Not Follow a Random Walk. *Proc. Natl. Acad. Sci.* **2014**, *111* (11), 3949–3954. https://doi.org/10.1073/pnas.1318967111.
(231) Ascione, F.; Vasaturo, A.; Caserta, S.; D'Esposito, V.; Formisano, P.; Guido, S. Comparison between Fibroblast Wound Healing and Cell Random Migration Assays in Vitro. *Exp. Cell Res.* **2016**, *347* (1), 123–132. https://doi.org/10.1016/j.yexcr.2016.07.015.
(232) Lauffenburger, D. A.; Horwitz, A. F. Cell Migration: A Physically Integrated Molecular Process. *Cell* **1996**, *84* (3), 359–369. https://doi.org/10.1016/S0092-8674(00)81280-5.
(233) Krause, M.; Gautreau, A. Steering Cell Migration: Lamellipodium Dynamics and the Regulation of Directional Persistence. *Nat. Rev. Mol. Cell Biol.* **2014**, *15* (9), 577–590. https://doi.org/10.1038/nrm3861.
(234) Shellard, A.; Mayor, R. All Roads Lead to Directional Cell Migration. *Trends Cell Biol.* **2020**, *30* (11), 852–868. https://doi.org/10.1016/j.tcb.2020.08.002.
(235) Park, J. S.; Kim, D. H.; Levchenko, A. Topotaxis: A New Mechanism of Directed Cell Migration in Topographic ECM Gradients. *Biophys. J.* **2018**, *114* (6), 1257–1263. https://doi.org/10.1016/j.bpj.2017.11.3813.
(236) Park, J.; Kim, D.-H.; Kim, H.-N.; Wang, C. J.; Kwak, M. K.; Hur, E.; Suh, K.-Y.; An, S. S.; Levchenko, A. Directed Migration of Cancer Cells Guided by the Graded Texture of the Underlying Matrix. *Nat. Mater.* **2016**, *15* (7), 792–801.

https://doi.org/10.1038/nmat4586.
(237) Hynes, R. O. The Evolution of Metazoan Extracellular Matrix. *J. Cell Biol.* **2012**, *196* (6), 671–679. https://doi.org/10.1083/jcb.201109041.
(238) Dicker, K. T.; Gurski, L. A.; Pradhan-Bhatt, S.; Witt, R. L.; Farach-Carson, M. C.; Jia, X. Hyaluronan: A Simple Polysaccharide with Diverse Biological Functions. *Acta Biomater.* **2014**, *10* (4), 1558–1570. https://doi.org/10.1016/j.actbio.2013.12.019.
(239) Wu, W.; Chen, L.; Wang, Y.; Jin, J.; Xie, X.; Zhang, J. Hyaluronic Acid Predicts Poor Prognosis in Breast Cancer Patients: A Protocol for Systematic Review and Meta Analysis. *Medicine (Baltimore).* **2020**, *99* (22), e20438. https://doi.org/10.1097/MD.0000000000020438.
(240) Auvinen, P.; Tammi, R.; Parkkinen, J.; Tammi, M.; Ågren, U.; Johansson, R.; Hirvikoski, P.; Eskelinen, M.; Kosma, V. M. Hyaluronan in Peritumoral Stroma and Malignant Cells Associates with Breast Cancer Spreading and Predicts Survival. *Am. J. Pathol.* **2000**, *156* (2), 529–536. https://doi.org/10.1016/S0002-9440(10)64757-8.
(241) Auvinen, P.; Tammi, R.; Kosma, V. M.; Sironen, R.; Soini, Y.; Mannermaa, A.; Tumelius, R.; Uljas, E.; Tammi, M. Increased Hyaluronan Content and Stromal Cell CD44 Associate with HER2 Positivity and Poor Prognosis in Human Breast Cancer. *Int. J. Cancer* **2013**, *132* (3), 531–539. https://doi.org/10.1002/ijc.27707.
(242) Wight, T. N. Provisional Matrix: A Role for Versican and Hyaluronan. *Matrix Biol.* **2017**, *60–61* (1), 38–56. https://doi.org/10.1016/j.matbio.2016.12.001.
(243) Toole, B. P. Hyaluronan: From Extracellular Glue to Pericellular Cue. *Nat. Rev. Cancer* **2004**, *4* (7), 528–539. https://doi.org/10.1038/nrc1391.
(244) Tammi, R. H.; Kultti, A.; Kosma, V.-M. M.; Pirinen, R.; Auvinen, P.; Tammi, M. I. Hyaluronan in Human Tumors: Pathobiological and Prognostic Messages from Cell-Associated and Stromal Hyaluronan. *Semin. Cancer Biol.* **2008**, *18* (4), 288–295. https://doi.org/10.1016/j.semcancer.2008.03.005.
(245) Bohaumilitzky, L.; Huber, A. K.; Stork, E. M.; Wengert, S.; Woelfl, F.; Boehm, H. A Trickster in Disguise: Hyaluronan's Ambivalent Roles in the Matrix. *Front. Oncol.* **2017**, *7* (OCT). https://doi.org/10.3389/fonc.2017.00242.
(246) Cowman, M. K. Hyaluronan and Hyaluronan Fragments. *Adv. Carbohydr. Chem. Biochem.* **2017**, *74*, 1–59. https://doi.org/10.1016/bs.accb.2017.10.001.
(247) Misra, S.; Hascall, V. C.; Markwald, R. R.; Ghatak, S. Interactions between Hyaluronan and Its Receptors (CD44, RHAMM) Regulate the Activities of Inflammation and Cancer. *Front. Immunol.* **2015**, *6* (MAY), 1–31. https://doi.org/10.3389/fimmu.2015.00201.
(248) Tian, X.; Azpurua, J.; Hine, C.; Vaidya, A.; Myakishev-Rempel, M.; Ablaeva, J.; Mao, Z.; Nevo, E.; Gorbunova, V.; Seluanov, A. High-Molecular-Mass Hyaluronan Mediates the Cancer Resistance of the Naked Mole Rat. *Nature* **2013**, *499* (7458), 346–349. https://doi.org/10.1038/nature12234.
(249) Holmes, M. W. A.; Bayliss, M. T.; Muir, H. Hyaluronic Acid in Human Articular Cartilage. Age-Related Changes in Content and Size. *Biochem. J.* **1988**, *250* (2), 435–441. https://doi.org/10.1042/bj2500435.
(250) Zeng, C.; Toole, B. P.; Kinney, S. D.; Kuo, J.; Stamenkovic, I. Inhibition of Tumor Growthin Vivo by Hyaluronan Oligomers. *Int. J. Cancer* **1998**, *77* (3), 396–401. https://doi.org/10.1002/(SICI)1097-0215(19980729)77:3<396::AID-IJC15>3.0.CO;2-6.
(251) Ghatak, S.; Misra, S.; Toole, B. P. Hyaluronan Oligosaccharides Inhibit Anchorage-Independent Growth of Tumor Cells by Suppressing the Phosphoinositide 3-Kinase/Akt

Cell Survival Pathway. *J. Biol. Chem.* **2002**, *277* (41), 38013–38020. https://doi.org/10.1074/jbc.M202404200.
(252) Fuchs, K.; Hippe, A.; Schmaus, A.; Homey, B.; Sleeman, J. P.; Orian-Rousseau, V. Opposing Effects of High-and Low-Molecular Weight Hyaluronan on CXCL12-Induced CXCR4 Signaling Depend on CD44. *Cell Death Dis.* **2013**, *4* (10). https://doi.org/10.1038/cddis.2013.364.
(253) Whatcott, C. J.; Han, H.; Von Hoff, D. D. Orchestrating the Tumor Microenvironment to Improve Survival for Patients with Pancreatic Cancer. *Cancer J. (United States)* **2015**, *21* (4), 299–306. https://doi.org/10.1097/PPO.0000000000000140.
(254) Gao, J. J.; Osgood, C. L.; Gong, Y.; Zhang, H.; Bloomquist, E. W.; Jiang, X.; Qiu, J.; Yu, J.; Song, P.; Rahman, N. A.; Chiu, H.-J.; Ricks, T. K.; Rizvi, F.; Hou, S.; Wilson, W.; Abukhdeir, A. M.; Seidman, J.; Ghosh, S.; Philip, R.; Pierce, W. F.; Bhatnagar, V.; Kluetz, P. G.; Pazdur, R.; Beaver, J. A.; Amiri-Kordestani, L. FDA Approval Summary: Pertuzumab, Trastuzumab, and Hyaluronidase–Zzxf Injection for Subcutaneous Use in Patients with HER2-Positive Breast Cancer. *Clin. Cancer Res.* **2021**, *27* (8), 2126–2129. https://doi.org/10.1158/1078-0432.CCR-20-3474.
(255) Lee, W. Comments on "Hyaluronidase: An Overview of Its Properties, Applications, and Side Effects." *Arch. Plast. Surg.* **2020**, *47* (6), 626–627. https://doi.org/10.5999/aps.2020.01571.
(256) Váradi, T.; Mersich, T.; Auvinen, P.; Tammi, R.; Tammi, M.; Salamon, F.; Besznyák, I.; Jakab, F.; Baranyai, Z.; Szöllosi, J.; Nagy, P. Binding of Trastuzumab to ErbB2 Is Inhibited by a High Pericellular Density of Hyaluronan. *J. Histochem. Cytochem.* **2012**, *60* (8), 567–575. https://doi.org/10.1369/0022155412448070.
(257) Skandalis, S. S.; Karalis, T. T.; Chatzopoulos, A.; Karamanos, N. K. Hyaluronan-CD44 Axis Orchestrates Cancer Stem Cell Functions. *Cell. Signal.* **2019**, *63*, 109377. https://doi.org/10.1016/j.cellsig.2019.109377.
(258) Karousou, E.; Misra, S.; Ghatak, S.; Dobra, K.; Götte, M.; Vigetti, D.; Passi, A.; Karamanos, N. K.; Skandalis, S. S. Roles and Targeting of the HAS/Hyaluronan/CD44 Molecular System in Cancer. *Matrix Biol.* **2017**, *59*, 3–22. https://doi.org/10.1016/j.matbio.2016.10.001.
(259) Müller, S.; Sindikubwabo, F.; Cañeque, T.; Lafon, A.; Versini, A.; Lombard, B.; Loew, D.; Wu, T.-D.; Ginestier, C.; Charafe-Jauffret, E.; Durand, A.; Vallot, C.; Baulande, S.; Servant, N.; Rodriguez, R. CD44 Regulates Epigenetic Plasticity by Mediating Iron Endocytosis. *Nat. Chem.* **2020**, *12* (10), 929–938. https://doi.org/10.1038/s41557-020-0513-5.
(260) Udabage, L.; Brownlee, G. R.; Nilsson, S. K.; Brown, T. J. The Over-Expression of HAS2, Hyal-2 and CD44 Is Implicated in the Invasiveness of Breast Cancer. *Exp. Cell Res.* **2005**, *310* (1), 205–217. https://doi.org/10.1016/j.yexcr.2005.07.026.
(261) Tammi, R.; MacCallum, D.; Hascall, V. C.; Pienimäki, J. P.; Hyttinen, M.; Tammi, M. Hyaluronan Bound to CD44 on Keratinocytes Is Displaced by Hyaluronan Decasaccharides and Not Hexasaccharides. *J. Biol. Chem.* **1998**, *273* (44), 28878–28888. https://doi.org/10.1074/jbc.273.44.28878.
(262) Cowman, M. K.; Lee, H. G.; Schwertfeger, K. L.; McCarthy, J. B.; Turley, E. A. The Content and Size of Hyaluronan in Biological Fluids and Tissues. *Front. Immunol.* **2015**, *6* (JUN), 1–8. https://doi.org/10.3389/fimmu.2015.00261.
(263) Schmaus, A.; Klusmeier, S.; Rothley, M.; Dimmler, A.; Sipos, B.; Faller, G.; Thiele, W.;

Allgayer, H.; Hohenberger, P.; Post, S.; Sleeman, J. P. Accumulation of Small Hyaluronan Oligosaccharides in Tumour Interstitial Fluid Correlates with Lymphatic Invasion and Lymph Node Metastasis. *Br. J. Cancer* **2014**, *111* (3), 559–567. https://doi.org/10.1038/bjc.2014.332.

(264) Gerecht, S.; Burdick, J. A.; Ferreira, L. S.; Townsend, S. A.; Langer, R.; Vunjak-Novakovic, G. Hyaluronic Acid Hydrogel for Controlled Self-Renewal and Differentiation of Human Embryonic Stem Cells. *Proc. Natl. Acad. Sci. U. S. A.* **2007**, *104* (27), 11298–11303. https://doi.org/10.1073/pnas.0703723104.

(265) Sapudom, J.; Ullm, F.; Martin, S.; Kalbitzer, L.; Naab, J.; Möller, S.; Schnabelrauch, M.; Anderegg, U.; Schmidt, S.; Pompe, T. Molecular Weight Specific Impact of Soluble and Immobilized Hyaluronan on CD44 Expressing Melanoma Cells in 3D Collagen Matrices. *Acta Biomater.* **2017**, *50*, 259–270. https://doi.org/10.1016/j.actbio.2016.12.026.

(266) Amorim, S.; Soares da Costa, D.; Pashkuleva, I.; Reis, C. A.; Reis, R. L.; Pires, R. A. 3D Hydrogel Mimics of the Tumor Microenvironment: The Interplay among Hyaluronic Acid, Stem Cells and Cancer Cells. *Biomater. Sci.* **2021**, *9* (1), 252–260. https://doi.org/10.1039/D0BM00843E.

(267) Bergman, K.; Elvingson, C.; Hilborn, J. J.; Svensk, G. G.; Bowden, T. Hyaluronic Acid Derivatives Prepared in Aqueous Media by Triazine-Activated Amidation. *Biomacromolecules* **2007**, *8* (7), 2190–2195. https://doi.org/10.1021/bm0701604.

(268) Wawryszyn, M. *Glycokonjugate - Strategien Und Moglichkeiten*, 1st ed.; Logos Verlag Berlin: Berlin, 2018.

(269) Bhattacharya, D. S.; Svechkarev, D.; Souchek, J. J.; Hill, T. K.; Taylor, M. A.; Natarajan, A.; Mohs, A. M. Impact of Structurally Modifying Hyaluronic Acid on CD44 Interaction. *J. Mater. Chem. B* **2017**, *5* (41), 8183–8192. https://doi.org/10.1039/C7TB01895A.

(270) Botha, C.; Kuntz, J.-F.; Moire, C.; Farcet, C.; Pfukwa, H.; Pasch, H. Molar Mass Analysis of Hydrophobically Modified Hyaluronic Acid by SEC-MALLS: Facing the Challenges of Amphiphilic Biomacromolecules. *Macromol. Chem. Phys.* **2018**, *219* (19), 1800233. https://doi.org/10.1002/macp.201800233.

(271) Banerji, S.; Wright, A. J.; Noble, M.; Mahoney, D. J.; Campbell, I. D.; Day, A. J.; Jackson, D. G. Structures of the Cd44–Hyaluronan Complex Provide Insight into a Fundamental Carbohydrate-Protein Interaction. *Nat. Struct. Mol. Biol.* **2007**, *14* (3), 234–239. https://doi.org/10.1038/nsmb1201.

(272) Jamison, F. W.; Foster, T. J.; Barker, J. A.; Hills, R. D.; Guvench, O. Mechanism of Binding Site Conformational Switching in the CD44–Hyaluronan Protein–Carbohydrate Binding Interaction. *J. Mol. Biol.* **2011**, *406* (4), 631–647. https://doi.org/10.1016/j.jmb.2010.12.040.

(273) Baneyx, G.; Baugh, L.; Vogel, V. Fibronectin Extension and Unfolding within Cell Matrix Fibrils Controlled by Cytoskeletal Tension. *Proc. Natl. Acad. Sci. U. S. A.* **2002**, *99* (8), 5139–5143. https://doi.org/10.1073/pnas.072650799.

(274) Baneyx, G.; Baugh, L.; Vogel, V. Coexisting Conformations of Fibronectin in Cell Culture Imaged Using Fluorescence Resonance Energy Transfer. *Proc. Natl. Acad. Sci. U. S. A.* **2001**, *98* (25), 14464–14468. https://doi.org/10.1073/pnas.251422998.

(275) Ou, J.; Deng, J.; Wei, X.; Xie, G.; Zhou, R.; Yu, L.; Liang, H. Fibronectin Extra Domain A (EDA) Sustains CD133+/CD44+ Subpopulation of Colorectal Cancer Cells. *Stem Cell Res.* **2013**, *11* (2), 820–833. https://doi.org/10.1016/j.scr.2013.05.009.

(276) Trujillo, S.; Vega, S. L.; Song, K. H.; San Félix, A.; Dalby, M. J.; Burdick, J. A.;

Salmeron-Sanchez, M. Engineered Full-Length Fibronectin–Hyaluronic Acid Hydrogels for Stem Cell Engineering. *Adv. Healthc. Mater.* **2020**, *2000989*, 2000989. https://doi.org/10.1002/adhm.202000989.

(277) Steier, A.; Muñiz, A.; Neale, D.; Lahann, J. Emerging Trends in Information-Driven Engineering of Complex Biological Systems. *Adv. Mater.* **2019**, *31* (26), 1806898. https://doi.org/10.1002/adma.201806898.

(278) Narkhede, A. A.; Crenshaw, J. H.; Crossman, D. K.; Shevde, L. A.; Rao, S. S. An in Vitro Hyaluronic Acid Hydrogel Based Platform to Model Dormancy in Brain Metastatic Breast Cancer Cells. *Acta Biomater.* **2020**, *107*, 65–77. https://doi.org/10.1016/j.actbio.2020.02.039.

(279) Zhao, Y. fang; Qiao, S. pei; Shi, S. liang; Yao, L. fen; Hou, X. lu; Li, C. feng; Lin, F. H.; Guo, K.; Acharya, A.; Chen, X. biao; Nie, Y.; Tian, W. ming; fang Zhao, Y.; pei Qiao, S.; liang Shi, S.; fen Yao, L.; lu Hou, X.; feng Li, C.; Lin, F. H.; Guo, K.; Acharya, A.; biao Chen, X.; Nie, Y.; ming Tian, W. Modulating Three-Dimensional Microenvironment with Hyaluronan of Different Molecular Weights Alters Breast Cancer Cell Invasion Behavior. *ACS Appl. Mater. Interfaces* **2017**, *9* (11), 9327–9338. https://doi.org/10.1021/acsami.6b15187.

(280) Kohda, D.; Morton, C. J.; Parkar, A. A.; Hatanaka, H.; Inagaki, F. M.; Campbell, I. D.; Day, A. J. Solution Structure of the Link Module: A Hyaluronan-Binding Domain Involved in Extracellular Matrix Stability and Cell Migration. *Cell* **1996**, *86* (5), 767–775. https://doi.org/10.1016/S0092-8674(00)80151-8.

(281) Yang, B. L.; Yang, B. L.; Savani, R. C.; Turley, E. A. Identification of a Common Hyaluronan Binding Motif in the Hyaluronan Binding Proteins RHAMM, CD44 and Link Protein. *EMBO J.* **1994**, *13* (2), 286–296. https://doi.org/10.1002/j.1460-2075.1994.tb06261.x.

(282) Yuan, H.; Tank, M.; Alsofyani, A.; Shah, N.; Talati, N.; LoBello, J. C.; Kim, J. R.; Oonuki, Y.; de la Motte, C. A.; Cowman, M. K. Molecular Mass Dependence of Hyaluronan Detection by Sandwich ELISA-like Assay and Membrane Blotting Using Biotinylated Hyaluronan Binding Protein. *Glycobiology* **2013**, *23* (11), 1270–1280. https://doi.org/10.1093/glycob/cwt064.

(283) Bano, F.; Banerji, S.; Howarth, M.; Jackson, D. G.; Richter, R. P. A Single Molecule Assay to Probe Monovalent and Multivalent Bonds between Hyaluronan and Its Key Leukocyte Receptor CD44 under Force. *Sci. Rep.* **2016**, *6* (1), 34176. https://doi.org/10.1038/srep34176.

(284) Banerji, S.; Hide, B. R. S.; James, J. R.; Noble, M. E. M.; Jackson, D. G. Distinctive Properties of the Hyaluronan-Binding Domain in the Lymphatic Endothelial Receptor Lyve-1 and Their Implications for Receptor Function. *J. Biol. Chem.* **2010**, *285* (14), 10724–10735. https://doi.org/10.1074/jbc.M109.047647.

(285) Hewitt, R.; Powe, D.; Morrell, K.; Balley, E.; Leach, I.; Ellis, I.; Turner, D. Laminin and Collagen IV Subunit Distribution in Normal and Neoplastic Tissues of Colorectum and Breast. *Br. J. Cancer* **1997**, *75* (2), 221–229. https://doi.org/10.1038/bjc.1997.37.

(286) Polyak, K.; Weinberg, R. A. Transitions between Epithelial and Mesenchymal States: Acquisition of Malignant and Stem Cell Traits. *Nat. Rev. Cancer* **2009**, *9* (4), 265–273. https://doi.org/10.1038/nrc2620.

(287) Di Martino, J. S.; Akhter, T.; Bravo-Cordero, J. J. Remodeling the Ecm: Implications for Metastasis and Tumor Dormancy. *Cancers (Basel).* **2021**, *13* (19).

https://doi.org/10.3390/cancers13194916.
(288) Bissell, M. J.; Hall, H. G.; Parry, G. How Does the Extracellular Matrix Direct Gene Expression? *J. Theor. Biol.* **1982**, *99* (1), 31–68. https://doi.org/10.1016/0022-5193(82)90388-5.
(289) Shimpi, A. A.; Fischbach, C. Engineered ECM Models: Opportunities to Advance Understanding of Tumor Heterogeneity. *Curr. Opin. Cell Biol.* **2021**, *72*, 1–9. https://doi.org/10.1016/j.ceb.2021.04.001.
(290) Kaplan, R. N.; Riba, R. D.; Zacharoulis, S.; Bramley, A. H.; Vincent, L.; Costa, C.; MacDonald, D. D.; Jin, D. K.; Shido, K.; Kerns, S. A.; Zhu, Z.; Hicklin, D.; Wu, Y.; Port, J. L.; Altorki, N.; Port, E. R.; Ruggero, D.; Shmelkov, S. V.; Jensen, K. K.; Rafii, S.; Lyden, D. VEGFR1-Positive Haematopoietic Bone Marrow Progenitors Initiate the Pre-Metastatic Niche. *Nature* **2005**, *438* (7069), 820–827. https://doi.org/10.1038/nature04186.
(291) Braun, S.; Vogl, F. D.; Naume, B.; Janni, W.; Osborne, M. P.; Coombes, R. C.; Schlimok, G.; Diel, I. J.; Gerber, B.; Gebauer, G.; Pierga, J.-Y.; Marth, C.; Oruzio, D.; Wiedswang, G.; Solomayer, E.-F.; Kundt, G.; Strobl, B.; Fehm, T.; Wong, G. Y. C.; Bliss, J.; Vincent-Salomon, A.; Pantel, K. A Pooled Analysis of Bone Marrow Micrometastasis in Breast Cancer. *N. Engl. J. Med.* **2005**, *353* (8), 793–802. https://doi.org/10.1056/nejmoa050434.
(292) Nelson, M. R.; Roy, K. Bone-Marrow Mimicking Biomaterial Niches for Studying Hematopoietic Stem and Progenitor Cells. *J. Mater. Chem. B* **2016**, *4* (20), 3490–3503. https://doi.org/10.1039/C5TB02644J.
(293) Hill, B. S.; Sarnella, A.; D'Avino, G.; Zannetti, A. Recruitment of Stromal Cells into Tumour Microenvironment Promote the Metastatic Spread of Breast Cancer. *Semin. Cancer Biol.* **2020**, *60* (July 2019), 202–213. https://doi.org/10.1016/j.semcancer.2019.07.028.
(294) Adamo, A.; Delfino, P.; Gatti, A.; Bonato, A.; Takam Kamga, P.; Bazzoni, R.; Ugel, S.; Mercuri, A.; Caligola, S.; Krampera, M. HS-5 and HS-27A Stromal Cell Lines to Study Bone Marrow Mesenchymal Stromal Cell-Mediated Support to Cancer Development. *Front. Cell Dev. Biol.* **2020**, *8* (November), 1–13. https://doi.org/10.3389/fcell.2020.584232.
(295) Buschhaus, J. M.; Humphries, B. A.; Eckley, S. S.; Robison, T. H.; Cutter, A. C.; Rajendran, S.; Haley, H. R.; Bevoor, A. S.; Luker, K. E.; Luker, G. D. Targeting Disseminated Estrogen-Receptor-Positive Breast Cancer Cells in Bone Marrow. *Oncogene* **2020**, *39* (34), 5649–5662. https://doi.org/10.1038/s41388-020-01391-z.
(296) Li, Y.; Li, L.; Brown, T. J.; Heldin, P. Silencing of Hyaluronan Synthase 2 Suppresses the Malignant Phenotype of Invasive Breast Cancer Cells. *Int. J. Cancer* **2007**, *120* (12), 2557–2567. https://doi.org/10.1002/ijc.22550.
(297) Jariyal, H.; Gupta, C.; Srivastava, A. Hyaluronic Acid Induction on Breast Cancer Stem Cells Unfolds Subtype Specific Variations in Stemness and Epithelial-to-Mesenchymal Transition. *Int. J. Biol. Macromol.* **2020**, *160*, 1078–1089. https://doi.org/10.1016/j.ijbiomac.2020.05.236.
(298) Porsch, H.; Bernert, B.; Mehić, M.; Theocharis, A. D.; Heldin, C.-H.; Heldin, P. Efficient TGFβ-Induced Epithelial–Mesenchymal Transition Depends on Hyaluronan Synthase HAS2. *Oncogene* **2013**, *32* (37), 4355–4365. https://doi.org/10.1038/onc.2012.475.
(299) Albeiroti, S.; Soroosh, A.; De La Motte, C. A. Hyaluronan's Role in Fibrosis: A Pathogenic Factor or a Passive Player? *Biomed Res. Int.* **2015**, *2015*.

https://doi.org/10.1155/2015/790203.
(300) Evanko, S. P.; Potter-Perigo, S.; Petty, L. J.; Workman, G. A.; Wight, T. N. Hyaluronan Controls the Deposition of Fibronectin and Collagen and Modulates TGF-B1 Induction of Lung Myofibroblasts. *Matrix Biol.* **2015**, *42*, 74–92. https://doi.org/10.1016/j.matbio.2014.12.001.
(301) Cicalese, A.; Bonizzi, G.; Pasi, C. E.; Faretta, M.; Ronzoni, S.; Giulini, B.; Brisken, C.; Minucci, S.; Di Fiore, P. P.; Pelicci, P. G. The Tumor Suppressor P53 Regulates Polarity of Self-Renewing Divisions in Mammary Stem Cells. *Cell* **2009**, *138* (6), 1083–1095. https://doi.org/10.1016/j.cell.2009.06.048.
(302) Pece, S.; Tosoni, D.; Confalonieri, S.; Mazzarol, G.; Vecchi, M.; Ronzoni, S.; Bernard, L.; Viale, G.; Pelicci, P. G.; Di Fiore, P. P. Biological and Molecular Heterogeneity of Breast Cancers Correlates with Their Cancer Stem Cell Content. *Cell* **2010**, *140* (1), 62–73. https://doi.org/10.1016/j.cell.2009.12.007.
(303) Dontu, G.; Abdallah, W. M.; Foley, J. M.; Jackson, K. W.; Clarke, M. F.; Kawamura, M. J.; Wicha, M. S. In Vitro Propagation and Transcriptional Profiling of Human Mammary Stem/Progenitor Cells. *Genes Dev.* **2003**, *17* (10), 1253–1270. https://doi.org/10.1101/gad.1061803.
(304) Liu, S.; Cong, Y.; Wang, D.; Sun, Y.; Deng, L.; Liu, Y.; Martin-Trevino, R.; Shang, L.; McDermott, S. P. P.; Landis, M. D. D.; Hong, S.; Adams, A.; D'Angelo, R.; Ginestier, C.; Charafe-Jauffret, E.; Clouthier, S. G. G.; Birnbaum, D.; Wong, S. T. T.; Zhan, M.; Chang, J. C. C.; Wicha, M. S. S.; D'Angelo, R.; Ginestier, C.; Charafe-Jauffret, E.; Clouthier, S. G. G.; Birnbaum, D.; Wong, S. T. T.; Zhan, M.; Chang, J. C. C.; Wicha, M. S. S. Breast Cancer Stem Cells Transition between Epithelial and Mesenchymal States Reflective of Their Normal Counterparts. *Stem Cell Reports* **2014**, *2* (1), 78–91. https://doi.org/10.1016/j.stemcr.2013.11.009.
(305) Brooks, M. D.; Burness, M. L.; Wicha, M. S. Therapeutic Implications of Cellular Heterogeneity and Plasticity in Breast Cancer. *Cell Stem Cell* **2015**, *17* (3), 260–271. https://doi.org/10.1016/j.stem.2015.08.014.
(306) Al-Hajj, M.; Wicha, M. S.; Benito-Hernandez, A.; Morrison, S. J.; Clarke, M. F. Prospective Identification of Tumorigenic Breast Cancer Cells. *Proc. Natl. Acad. Sci. U. S. A.* **2003**, *100* (7), 3983–3988. https://doi.org/10.1073/pnas.0530291100.
(307) Ginestier, C.; Hur, M. H.; Charafe-Jauffret, E.; Monville, F.; Dutcher, J.; Brown, M.; Jacquemier, J.; Viens, P.; Kleer, C. G.; Liu, S.; Schott, A.; Hayes, D.; Birnbaum, D.; Wicha, M. S.; Dontu, G. ALDH1 Is a Marker of Normal and Malignant Human Mammary Stem Cells and a Predictor of Poor Clinical Outcome. *Cell Stem Cell* **2007**, *1* (5), 555–567. https://doi.org/10.1016/j.stem.2007.08.014.
(308) Barkan, D.; Kleinman, H.; Simmons, J. L.; Asmussen, H.; Kamaraju, A. K.; Hoenorhoff, M. J.; Liu, Z. Y.; Costes, S. V.; Cho, E. H.; Lockett, S.; Khanna, C.; Chambers, A. F.; Green, J. E. Inhibition of Metastatic Outgrowth from Single Dormant Tumor Cells by Targeting the Cytoskeleton. *Cancer Res.* **2008**, *68* (15), 6241–6250. https://doi.org/10.1158/0008-5472.CAN-07-6849.
(309) Barney, L. E.; Hall, C. L.; Schwartz, A. D.; Parks, A. N.; Sparages, C.; Galarza, S.; Platt, M. O.; Mercurio, A. M.; Peyton, S. R. Tumor Cell-Organized Fibronectin Maintenance of a Dormant Breast Cancer Population. *Sci. Adv.* **2020**, *6* (11), 1–13. https://doi.org/10.1126/sciadv.aaz4157.
(310) Li, W.; Ma, H.; Zhang, J.; Zhu, L.; Wang, C.; Yang, Y. Unraveling the Roles of

CD44/CD24 and ALDH1 as Cancer Stem Cell Markers in Tumorigenesis and Metastasis. *Sci. Rep.* **2017**, *7* (1), 13856. https://doi.org/10.1038/s41598-017-14364-2.
(311) Simeonov, K. P.; Byrns, C. N.; Clark, M. L.; Norgard, R. J.; Martin, B.; Stanger, B. Z.; Shendure, J.; McKenna, A.; Lengner, C. J. Single-Cell Lineage Tracing of Metastatic Cancer Reveals Selection of Hybrid EMT States. *Cancer Cell* **2021**, *39* (8), 1150-1162.e9. https://doi.org/10.1016/j.ccell.2021.05.005.
(312) Burdick, J. A.; Prestwich, G. D. Hyaluronic Acid Hydrogels for Biomedical Applications. *Adv. Mater.* **2011**, *23* (12), H41–H56. https://doi.org/10.1002/adma.201003963.
(313) Szklanny, A. A.; Neale, D. B.; Lahann, J.; Levenberg, S. Stepwise Cell Seeding on Tessellated Scaffolds to Study Sprouting Blood Vessels. *J. Vis. Exp.* **2021**, *2021* (167), 1–19. https://doi.org/10.3791/61995.
(314) Lu, H.; Hoshiba, T.; Kawazoe, N.; Chen, G. Comparison of Decellularization Techniques for Preparation of Extracellular Matrix Scaffolds Derived from Three-Dimensional Cell Culture. *J. Biomed. Mater. Res. Part A* **2012**, *100A* (9), n/a-n/a. https://doi.org/10.1002/jbm.a.34150.
(315) Szklanny, A. A.; Debbi, L.; Merdler, U.; Neale, D.; Muñiz, A.; Kaplan, B.; Guo, S.; Lahann, J.; Levenberg, S. High-Throughput Scaffold System for Studying the Effect of Local Geometry and Topology on the Development and Orientation of Sprouting Blood Vessels. *Adv. Funct. Mater.* **2020**, *30* (18), 1901335. https://doi.org/10.1002/adfm.201901335.
(316) Miller, J. S.; Stevens, K. R.; Yang, M. T.; Baker, B. M.; Nguyen, D.-H. T.; Cohen, D. M.; Toro, E.; Chen, A. A.; Galie, P. A.; Yu, X.; Chaturvedi, R.; Bhatia, S. N.; Chen, C. S. Rapid Casting of Patterned Vascular Networks for Perfusable Engineered Three-Dimensional Tissues. *Nat. Mater.* **2012**, *11*. https://doi.org/10.1038/NMAT3357.
(317) Gariboldi, M. I.; Butler, R.; Best, S. M.; Cameron, R. E. Engineering Vasculature : Architectural Effects on Microcapillary-like Structure Self-Assembly. *PLoS One* **2019**, *14* (1), 1–13. https://doi.org/10.1371/journal.pone.0210390.
(318) Blache, U.; Guerrero, J.; Güven, S.; Klar, A. S.; Scherberich, A. Microvascular Networks and Models, In Vitro Formation. In *Vascularization for Tissue Engineering and Regenerative Medicine*; Springer International Publishing, 2018; pp 1–40. https://doi.org/10.1007/978-3-319-21056-8_9-1.
(319) Wong, K. H. K.; Chan, J. M.; Kamm, R. D.; Tien, J. Microfluidic Models of Vascular Functions. *Annu. Rev. Biomed. Eng.* **2012**, *14* (1), 205–230. https://doi.org/10.1146/annurev-bioeng-071811-150052.
(320) Jansen, K. A.; Bacabac, R. G.; Piechocka, I. K.; Koenderink, G. H. Cells Actively Stiffen Fibrin Networks by Generating Contractile Stress. *Biophys. J.* **2013**, *105* (10), 2240–2251. https://doi.org/10.1016/j.bpj.2013.10.008.
(321) Pollet, A. M. A. O.; den Toonder, J. M. J. Recapitulating the Vasculature Using Organ-on-Chip Technology. *Bioengineering*. MDPI AG March 2020. https://doi.org/10.3390/bioengineering7010017.
(322) Hasan, A.; Paul, A.; Vrana, N. E.; Zhao, X.; Memic, A.; Hwang, Y. S.; Dokmeci, M. R.; Khademhosseini, A. Microfluidic Techniques for Development of 3D Vascularized Tissue. *Biomaterials*. Elsevier Ltd 2014, pp 7308–7325. https://doi.org/10.1016/j.biomaterials.2014.04.091.
(323) Gauvin, R.; Chen, Y.-C.; Lee, J. W.; Soman, P.; Zorlutuna, P.; Nichol, J. W.; Bae, H.; Chen, S.; Khademhosseini, A. Microfabrication of Complex Porous Tissue Engineering

Scaffolds Using 3D Projection Stereolithography. *Biomaterials* **2012**, *33* (15), 3824–3834. https://doi.org/10.1016/J.BIOMATERIALS.2012.01.048.
(324) Coscoy, S.; Baiz, S.; Octon, J.; Rhoné, B.; Perquis, L.; Tseng, Q.; Amblard, F.; Semetey, V. Microtopographies Control the Development of Basal Protrusions in Epithelial Sheets. *Biointerphases* **2018**, *13* (4), 041003. https://doi.org/10.1116/1.5024601.
(325) Frampton, J. P.; White, J. B.; Simon, A. B.; Tsuei, M.; Paczesny, S.; Takayama, S. Aqueous Two-Phase System Patterning of Detection Antibody Solutions for Cross-Reaction-Free Multiplex ELISA. *Sci. Rep.* **2015**, *4* (1), 4878. https://doi.org/10.1038/srep04878.